
# A new semi-empirical method based on a distorted tetragonal scheme for the structure prediction and alloy design of multiple-component alloys

**By:**

Zhao Yuan, Leong

A thesis submitted in partial fulfilment for the degree of Doctor of Philosophy

The University of Sheffield

Faculty of Engineering

Department of Materials Science & Engineering

6th October 2016

## Abstract

High Entropy Alloys (HEA) are many-component (>4), near equiatomic compositions that by definition, forms disordered single phases, but are also known to form ordered phases such as C14 Laves, B2, Sigma etc. Understanding of the HEA phase stability is limited due to lack of knowledge of HEA thermodynamics as their stoichiometry is located at, or near the centre of their corresponding phase diagrams. Utilising HEAs in industrial and/or functional applications requires this understanding for successful design of HEA compositions. The original contribution of this thesis is the development of a simple, semi-empirical model that allows the prediction of some HEA properties (relative phase stability, hardness) that can be easily implemented. The model is developed through initial analysis of HEAs exploring the influence of the electronic density on phase stability utilising the Thomas-Fermi-Dirac equation for constrained neutral atoms; and the influence of a possible reduction in valence orbital degeneracy due to the breaking of symmetry from changes in phase. The hypotheses formed from this analysis are further compared with robust ab-initio calculations following the Rigid Band Approximation within Density Functional theory. The final two chapters examine the construction of the proposed model and its refinement; experimental validation of the model is performed through an engineering of a possible replacement for the Stellite family of Co-Cr alloys, which has been optimised for wear resistance. Experimental validation shows good results with respect to the predicted values.

# 1. Preface

## 1.1 Publications

List of included publications:

I. **Electron Density analysis of multi-principal component alloys through the fourth-order Runge-Kutta solution of the Thomas-Fermi-Dirac equation**
   Zhaoyuan Leong, Russell Goodall, Iain Todd.
   *Physics Review Letters, In peer-review.*

II. **The Effect of Electronic Structure on the Phases Present in High-Entropy Alloys**
   Zhaoyuan Leong, Jan S. Wróbel, Sergei L. Dudarev, Russell Goodall, Iain Todd, Duc Nguyen-Manh.
   *Nature Scientific Reports, Accepted.*

Comments on contribution:

I. Experimental (100%), Calculations (100%), Analysis (100%), Data presentation (100%), Literature review (100%), and Writing (100%).
II. Experimental (100%), Calculations (__0%), Analysis (_50%), Data presentation (_90%), Literature review (100%), and Writing (_75%).

Other publications:

1. **Crystalline Structures of Some High Entropy Alloys Obtained by Neutron and X-ray Diffraction**, U. Dahlborg, J. Cornide, M. Calvo-Dahlborg, T. Hansen, Z. Leong, L. Asensio Dominguez, S. Chambreland, A. Cunliffe, R. Goodall, and I. Todd, *Acta Physica Polonica A, 2015.*
2. **Combined Atom Probe Tomography and TEM Investigations of CoCrFeNi, CoCrFeNi-Pd x (x=0.5, 1.0 and 1.5) and CoCrFeNi-Sn**, U. Dahlborg, J. Cornide, M. Calvo-Dahlborg, T. Hansen, Z. Leong, L. Asensio Dominguez, S. Chambreland, A. Cunliffe, R. Goodall, and I. Todd, *Acta Physica Polonica A, 2015.*
3. **Structure and properties of some CoCrFeNi-based high entropy alloys,** J. Cornide, U. Dahlborg, Z. Leong, L. Asensio Dominguez, J. Jurasze, S. Jouen, T. Hansen, R. Wunderlich, S. Chambreland, I. Todd, R. Goodall and M. Calvo-Dahlborg, *TMS 2015 Supplemental Proceedings*, 2015.
4. **Structure of some $CoCrFe_yNi$ and $CoCrFeNiPd_x$ multicomponent HEA alloys by diffraction techniques,** U. Dahlborg, J. Cornide, M. Calvo-Dahlborg, T.C. Hansen, A. Fitch, Z. Leong, S. Chambreland, and R. Goodall, *Journal of Alloys and Compounds,* 2016.

## 1.2 Acknowledgements

First and foremost I would like to thank Russell Goodall for his tremendous encouragement in the course of supervising this project as his keen eye for the silver lining has kept me going more than once, and in also for both allowing me the freedom to pursue whatever crazy ideas I may have come up with but always guiding me back to the path when I do (inevitably) stray.

Next, I would like to express my gratitude to Iain Todd, from whom my enthusiasm for research was developed during my Master's project and encouraged me to pursue the PhD, and continued to guide and offer invaluable advice throughout the PhD.

I also value the advice given freely by Pearl Sullivan and Alvin Tan, which helped me with my decision of choosing between academia and industry; without which, this thesis would not have come into being.

Many thanks to my fellow rapid-solidification cohort. In no particular order, Phil Mahoney, Huang Yuhe, Gao Junheng, for their patience at my occasional self-mocking diatribes, help, friendship, and general advice on all things under the sun; Gautam Anand for the much-appreciated talks we have had on the theoretical tools of the trade. The technical staff at the department has also been superb and invaluable, and have helped in so many ways throughout all of the research work. I would like to in particular thank Paul Hawksworth for just being there to offer a word of advice whenever needed, especially during those days when the arc-melter was inevitably near-dead. Finally, I would like to express my gratitude for one particular individual who thinks himself divine, as his general nonchalance (and implicit support) when things going south - 'Where's the fun if it's easy?' has been a particular source of inspiration. You know who you are.

Finally, at the risk of sounding cliché, I would like to dedicate this thesis to my parents, who have provided a firm foundation on which to build all of this from. And of course, Phoebe, without whom life would be slightly different.

## Table of Contents

# 2. Literature review

## Table of Contents

## Symbols and Abbreviations

| | |
|---|---|
| $\delta$ | Atomic size mismatch |
| $\Delta H$ | Change in Enthalpy |
| $\Delta S$ | Change in Entropy |
| $\Delta G$ | Change in Gibbs free energy |
| $\nabla$ | Laplace operator |
| $\Omega$ | Empirical parameter used in HEA prediction defined as the ratio of $T_m/T_{crit}$ |
| $\mu$ | Chemical potential |
| BCC | Body-centred Cubic |
| C14 | C14 Laves Phase |
| CALPHAD | Computer coupling of phase diagrams and thermochemistry |
| $e$ | Rest charge of an electron |
| $E_F$ | Fermi energy |
| $E_{TF}$ | Thomas-Fermi energy |
| ELF | Electron localisation function |
| FCC | Face-centred Cubic |
| $\hbar$ | Reduced Planck constant |
| $\hat{H}$ | Hamiltonian |
| HEA | High-entropy Alloy |
| Hv | Hardness in units Vickers |
| m | Mass of a particle |
| $n_{WS}$ | Electron density at the Wigner-Seitz radius |
| $n(r)$ | Electron density |
| N | Number of electrons |
| $p(r)$ | Momentum operator |
| R | Gas constant |
| T | Temperature in units Kelvin |
| $T_{crit}$ | Critical temperature |
| $T_m$ | Melting temperature |
| $V(r)$ | Electrostatic potential |
| VEC | Valence Electron Concentration |
| $X_{Allen}$ | Allen electronegativity |
| Z | Atomic number |

## Tables of figures

## 2.1 Background

Until recently, it was accepted that the addition of too many elemental components in significant quantity into a solid solution to form an alloy would cause the formation of undesirable intermetallic structures that weaken its mechanical properties. This idea is grounded in several thermodynamic and phase diagram analyses that have been extrapolated from existing data. The design paradigm of alloys was thus restricted to mostly a single principal component with slight changes to the compositions (typically <10%) and/or through heat treatment to modify the microstructure. Alloying additions may also modify the chemical properties of the alloy, such as the addition of chromium to form stainless steel. Alloys that form simple phases with FCC, BCC, and some orthorhombic structures are preferred as they possess increased ductility (due to the availability of increased slip systems), allowing alloying additions to 'tune' the end-product's mechanical properties.

High-entropy Alloys (HEAs) are a recently developed class of alloy (near equimolar compositions consisting of >4 components) that challenge this perception. First reported as a curiosity by Cantor *et al.*, the equimolar 5-component CoCrFeNiMn composition (Alloying components for all compositions in this thesis are presented in atomic percent) was observed to be a FCC solid solution [1]. Further studies on equimolar multicomponent alloys have attributed the solid solution stabilisation mechanism to the increased entropy of mixing arising from its multiple components [2,3] – hence termed HEAs, as characterisation of this class of alloys show that for some, complex phases as predicted from thermodynamic databases do not form [2–5]. For ease of discussion in this thesis, the simple phase is defined as a phase derived from the FCC, BCC or HCP structures; with complex phases being those from all other structures [2] or with ordering [6]. Complex phases are also commonly referred to as intermetallics in other fields.

HEAs are also known as multi-component alloys in the open literature as the stabilisation effects of the simple phases have not yet been fully investigated [6–10] and there is disagreement over the attributes of entropy, i.e. which entropies (Mixing, magnetic, electronic, and vibrational) contribute to HEA phase stability. Characterisation of well-known simple-phase compositions such as CoCrFeNi and CoCrFeNiPd using advanced techniques such as neutron diffraction have shown the microstructure to be composed of

multiple simple FCC phases that possess similar lattice parameters [9]. Furthermore, heat treatment of CoCrFeNiMn has shown the precipitation of a complex phase at the grain boundaries [7], suggesting that many HEA compositions do not exist as a single solid solution, and are likely to be non-ideal thermodynamically [11]. Despite these results, the simple phases remain dominant in these compositions, allowing inferences, methods, parameters developed from previous analysis [12–16] to still remain relevant. In the following discussions the term HEA is used to apply not just to equimolar multi-component alloys, but also near equimolar compositions.

## 2.2 Relationship between properties and structure / composition

### 2.2.1 The conundrum of the single phase

The main critique behind the prediction of HEA phases from thermodynamic databases using the CALPHAD methodology is the lack of suitable databases for many component systems [2]. Early predictions on HEA systems by Durga *et al.* focused on Fe-containing HEAs, as the Fe thermodynamic databases have been extensively studied [4]. The predicted phases are found to be loosely in agreement with experimental results, with multiple phases being predicted, which has been attributed to a lack of ternary phase diagram [5]. Senkov *et al.'s* [5] subsequent improved CALPHAD methodology that includes consideration of binary and ternary systems shows that, even for these results, most of the predicted phases contain multiple simple phases (CoCrFeNi is predicted to contain FCC and Sigma phases; and CoCrFeNiMn FCC and BCC phases) [5], showing similar prediction trends to Durga [4] that are not present experimentally. Comparison of phases present at the melting temperature, however, shows good agreement with experiment [5], suggesting the non-equilibrium nature of these alloys [7] which may be attributed to the slow diffusion of HEAs [2]. This hypothesis was mainly based on secondary observations such as the retention of nanocrystals and its actual impact in HEA formation has been called into question [a1, a2]. Further discussion of this topic will be continued below.

The single phase nature of HEAs has been called into question as the structure of some HEAs were investigated utilising atom probe tomography and neutron diffraction [5] where CoCrFeNiCu [8,17] and CoCrFeNiPd [18] compositions were found to consist of multiple simple FCC phases that possess lattice parameters with very similar values. In the previously

mentioned CALPHAD studies the CoCrFeNiCu composition is predicted to contain two FCC phases at the melting temperature, and two FCC, BCC, and a Sigma phase at 600$^{o}$C [5]; and two FCC and two BCC phases by Durga *et al.* [4]. The presence of multiple simple FCC phases in the as-cast condition instead of the expected single phase solid solution is suggestive of the non-trivial nature of phase stabilities of the HEA class of alloys.

Furthermore CoCrFeNiMn, which has traditionally been considered to be a single simple phase HEA, forms complex Sigma phase precipitates at the grain boundaries on undergoing long duration heat treatment [7]. The authors of this communication, Pickering *et al.* suggest that HEAs may be inherently thermodynamically metastable. This argument is further strengthened by the grain-boundary precipitation observed in the CoCrFeNiMn composition under prolonged heat treatments between 500-700°C, as shown by Otto *et al.* [19].

The term metastable is used to indicate the timescale needed to achieve thermodynamic equilibrium, attributed to the slow diffusion arising from the multiple alloying components of different size [2]. Although precipitation of the Sigma phase is attributed to the thermodynamics of the system, these have not been explicitly considered. The thermodynamic parameters of HEAs will be discussed later below.

While the inherent instability of these structures is thus acknowledged, reported results have also shown that the CrFeCoNiMn solid-solution as-cast structure remains as the majority phase for heat-treatments when annealed below a defined temperature, unless: a) heat treated for 500h, at which point grain-boundary precipitates appear [7,19], or b) the composition is subjected to severe plastic deformation [20]. As such, although these compositions have been revealed to possess more complicated structures than previously thought, previous studies involving treatment of the system as a single simple phase can lead to good predictions of the majority structure [21–24], showing that a 'cocktail effect' [2] approximation may be used. These approximations involving HEAs are therefore used in the following analyses in this thesis.

Some key benefits that HEAs may bring to alloy development are:

1. The stabilised simple phase is retained as the majority structure near room temperatures and if not subjected to severe plastic deformation, and may be considered to be process-independent under these conditions [17].
2. The broad range of elements that can be included in the design of a HEA allow the tuning of beneficial chemical properties [21–25].
3. Careful control of a HEA composition's stoichiometry allows tuning of mechanical properties [21–24].

### 2.2.2 Hardness and mechanical properties

**Table 1.** Phases in HEAs according to their typical hardness values, with examplars of their corresponding phases [3].

| Type | Examples | Typical hardness (HV) |
|---|---|---|
| Valence compounds | Carbides, borides, silicides | 1000–4000 |
| Intermetallic phases with non-simple structures | $\sigma$, Laves, $\eta$ | 650–1300 |
| BCC and derivatives | BCC, B2, Heusler | 300–700 |
| FCC and derivatives | FCC, $L1_2$, $L1_0$ | 100–300 |

Due to the unique simple phase stabilising mechanisms of HEAs and the lack of a single principal element, their mechanical properties are very different from those of its constituent components. As a result the mechanical properties of HEAs require additional study, and are not yet fully explored, with those present in the literature limited to mainly compression and hardness testing [9–13]. From these studies, the mechanical properties of HEAs are found to rely on the mechanical and crystal structure of the alloy. With regards to the bulk hardness of the composition, this can be understood to depend on the volume fraction of each phase present, and the microstructure of the alloy [2]. Table 1 above illustrates the typical hardness shown by FCC, BCC, complex phases, and carbide-group compounds [3]. The carbide-group compounds exhibit highest hardness values associated with the covalent bonding of these compounds, followed by complex / intermetallic phases that demonstrate covalent-metallic bonding [27–30], and finally FCC / BCC phases that possess metallic bonding. Alloy hardness can thus be estimated with knowledge of the phase fraction and phase evolution and, as may be expected, alloys which contain complex phase stabilising elements are observed to be harder and less ductile. The stoichiometry of simple phase containing HEAs may be modified to include a higher proportion of complex phase stabilising components to control the phase fraction, increasing their mechanical

properties [21–25]. In line with estimates from the hardness of the phases, the yield strength of HEAs decreases as the transition from FCC to BCC phase with a corresponding increase in the Young's Modulus, as in the case for $FeCoNi(AlSi)_x$ alloys [31].

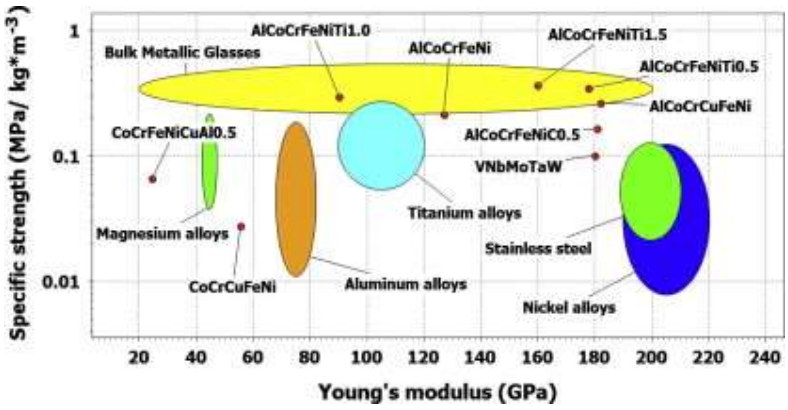


**Figure 1.** Structural map of HEA showing the occupying a large region in the structural map owing to the multiple selection of alloying compounds and tuneability of phase fraction depending on composition [14].

The structural map in Figure 1 above demonstrates the wide range of mechanical properties that HEAs may adopt, primarily attributed to the combination of phases that can be present. The effect of alloying a simple FCC phase CoCrFeNiMn HEA composition with Al additions to induce BCC formation on the mechanical properties was studied by He *et al.* [32]. The resultant hardness was found to be strongly dependent on the stable phase of the system as a result of the alloying addition with <8% Al (FCC), 9-16% (FCC-BCC), >17% (BCC), respectively. The hardness is observed to increase rapidly between additions of 9-16% of Al addition, achieving stable hardness values by 20% alloying addition. The tensile strength and ductility of the alloys are found to decrease with increasing alloying addition as may be expected from a FCC to BCC transition, as the BCC structure contains fewer slip planes. The 8-16% Al region demonstrates clearly the possibly of tuning the mechanical properties through its alloying addition so as to obtain a mixed-phase structure.

The effect of complex Sigma phase precipitation in equimolar CoCrFeNi, CoCrFeNiMn through the addition of V was studied by Salischev *et al.* [21], where the hardness was observed to increase from 160 HV (CoCrFeNi) to 524 HV (CoCrFeNiV), and from 170 HV (CoCrFeNiMn) to 650 HV (CoCrFeNiMnV). The tensile strength of the vanadium containing compositions reduced, exhibiting brittle fracture linked to the precipitation of the Sigma

phase. Precipitation of the Sigma phase is attributed to poor compatibility of vanadium with the other alloying elements, following HEA semi-empirical rules [16].

Other than the effect of the composition's structure, Sriharitha *et al.* attributed the strength of CoCrFeNiCuAl HEAs to grain size strengthening, solid solution strengthening, and order strengthening [33,34]. This solid solution hardening effect was further studied by Toda-Caraballo and Rivera-Díaz-del-Castillio [35], in which a prediction scheme to predict the effect of solid solution hardening on the mechanical properties of HEAs was developed. In the paper, the predicted yield strength was found to indeed, increase, in tandem with the experimental yield strength of several HEA compositions. A deviation from the linear trend was observed at increased yield stress values that are attributed to the presence of complex phase such as $Fe_2Ti$. This may be possibly attributed to the difference in the bonding mechanism of complex phases in the electronic structure, which may be expressed as a ratio of the bulk modulus to the shear modulus [36]. Lower ratios indicate increased directionality of bonding as the shear modulus increases, which lead to a corresponding increase in hardness [37].

### 2.2.3 Magnetic properties

There has been some evidence linking the phase and composition of HEAs to their magnetic properties, and magnetic phenomena as expected from behaviour of other magnetic systems. Zhang *et al.* in their communication show the $FeCoNi(AlSi)_x$ compositional family achieves higher saturated magnetisation than $CoCrFeNiAl_x$ due to the presence of the FCC phase. The higher atomic packing density of the simple FCC phase should lead to a higher total magnetic moment per unit volume than the simple BCC structure, or other complex structures [31], although a trade-off may be needed to obtain increased mechanical properties.

Despite possessing lower packing density of the BCC/B2 structure and its suggested lower saturated magnetisation, Kao *et al.* reports higher saturated magnetisation values the BCC $CoCrFeNiAl_{2.0}$ composition, than $CoCrFeNiAl_x$ (x = 0.25, 0.5, 0.75, 1.0, and 1.25) where FCC and mixed FCC-BCC simple phases are present [17]. Similarly, for Ti addition to the CoCrFeNi composition which results in the stabilisation of the complex Laves phase [22], which with lower packing density (0.71) than the simple FCC phase (0.74) may be expected to have lower saturated magnetisations, but these are reported to be higher. The unexpected

change may be a result of the change in bonding directionality at the atomic level when transitioning from the simple FCC structure to the complex Laves structure, leading to a deviation from Vegard's law [39], and thus the inapplicability of using the packing density to describe the magnetic moment per unit volume.

The saturated magnetisations measured by Shun *et al.* [22], with CoCrFeNi (1.51 Emu/g), $CoCrFeNiTi_{0.5}$ (0.33 Emu/g), $CoCrFeNiTi_{0.8}$ (1.37 Emu/g), and $CoCrFeNiTi_{1.0}$ (1.51 Emu/g) possess superparamagnetic-like properties, which were attributed to 'the appearance of nanoparticle assemblies embedded in the amorphous phase due to the increment of Ti addition'. However, the blocking temperature, $T_B$ and Curie temperature, $T_C$ for these compositions are in the region of 0-50k ($T_B$) and 100-150k($T_C$) making them unsuitable for practical use.

Development of HEA compositions with Curie temperatures near room temperature remains essential for them to be used as magnetic materials [18,40,41]. Investigations into $CoCrFeNiPd_x$ compositions have shown them to increase in saturated magnetisation at room temperature and Curie temperature [18]. The $T_C$ is found to be dependent on the amount of Pd addition and these results suggest that HEAs may be good materials for consideration as next-generation magnetocaloric materials. In following work, Lucas *et al.* investigate the dependency of the $T_C$ and magnetic entropy on $CoCr_xFeNi$ compositions as a function of Cr addition and mechanical deformation, where it is found that increased Cr addition and cold-rolling results in a higher $T_C$. It is suggested that the antiferromagnetic nature of Cr contributes to $T_C$ values [6].

The deleterious effect of Cr on $T_C$ is confirmed in detail by Kormann *et al.* [41], utilising Density Functional Theory in combination with Mean Field Theory to model the $T_C$ and saturated magnetisation behaviour of $CoCr_xFeNiA_y$ HEA alloys, where A = Ag, Au, Pd, and Cu. For $CoCr_xFeNiAg_y$, $CoCr_xFeNiAu_y$, $CoCr_xFeNiPd_y$, and $CoCr_xFeNiCu_y$ compositions studied, Cr addition was found to decrease both $T_C$ and saturated magnetisation.

While the magnetic behaviour of HEAs are accepted to vary depending on compositional additions [6,22,38], the dependence of the maximum magnetisation and Curie temperature is not easily described by changes in composition or structure, as it is affected by the spin-

orbit interaction at the atomic level. The magnetic interactions between atoms can affect the phase present in HEA compositions; Niu *et al.* [6] suggest that the influence of antiferromagnetic Cr in the CoCrFeNi composition leads to ordering in the structure that reduces the net magnetic moment of the structure to 36% that of the disordered structure. This ordering is driven by the energetic preference of antiferromagnetic Cr to spatially separate to lower the overall energy, and is shown by Klaver *et al.* [42] to exist for Cr solutes in a Fe solvent. It is noteworthy that in the work of Pickering *et al.* [7] on CoCrFeNiMn the phase that forms on heat treatment is Cr-rich. Additional work on ternary Fe-Cr-Ni alloy systems by Wrobel *et al.* [43] furthermore predicts the existence of an ordered structure existing near the middle of the phase diagram, corroborating Niu *et al.*'s [6] study. Magnetic frustration in CoCrFeNi alloys appears to be influenced by both alloy preparation methods as well as mechanical deformation; in Niu *et al.*'s [6] study a CoCrFeNi sample prepared through mechanical alloying (50 Emu/g) possessed a higher magnetisation as compared with a CoCrFeNi sample produced through the arc-melting and casting method (23 Emu/g). Furthermore mechanical deformation of the as-cast CoCrFeNi (26 Emu/g) is found to increase the magnetisation, in agreement with the results presented by Lucas *et al.* [40].

Despite the general agreement in trends of studies involving CoCrFeNi based compositions, the maximum magnetisation achieved between studies is found to vary, e.g. Niu *et al.* [6] report a value of 23 Emu/g for the as-cast CoCrFeni, Shun *et al.* [22] report a value of 1.51 Emu/g for CoCrFeni, Kao *et al.* [38] report 50 Emu/cc (Apx. 8 Emu/g), and Lucas *et al.* [18] report CoCrFeNi as paramagnetic in their 2011 paper. Inspection of the magnetic testing methods show that:

1. Not all of the alloys were tested at a temperature well below $T_C$
2. Only Niu *et al.* [6] performed measurements up to 198.9 kA/m (Apx 2,500 Oe) – Kao *et al.* [38] performed the measurements at 100 Oe while in the other communications the measurement fields were unspecified. As the $T_C$ of CoCrFeNi alloys is 130 [40], experiments that have been performed at temperatures above its $T_C$, and below the field required for saturation magnetisation may not fully reveal information on the nature of CoCrFeNi, or indeed, any HEA composition's spin properties resulting from the Pauli exclusion principle.

## 2.3 Core stabilisation effects

The simple phases that are surprisingly present in HEAs are of primary interest in the field as many properties are strongly dependent on the phase present. The alloying components in HEAs also contribute to their properties, and also affect the phase formed. The ability to predict phase stabilities of new compositions is thus essential to a HEA development strategy. Yeh *et al.* [3] present several core simple-phase stabilisation effects, identified as:

1. High-entropy effect: HEAs form simple phases contradicting predictions from the Gibbs phase rule that is attributed to the high mixing entropy, due to the multiple principal components existing in near-equiatomic ratios, resulting in the solubility range being pushed lower into simple phase formation.
2. Cocktail effect: HEA components interact in a complex way to determine the properties. The addition of Al to CoCrFeNiCu is given by Tsai *et al.* [2] as an example, where Al is a simple FCC structure with low-melting point and the relatively weak bonds that on addition hardens the CoCrFeNiCuAl composition partly due to the formation of a simple BCC structure, and partly due to the bonding effects exhibited by Al. The macroscopic properties of HEAs are hence a function of both the interatomic interaction between alloying components, and the structure.
3. The sluggish diffusion effect: Diffusion in HEAs is thought to be slower than conventional alloys [44]. This is attributed to large differences in the atomic environment of the multi component solid solution, there will be a fluctuation in the lattice potential energy that leads to a lower diffusion rate [45]. This is affected by 1. Different diffusion rates of each alloying component due to the size difference, and 2. A minimising of the energy through the formation of local configurations. When an atom moves into a new vacancy it will not be as preferable to move it from a low energy to a higher energy site. Diffusion effects are thus thought to require a longer amount of time and allows for better high-temperature strength and structural stability. In their study, Tsai *et al.* [45] showed that the diffusion of Ni in CoCrFeNiMn is 50% higher than in Cr-Fe-Ni. The recent discovery of a complex Sigma phase in heat-treated CoCrFeNiMn [7] that was is also attributed to sluggish diffusion effects.
4. The lattice distortion effect – The size difference between alloying elements of HEAs are thought to contribute to a lattice distortion effect that leads to solid solution

strengthening. This effect may also allow the tuning of electrical properties and $T_c$ [46].

Of the four identified HEA stabilisation effects, the high entropy effect may be described by thermodynamic parameters of the entropy of mixing and enthalpy of mixing; the cocktail effect may be considered to be derived from the interaction between the valence electrons of each contribution; and both the sluggish diffusion and lattice distortion effects are linked through the atomic size difference and enthalpy of mixing [47]. Collectively, these effects that affect HEA phase stability may be sub-divided into thermodynamic-based parameters and parameters based on the Hume-Rothery rules of alloying.

Of the remaining two effects, the most controversial in current literature is the sluggish diffusion effect [a1, a2]. The hypothesis was initially reliant on secondary observations (of precipitations of nanocrystals in HEA compositions); further tests done to validate the hypothesis have offered mixed results. One issue is that the current data available is unable to validate this hypothesis; instead analysis of measured diffusion values for the $CoCrFeMn_{0.5}Ni$ composition are found to be actually higher than in conventional materials [a1]. Current diffusion data is very limited, and validation of this hypothesis will required high-quality experimental diffusion data for a variety of compositions.

### 2.3.1 Thermodynamic parameters

An introduction to thermodynamics is briefly given before proceeding into some analyses from literature into the role of thermodynamics in HEAs. The study of thermodynamics relates natural phenomena to the quantity of energy exchanged between a system and its surroundings. The measureable properties in any system are linked through a relationship describing the state of the system, which may be expressed as a state function:

$$P = f(N, V, T) \tag{1}$$

where P is the pressure, V is the volume, N is the number of moles, and T is the temperature in Kelvin. As a consequence of the first law of thermodynamics, the change internal energy, $\Delta U$ is defined as the sum of the heat input, Q into the system and the work done by the system, W:

$$\Delta U = Q - W \tag{2}$$

The second and third law of thermodynamics introduce entropy change, $\Delta S$, which in statistical thermodynamics is a delocalisation of energy caused by the change from a system with fewer available microstates to one with an increased number of available microstates for occupation [48]. The number of accessible microstates at 0K is zero. The remaining thermodynamic potentials used to represent the state of the system may be derived from the above properties. The thermodynamic potentials that are related to the discussion here are the enthalpy, $H = U + PV$ and Gibbs energy, $G = H - T\Delta S$.

#### 2.3.1.1 Entropy effects on simple and complex phase presence in HEAs

The thermodynamic stability of HEAs resulting from multiple alloying components in near-equimolar proportions is thought to be dependent on its configurational entropy, $\Delta S_{conf}$ where the microstates correspond to the number of macrostates, given by the relationship formulated by Planck from Boltzmann's original form as:

$$\Delta S_{conf} = R\ Log\ N \tag{3}$$

This formula is wholly dependent on the number of ways it is possible to arrange the total number of elements in equimolar ratios in the unit cell of a simple phase solid solution, and scales with the number of components. The number of possible configurations of equiatomic compositions that may be derived from the periodic table grows increasingly larger the higher the number of required components. For example, even in limiting oneself to 13 metallic elements to form equiatomic HEA systems of components numbering between 5 and 13 would return at least 7,099 possible combinations [49]. Additionally, the exact simple phase that will be present in HEAs will be unknown prior to verification making it difficult to determine $\Delta S_{conf}$ exactly.

Otto [50] made investigations into the effects of entropy and enthalpy by substituting components of CoCrFeNiMn with elements of similar crystal structures and comparable electronegativities. It was found that single simple phase and not complex phase containing compositions possess configurational entropy close to that of an ideal solid solution; the contribution of $\Delta S_{conf}$ to $\Delta G_{conf}$ only becomes dominant then due to the non-ordered structure. High configurational entropy by itself is thus shown to not provide a good *a priori* indicator of what simple phases will be present in HEA alloys; added to this fact is that

information on the phase present can only be obtained after experimental characterisation which limits the use of $\Delta S_{conf}$ as a parameter that clarifies only the possible reason that a particular phase is stabilised.

In the previous study by Otto, the role of enthalpy of formation was most closely studied, with less focus on entropic configurations other than the configurational entropy. Ma *et al.* [51] communicated the results of entropy contributions (magnetic, vibrational, electronic and configurational) on a CoCrFeNiMn HEA composition utilising DFT. Contrary to previous assumptions that the magnetic, vibrational, and electronic entropy are small compared to the configurational entropy, Ma *et al.* [51] report that the electronic and magnetic entropy can contribute up to 50% of the configurational entropy, while the vibrational entropy may contribute up to four times the configurational entropy value, dependent on temperature. Lucas *et al.*'s [18] study on CoCrFeNiPd HEA alloys report that the alloying of CoCrFeNi with Pd causes a change in the configurational entropy similar in magnitude to the change in the vibrational entropy. Considering that their experiments were performed at room temperature, their conclusions agree well with Ma *et al.* [51]

Considering the difficulties that arise in describing the entropic effect, use of the entropy parameter to describe the system may be ill-advised as the full influence of the entropic effects are not yet well understood, or researched. Tomilin and Kaloshkin [52] argue that based on the current literature [50,53,54] HEAs are actually multicomponent regular solutions that are assumed to be randomly distributed, which is only kinetically stable at low enthalpies of formation. From the point of view of the enthalpy of mixing, when $\Delta H_{conf}$ is close to zero, the solution is close to ideal, and it becomes energetically inefficient to form a complex phase [52]. This is backed up by experimental evidence which has found that $\Delta H_{conf}$ works well to discriminate between simple and complex phase formation in HEAs [2,15,49,50,54].

#### 2.3.3.2 Balancing of the thermodynamic parameters at equilibrium

Thermodynamically, it follows that for the simple phase to be stabilised, the entropic contribution of the Gibbs energy of mixing must be equivalent to the enthalpy of mixing, $\Delta H_{conf}$ such that:

$$\Delta G_{conf} = \Delta H_{conf} - T\Delta S_{conf} = 0 \quad (4)$$

At $\Delta G_{conf} = 0$, $\Delta H_{conf} = T\Delta S_{conf}$ and the simple phase stabilised by $\Delta S_{conf}$ is at equilibrium with the ordering of the compositional components i.e. the complex phase. The critical temperature, $T_{Crit}$ is defined as the temperature at which for a particular composition $\Delta G_{conf} = 0$ and is given by [15,55]:

$$T_{Crit} = \frac{|\Delta H_{conf}|}{\Delta S_{conf}} \quad (5)$$

The critical temperature is expressed as a ratio of the absolute value of $\Delta H_{conf}$. By convention in HEA research [3,11,42,50,51], $\Delta H_{conf}$ is approximated using sub-regular solution model based on the Miedema approximation for binary pairs [56–58] which evaluates $\Delta H_{conf}$ based on the electron density at the Wigner-Seitz boundary, electronegativity, and a hybridisation term. Cunliffe *et al.* [55] hypothesised that when the critical temperature of a potential HEA composition is higher than its solidus temperature the high entropy phase is suppressed. In their communication, $(TiZrNbCu)_{1-x}Ni_x$ where x = 0.125, 0.15, 0.2, and 0.25 were synthesised; for the x = 0.125 and x = 0.15 compositions where $T_{Crit} \leq T_m$where $T_m$ is the melting temperature determined from DSC experiments, the precipitation of a dual phase microstructure containing Nb and a simple BCC phase was observed. At x = 0.2 and x = 0.25 it was observed that $T_{Crit} > T_m$ and the microstructure contained precipitation of complex $Ni_{42}(ZrTi)_{58}$ and $Cu_{10}Zr_7$ phases.

Yang *et al.* [15] have also independently suggested a parameter, Ω defined as:

$$\Omega = \frac{T_m \Delta S_{conf}}{|\Delta H_{conf}|} = \frac{T_m}{T_{Crit}} \quad (6)$$

where $T_m$is determined from the weighted average of the melting temperature of the alloying components, that when used in combination with the atomic size mismatch, $\delta$ in a two-dimensional plot allows partial discrimination mainly between simple and complex phases of HEAs. It was empirically determined that $\Omega \geq 1.1$ and $\delta \leq 6.6\%$ (here $\delta$ represents the atomic size difference between the alloying components) should be used as a criterion for formation of the simple phase from their results.

Despite the good distinction between simple and complex phases through the two-dimensional $\delta - \Omega$ plot, analysis of Eq. 6 shows that when $\Delta H_{conf} > 0$, $T_{Crit}$ may be defined

mathematically as the point at which $\Delta G_{conf} = 0$. However when $\Delta H_{conf} \leq 0$, the required $\Delta G_{conf} = 0$ criteria cannot be reached, and has no thermodynamical meaning for binary alloys [11]. Poletti and Batezzati [11] introduced a thermodynamic scheme that corrects the $\Delta G_{conf}$ for non-ideal behaviour using the regular solution model with binary enthalpy contributions obtained via the Miedema approximation [56,57]. A plot of the ratio of corrected $T_{Crit}$ value to $T_m$ against $\delta$ indicates good separation between simple and complex phases that is comparable to the discrimination offered by the method of Yang and Zhang.

#### 2.3.3.3 Validity of the enthalpy of mixing approximated from the Miedema model

As mentioned previously, the empirical $\Delta H_{conf}$ parameter is approximated from the Miedema model [56–58] using the sub-regular solution model to extrapolate from binary pairs. The general form of this approximation is based on the interaction between the volumetric effect, chemical potential for electronic charge, and change in the electron density at the Wigner-Seitz boundary as a basis for evaluation [58]. The proportionality between neighbouring atoms may be given by [57]:

$$\Delta H \propto -P(\Delta \mathrm{X}^*)^2 + Q\left(\Delta {n_{WS}}^{1/3}\right)^2 \tag{7}$$

where P and Q are constants related to combinations on metals depending on their valences [3], $\Delta \mathrm{X}^*$ is Miedema's electronegativity difference and $\Delta {n_{WS}}^{1/3}$ is the difference in the electron density at the Wigner-Seitz boundary. Electronegativity is linked to the valence electrons of an atom, even such that the Allen electronegativity scales is defined as the average energy of the valence electrons of an atom at the ground state [59]. These parameters have been shown to be able to some extent to distinguish between simple and complex phase formation in HEAs, and will be discussed further on (*c.f.* section 2.3.2.) It is sufficient to first discuss, here, that previous studies have shown that the structure of a composition may be strongly related to the valence electron concentration, famously used to explain the stability of FCC and BCC brass by Hume-Rothery [60,61], and shown to also apply to a wide variety of other structures, including HEAs [12,61,62]. The stability of these phases might be attributed to the dependence of the size changes of the Wigner-Seitz

radius and its corresponding density depending on the electronic structure of the composition.

It must, however be noted that Miedema's empirical model finds itself at odds with modern interpretations of quantum mechanics as the empirical model modifies the work function term to new values, $\Delta X^*$ to achieve agreement with experimental $\Delta H$ values [63,64]. Furthermore although the empirical values show good relationship with VEC, there is a deviation between the ratio between the enthalpy of mixing and the difference in the number of valence electrons squared, $\frac{\Delta H}{\Delta N^2}$, which has been shown to start deviating from theoretical predictions between 4 < n < 7, regarded as a zone of complex phase presence in HEAs [12,13].

### 2.3.2 Hume-Rothery rules of alloying

The Hume-Rothery rules of alloying provide a set of guidelines by which a solid solution may form as a result of substitutional alloying. These rules have been invoked to describe the solid solution stability of HEAs. The Hume-Rothery rules are not well defined, as different factors were stressed by Hume-Rothery at different times, though it is generally recognised that the rules in order of importance are the atomic size effect, the electronegativity, and the electron concentration [65]. The first two parameters are considered to have the most impact on solid solution formation while the valence electron concentration parameter is considered to be a secondary effect [11,65].

a. Atomic Size Factor

The atomic size factor rule is defined by Hume-Rothery [66] to be a restriction on solid solubility arising from the lattice distortion affecting substitutional solubility when the atomic diameters of the solute and solvent differ by more than 14%. This Hume-Rothery rule was further investigated by Waber *et al.* [16] who applied the parameter to 1423 terminal solid solutions and found that the rule correctly predicted over 90% of the solid solubility when compared to experimental observation. For atoms with similar atomic sizes the solid solution that forms is considered to be complete, or extensive. Extensive solid solubility is found to only partially comply with Hume-Rothery rules (of 804 compositions investigated only 50% were found to match the Hume-Rothery rule).

A more simple explanation of Hume-Rothery rules may be considered by treating the solute and solvent in terms of an isotropic elastic continuum [47,67,68]. Darken and Gurry [69] show that the solid solubility reduces to 1 at% when the strain energy exceeds $4k_BT$ per atom, where $k_B$ is the Boltzman's constant and T is the temperature in Kelvin. While the strain accommodated in the structure is increased as a function of temperature, the strain in the solvent matrix should be minimised, as excess strain can act as a driving force for nucleation, leading to the possible nucleation and growth of secondary structures under favourable conditions [68].

One issue with the atomic size factor is the determination of the atomic radius. In HEAs [15,70] and other systems the atomic radius is typically defined as the half the nearest-neighbour distance in the crystal structure of a pure metal. In reality, the atomic radius will most likely depend on factors such as the coordination number of its environment resulting from the interaction of its valence electrons.

Mott [39] studied the quantum mechanical basis for the isotropic elastic continuum and found that the energy of an atom was more dependent on the atomic volume than on its coordination number; explaining the reason that a metal atom placed into a hole of its own size retains its original energy. That is, although the interaction between d-orbitals determines the interatomic distance between transition metals, it is the atomic volume that contributes to its energy.

The atomic size factor has been invoked with good results for prediction of the formation of both HEAs and bulk metallic glasses. As mentioned earlier, Yang and Zhang [15] used a two-dimensional plot of $\Omega$ against the atomic size mismatch, $\delta$ to successfully discriminate between simple phase, complex phase, and bulk metallic glass formation. Large atomic size mismatch is found to aid formation of bulk metallic glasses, due to increased difficulties for diffusion [71], while $\Omega \geq 1.1$ and $\delta \leq 6.6\%$ should be used as a criterion for formation of the simple phase from their results, largely showing adherence to Hume-Rothery rules. The complete discrimination between simple and complex phases is not yet achieved and may be attributed to the earlier inconsistencies with the thermodynamic approaches as discussed earlier, or the reduced accuracy from approximating the atomic radii with the radii of the alloying element in its pure metal state or from the role of other, unknown factors.

b. Electronegativity

Electronegativity is defined as the ability of an atom to attract electrons towards itself. The electronegativity rule is an electrochemical effect employed to describe the electronic interactions between the constituent components of an alloy composition [61]. In a binary system this is evaluated by taking the difference in the Pauling electronegativity between the two constituent elements. An electronegativity difference of zero would imply that both pairs of electrons possess the same tendency to attract electrons and the electrons will be shared between both atoms, while a large electronegativity difference would imply that the resulting charge transfer is more favourable towards the formation of a compound phase [65].

Electronegativity values cannot be directly measured, so they must be measured indirectly from other atomic or molecular properties. The first electronegativity scale was introduced by [72] based on the analysis of the heats of formation and combustion of gaseous molecules. Deviations from this constructed scale are found to increase in tandem with the ionic character of the bonds studied. A number of additional scales use the properties of free atoms as a measure of their reactivities. Some of these scales are tabulated below.

**Table 2.** Different electronegativity scales and their methods of derivation.

| Electronegativity Scale | Method | Reference |
|---|---|---|
| Pauling | Derived from measures of the heats of formation and combustion of gaseous molecules. | [72] |
| Mulliken | Derived from the average of the ionisation potential and electron affinity, calculated for suitable valence states of the element. | [73] |
| Gordy | Derived from a potential given as $\frac{(Z_{eff})e}{r}$, where $(Z_{eff})e$ is the effective nuclear charge a neutral atom acting on a valence electron at a distance from its nucleus, equivalent to its single covalent bond radius, r. | [74] |
| Walsh | Derived from the stretching force constant of an A-H bond that is found to increases as a function of electronegativity. | [75] |

| | | |
|---|---|---|
| Sanderson | Derived from the ratio of the average electronic density of an atom to that of an inert, hypothetical isoelectronic atom. | [76] |
| Alfred-Rochow | Derived from the force of attraction between the nucleus and an electron from a bonded atom using Columb's law, defined as $\frac{(Z_{eff})e^2}{r^2}$ where $(Z_{eff})e$ is the effective nuclear charge and r is the covalent radius of the atom. | [77] |
| Phillips | Derived from the dielectric charge transfer of atoms in a given valence states. | [78] |
| Martynov & Batsanov | Derived from the square root of the mean of successive ionisation potentials of an atom's valence electrons. | [79] |
| Allen | Derived from the the average one-electron energy of the valence-shell electrons in a ground-state free atom given by $\frac{m\,E_p+n\,E_s}{m+n}$, where m and n are the number of p and s valence electrons, and $E_p$ and $E_s$ are the averaged total energy difference between a ground-state neutral atom and an ionised atom. | [59] |

Newly derived electronegativity scales are normally constructed to address inaccuracies that are present in previous scales. These discrepancies are due to the fact that most scales are based on a particular point of reference from the properties of the free atoms, and that for different applications the electronic structure of the atom may be such that these points of reference become inaccurate when used [80]. Electronegativity scales may be broadly divided into either absolute scales, or Pauling-like scales. Absolute scales originate from Parr's [81] 1934 communication which showed that electronegativity analysed from the viewpoint of Density Functional Theory is equivalent to the negative of $\mu$, the electronic chemical potential and this value is constant for any chemical system, atom, ion or molecule. The chemical potential may be defined by the function $= \frac{\partial E}{\partial N} V$, where E is the electronic energy, N is equivalent to the number of electrons, and V is the potential of the nuclei. It is further shown that the Mulliken electronegativity, the average of the ionisation energy and the electron affinity is a good approximation of $\mu$, and that the Mulliken

electronegativity is termed the 'absolute electronegativity' in reference to its near equality to this property, $-\mu$.

In HEAs the electronegativity parameter used for most predictions is the ubiquitous Pauling scale [2,3,12,50,70,82]. Poletti *et al.* [11] used a 2-dimensional plot of the Allen scale electronegativity difference, $\Delta X_{Allen}$ against the atomic radius mismatch, $\delta$ to show separation between the formation of simple and complex phases. For values ranging between: 1. $1\% < \delta < 6\%$, and 2. $3 < \Delta X_{Allen} < 6$, only simple phase formation is observed for all calculated compositions. The discrimination between the simple and complex phase functions extremely well despite the fact that the exact nature of the delocalised electrons in transition metals is not well defined [59], a critique that Allen *et al.* [59] themselves acknowledge. Furthermore, all tested compositions possess components mainly located from the different groups within the fourth period, and complete separation of simple/complex phase solutions are not completely known.

c. Valence electron concentration

The valence electron concentration (VEC) is defined as the number of electrons in the outermost orbital that play a role in bonding mechanisms. This parameter is of importance when the size factor and the electronegativity difference is of minor importance [61]. In general, the electronic concentration effect are in part attributed to the observation that certain crystal structures (FCC, BCC, HCP) are linked to known values of electron concentration per atom ratios [11,61].

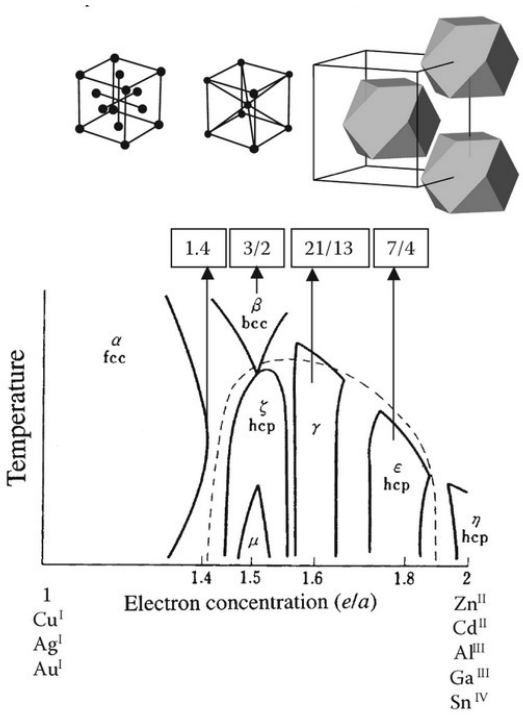


**Figure 2.** Phase diagram of some elements shown in a 2-D plot of Temperature against the electron concentration, e/a, showing the dependence on the phase of the material [61].

This is illustrated in Figure 2 which schematically represents a composite phase diagram of noble metals alloyed with non-noble metals, represented in terms of the average itinerant electrons per atom ratio, e/a. It is observed that the FCC, BCC and HCP phases tend to appear at particular e/a ratios, regardless of the alloying addition added. Hence it may be said that for complete solid solubility, the phase of the solute and the solvent should be similar.

The electron concentration as defined and used in describing the Hume-Rothery rules is the average itinerant electrons per atom, e/a. Another definition that is used to describe the electron concentration is the number of electrons in the valence band, the valence electron concentration or VEC. The valence electron concentration is an important tool in determining phase stability in quantum mechanics. From band theory, the valence electrons are quantised into discrete levels which in a metal forms a continuum that is known as a band. The valence electrons form bands that are close to the Fermi level, the total chemical potential of the solid at 0 K.

The stability of phases exhibiting metallic bonding may related to the valence electron concentration, because the Fermi surface of any phase, which is an abstract boundary in momentum space derived from the periodicity and symmetry of the lattice, interacts with the bands at the Fermi level. For a host of competing structures, the availability of accommodation into lower energy bands, depending on the Fermi surface would thus lead to a phase's stability over others [11]. The valence electron parameter with regards to phase stability has been investigated with various ab-initio methods, such as showing good validation with regards to predicting the phases present in the Cu-Zn [60], in AB transition metal aluminides [83], and in transition metal systems [84]; although again, the determination of the average valence electron concentration is non-trivial due to electronic effects [59,61]. It is expected that HEAs with a greater number of principal components will display increased interactions.

Study of HEAs as a function of the valence electron concentration shows that the stability of the simple FCC and BCC phase is well delineated by this parameter [12,70]. In general, the simple FCC structure is stabilised at VEC > 8, mixed simple phases of FCC/BCC and intermetallics are found between 7 < VEC < 8, and the BCC phase is stabilised at VEC < 7. These values are found to be independent of the stoichiometry of the compositional components, but the simple-complex phase transition points may change depending on the elements present in the composition. This effect may be linked to the chemical bonding arising from the electronic structure.

### 2.3.3 Validity of empirical prediction parameters

Together, the thermodynamic and Hume-Rothery parameters that have been discussed form the basis of semi-empirical/empirical structure predictions of HEAs. These parameters have been used together in various 2-dimensional (2-D) plots to derive guidelines for the formation of HEA simple phases.

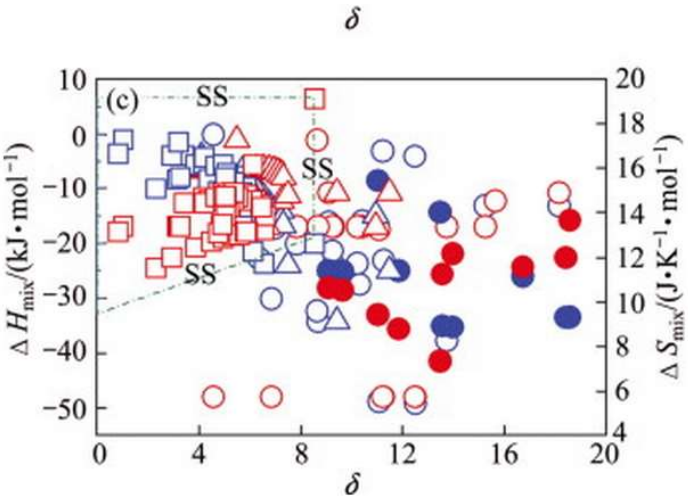


**Figure 3.** Dependence of the enthalpy of mixing, $\Delta H_{Mix}$ and entropy of mixing, $\Delta H_{Mix}$ when plotted against the atomic size difference, $\delta$ on the phase formed [70].

A plot of the thermodynamic parameters against the atomic mismatch has shown the ability to segregate HEA compositions into zones where simple phases and complex phases form. In the figure the symbols represent, ○: equiatomic amorphous alloys; •: non-equiatomic amorphous alloys; □: solid solution phases. and Δ: intermetallic phases.

The empirical rules shown here appear to be bounded by a dashed box, which has been drawn to guide the eye and as a result the exact limits for which values of the enthalpy of mixing and atomic size different need to be reached to obtain a solid solution phase cannot be determined, and as such the results here can only be used as a vague guideline in alloy design. Furthermore, the discrimination is not perfect as some overlap exists between these areas of stability – most obviously, several intermetallic phases appear in the bounded box, that are not, in fact, distinctly separated from the solid solution alloys.

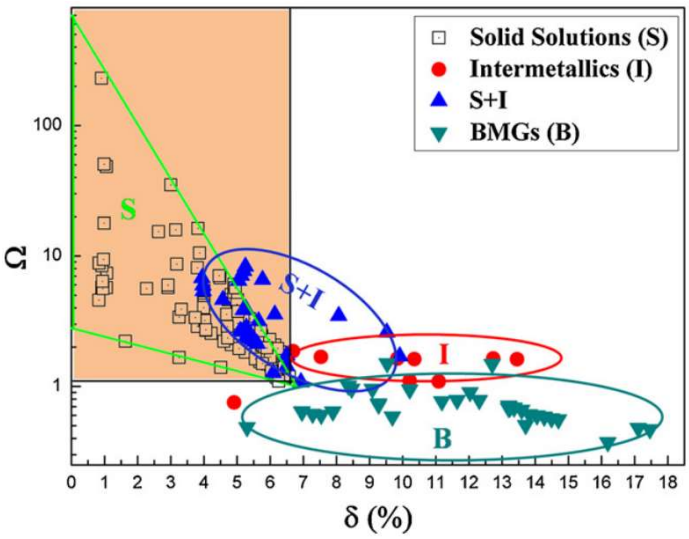


**Figure 4.** Dependence of the parameter Ω against the atomic size difference, $\delta$ on the phase formed [15]

In their publication, Yang and Zhang attempt to obtain an improved empirical ruleset for HEA alloy design through the analysis of the atomic size difference. The results are shown in Figure 4 where the y-axis is derived from a critical temperature for HEAs from the relationship:

$$\Omega = \frac{T_m \Delta S_{conf}}{|\Delta H_{conf}|} = \frac{T_m}{T_{Crit}} \tag{8}$$

When judged by the eye, the plot in Figure 4 appears to offer increased discrimination between the intermetallic, mixed phases (where simple phases co-exist with intermetallic phases), bulk metallic glasses (signified by the term BMGs in the plot), and the simple phases. It is an interesting point that in both analyses, these rough empirical parameters may be used to distinguish in very simple plots the approximate areas of formation of not only solid solutions and intermetallic compounds from one another, but also the bulk metallic glasses.

While it appears that discrimination between simple and complex phases is much more obvious, there remains some overlap between the formation of solid solution and intermetallic phases. Thus, although the reformulation of thermodynamic parameters to obtain the parameter Ω is successful, the overlap in Figure 4 suggests some secondary factor (or more) that remains unaccounted for.

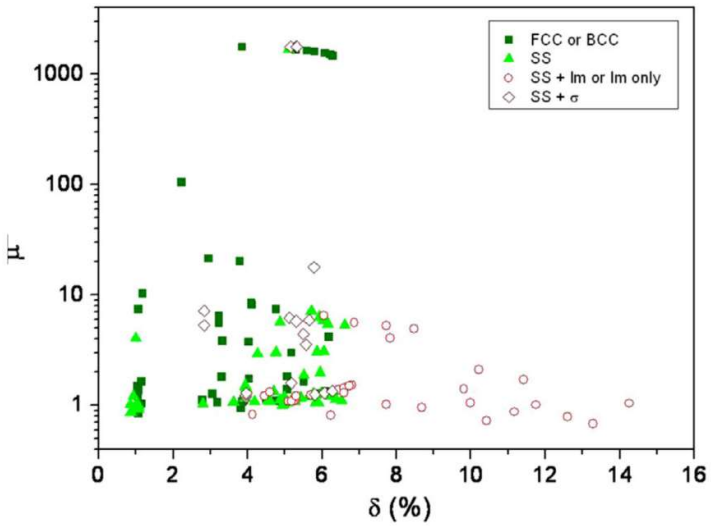


**Figure 5.** Dependence of the parameter $\mu$ (*cf.* Eq. X) plotted against the radial mismatch, $\delta$ [11]. The plot shows HEAs tend to form at high values of $\mu$, corresponding to temperature values below the melting temperature

The usage of ideal thermodynamic parameters in HEA systems was hypothesised to have no meaning thermodynamically by Poletti *et al.* [43], attributed to the non-ideal nature of HEAs. Shown in Figure 5, Poletti *et al.* present a plot of $\mu = \frac{T_M}{T_{SC}}$ where $T_M$ is the melting temperature and $T_{SC}$ is the temperature at which the free energy of mixing experiences an inflection at its spinodal point(s).

The plot shows HEAs tend to form at high values of $\mu$, corresponding to temperature values below the melting temperature. This finding is in agreement with Cunliffe *et al.*'s report where where $T_{Crit} \leq T_m$ corresponds with the formation of a BCC HEA [55], although Poletti *et al.*'s formulation of $\mu$ is considered to be a refinement of the parameter presented by Cunliffe *et al.* (which considered the HEA to be a near-ideal solid solution)

The use and relative success of the $\mu$ parameter emphasises the non-ideal behaviour of HEAs [85]. This highlights also the requirement for alternative means of prediction of HEA phase that goes beyond the currently established 'simple' thermodynamic and semi-empirical parameters [2,45,49,50].

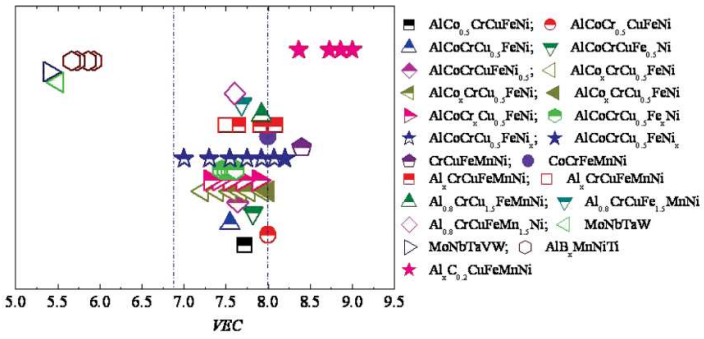


**Figure 6.** Relationship between VEC and simple FCC/BCC phases in HEA systems [12]. The figure is separated into three zones: the left-most zone represents a zone of BCC stability for the encompassed compositions, the middle zone shows a regions of BCC+FCC stability, while the right-most zone presents compositions that are FCC stable.

The previous figures considered solid-solubility in HEAs using mainly thermodynamic parameters. In the periodic table of the elements, it is known that specific values of valence electron concentration represents stability of certain phases (*i.e.* tetragonal, HCP, BCC, FCC *etc.*); this has famously been studied by Hume-Rothery as the itinerant electron per atom (*e/a*) rule and used to explain the stability between brass and bronze. By making the assumption that HEAs can be approximated as an ideal solid solution, the mean value of the valence electron concentration weighted according to a composition's alloying elements, can be taken to be representative of it.

In Figure 6 above, Guo *et al.* attempted to use the valence electron parameter to discriminate between the formation of simple FCC phase and simple BCC phase. The figure is separated into three zones: the left-most zone represents a zone of BCC stability for the encompassed compositions, the middle zone shows a regions of BCC+FCC stability, while the right-most zone presents compositions that are FCC stable. The overall separation of the different phases are quite good, although one interesting observation is that of the selected compositions, approximately half or more are Al, Co, Cr, Cu, Fe, and Ni containing compositions.

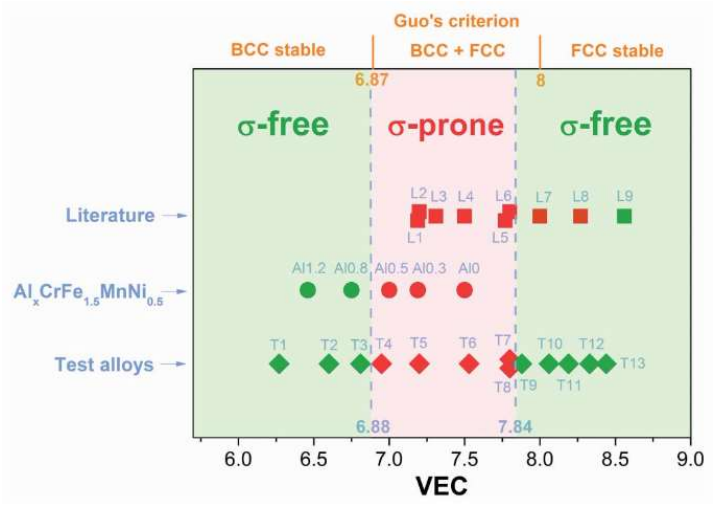


**Figure 7.** Relationship between VEC and Sigma phase formation [86] for $Al_xCrFe_{1.5}Ni_{0.5}$ alloy compositions. The sigma phase forms between 6.88 < VEC < 7.84.

In Figure 7 Tsai *et al.* [76] furthered Guo's VEC analysis and found that the previously identified areas for FCC+BCC formation also proved to be a zone for complex Sigma phase formation dependent on the composition. This observations highlights that the approximation made by averaging the VEC (which may be considered to be the empirical VEC), can lead to vary different predicitons of stability, depending on the composition of the alloy, although the approximate trends still appear to hold true.

As a corrolary of the previous observation, the defined zone for complex phase formation (here, the Sigma phase) was found to vary depending on the composition of the alloy system. Two reasons for this might exist, the first of which is attributed to the inaccuracy of the emprical VEC, whilst the second attempts to address the problem from a semi-empirical perspective.

1. The VEC parameter, even for the pure transition metals is highly dependent on the electronic structure, and as such can only be determined precisely from experimental data, or from robust *ab-initio* simulations. The deviations observed here may represent the inaccuracy of the empirical VEC.
2. Some secondary effect (or more) that influences the phase stability of HEAs is not fully captured by the plot of VEC as shown in Figure 7. Further analysis and development is this required.

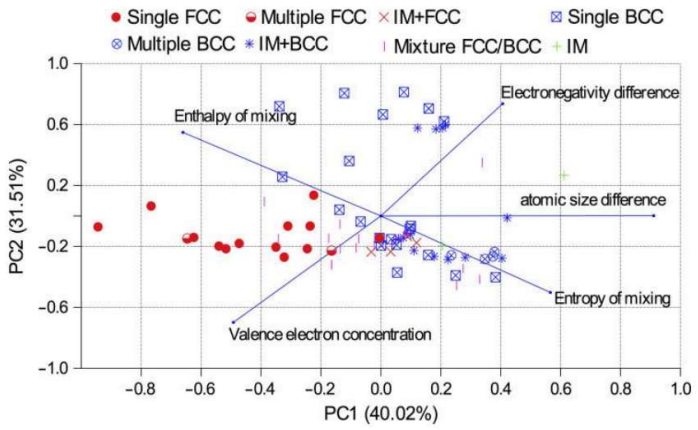


**Figure 8.** Biplot of first two principal components from Dominguez *et al.'s* Principal Component Analysis [13]. The phases appear the most fenced in around the lines representing the enthalpy of mixing and the valence electron concentration.

Dominguez *et al.* [13] performed a principal component analysis of both thermodynamic and Hume-Rothery parameters to try and address some of the observations presented above. Figure 8 presents a biplot of the first two principal components of the resultant analysis. The biplot shows that the simple FCC phases cluster around the enthalpy of mixing and valence electron concentration axis, the simple BCC phase compositions cluster around the enthalpy of mixing and the electronegativity difference axes, while the complex phases (intermetallics) are found to be located in the lower right quadrant in the region bordered by the valence electron concentration and the entropy of mixing.

It is therefore suggested that the simple/complex phase stability of HEAs may be discriminated through a two-dimensional plot of the valence electron and the enthalpy of mixing, as shown in Figure 9.

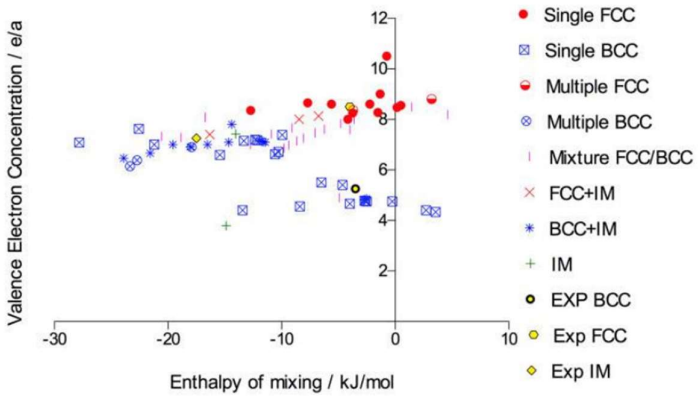


**Figure 9.** Two-dimensional plot of valence electron concentration against the enthalpy of mixing showing discrimination between simple and complex phases [13]. Compositions containing the simple FCC phase are observed to be distinguishable from compositions showing the simple BCC phase. Complex structures are characterised by negative enthalpy of mixing values.

The partitioning in Figure 9 may be attributed to the fact that the enthalpy of mixing is in itself based on the valence electron concentration [11] as admitted by Miedema in his formulation of the enthalpy of mixing [61]. Miedema's enthalpy of mixing is derived from the electron density at the Wigner-Seitz border as well as a modified electronegativity difference for binary cells. The formulation of the Wigner-Seitz cell is dependent on the bonding of the atom, as the cell may not be symmetrical due to electron effects. If the bond is partially covalent or has a higher energy, there may be significant deviations from the valence electron parameter. The incomplete phase discrimination evidenced in the two-dimensional plot may arise from the non-compliance of the Miedema model with quantum mechanics principles as discussed in Section 2.3.3.3. This is discussed further in the first results chapter, Chapter 4.

## 2.4 Chemical bonding of HEAs

The three types of chemical bonds, covalent bonds, ionic bonds and metallic bonds are often useful to describe the attraction between atoms that allow the formation of chemical compounds. The least well understood of these is the metallic bond, whose standard description relies on band structure theory and implies the lack of a band gap separating the valence and conduction bands [87,88]. Band structure theory relies on the momentum/reciprocal space representation of a crystal structure, and it is the absence of a physical space representation that presents difficulties in establishing the physical

significance of the metallic bond's delocalised electrons that is present in theories of chemical bonding. Early theories of chemical bonding did not consider the metallic bond [72,89], while later considerations promoted the near free-electron model [61]. Later experimental work determining the Fermi surface of metals showed that metallic bonding was better described as partially delocalised covalent bonds [90] as they were found to not be spherical, as would be expected for perfectly delocalised electrons.

The relationships between structure and properties of metals and alloys may be described by identifying the distribution of electron density with bonding directionality [30]. In HEAs, the complex phase stabilisation of alloying additions with covalent character may be described as possessing directional bonding. For example, sufficient addition of V or Ti to the CoCrFeNi composition is known to destabilise the simple FCC phase to Sigma and C14 Laves complex phases [22], and is often described as possessing bonding directionality. Analysis of Sigma and C14 complexes that are ordered (intermetallics) have shown that they possess some degree of covalency [27].

The nature of bonding directionality has been investigated by Eberhart [30]. This analysis of the charge density topology is based on Bader's Electron Localisation Function (ELF) that identifies the critical points of the charge density i.e. where no electron flow is taking place as regions of interest that is shown to return a picture consistent with classical chemical bonding [91]. Further comparison between the bond redistribution in response to a strained system and the above mentioned charge redistribution of the bond critical points shows a good correlation between the both. Indeed, it is shown in Eberhart's analysis that transition metals with a valency near ten (Cu, Ag, Au, and Pd) possess fairly anisotropic bonding properties in comparison to Al.

Similarly, an analysis utilising Becke and Edgecombe's ELF function that partitions the charge density of the electron spin energy difference [92] presents metallic bonding as delocalised electrons with covalent character [28]. Silvi and Gatti identify the critical points of metallic Li, Na, K, V, Al, Ca, Sc, and Cu to be located at the octahedral and tetrahedral centres [28], which in agreement with the analysis performed by Edgecombe [92]. The partial covalent bond character referred to by Silvi and Gatti refers not to any ionic competition but to the fact that the electronic occupation at the critical points are typically low, attributed to high coordination of atoms and to strong repulsion from the nucleus, leading to increased

clustering of these critical points around the nucleus. A similar ELF analysis performed on intermetallic compounds alpha-Si, $CaAl_2Si_2$, $SrAl_2$, $BaAl_4$, $CaAl_2$, alpha-Al show distinctive structuring and high localisation of electrons, indicating bonding with increased covalent character [28] that is consistent with the covalent nature of Laves phases investigated.

Although these findings begin to elucidate on the bonding difference between simple and complex phases, these theoretical analyses are based on concepts not widely used in concepts of bonding or alloy design. In Lee and Hoffman's paper, an attempt is made by using ab-initio quantum mechanical methods as a numerical laboratory to "build an understanding of alloy and intermetallic structure using concepts already familiar to the chemistry community" [93]. In this work, it is hypothesised that a metallic structure's FCC → BCT → BCC transformation, or vice versa, is analogous to a molecular Jahn-Teller distortion by means of a change in the point group symmetry; a modified Bloch function of the periodic lattice is used to determine the effect of a this symmetry change. It is shown that the change in energy between the distorted structures as a function of the valence electron concentration is in good agreement with the results predicted by Pettifor [94].

In general, Lee and Hoffman conclude that a Jahn-Teller like distortion for metals and alloys may exist, represented by translation and rotational symmetry elements. Furthermore, the Jahn-Teller like distortions are influenced by the number of Fermi surface states and their availability of the states and their orbitals for distortion, and intermetallic formation is found to only occur at the nodal points between FCC and BCC stability [93]. The results of this analysis are in good agreement with the dependency of HEA valence electron concentration on phase stability.

It becomes apparent that the covalent-like character of metallic bonding may strongly influence the phase stability of an alloy. Simplifying the alloy design scheme for HEAs may therefore require the understanding of the composition at the atomic level, and usage of quantum mechanics models to be achieved.

## 2.6 Theory of quantum mechanics for phase stability predictions

### 2.6.1 Schrodinger equation

Quantum mechanics is the study of physics at very small scales, and may be applied to investigate the electronic structure of HEAs arising from interactions between the alloying

elements. The electronic structure is defined as the state of motion of electrons in an electrostatic field created by a stationary nuclei [95]. Within quantum mechanics, electrons possess wavelike properties which may be interpreted in several ways [96,97]. The Schrodinger equation [97] is invoked to describe the properties of electrons as a function of its wavefunction. The classical non-realivistic expression for the energy of a particle is given by the sum of the kinetic energy, $E_K$ and the potential energy, $E_P$:

$$E = E_K + E_P = \frac{p^2}{2m} + V(x) \tag{9}$$

where m is the mass of the particle, p is its momentum and V(x) is the potential energy along the x axis. The De Broglie hypothesis is invoked to represent wave-particle duality with frequency, $\omega$ and wavenumber, $k$ by substituting $p = \hbar k$ and $E = \hbar\omega$. Here $\hbar$ is the reduced Planck constant. Eq. 9 transforms to:

$$\hbar\omega = \frac{\hbar^2 k^2}{2m} + V(x) \tag{10}$$

A travelling wave may be described to consist of combinations of its sinusoidal functions, $y = y^0 \sin(kx - \omega t)$ and $y = y^0 \cos(kx - \omega t)$. As the De Broglie hypothesis describes the electron as a wave moving around the nucleus, the Euler identity, $e^{ix} = \cos(x) + i\,\sin(x)$ transforms this into the complex form with the wavefunction written as:

$$\varphi(x,t) = Ae^{i(kx-\omega t)} \tag{11}$$

From Eq. 11, its partial derivatives are:

$$\frac{\partial\varphi}{\partial t} = -i\omega\varphi \text{ and } \frac{\partial^2\varphi}{\partial x^2} = -k^2\varphi \tag{12}$$

Modifying Eq. 10 so that Eq. 10 $\times\varphi = \hbar\omega.\varphi$, and substituting Eq. 12, Eq. 10 transforms to the time-dependent Schrodinger equation for a particle:

$$i\hbar\left(\frac{\partial}{\partial t}\varphi(x,t)\right) = \frac{-\hbar^2}{2m}\left(\frac{\partial^2}{\partial x^2}\varphi(x,t)\right) + V(x)\varphi(x,t) \tag{13}$$

From Eq. 13, the 3-dimensional time-independent Schrodinger may be expressed as:

$$E\varphi(r) = \hat{H}\varphi(r) \tag{14}$$

where $\nabla^2$is the Laplacian operator defined as $\nabla = \frac{\partial}{\partial x} + \frac{\partial}{\partial y} + \frac{\partial}{\partial z}$ and $\widehat{H}$ is the Hamiltonian operator corresponding to the total energy of the system. The $\widehat{H}$ in Eq. Q6 is given by:

$$\widehat{H} = \frac{-\hbar^2}{2m}(\nabla^2) + V(r) \tag{15}$$

Eq. Q6 can be solved for the one-electron hydrogen atom by presenting the Laplacian operator in its polar coordinates form and has the separable form of:

$$\varphi(r, \theta, \phi) = NR_{n,l}(r)\, P_l^m(cos\theta)\, e^{im\phi} \tag{16}$$

where the solution of the wavefunction is given by its dependence on the radial distance, $r$, polar angle $\theta$, and azimuth angle, $\phi$ and designated by the quantum numbers $n, m, and\ l$. For a system with >1 particle, i.e. $N_e$ electrons and $N_n$ neutrons that would obey the stationary Schrodinger equation the coulombic interactions will have to be accounted for, such that:

$$\widehat{H} = \hat{T}_e + \hat{V}_{en} + \hat{V}_{ee} + \hat{V}_{nn} \tag{17}$$

where $\hat{T}_e$ corresponds to the total kinetic energy of the electrons, and the total potential energy is dependent on the electron-nucleon interaction, $\hat{V}_{en}$, the electron-electron interaction, $\hat{V}_{ee}$ and the nucleon-nucleon interaction $\hat{V}_{nn}$. The Pauli principle must also be adhered to, mathematically, the wavefunction will be antisymmetric upon the exchange of any pair of particles:

$$\varphi(\overrightarrow{r_1}\sigma_1, \overrightarrow{r_2}\sigma_2) = -\varphi(\overrightarrow{r_2}\sigma_2, \overrightarrow{r_1}\sigma_1) \tag{18}$$

The exact solution for the many-body Hamiltonian in Eq. 17 is impossible for systems containing more than one electron due to coupling between electrons arising from coulombic interactions. Approximations of Eq. 17 may be divided into two classes, one based on wavefunction-methods such as Hartree-Fock [98] and the second based on density methods. The following discussion will cover to methods pertaining to the electron density solutions, which is the dominant method for quantum mechanical simulation of periodic systems and employed in this thesis using the CASTEP code [99].

### 2.6.2 Thomas-Fermi method

Thomas [100] and Fermi [101] independently proposed a statistical method to approximate the distribution of electrons in a many-body system in a semi-classical way, thus avoiding the requirement of solving the N-body wavefunction problem. Lenz [102] demonstrated that the equation could be derived as a functional of the electron density and the method itself is often viewed as a precursor to the Density Functional Theory. The Thomas-Fermi method was later refined by Dirac [96] to account for the exchange energy arising from the Pauli Exclusion Principle. The disadvantage of this method is the inability to inspect the individual features of the atomic structure [98,103].

The Thomas-Fermi approximation may be derived through several methods. Here, the electron density of the system is first derived. The number of electrons in a system can be obtained from phase space, as the fraction

$$\mathrm{d}N = \left(\frac{2}{h^3}\right)\left(\frac{4}{3}\right)\pi\, p^3\, dV \tag{19}$$

Therefore, the number density n(r) = $\mathrm{d}N/dV$:

$$n = \left(\frac{2}{h^3}\right)\left(\frac{4}{3}\right)\pi\, p(r)^3 \tag{20}$$

Now, the semi-classical formula for the Fermi energy may be obtained with the relation from:

$$p(r) = mv \tag{21}$$

such that:

$$E_F = \frac{p(r)^2}{2m} + V(r) \tag{22}$$

$$V(r) = E_F - \frac{p(r)^2}{2m} \tag{23}$$

The semi-classical number density can then be obtained by eliminating p(r). Combining Eq. 23 into Eq. 20:

$$n(r) = \frac{8\pi}{3h^3}\left[2m(E_F - V(r))\right]^{3/2} \tag{24}$$

Now that a relationship between density, Fermi energy, and the potential has been established, an energy functional dependent on the electron density may be formulated. Starting from the Schrodinger Hamiltonian, the energy of the system can be considered to consist of electron-electron, electron-neutron, neutron-neutron interactions, and the kinetic energy. From Eq. 19, the kinetic energy of an electron at position r may also be derived from as a function of the fraction of electrons present where F = dN/dP. Hence:

$$T(r) = \int n(r) \int_0^{p=p(r)} \frac{p^2}{2m} \left(\frac{3\,\pi\,p^2}{\pi\,p(r)^3}\right) dp\,dr \tag{25}$$

$$T(r) = \int \frac{3\,n(r)}{2m} \int_0^{p=p(r)} \frac{p^4}{p(r)^3} dp\,dr \tag{26}$$

$$T(r) = \int \frac{3\,n(r)}{10\,m} p(r)^2\,dr \tag{27}$$

From Eq. 20 where:

$$p(r) = \left(\frac{3\,n(r)\,h^3}{8\,\pi}\right)^{1/3} \tag{28}$$

Therefore Eq. 27 transforms into:

$$T(r) = \int \frac{3\,n(r)}{10\,m} \left(\frac{3\,n(r)\,h^3}{8\,\pi}\right)^{2/3} dr \tag{29}$$

$$T(r) = \frac{3\,h^2}{10\,m} \left(\frac{3}{8\,\pi}\right)^{2/3} \int\ n(r)^{5/3}\ dr \tag{30}$$

which is the form of the kinetic energy of the system. The potential of the electron-neutron interaction can be given by the potential energy of an electron from the nucleus centre by:

$$V_{en} = -Z\,n(r) \int \frac{e^2}{r} dr \tag{31}$$

The electron-electron interaction may be given as:

$$V_{ee} = n(r)n(r') \int \frac{e^2}{2(r-r')} dr'dr \tag{32}$$

Combining Eq. 30, 31, and 32, the energy functional of the Thomas-Fermi equation is thus:

$$E_{TF} = \frac{3\,h^2}{10\,m} \left(\frac{3}{8\,\pi}\right)^{2/3} \int\ n(r)^{5/3}\ dr - Z\,e^2 \int \frac{n(r)}{r} dr + e^2 \int \frac{n(r)n(r')}{2(r-r')} dr'dr \tag{33}$$

The energy of the system must be minimised with respect to the electron density. The condition for minimisation is $\int n(r)\, dr = N$ when $n(r) \geq 0$. A Lagrange multiplier, $\mu$ is introduced to minimise the energy such that:

$$\frac{\delta(E_{TF}+\mu \int n(r)dr)}{\delta\, n(r)} = 0 \tag{34}$$

Following this condition, Eq. 33 may be re-written as:

$$\frac{3\,h^2}{10\,m}\left(\frac{3}{8\,\pi}\right)^{2/3}\frac{5}{3}\, n(r)^{2/3} - \frac{Z\,e^2}{r} + e^2 \int \frac{n(r')}{2(r-r')} dr' + \mu = 0 \tag{35}$$

Utilising the condition for minimisation given by the Lagrange operator, Eq. 20, and that $\frac{dE}{dN} = E_F = -\mu$ [104], we obtain the general solution for the Thomas-Fermi equation:

$$V(r) = E_F - \left(\frac{p^2}{2m}\right) \tag{36}$$

$$V(r) = -\mu - \left(\frac{h^2}{2m}\right)\left(\frac{3}{8\,\pi}\right)^{2/3} n(r)^{2/3} \tag{37}$$

Since $\frac{3\,h^2}{10\,m}\left(\frac{3}{8\,\pi}\right)^{2/3}\frac{5}{3}\, n(r)^{2/3}$ cancels out the T(r) term from Eq. 29, Eq. 37 transforms into:

$$V(r) = -\frac{Z\,e^2}{r} + e^2 \int \frac{n(r')}{2(r-r')} dr' \tag{38}$$

Applying the Poisson relationship for the total number of electrons for a spherical symmetry to the above equation then returns the following:

$$\nabla^2 V(r) = 4\,\pi e^2 \big(\, Z\, dr - n(r)\big) \tag{39}$$

$$\nabla^2 V(r) = 4\,\pi e^2\, Z\, dr - \frac{32\pi^2 e^2}{3h^3}[2m(E_F - V(r))]^{3/2} \tag{40}$$

$$\nabla^2 V(r) = 4\,\pi e^2\, Z\, dr - \left(\frac{2\pi}{h}\right)^3 \left(\frac{4e^2}{3\,\pi}\right)[2m(E_F - V(r))]^{3/2} \tag{41}$$

Normalising against the Bohr radius, where $a_0 = \frac{h^2}{4\,m\,\pi^2\,e^2}$ gives:

$$\nabla^2 V(r) = 4\,\pi e^2\, Z\, dr - \frac{4e^2}{3\,\pi}\left[\frac{2(E_F - V(r))}{e^2\left(\frac{h^2}{4\,m\,\pi^2\,e^2}\right)}\right]^{3/2} \tag{42}$$

$$\nabla^2 V(r) = 4\,\pi e^2\,Z\,dr - \frac{4e^2}{3\,\pi}\left[\frac{2(E_F - V(r))}{e^2 a_0}\right]^{3/2} \tag{43}$$

To reduce the above equation to the general dimensionless form of the Thomas-Fermi equation with spherical symmetry, the following relationships are used [104]:

$$\frac{Z\,e^2\varphi(x)}{r} = V(r) - E_F \tag{44}$$

$$r = b\,x \tag{45}$$

The boundary conditions are $V(r) \to 0$ as $r \to \infty$, such that the $4\,\pi e^2\,Z\,dr$ term may be eliminated and now:

$$\frac{1}{e^2}\nabla^2(V(r)) = -\frac{4}{3\,\pi}\left[\frac{2(E_F - V(r))}{e^2 a_0}\right]^{3/2} \tag{46}$$

$$\left(\frac{Z}{b^3\,x}\right)\frac{\mathrm{d}^2}{dx^2}\left(\varphi(x)\right) = \left(\frac{4}{3\,\pi}\right)\left(\frac{2\,Z}{a_0\,b\,x}\right)^{3/2}\varphi(x)^{3/2} \tag{47}$$

$$\frac{\mathrm{d}^2}{dx^2}\left(\varphi(x)\right) = \left[\left(\frac{4}{3\,\pi\,Z}\right)\left(\frac{2\,Z}{a_0}\right)^{3/2} b^{3/2}\right]\frac{\varphi(x)^{3/2}}{x^{1/2}} \tag{48}$$

To reduce Eq. 48 to the dimensionless form, b must be set so that the content of the bracket is equivalent to unity. Therefore the following equation must be satisfied:

$$\left(\frac{4}{3\,\pi\,Z}\right)\left(\frac{2\,Z}{a_0}\right)^{3/2} b^{3/2} = 1 \tag{49}$$

And the following relationship may be obtained from Eq. 49:

$$b^{3/2} = \left(\frac{3\,\pi}{4\,Z}\right)\left(\frac{Z\,a_0}{2}\right)^{3/2} \tag{50}$$

$$b = \left(\frac{9\,\pi^2\,Z^2}{128}\right)^{1/3} a_0 \tag{51}$$

Thereby allowing the dimensionless general Thomas-Fermi equation for neutral, non-isolated atoms following the spherical approximation to be given as:

$$\frac{d^2\varphi(x)}{dx^2} = \frac{\varphi(x)^{3/2}}{x^{1/2}} \tag{52}$$

Dirac introduced modifications into the Thomas-Fermi equation above to account for exchange. The modified Thomas-Fermi-Dirac equation is as follows:

$$\frac{d^2\varphi(x)}{dx^2} = x\left[\varepsilon + \left(\frac{\varphi(x)}{x}\right)^{1/2}\right]^3 \quad (53)$$

with the following boundary conditions:

$$\varphi(0) = 1 \quad (54)$$

$$\left(\frac{d\varphi}{dx}\right)_{x=x_0} = \frac{\varphi(x_0)}{x_0} \quad (55)$$

Eq. 52 and 53 are based on a spherical approximation of the electron cloud, which is not exact, but forms a reasonable approximation [105]. As the energy terms are taken for a homogenous electron gas, the approximation returns inexact results for molecular systems but are considered reasonable for metals [106], and may also be applied to systems containing multiple elements. The equations may be solved using the Feynman-Metropolis-Teller method [105] whereby a semi-convergent power series of the form:

$$\varphi(x) = 1 + a_n(x)^{n/2} + \cdots, \text{ n>1} \quad (56)$$

may be expressed where $a_n$ represents the coefficients of the expansion. Once the initial slope, $a_2$ is selected the remaining coefficients may be determined. Ren *et al.* [17] used a fourth-order Runge-Kutta to solve Eq. 53 with good results, when comparing with known values of electronic densities of selected elements from the periodic table.

### 2.6.3 Hohenberg-Kohn theorems

The Thomas-Fermi approach was the first theory that was developed to describe the properties of atoms based on an electronic density but faces several limitations: i.e the total energies are inaccurate, the electron density diverges near the nucleus and does not decay as $r \to \infty$.

It was not until the development of the Hohenberg-Kohn theorems [107] which provided explicit proof that the energy of a system of particles can be written as a function of the electronic density that led to the development of density functional theory and more accurate functions. The theorems are:

Theorem 1: For any system of interacting particles in an external potential, the density is uniquely determined.

Theorem 2: A universal functional for the energy can be determined in terms of the density. The exact ground state is the global minimum of this functional.

Application of the Hohenberg-Kohn theorems then allows the ground state of any system of interacting particles to be found as long as the external potential is minimised, and the various properties arising from the electronic interactions.

This can be seen from a simple thought experiment where we assume that for a specified system the external potential, $V(r)$ has been defined. It is further assumed that the kinetic energy, $\hat{T}_e$ and the electron-electron interaction energy, $\hat{V}_{ee}$ is reliably approximated and therefore, the ground state is simply the minimum of the external potential, or the sum of $\hat{T}_e$, $\hat{V}_{ee}$, and potential energy, $\hat{V}_{en}$ as a function of the electronic density, $n(r)$. It can also be assumed that $V(r)$ is dependent on a parameter, $a$, which can be the lattice constant in a particular crystal, or the angle of the crystal structure. Since the energy can be determined as a function of the electron density and $V(r)$, a value of $a$ that minimises the energy can be computed and in this way, various properties associated with the ground state of the compound can be obtained (e.g. lattice parameters, compressibility, elastic constants, phonon vibrations etc.). Although this is possible theoretically, in practice the minimisation of the external potential is numerically difficult due to the complexity of the equation. Furthermore, values of $\hat{T}_e$ and $\hat{V}_{ee}$ must be approximated accurately.

### 2.6.4 The Kohn-Sham equations

The minimisation of an explicit energy functional is one of the ways that the ground state can be obtained. One example of this is the minimisation of Thomas-Fermi energy functional as given in Eq. 33. As mentioned previously, the classical approximations made in the Thomas-Fermi approximation and the lack of an exchange-correlation functional lead to inaccuracies in the approximation, especially with regards to large atoms or molecules with covalent type bonding. The Kohn-Sham equations offer an alternative that does not work in terms of the electronic density but instead includes a wave-function which incorporates the exchange-correlation functional that is missing from the Thomas-Fermi approximation. The energy of the system, or the Hamiltonian is described by Eq. 17 as the sum of the kinetic energy, electron-neutron interaction, electron-electron interaction, and nucleon-nucleon interaction:

$$\widehat{H} = \hat{T}_e + \hat{V}_{en} + \hat{V}_{ee} + \hat{V}_{nn} \tag{57}$$

and the energy of the ground state can be written as:

$$E_0 = min_{p\to N}\left(F(p) + \int p(r).\hat{V}_{en}dr\right) \tag{58}$$

where $F(p) = \hat{T}_e(p) + \hat{V}_{ee}(p)$. In Chapter 2.8.2, the Thomas-Fermi method sought to solve $F(p)$ by using classical theory to approximate values of $\hat{T}_e\ and\ \hat{V}_{ee}$ so that:

$$F(p) = \hat{T}_e^{Classical}(p) + \hat{V}_{ee}^{Classical}(p) + E_{Non-Classical}(p) \tag{59}$$

where $F(p)$ is the sum of the classical kinetic energy and electron-electron interaction term, as well as the contributions from non-classical effects. The Thomas-Fermi approximation for the kinetic and interaction term is not equal to the true kinetic energy and interaction term due to non-classical effects. Kohn and Sham accounted for this by calling the non-classical contribution to the total energy as the exchange-correlation energy, $E_{XC}(p)$ so that:

$$E_{XC}(p) = \left[\hat{T}_e(p) - \hat{T}_e^{Classical}(p)\right] + \left[\hat{V}_{ee}(p) - \hat{V}_{ee}^{Classical}(p)\right] \tag{60}$$

With this in mind, the energy of the system then becomes:

$$E(p) = \hat{T}_e(p) + \hat{V}_{en}(p) + \hat{V}_{ee}(p) + \hat{V}_{nn}(p) + E_{XC}(p) \tag{61}$$

To obtain the Kohn-Sham equations, the variational principle is applied so that a fictitious system of non-interacting electrons that generate the same density as the defined system is obtained, and is defined by a local effective external potential. The lowest energy of the orbitals of this system is:

$$\left(-\frac{1}{2}\nabla^2 + V_{eff}(r)\right)\varphi_i(r) = \varepsilon_i\varphi_i(r) \tag{62}$$

where $V_{eff}$ is the effective potential, $\varphi_i$ is the wavefunction, and $\varepsilon_i$ is the orbital energy of the corresponding Kohn-Sham orbital. $V_{eff}(r)$ is defined as:

$$V_{eff}(r) = \int \frac{p(r)}{r-r'}dr' + V_{XC}(r) + V_{Ext}(r) \tag{63}$$

and the electron density may be described using the Born approximation as:

$$p(r) = \sum_i^N |\varphi_i(r)|^2 \tag{64}$$

The Kohn-Sham equation appears to take a form similar to the Schrodinger equation, the key difference being that the potential of the Kohn-Sham equation is a function of the electronic density. The numerical solution to the Kohn-Sham equations may then be obtained by inserting a basis function and expanding the equation to obtain eigenvalue for each available solution. Due to the fact that the equations are coupled and non-linear, the solution has to be self-consistent. Self-consistent in this sense, means that the trial input electron density must be equivalent to the Kohn-Sham solution of $\varphi_i(r)$, such that the electron density, $p(r)$ is equivalent to the trial electron density used to generate the Kohn-Sham potential, $V_{eff}(r)$, up to a specified margin. The Kohn-Sham equation is classed as a type of density functional, as the Kohn-Sham potential is dependent on the electronic density. Although other types of density functional theory schemes have been devised, such as the orbital-free density functional theory [108] which aims to develop a better representation of the kinetic energy term in terms of the density to remove the need for Kohn-Sham orbitals, the Kohn-Sham density functional theory is currently most widely employed due to its reputation for accuracy, efficiency and reliability [109]. The Kohn-Sham density functional theory is used in this thesis and further discussion will focus on this aspect.

### 2.6.5 Kohn-Sham Density Functional Theory – Types and options

Basis sets are employed to represent the Kohn-Sham orbital and are sets of equations that represent molecular orbitals of interest that are to be studied. In this way, the interactions between different systems of different elements can be studied. The type of system investigated using the Kohn-Sham equations has a large bearing on the type of basis functions employed to expand the Kohn-Sham equation. The basis sets may be roughly divided into:

1. Atomic basis sets, also known as localised basis sets
2. Plane-wave basis sets, also known as non-localised basis sets

Atomic basis sets are so-called as the functions are centred on a point in space that represents the nuclei, and may be further sub-divided into slater-type orbitals, based on the equations developed by Slater [110] and whose coefficient were later refined by Clementi from first-principles [111], and Gaussian-type orbitals to describe the molecular orbitals.

Gaussian-type orbitals [112] utilise two or more Gaussian functions to approximate the molecular orbitals. The use of Gaussian-type orbitals offer a speedup in comparison to Slater type-orbitals of 4-5 orders of magnitude as their integrals can be evaluated analytically. To obtain comparable accuracy to Slater-type orbitals, more Gaussian must be added together to improve accuracy. As the trade-off between computation speed and accuracy is often an unknown variable, when Gaussian-type orbitals are employed as a basis set they must be carefully checked to ensure accuracy of the final solution.

Plane-wave basis sets take advantage of Bloch's theorem [88], which states that for a periodic system where the effective potential, $V(r)$ possesses translational symmetry, the wavefunction can be written as:

$$\varphi_k = e^{i\,k.r}\mu_k(r) \tag{65}$$

where the left-hand side of the equation represents the cell periodic part, and the right-hand side of the equation is represented by a wavelike part which can be expended and represented as plane waves whose wave vectors are equal to the reciprocal space vector of the crystal being investigated. In the equation, $\mu(r)$ has the same periodicity as $V(r)$, and k, the reciprocal space, lies within the same reciprocal unit cell. Using Bloch's theorem then allows the problem of a system with an infinite number of electrons to be simplified to that of an infinite amount of reciprocal space vectors into the first Brillouin zone of the representative periodic cell, where the electronic wavefunction at each k point can be represented by a plane wave basis set.

Using a non-localised basis set offers the benefit that the functions are orthogonal, enhancing computational speed, and the relative accuracies of the energies calculated using this method. This makes them very suitable for obtaining the information of the electronic structure of periodic structures. In comparison, computing results for inhomogenous systems such as glasses or isolated systems requires higher computational power due to the large numbers of basis functions needed per periodic cell.

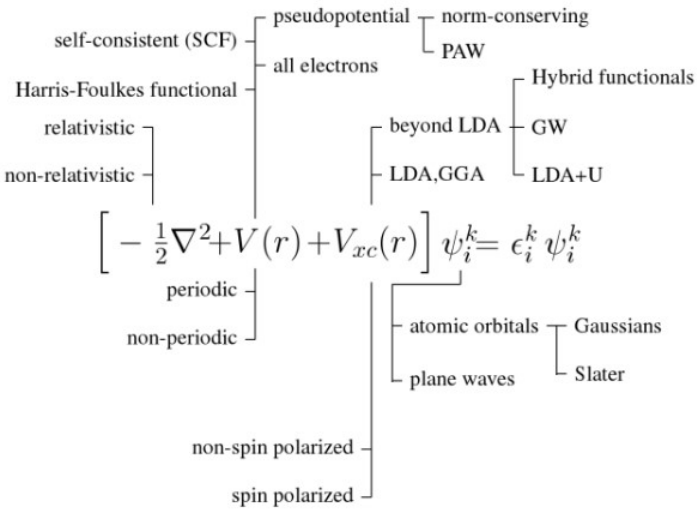


**Figure 10.** Truncated list of options for DFT calculations [109].

Other than the discussed options for the selection of the basis set, several other options exist in applying the DFT calculations for practical purposes. A simplified list of these is shown in Figure 10, where it can be seen that options exist for the calculation of all three remaining terms of the Kohn-Sham equation. Estimation of the exchange functional, $V_{XC}(r)$ term can be summarised mainly into the following methods, shown in Table 3:

**Table 3.** Summary of methods of estimation of the exchange correlation, $V_{XC}(r)$ in DFT methods, and some issues associated with them.

| Name | Description | Issues |
|---|---|---|
| Local Density Approximation (LDA) | Derived from the homogenous electron gas model | • Underestimation of band gap<br>• Fails in situations where there is a rapid change in electron density such as in molecules |
| Generalised Gradient Approximation (GGA) | Corrects the LDA functional by considering the gradient of the electron density | • Reduces error for magnetic solids<br>• Softens the bonds resulting in increased lattice constants and decreased bulk modulus<br>• Does not account for Van der Walls forces |
| Hubbard Correction for Correlated Ground States (LDA+U/GGA+U) | Corrects the error for strongly-correlated materials by introducing a Hubbard term into the energy equation | |
| Hybrid Methods | Combines weighted values of Hartree-Fock exchange energy with exchange-correlation terms from other sources | • Increased accuracy in calculating total energies due to better representation of exchange<br>• Increased computational cost |

Of the two terms left, the Kohn-Sham potential, $V(r)$ may, generally, be described by a Coulomb potential or by an effective potential:

**Table 4.** Summary of the all-electron potential and pseudopotentials used in DFT, and key issues related to them.

| Potential | Description | Issues |
|---|---|---|
| All-electron potential | A Columbic potential term is used to represent a defined system of fixed electrons, neglecting exchange and correlation effects. | • Does not take into account exchange and correlation effects.<br>• Computationally taxing |
| Pseudopotential [113] | An effective potential is used to describe the core electrons, while the valence electrons wavefunctions are replaced with pseudo wlecavefunctions which are smoother in the core region. | • Computationally faster<br>• Does not work well for transition metals due to no clear distinction between the tightly bound core electrons and loosely bound valence electrons. |

### 2.6.6 Rigid Band Approximation (RBA)

One simplification that may be used with random solid solutions is the rigid band approximation (RBA) [60,114,115]. The RBA theory asserts that the electronic bandstructure of pure materials remains unchanged upon alloying and only the filling of the bandstructure up to the Fermi level changes, depending on the valence electron concentration of the alloyed system, in comparison to the unalloyed material. More rigorously, the RBA can be understood to be explained by the following:

For ease of discussion, the equations in this section will be expressed using Dirac notation. The Schrodinger equation for a pure material is:

$$H^0\left|\varphi_i^0(r)\right> = \varepsilon_i^0\left|\varphi_i^0(r)\right> \tag{66}$$

where $H^0$ is the Hamiltonian of the pure material, $\varphi_i(r)$ is the wavefunction, and $\varepsilon_i^0$ is the energy of $|\varphi_i(r)>$. As stated previously the Hamiltonian may be simplified so that it is a function of kinetic energy, $-\frac{1}{2}\nabla^2$ and a potential, $V(r)$:

$$H^0 = -\frac{1}{2}\nabla^2 + V(r) \tag{67}$$

Upon alloying, the Hamiltonian changes so that:

$$H = H^0 + \Delta V(r) \tag{68}$$

where $\Delta V(r)$ is the perturbing potential associated with the alloying addition. Similarly, the wavefunction of the system may be written as:

$$|\varphi_i(r)>=|\varphi_i^0(r)>+|\Delta\varphi_i^0(r)> \tag{69}$$

where $|\Delta\varphi_i^0(r)>$ is the perturbed wavefunction of the system arising from the alloying addition. Since the energy associated with the metallic crystal is a function of the electron density, it can be written as:

$$\varepsilon_i =< \varphi_i(r)|H|\varphi_i(r)> \tag{70}$$

Therefore, the change in energy, $\Delta E$ can be shown to be:

$$\Delta\varepsilon_i = \varepsilon_i - \varepsilon_i^0 \tag{71}$$

$$\Delta\varepsilon_i =< \varphi_i(r)|H|\varphi_i(r)> -< \varphi_i(r)|H^0|\varphi_i(r)> \tag{72}$$

$$\Delta\varepsilon_i = \begin{pmatrix} < \varphi_i^0(r)|H|\varphi_i^0(r)> +< \Delta\varphi_i^0(r)|H|\varphi_i^0(r)> - \\ < \varphi_i^0(r)|H^0|\varphi_i^0(r)> +< \varphi_i^0(r)|H^0|\Delta\varphi_i^0(r)> \end{pmatrix} \tag{73}$$

$$\Delta\varepsilon_i = \begin{pmatrix} < \varphi_i^0(r)|\Delta V(r)|\varphi_i^0(r)> +< \Delta\varphi_i^0(r)|H^0|\varphi_i^0(r)> + \\ < \Delta\varphi_i^0(r)|\Delta V(r)|\varphi_i^0(r)> +< \varphi_i^0(r)|H^0|\Delta\varphi_i^0(r)> \end{pmatrix} \tag{74}$$

For the orthogonality condition if $\Delta\varphi_i^0 \neq \varphi_i^0$, then $< \Delta\varphi_i^0(r)|\varphi_i^0(r)>= 0$ and therefore the equation becomes:

$$\Delta\varepsilon_i =< \varphi_i^0(r)|\Delta V(r)|\varphi_i^0(r)> \tag{75}$$

If the valence electrons are delocalised and following the free electron approximation:

$$\Delta\varepsilon_i =< \Delta V(r)> \tag{76}$$

As long as $\Delta\varepsilon_i$ is a constant for each point in reciprocal space, the density of shapes of the alloy would have the same shape as that of the pure material. From the above equation, it can be seen that the change in energy is constant throughout the bandstructure and equivalent to the integrated average of $\Delta V(r)$, which is the perturbing potential associated with the alloying addition. One key point is that the density of states is only considered similar to the unalloyed system if the valency of the solute does not differ from the pure unalloyed material. In the case where the valency of the solute is dissimilar to the unalloyed material, all features of the RBA remain the same other than the shape of the Density of States changes in the alloy and must be recomputed [116,117]. The RBA has been used to successfully explain the Hume-Rothery rules [60,116–118], and its application can be used to describe the phase stability of alloys in terms of the unalloyed composition as a function of the valence electrons.

### 2.6.7 Phase stability using DFT and key challenges

The relative phase stabilities of a particular system can be understood in terms of the energy of formation of the system as a function of the designated structures, which can be calculated as long as the chemical composition and atomic positions of the structure in question are known. The energies of selected structures may be compared with one another to determine the lowest energy structure, and hence the most energetically favourable one. An example of this is shown in Figure 11 which represents the lowest energy of various structures for the Au-Cu system [119], that have been calculated using the VASP code [120–122] which uses a plane-wave basis set. The lowest-energy structures are displayed in Figure 11 at the equivalent Au fraction.

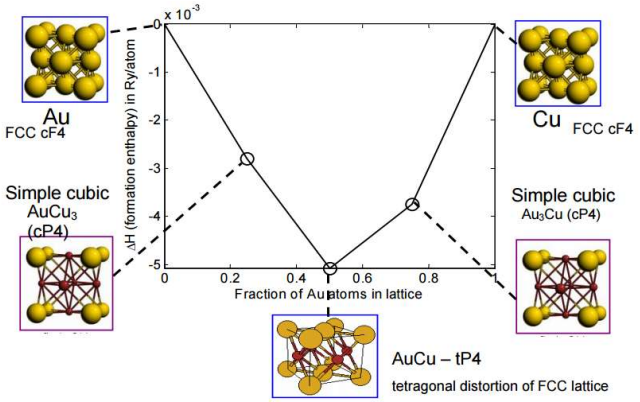


**Figure 11.** Lowest-energy structures in an Au-Cu system as a function of the fraction of Au atoms in the lattice [119]. The energy values are calculated using the VASP code [104–106], and representative structures are shown as well.

When computing for multi-component systems with >3 alloying components, some key issues that must be resolved are:

1. Identification of the structures to be tested for a given alloy composition. For example, in the CoCrFeNi equimolar HEA composition: the 6 binary phase diagrams of Co-Cr, Co-Fe, Co-Ni, Cr-Fe, Cr-Ni, and Fe-Ni lists amongst the possible structures the FCC, BCC, HCP, and Sigma phases [123]. Further ternary phase diagrams may give additional information on the possible structures present, which may be inaccurate depending on the usage of less well known alloying additions [5].
2. The exact chemical composition of a particular structure is not known precisely, and may impact the accuracy of the calculations. While research into HEAs is mainly driven by the concept of the search for single-phase solid-solution compositions [3,44,86], in practice, this is not always observed experimentally [6,8–10,21,124] which presents issues in the construction of an equivalent structure that is representative of the microstructural features of an alloy composition that is grounded in reality.
3. For *a priori* calculations of alloy compositions for alloy design, the structural parameters of the alloy composition are unknown even with prior analysis utilising binary and ternary phase diagrams due to straining of the lattice from atomic size mismatch [47]. The parameters must thus be obtained by minimising the Hartree-Fock energy as a function of the lattice parameter to obtain their most stable self-

consistent values. As such, the selection of the potential and basis set that is important to a model multi-component solid solution, as depending on the chemical bonding between constituent elements, the valency of the transition elements may differ leading to either an overestimation or underestimation of the structural parameters due to the pseudopotential chosen. This can be rectified through experimental verification with experimental results, which limits predictive *a priori* use.

These issues are summarised briefly in the table below:

**Table 5.** Summary of key issues associated with running DFT calculations.

| Issue | Problem | Resolution |
|---|---|---|
| Identification of competing structures | Determining competing structures of an alloy composition | Checking with binary phase diagrams, Experimental |
| Chemical composition of structures | Representing the chemical disorder of simple and complex phases accurately | Special Quasirandom Structure (SQS), Virtual Crystal Approximation, Experimental |
| Inclusion of correct structural parameters | Determining accurate structural parameters for calculations | Geometry optimisation, Mathematical Models, Experimental |

## 2.7 Summary

From the literature review, several key points regarding phase stability in HEAs are noted. Firstly, from the semi-empirical and empirical parameters, of the various available electronegativity scales only the Pauling electronegativity scale is most frequently employed in HEA prediction, which typically takes into account chemical bonds such as covalent and ionic bonds. Other electronegativity scales which are derived from other assumptions may possess increased accuracy. As an approximation, the Mulliken electronegativity is considered to be equivalent to the Fermi energy at 0 K; and the Mulliken electronegativity of the first valence electron may be a better measure of the energetics of an element, and its interaction with other pure elements.

The chemical bonds of HEAs are metallic bonds, whose electrons are delocalised in a sphere-like distribution around the atom and may be described as quantised bands of energy levels. The metallic bonds possess some covalent characteristics which depend on the alloying element, and may exhibit increased directional bonding (bonding with covalent like character) that is associated with the complex phases. This may only be probed through analysis of the electronic structure. A simple method suited to this analysis is the Thomas-Fermi-Dirac approximation as the electron density is fairly uniform due to strong screening by the nucleus.

The above two observations strongly suggest that the phase stability of HEAs are co-related to the Fermi energy and electron bonding directionality of the alloy, both of which are features of the electronic structure. The structural stability may be considered from an electronic structure perspective using ab-initio modelling tools. Furthermore, the semi-empirical parameters used in the prediction of HEA phase stability such as Miedema's enthalpy of mixing are not clearly grounded in quantum mechanical rules and hence, not exact, requiring quantum mechanical treatment for improvement of accuracy. The rigid band approximation may be employed as the approximation can be used to describe the validity of Hume-Rothery rules, which are employed in the prediction of HEA stability.

Finally, although ab-initio density functional theory offers many advantages, they are best employed to describe known systems as many of a system's parameters such as the crystal structure, chemical composition, and cell parameters must otherwise be found for the

ground state, and these values are very sensitive to the approximations, potentials, and basis sets used. A better semi-empirical model that includes more quantum mechanical principles needs to be made available to predict the stability of HEAs to expedite alloy design. Knowledge of the phase structure of potential HEA compositions, across the entire stoichiometry range, will allow compositions of interest to be pinpointed.

Therefore, the following results chapters in this thesis can be split into:

1. The investigations of whether consideration of quantum mechanical principles can increase the accuracy of predictions of HEA phase presence/stability (Chapters 3 & 4).
2. Development a simple predictive scheme that includes quantum mechanical principles which allows for the possibility to design a multiple component system so that an alloy composition which possesses desired combinations simple and complex structures Chapters (5 and 6).

## 2.9 References


[1] B. Cantor, I.T.H. Chang, P. Knight, A.J.B. Vincent, Microstructural development in equiatomic multicomponent alloys, Materials Science and Engineering A, Phys. Rev. B Condens. Matter. 375–377 (2004) 213–218.

[2] M.-H. Tsai, J.-W. Yeh, High-Entropy Alloys: A Critical Review, Mater. Res. Lett. 2 (2014) 107–123. doi:10.1080/21663831.2014.912690.

[3] J.W. Yeh, Recent progress in high—entropy alloys, Ann. Chim. - Sci. Mater. 31 (2006) 633–648.

[4] A. Durga, K.C. Hari Kumar, B.S. Murty, Phase Formation in Equiatomic High Entropy Alloys: CALPHAD Approach and Experimental Studies, Trans. Indian Inst. Met. 65 (2012) 375–380. doi:10.1007/s12666-012-0138-5.

[5] O.N. Senkov, J.D. Miller, D.B. Miracle, C. Woodward, Accelerated exploration of multi-principal element alloys with solid solution phases, Nat. Commun. 6 (2015) 6529. doi:10.1038/ncomms7529.

[6] C. Niu, A.J. Zaddach, A.A. Oni, X. Sang, J.W. Hurt, J.M. LeBeau, C.C. Koch, D.L. Irving, Spin-driven ordering of Cr in the equiatomic high entropy alloy NiFeCrCo, Appl. Phys. Lett. 106 (2015) 161906. doi:10.1063/1.4918996.

[7] E.J. Pickering, R. Munoz-Moreno, H.J. Stone, N.G. Jones, Precipitation in the equiatomic high-entropy alloy CrMnFeCoNi, Scr. Mater. 113 (2016).

[8] J. Cornide, M. Calvo-Dahlborg, S. Chambreland, L.A. Dominguez, Z. Leong, U. Dahlborg, A. Cunliffe, R. Goodall, I. Todd, Combined atom probe tomography and TEM investigations of CoCrFeNi, CoCrFeNi-Pdx (x=0.5, 1.0, 1.5) And CoCrFeNi-Sn, Acta Phys. Pol. A. 128 (2015).

[9] U. Dahlborg, J. Cornide, M. Calvo-Dahlborg, T.C. Hansen, Z. Leong, L.A. Dominguez, S. Chambreland, A. Cunliffe, R. Goodall, I. Todd, Crystalline structures of some high entropy alloys obtained by neutron and x-ray diffraction, Acta Phys. Pol. A. 128 (2015).

[10] M. Calvo-Dahlborg, J. Cornide, Tobola, D. Nguyen Manh, J.S. Wróbel, J. Juraszek, S. Jouen, U. Dahlborg, Effect of Pd on structural and magnetic properties of high entropy CoCrFeNiPd alloys. In preparation, (2016).

[11] M.G. Poletti, G. Fiore, B.A. Szost, L. Battezzati, Search for high entropy alloys in the X-NbTaTiZr systems (X = Al, Cr, V, Sn), J. Alloys Compd. 620 (2015) 283–288.

[12] S. Guo, N. C, L. J, L.C. T, Effect of valence electron concentration on stability of fcc or bcc phase in high entropy alloys, J. Appl. Phys. 109 (2011) 10.

[13] L.A. Dominguez, R. Goodall, I. Todd, Prediction and validation of quaternary high entropy alloys using statistical approaches, Mater. Sci. Technol. 31 (2015) 1201–1206.

[14] Y. Zhang, Z.P. Lu, S.G. Ma, P.K. Liaw, Z. Tang, Y.Q. Cheng, M.C. Gao, Guidelines in predicting phase formation of high-entropy alloys, MRS Commun. 4 (2014) 57–62. doi:10.1557/mrc.2014.11.

[15] X. Yang, Y. Zhang, Prediction of high-entropy stabilized solid-solution in multi-component alloys, Mater. Chem. Phys. 132 (2012) 233–238. doi:10.1016/j.matchemphys.2011.11.021.

[16] J.T. Waber, K.J. Gschneidner, A.C. Larson, M.Y. Prince, Prediction of solid solubility in metallic alloys, 1962.

[17] H. Zhang, Y.-Z. He, Y. Pan, S. Guo, Thermally stable laser cladded CoCrCuFeNi high-entropy alloy coating with low stacking fault energy, J. Alloys Compd. 600 (2014) 210–214. doi:10.1016/j.jallcom.2014.02.121.

[18] M.S. Lucas, L. Mauger, J. Munoz, Y. Xiao, A.O. Sheets, S.L. Sematin, Magnetic and vibrational properties of high-entropy alloys, J. Appl. Phys. 109 (2011) 7.

[19] F. Otto, A. Dlouhý, K.G. Pradeep, M. Kuběnová, D. Raabe, G. Eggeler, E.P. George, Decomposition of the single-phase high-entropy alloy CrMnFeCoNi after prolonged anneals at intermediate temperatures, Acta Mater. 112 (2016) 40–52. doi:10.1016/j.actamat.2016.04.005.

[20] B. Schuh, F. Mendez-Martin, B. Völker, E.P. George, H. Clemens, R. Pippan, A. Hohenwarter, Mechanical properties, microstructure and thermal stability of a nanocrystalline CoCrFeMnNi high-entropy alloy after severe plastic deformation, Acta Mater. 96 (2015) 258–268. doi:10.1016/j.actamat.2015.06.025.

[21] G.A. Salishchev, M.A. Tikhonovsky, D.G. Shaysultanov, N.D. Stepanov, A.V. Kuznetsov, I.V. Kolodiy, A.S. Tortika, O.N. Senkov, Effect of Mn and V on structure and mechanical properties of high-entropy alloys based on CoCrFeNi system, J. Alloys Compd. 591 (2014) 11–21. doi:10.1016/j.jallcom.2013.12.210.

[22] T.T. Shun, L.Y. Chang, M.H. Shiu, Microstructures and mechanical properties of multiprincipal component CoCrFeNiTix alloys, Mater. Sci. Eng. A. 556 (2012) 170–174.

[23] N.D. Stepanov, D.G. Shaysultanov, G.A. Salishchev, M.A. Tikhonovsky, E.E. Oleynik, A.S. Tortika, O.N. Senkov, Effect of V content on microstructure and mechanical properties of the CoCrFeMnNiVx high entropy alloys, J. Alloys Compd. 628 (2015) 170–185. doi:10.1016/j.jallcom.2014.12.157.

[24] W.R. Wang, W.L. Wang, S.C. Wang, Y.C. Tsai, C.H. Lai, J.W. Yeh, Effects of Al addition on the microstructure and mechanical property of AlxCoCrFeNi high-entropy alloys, Intermetallics. 26 (2012) 44–51.

[25] C.-C. Juan, C.-Y. Hsu, C.-W. Tsai, W.-R. Wang, T.-S. Sheu, J.-W. Yeh, S.-K. Chen, On microstructure and mechanical performance of AlCoCrFeMo0.5Nix high-entropy alloys, Intermetallics. 32 (2013) 401–407. doi:10.1016/j.intermet.2012.09.008.

[26] Y. Brif, M. Thomas, I. Todd, The use of high-entropy alloys in additive manufacturing, Scr. Mater. 99 (2015) 93–96. doi:10.1016/j.scriptamat.2014.11.037.

[27] A. Savin, R. Nesper, S. Wengert, T.F. Fässler, ELF: The Electron Localization Function, Angew. Chem. Int. Ed. Engl. 36 (1997) 1808–1832. doi:10.1002/anie.199718081.

[28] B. Silvi, C. Gatti, Direct Space Representation of the Metallic Bond, J. Phys. Chem. A. 104 (2000) 947–953. doi:10.1021/jp992784c.

[29] M. Aoki, D.G. Pettifor, Directional bonding in atomistic simulations, Mater. Sci. Eng. A. 176 (1994) 19–24. doi:10.1016/0921-5093(94)90954-7.

[30] M.E. Eberhart, The metallic bond: Elastic properties, Acta Mater. 44 (1996) 2495–2504. doi:10.1016/1359-6454(95)00347-9.

[31] Y. Zhang, T. Zuo, Y. Cheng, P.K. Liaw, High-entropy Alloys with High Saturation Magnetization, Electrical Resistivity, and Malleability, Sci. Rep. 3 (2013). doi:10.1038/srep01455.

[32] J.Y. He, W.H. Liu, H. Wang, Y. Wu, X.J. Liu, T.G. Nieh, Z.P. Lu, Effects of Al addition on structural evolution and tensile properties of the FeCoNiCrMn high-entropy alloy system, Acta Mater. 62 (2014) 105–113. doi:10.1016/j.actamat.2013.09.037.

[33] R. Sriharitha, B.S. Murty, R.S. Kottada, Alloying, thermal stability and strengthening in spark plasma sintered AlxCoCrCuFeNi high entropy alloys, J. Alloys Compd. 583 (2014) 419–426. doi:10.1016/j.jallcom.2013.08.176.

[34] C.-J. Tong, M.-R. Chen, J.-W. Yeh, S.-J. Lin, S.-K. Chen, T.-T. Shun, S.-Y. Chang, Mechanical performance of the Al x CoCrCuFeNi high-entropy alloy system with

multiprincipal elements, Metall. Mater. Trans. A. 36 (2005) 1263–1271. doi:10.1007/s11661-005-0218-9.

[35] I. Toda-Caraballo, P.E.J. Rivera-Díaz-del-Castillo, Modelling solid solution hardening in high entropy alloys, Acta Mater. 85 (2015) 14–23. doi:10.1016/j.actamat.2014.11.014.

[36] P. Ravindran, L. Fast, P.A. Korzhavyi, B. Johansson, J. Wills, O. Eriksson, Density functional theory for calculation of elastic properties of orthorhombic crystals: Application to TiSi2, J. Appl. Phys. 84 (1998) 4891. doi:10.1063/1.368733.

[37] H.-Y. Chung, M.B. Weinberger, J.-M. Yang, S.H. Tolbert, R.B. Kaner, Correlation between hardness and elastic moduli of the ultraincompressible transition metal diborides RuB[sub 2], OsB[sub 2], and ReB[sub 2], Appl. Phys. Lett. 92 (2008) 261904. doi:10.1063/1.2946665.

[38] Y.-F. Kao, S.-K. Chen, T.-J. Chen, P.-C. Chu, J.-W. Yeh, S.-J. Lin, Electrical, magnetic, and Hall properties of AlxCoCrFeNi high-entropy alloys, J. Alloys Compd. 509 (2011) 1607–1614. doi:10.1016/j.jallcom.2010.10.210.

[39] N.F. Mott, The cohesive forces in metals and alloys, Rep. Prog. Phys. 25 (1962) 218–243. doi:10.1088/0034-4885/25/1/306.

[40] M.S. Lucas, D. Belyea, C. Bauer, N. Bryant, E. Michel, Z. Turgut, S.O. Leontsev, J. Horwath, S.L. Semiatin, M.E. McHenry, C.W. Miller, Thermomagnetic analysis of FeCoCrxNi alloys: Magnetic entropy of high-entropy alloys, J. Appl. Phys. 113 (2013) 17A923. doi:10.1063/1.4798340.

[41] F. Kormann, D. Ma, D.D. Belyea, M.S. Lucas, C.W. Miller, B. Grabowski, H.F. Sluiter, “Treasure maps” for magnetic high-entropy-alloys from theory and experiment, Appl. Phys. Lett. 107 (2015).

[42] T.P.C. Klaver, R. Drautz, M.W. Finnis, Magnetism and thermodynamics of defect-free Fe-Cr alloys, Phys. Rev. B. 74 (2006). doi:10.1103/PhysRevB.74.094435.

[43] J.S. Wróbel, D. Nguyen-Manh, M.Y. Lavrentiev, M. Muzyk, S.L. Dudarev, Phase stability of ternary fcc and bcc Fe-Cr-Ni alloys, Phys. Rev. B. 91 (2015) 21408.

[44] K.-H. Cheng, C.-H. Lai, S.-J. Lin, J.-W. Yeh, Recent progress in multi-element alloy and nitride coatings sputtered from high-entropy alloy targets, Ann. Chim. Sci. Matér. 31 (2006) 723–736. doi:10.3166/acsm.31.723-736.

[45] K.-Y. Tsai, M.-H. Tsai, J.-W. Yeh, Sluggish diffusion in Co–Cr–Fe–Mn–Ni high-entropy alloys, Acta Mater. 61 (2013) 4887–4897. doi:10.1016/j.actamat.2013.04.058.

[46] A. Sadoc, B. Mercey, C. Simon, D. Grebille, W. Prellier, M.-B. Lepetit, Large Increase of the Curie Temperature by Orbital Ordering Control, Phys. Rev. Lett. 104 (2010). doi:10.1103/PhysRevLett.104.046804.

[47] J.W. Christian, The theory of transformations in metals and alloys. Pt. 2: [...], 3. ed, Pergamon, Amsterdam, 2002.

[48] F.L. Lambert, Entropy Is Simple, Qualitatively, J. Chem. Educ. 79 (2002) 1241. doi:10.1021/ed079p1241.

[49] J.W. Yeh, S.K. Chen, S.J. Lin, J.Y. Gan, T.S. Chin, T.T. Shun, C.H. Tsau, S.Y. Chang, Nanostructured high-entropy alloys with multiple principal elements: Novel alloy design concepts and outcomes, Adv. Eng. Mater. 6 (2004) 299–303.

[50] F. Otto, Y. Yang, H. Bei, E.P. George, Relative effects of enthalpy and entropy on the phase stability of equiatomic high-entropy alloys, Acta Mater. 61 (2013) 2628–2638. doi:10.1016/j.actamat.2013.01.042.

[51] D. Ma, B. Grabowski, F. Körmann, J. Neugebauer, D. Raabe, Ab initio thermodynamics of the CoCrFeMnNi high entropy alloy: Importance of entropy contributions beyond the configurational one, Acta Mater. 100 (2015) 90–97. doi:10.1016/j.actamat.2015.08.050.

[52] I.A. Tomilin, S.D. Kaloshkin, “High entropy alloys”—“semi-impossible” regular solid solutions?, Mater. Sci. Technol. 31 (2015) 1231–1234. doi:10.1179/1743284715Y.0000000028.

[53] Y. Zhang, T.T. Zuo, Z. Tang, M.C. Gao, K.A. Dahmen, P.K. Liaw, Z.P. Lu, Microstructures and properties of high-entropy alloys, Prog. Mater. Sci. 61 (2014) 1–93.

[54] Y. Zhang, Y.J. Zhou, Solid Solution Formation Criteria for High Entropy Alloys, Mater. Sci. Forum. 561–565 (2007) 1337–1339. doi:10.4028/www.scientific.net/MSF.561-565.1337.

[55] A. Cunliffe, J. Plummer, I. Figueroa, I. Todd, Glass formation in a high entropy alloy system by design, Intermetallics. 23 (2012) 204–207. doi:10.1016/j.intermet.2011.12.006.

[56] A.R. Miedema, The electronegativity parameter for transition metals: Heat of formation and charge transfer in alloys, J. Common Met. 32 (1973) 117–136. doi:10.1016/0022-5088(73)90078-7.

[57] H. Bakker, A. Miedema, Enthalpies in alloys: Miedemaś semi-empirical model, Trans Tech Publications, Uetikon-Zuerich, Switzerland ; Enfield, N.H, 1998.

[58] F.R. de Boer, ed., Cohesion in metals: transition metal alloys, 2., print, North Holland, Amsterdam, 1988.

[59] L.C. Allen, Electronegativity is the average one-electron energy of the valence-shell electrons in ground-state free atoms, J. Am. Chem. Soc. 111 (1989) 9003–9014. doi:10.1021/ja00207a003.

[60] A. Paxton, M. Methfessel, D.G. Pettifor, A bandstructure view of the Hume-Rothery electron phases, Proc. R. Soc. A. 453 (1997) 1493.

[61] U. Mizutani, Hume-Rothery rules for structurally complex alloy phases, CRC Press, Boca Raton, 2011.

[62] W. Hume-Rothery, R.E. Smallman, C.W. Haworth, The Structure of Metals and Alloys, The Institute of Metals, Carlton House Terrace, London SW1Y 5DB, UK, 1988.

[63] D.G. Pettifor, Theory of the Heats of Formation of Transition-Metal Alloys, Phys. Rev. Lett. 42 (1978) 846.

[64] D.G. Pettifor, A Quantum Mechanical Critique of the Miedema Rules for Alloy Formation, Solid State Phys. 40 (1987) 43–92.

[65] Y.M. Zhang, J.R.G. Evans, S. Yang, The prediction of solid solubility of alloys: Development and application of Hume-Rothery's rules, J. Cryst. Phys. Chem. 1 (2010) 81–97.

[66] W. Hume-Rothery, G.W. Mabbott, K.M.C. Evans, The Freezing Points, Melting Points, and Solid Solubility Limits of the Alloys of Silver, and Copper with the Elements of the B Sub-Groups, Philos. Trans. R. Soc. Math. Phys. Eng. Sci. 233 (1934) 1–97. doi:10.1098/rsta.1934.0014.

[67] F.R.N. Nabarro, The Strains Produced by Precipitation in Alloys, Proc. R. Soc. Math. Phys. Eng. Sci. 175 (1940) 519–538. doi:10.1098/rspa.1940.0072.

[68] D. Kashchiev, Nucleation basic theory with applications, Butterworth Heinemann, Oxford; Boston, 2000. http://www.engineeringvillage.com/controller/servlet/OpenURL?genre=book&isbn=9780750646826 (accessed February 20, 2016).

[69] L.S. Darken, R.W. Gurry, M.B. Bever, Physical chemistry of metals, 2002.

[70] S. Guo, C.T. Liu, Phase stability in high entropy alloys: Formation of solid-solution phase or amorphous phase, Prog. Nat. Sci. Mater. Int. 21 (2011) 433–446. doi:10.1016/S1002-0071(12)60080-X.

[71] A.L. Greer, N. Karpe, J. Bøttiger, Diffusional aspects of the solid state amorphization reaction, J. Alloys Compd. 194 (1993) 199–211. doi:10.1016/0925-8388(93)90003-6.

[72] L. Pauling, THE NATURE OF THE CHEMICAL BOND. IV. THE ENERGY OF SINGLE BONDS AND THE RELATIVE ELECTRONEGATIVITY OF ATOMS, J. Am. Chem. Soc. 54 (1932) 3570–3582. doi:10.1021/ja01348a011.

[73] R.S. Mulliken, A New Electroaffinity Scale; Together with Data on Valence States and on Valence Ionization Potentials and Electron Affinities, J. Chem. Phys. 2 (1934) 782. doi:10.1063/1.1749394.

[74] W. Gordy, A New Method of Determining Electronegativity from Other Atomic Properties, Phys. Rev. 69 (1946) 604–607. doi:10.1103/PhysRev.69.604.

[75] A.D. Walsh, Factors Affecting Bond Strengths. I. A Possible New Definition of Electronegativity, Proc. R. Soc. Math. Phys. Eng. Sci. 207 (1951) 13–22. doi:10.1098/rspa.1951.0093.

[76] R.T. Sanderson, Electronegativities in inorganic chemistry: A revision of atomic charge data, J. Chem. Educ. 32 (1955) 140. doi:10.1021/ed032p140.

[77] A.L. Allred, E.G. Rochow, A scale of electronegativity based on electrostatic force, J. Inorg. Nucl. Chem. 5 (1958) 264–268. doi:10.1016/0022-1902(58)80003-2.

[78] J.C. Phillips, Dielectric Definition of Electronegativity, Phys. Rev. Lett. 20 (1968) 550–553. doi:10.1103/PhysRevLett.20.550.

[79] A.I. Martynov, Batsanov, S. S, New approach to the determination of atom electronegativity, Zhurnal Neorganicheskoj Khimii. 25 (1980) 3171–3175.

[80] R.G. Pearson, Electronegativity scales, Acc. Chem. Res. 23 (1990) 1–2. doi:10.1021/ar00169a001.

[81] R.G. Parr, R.A. Donnelly, M. Levy, W.E. Palke, Electronegativity: The density functional viewpoint, J. Chem. Phys. 68 (1978) 3801. doi:10.1063/1.436185.

[82] D. Miracle, J. Miller, O. Senkov, C. Woodward, M. Uchic, J. Tiley, Exploration and Development of High Entropy Alloys for Structural Applications, Entropy. 16 (2014) 494–525. doi:10.3390/e16010494.

[83] D. Nguyen-Manh, D.G. Pettifor, Electronic structure, phase stability, and elastic moduli of AB transition metal aluminides, Intermetallics. 7 (1999).

[84] D.G. Pettifor, Theory of the crystal structures of transition metals, J. Phys. C Solid State Phys. 3 (1970) 367–377. doi:10.1088/0022-3719/3/2/018.

[85] E. Petrishcheva, R. Abart, Exsolution by spinodal decomposition in multicomponent mineral solutions, Acta Mater. 60 (2012) 5481–5493. doi:10.1016/j.actamat.2012.07.006.

[86] M.-H. Tsai, K.-Y. Tsai, C.-W. Tsai, C. Lee, C.-C. Juan, J.-W. Yeh, Criterion for Sigma Phase Formation in Cr- and V-Containing High-Entropy Alloys, Mater. Res. Lett. 1 (2013) 207–212. doi:10.1080/21663831.2013.831382.

[87] N.W. Ashcroft, N.D. Mermin, Solid state physics, Holt, Rinehart and Winston, New York, 1976.

[88] C. Kittel, Introduction to solid state physics, 8th ed, Wiley, Hoboken, NJ, 2005.

[89] G.N. Lewis, K.S. Pitzer, Valence and the structure of atoms and molecules, Dover Publications, New York, 1966.

[90] K. Okumura, I.M. Templeton, The Fermi Surface of Caesium, Proc. R. Soc. Math. Phys. Eng. Sci. 287 (1965) 89–104. doi:10.1098/rspa.1965.0170.

[91] R.F.W. Bader, J. Hernández-Trujillo, F. Cortés-Guzmán, Chemical bonding: From Lewis to atoms in molecules, J. Comput. Chem. 28 (2007) 4–14. doi:10.1002/jcc.20528.

[92] A.D. Becke, K.E. Edgecombe, A simple measure of electron localization in atomic and molecular systems, J. Chem. Phys. 92 (1990) 5397. doi:10.1063/1.458517.

[93] S. Lee, R. Hoffmann, Bcc and Fcc Transition Metals and Alloys: A Central Role for the Jahn−Teller Effect in Explaining Their Ideal and Distorted Structures, J. Am. Chem. Soc. 124 (2002) 4811–4823. doi:10.1021/ja0114557.

[94] D.G. Pettifor, Structure Maps for Ordered Intermetallics, in: C.T. Liu, R.W. Cahn, G. Sauthoff (Eds.), Ordered Intermet. — Phys. Metall. Mech. Behav., Springer Netherlands, Dordrecht, 1992: pp. 47–59. http://link.springer.com/10.1007/978-94-011-2534-5_4 (accessed April 27, 2016).

[95] J. Simons, An introduction to theoretical chemistry, Cambridge University Press, Cambridge ; New York, 2003.

[96] P.A.M. Dirac, Note on Exchange Phenomena in the Thomas Atom, Math. Proc. Camb. Philos. Soc. 26 (1930) 376. doi:10.1017/S0305004100016108.

[97] D.J. Griffiths, Introduction to quantum mechanics, Prentice Hall, Englewood Cliffs, N.J, 1995.

[98] T. Tsuneda, Density functional theory in quantum chemistry, 2014. http://public.eblib.com/choice/publicfullrecord.aspx?p=1698251 (accessed August 8, 2016).

[99] S.J. Clark, M.D. Segall, C.J. Pickard, P.J. Hasnip, M.I.J. Probert, K. Refson, M.C. Payne, First principles methods using CASTEP, Z. Für Krist. - Cryst. Mater. 220 (2005). doi:10.1524/zkri.220.5.567.65075.

[100] L.H. Thomas, The calculation of atomic fields, Math. Proc. Camb. Philos. Soc. 23 (1927) 542. doi:10.1017/S0305004100011683.

[101] E. Fermi, Un metodo statistico per la determinazione di alcune priorieta dell'atome, Rend Accad Naz Lincei. 6 (1927) 32.

[102] W. Lenz, Über die Anwendbarkeit der statistischen Methode auf Ionengitter, Z. Für Phys. 77 (n.d.) 713–721. doi:10.1007/BF01342150.

[103] B.K. Vaĭnshteĭn, Structure analysis by electron diffraction, Pergamon Press, Oxford; New York, 1964. http://catalog.hathitrust.org/api/volumes/oclc/10431633.html (accessed August 8, 2016).

[104] L. Spruch, Pedagogic notes on Thomas-Fermi theory (and on some improvements): atoms, stars, and the stability of bulk matter, Rev. Mod. Phys. 63 (1991) 151–209. doi:10.1103/RevModPhys.63.151.

[105] R.P. Feynman, N. Metropolis, E. Teller, Equations of State of Elements Based on the Generalized Fermi-Thomas Theory, 1949. http://www.osti.gov/servlets/purl/4417654-BCgOtj/native/ (accessed April 20, 2016).

[106] J. Kohanoff, Electronic structure calculations for solids and molecules: theory and computational methods, Cambridge University Press, Cambridge, UK ; New York, 2006.

[107] P. Hohenberg, W. Kohn, Inhomogeneous Electron Gas, Phys. Rev. 136 (1964) B864–B871. doi:10.1103/PhysRev.136.B864.

[108] M. Pearson, E. Smargiassi, P.A. Madden, Ab initio molecular dynamics with an orbital-free density functional, J. Phys. Condens. Matter. 5 (1993) 3221–3240. doi:10.1088/0953-8984/5/19/019.

[109] I. Kondov, G. Sutmann, Centre Européen de Calcul Atomique et Moléculaire, Tutorial "Multiscale Modelling Methods for Applications in Materials Science," eds., Multiscale

modelling methods for applications in materials science: CECAM tutorial, 16 - 20 September 2013, Forschungszentrum Jülich ; lecture notes, Forschungszentrum, Zentralbibliothek, Jülich, 2013.

[110] J.C. Slater, Atomic Shielding Constants, Phys. Rev. 36 (1930) 57–64. doi:10.1103/PhysRev.36.57.

[111] E. Clementi, D.L. Raimondi, Atomic Screening Constants from SCF Functions, J. Chem. Phys. 38 (1963) 2686. doi:10.1063/1.1733573.

[112] S.F. Boys, Electronic Wave Functions. I. A General Method of Calculation for the Stationary States of Any Molecular System, Proc. R. Soc. Math. Phys. Eng. Sci. 200 (1950) 542–554. doi:10.1098/rspa.1950.0036.

[113] P. Schwerdtfeger, The Pseudopotential Approximation in Electronic Structure Theory, ChemPhysChem. 12 (2011) 3143–3155. doi:10.1002/cphc.201100387.

[114] Electrons in finite and infinite structures., Springer-Verlag New York, Place of publication not identified, 2013.

[115] D. Nguyen-Manh, A. Paxton, D.G. Pettifor, A. Pasturel, On the phase stability of transition metal trialuminide compounds, Intermetallics. 3 (1995) 9–14.

[116] S. Raimes, The rigid-band model, J. Phys. Radium. 23 (1962) 639–643. doi:10.1051/jphysrad:019620023010063901.

[117] E.A. Stern, Rigid-Band Model of Alloys, Phys. Rev. 157 (1967) 544–551. doi:10.1103/PhysRev.157.544.

[118] J.L. Beeby, Electronic Structure of Alloys, Phys. Rev. 135 (1964) A130–A143. doi:10.1103/PhysRev.135.A130.

[119] M. Mihalkovic, M. Widom, et al., CMU Alloy Database, (n.d.). http://alloy.phys.cmu.edu/.

[120] G. Kresse, J. Furthmüller, Efficient iterative schemes for ab initio total-energy calculations using a plane-wave basis set, Phys. Rev. B Condens. Matter. 54 (1996).

[121] G. Kresse, J. Furthmüller, Efficiency of ab-initio total energy calculations for metals and semiconductors using a plane-wave basis set, Comput. Mater. Sci. 6 (1996).

[122] G. Kresse, J. Hafner, *Ab initio* molecular dynamics for liquid metals, Phys. Rev. B. 47 (1993) 558–561. doi:10.1103/PhysRevB.47.558.

[123] P. Villars, H. Okamoto, K. Cenzual, eds., ASM Alloy Phase Diagrams Database, ASM International, Materials Park, OH, 2006. http://www1.asminternational.org/AsmEnterprise/APD.

[124] J. Cornide, U. Dahlborg, Z. Leong, L.A. Dominguez, J. Juraszek, S. Jouen, T. Hansen, R. Wunderlich, S. Chambreland, I. Todd, R. Goodall, M. Calvo-Dahlborg, Structure and Properties of Some CoCrFeNi-Based High Entropy Alloys, in: TMS2015 Supplemental Proceedings, 2015.

[a1] D.B. Miracle, O.N. Senkov, A critical review of high entropy alloys and related concepts, Acta Mater. 122 (2017) 448–511. doi:10.1016/j.actamat.2016.08.081.

[a2] E.J. Pickering, N.G. Jones, High-entropy alloys: a critical assessment of their founding principles and future prospects, International Materials Reviews. 61 (2016) 183–202. doi:10.1080/09506608.2016.1180020.

# 3. Experimental and Numerical Methods

## Table of Contents

## 3.1 Alloy synthesis – Arc melting


**Figure 12.** Figure showing the Edmund Buhler MAM 1 arc-melter.

Alloy synthesis was carried out in a small-scale Edmund Buhler MAM 1 arc-melter, displayed in Figure 12. The individual key components are labelled as 1. The main chamber, 2. Copper water-cooled melting hearth and casting hearth (not shown), 3. Valve-controlled suction device for attachment to casting hearth, and 4. Range of copper moulds for casting. Close-up images of the demarked components can be found in Figure 13.

The synthesis of samples is preceded by weighing out the alloying elements of at least 99.9% purity. All alloying elements are polished with grit paper to remove any potential oxide layer and contaminants from the surface of the metal. The metals are subsequently cleaned by sonicating in an acetone-filled beaker. The sonication is performed at the minimum amplitude for 5 minutes to ensure that re-oxidisation does not occur resulting from excessive energy transfer. The alloying elements of the selected composition are weighed out so that 5 g of the composition is made. The weigh-out is measured to an accuracy of 0.1g for each individual component and their weights are recorded.

The weighted-out components are inserted into one of the crucibles in the melting hearth with a small titanium ingot in the centre crucible, to act as an oxygen getter; the melting hearth is then sealed into the vacuum chamber, and the chamber is depressurised to 0.3 $\times 10^5$ Pa and flushed with argon to 0.7$\times 10^5$ Pa. This process is repeated thrice to flush as much air as possible from the chamber to reduce the chance of oxidisation of the material during the melting process. The chamber is then further depressurised to $1\times 10^{-3}$ Pa. On reaching the targeted pressure, the evacuated chamber is re-filled with Ar to 0.2 $\times 10^5$ Pa and the DC power supply is activated so that current flows from the tungsten carbide tip acting as a cathode to the crucible base that acts as an anode. The alloying components located in the crucible is then melted.

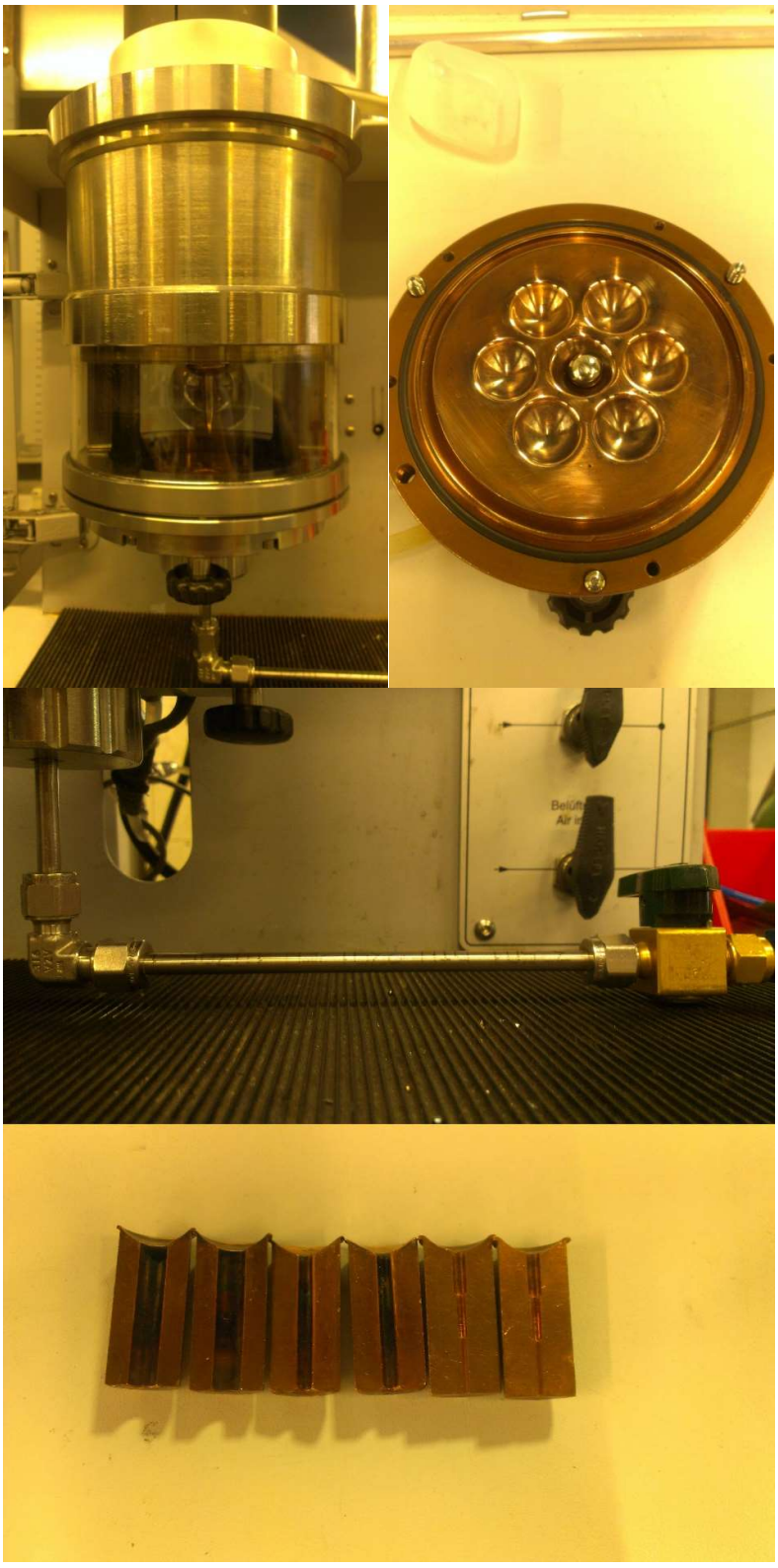

**Figure 13.** Images of the arc-melter. From top-left, clockwise: The vacuum chamber, copper hearth with titanium getter, suction-casting attachment, and copper moulds.

The ingots were re-melted three times to improve compositional homogeneity of the alloy; after retrieving the melted sample, it is sectioned in half to be visually inspected for possible signs of segregation of the alloying components. In the event of segregated or un-melted constituents, the samples were further re-melted as required until good mixing was achieved. The melted ingot is then weighted for comparison with the pre-melted components to determine the amount of raw materials that have been lost in the synthesis.

Once an ingot has been melted, they may then be cast in the casting hearth into a desired shape. The procedure for the operation of the casting hearth when attached to the vacuum chamber (*cf.* Figure 13. (a)) is similar to that of the melting hearth with one addition: prior to depressurisation the secondary vacuum chamber and its attachment (*cf.* Figure 13. (c)) is pressurised to -0.7 gauge pressure so that a pressure differential is created between the vacuum chamber and the secondary chamber after the Argon back-filling process, allowing the molten composition to be sucked into the water-cooled copper hearth. A selection of copper moulds are available (*cf.* Figure 13. (d)).

For standard XRD characterisation experiments and compression testing the 3 mm diameter rod shape is used and in the event that a particular composition possesses high viscosity which prevents casting in the 3 mm diameter die, the 6 mm diameter rod shape is used for enhanced flow; for hardness indentation and scratch testing the samples are cast into 2 mm x 6 mm x 10 mm rectangular ingots.

## 3.2 X-ray diffraction

Transmission XRD experiments of powder produced by rasping samples in the as-cast condition were conducted on a STOE Stadi diffractometer utilising a Mo k-α monochromated source. This method was chosen over reflective XRD to ease characterisation of complex phase containing HEA compositions that were too brittle to be ground and polished due to their tendency to fragment mid-grinding.

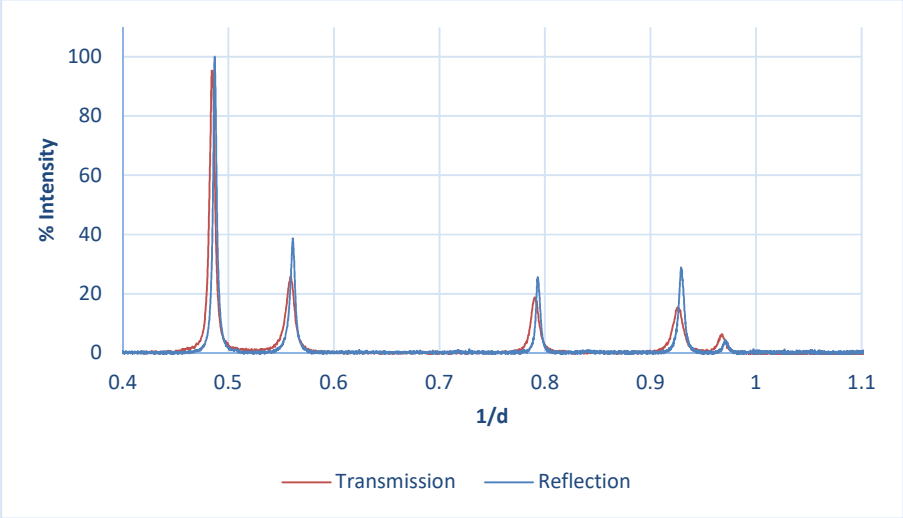


**Figure 14.** Comparison of XRD traces of the CoCrFeNi composition obtained from transmission XRD and reflection XRD.

Figure 14 shows a comparison of the XRD patterns of a HEA CoCrFeNi composition cast into a 3 mm rod determined and rasped using a transmission XRD method from a Mo source versus the bulk sample using a reflective XRD method in a Bruker D2 Phaser using radiation from a Cu source. The difference in peak positions is attributed to the rasping process that reduces the strain in the CoCrFeNi alloy system. For the transmission XRD data, the {311} peak is indexed at $d^{-1} = 0.927\dot{A}^{-1}$which corresponds to a lattice parameter of $3.578\ \dot{A}$; while for the reflection data the {311} peak is indexed at $d^{-1} = 0.929\dot{A}^{-1}$ which corresponds to a lattice parameter of $3.570\ \dot{A}$. The difference in accuracy between the as-cast sample and the rasped sample amounts to $0.008\ \dot{A}$, which is 0.2 %. Generally, determination of lattice parameters is only accurate up to two decimal places for standard laboratory equipment and is normally sufficient for characterisation purposes. As such, the characterisation of the sample using transmission XRD is considered to be useable in determining the structure present in the HEAs sample here and as representative of the as-cast condition for the analyses required in this work. Further comparison of experimental data with equivalent literature data it was found that similar phases present in the XRD pattern despite the lower resolution of the radiation source [4–7].

All transmission XRD samples were run from 17° - 50° with a step size of 0.02 for four hours and the XRD patterns were Rietveld refined using reference instrument diffraction profiles. The angle chosen is sufficient to index the first 5 peaks of the FCC structure: the {111}, {200},

{220}, {311}, and {222} peaks. In general, for peak identification the peak positions and general peak intensities are required to match at least three peaks of a reference database, or the Bragg reflections of a known structure, and the chosen angles of $2\theta = 17°$ to $50°$ are deemed to be sufficient for phase detection.

All XRD values are presented as a function of the percentage intensity and reciprocal lattice, $d^{-1}(\dot{A}^{-1})$. Characterisation of the XRD results was performed utilising indexed patterns from the PDF4+ database as a guide; following which a Rietveld refinement on the lattice parameters and structure was performed on the data using the GSAS software package [a1].

It should be recognised that, while commonly used for characterisation of the structure of metals and alloys, standard XRD may not detect lower intensity peaks associated with smaller phase fractions due to low resolution or poor signal-to-noise ratios, and also may not discriminate precisely between such effects as depth profile information and compositional variation from segregation, for example. However, for the current goal it is a suitable characterisation method as the RBA technique is itself a DFT-based electronic structure method suitable for predictions in situations of incomplete knowledge, and a complete experimental investigation of structure and properties would naturally follow.

## 3.3 Hardness testing

Hardness testing is performed on samples that have been cast into rectangular ingots of dimensions 2 mm x 6 mm x 10 mm. The samples are ground and polished to obtained a good surface finish and are tested on a standard Vickers indenter using a diamond pyramidal-shaped tip using a load of 10 kg. At least 5 indents are made and the average hardness of the composition can then be determined.

## 3.4 Compression testing

Compression testing samples are prepared by sectioning as-cast 3 mm rods so that the length to diameter ratio of the rods are 2.0 +/- 0.1 (6 mm) following ASTM E9-89A standards for compression testing; the rods are polished so that the ends are parallel to one another within 0.0127 mm in preparation for compression testing. The parallelism is checked by measuring the distance between both ends at the opposing edges of the cylinder using a electronic micrometer which is accurate up to 0.005 mm. The compression tests were conducted on a Zwick/Roell Z050 TH testing device at a constant strain rate of $2 \times 10^{-4} s^{-1}$

using a 50 kN load, while the degree of compression is determined from the crossheads. At least two samples of each composition, synthesised separately, were tested to check the reproducibility of the compression testing results.

The engineering stress-strain curves are converted into true stress-strain curves using the following formula:

$$\sigma_T = \sigma_E(1 + \varepsilon_E) \tag{1}$$

$$\varepsilon_T = Ln(1 + \varepsilon_E) \tag{2}$$

where $\sigma_T$ is the true stress, $\sigma_E$ is the engineering stress, $\varepsilon_T$ is the true strain, and $\varepsilon_E$ is the engineering strain.

## 3.5 Statistical analysis: Cluster analysis and probability density function

The cluster centre in cluster analysis is obtained by minimising the sum of the Euclidean distance, $d_{Euclidean}$ between members of all identified clusters. In the case of an analysis on a xy grid, the equation to be minimised is:

$$d_{Euclidean} = \sqrt{(x_n - x_c)^2 + (y_n - y_c)^2} \tag{3}$$

where the coordinates $(x_n, y_n)$ represents the coordinate of the n$^{th}$ member of an identified cluster, while $(x_c, y_c)$ represents the coordinate of the cluster's centre. The location of the cluster centre can be determined by minimising the sum of the Euclidean distances for all members across all identified clusters, $Min(\sum d_{Euclidean})$. In this thesis, $Min(\sum d_{Euclidean})$ is obtained by using the solver add-in of MS Excel, with a convergence value of $1\times10^{-5}$, mutation rate of 0.15, and a population size of 100.

Once the coordinates of the cluster centre have been determined, the cluster standard deviation for the x and y axis can be determined using the following relationships:

$$\sigma_x = \sqrt{\frac{1}{n}\sum_{i=1}^{n}(x_n - x_c)^2}\,,\ \sigma_y = \sqrt{\frac{1}{n}\sum_{i=1}^{n}(y_n - y_c)^2} \tag{4}$$

The distribution of the clusters can also be analysed using a probability density function. The analysis is performed on the Mathematica 10 [8] suite utilising the SmoothHistogram function which uses a smooth kernel distribution estimate. This estimate has the general form of:

$$\frac{1}{nh}\sum_{i=1}^{n} K\left(\frac{x-x_i}{h}\right) \quad (5)$$

where *K* is a weighting function known as the kernel, and h is a smoothing parameter known as the bandwidth. In the analysis of this thesis the selection of the kernel was left to Mathematica [8] while selection of the bandwidth was estimated using the mean of Silverman's normal distribution approximation given by:

$$h = 1.06\,\hat{\sigma}\,n^{-0.2} \quad (6)$$

where $\hat{\sigma}$ is the standard deviation and n is the dataset length.

## 3.6 4th order Runge-Kutta solution of the Thomas-Fermi-Dirac function

The Thomas-Fermi-Dirac equation is solved in this thesis using a 4th order Runge-Kutta method. The method can be used to solve an ordinary differential equation of the form:

$$\frac{dy}{dx} = f(x,y), y(0) = y_0 \quad (7)$$

In which case *y* may be written as:

$$y_{i+1} = y_i + (a_1k_1 + a_2k_2 + a_3k_3 + a_4k_4)h \quad (8)$$

which may be equated with a semi-convergent Taylor expansion so that:

$$y_{i+1} = y_i + \sum_{j=1}^{n}\left[\left(\frac{1}{a!}\right)\left(\frac{d^jy}{dx^j}\right)(x_{i+1} - x_i)^j\right] \quad (9)$$

Comparing Equation 8 with 9, $h = (x_{i+1} - x_i)$ , $a_n$ are the related coefficients of expansion, and $k_n$ is a function of $\left(\frac{dy}{dx}\right)^n$. The general solution used may be written as:

$$y_{i+1} = y_i + \frac{1}{6}(k_1 + 2k_2 + 2k_3 + k_4)h \quad (10)$$

By defining $\frac{dy}{dx} = f(x_i, y_i)$, the coefficients $k_n$ may be written as:

$$k_1 = f(x_i, y_i)$$

$$k_2 = f\left(x_i + \frac{1}{2}h, y_i + \frac{1}{2}k_1h\right)$$

$$k_3 = f\left(x_i + \frac{1}{2}h, y_i + \frac{1}{2}k_2h\right)$$

$$k_4 = f(x_i + h, y_i + k_3 h) \tag{11}$$

Equation 10 is the general solution for a first order differential equation. The solution for a 2nd order differential equation may be solved by converting the second order differential equation

$$\frac{d^2y}{dx^2} + \frac{dy}{dx} + y = C \tag{12}$$

into two first order differential equations of the form:

$$\frac{dy}{dx} = z$$

$$\frac{dz}{dx} = C - y - z \tag{13}$$

so that the general solution from Equation 10 can now be used to solve Equations 13. The solution to the Thomas-Fermi-Dirac approximation in Chapter 4 is achieved using the method described above, and computed in Mathematica [8]; and the code is shown in the Appendix. The 4th order Runge-Kutta method may be implemented computationally to solve the Thomas-Fermi-Dirac approximation by first defining the equations and the boundary conditions:

$$\frac{d^2y}{dx^2} = x\left[\left(\frac{y(x)}{x}\right)^{1/2} + \varepsilon\right]^3 \tag{14}$$

$$y(0) = 1 \tag{15}$$

$$\left(\frac{dy}{dx}\right)_{x=x_0} = \frac{y(x_0)}{x_0} \tag{16}$$

A semi-convergent expansion of Eq. 2 may then be written as [9]:

$$y(x) = 1 + a_n(x)^{n/2} + \ldots, \text{ up to n = 13} \tag{17}$$

where $a_n$ represents the coefficients of the expansion which may be obtained by inserting Eq. 17 into Eq. 14 and comparing coefficients of similar power exponents from both sides of the equation, with the exception of the coefficient $a_2$ which is defined as the initial slope of the TFD equation, where $a_2 = \varphi'(0)$. $a_2$ coefficients lie between -1.7 and -1.5, and the numerical solution of the TFD equation may then obtained by determining the minimised

electron density, n(x) in this range by using Equations 10 and 11 to solve both first order differential equations, Equation 14 and 16.

Since the initial slope has been defined as $-1.7 < a_2 < -1.5$, the step size $h = (x_{i+1} - x_i)$ must also be defined for the algorithm to function. For the calculations in this thesis, $h = 50$. The electron density and its associated Wigner-Seitz radius may then be computed. For a known crystal structure, the $r_{ws}$ may be approximated from the mean volume, V per atom, N of the unit cell where each atom is considered to be spherical, hence leading to:

$$r_{ws} = \frac{3V}{4N\pi}^{1/3} \tag{18}$$

The electron density for this Wigner-Seitz radius may then be selected from the list of solutions of Equation 90, given by the 4$^{th}$ order Runge-Kutta method.

## 3.8 References


[1] U. Dahlborg, J. Cornide, M. Calvo-Dahlborg, T.C. Hansen, Z. Leong, L.A. Dominguez, S. Chambreland, A. Cunliffe, R. Goodall, I. Todd, Crystalline structures of some high entropy alloys obtained by neutron and x-ray diffraction, Acta Phys. Pol. A. 128 (2015).

[2] M. Calvo-Dahlborg, J. Cornide, Tobola, D. Nguyen Manh, J.S. Wróbel, J. Juraszek, S. Jouen, U. Dahlborg, Effect of Pd on structural and magnetic properties of high entropy CoCrFeNiPd alloys. In preparation, (2016).

[3] J. Cornide, U. Dahlborg, Z. Leong, L.A. Dominguez, J. Juraszek, S. Jouen, T. Hansen, R. Wunderlich, S. Chambreland, I. Todd, R. Goodall, M. Calvo-Dahlborg, Structure and Properties of Some CoCrFeNi-Based High Entropy Alloys, in: TMS2015 Supplemental Proceedings, 2015.

[4] J. Cornide, M. Calvo-Dahlborg, S. Chambreland, L.A. Dominguez, Z. Leong, U. Dahlborg, A. Cunliffe, R. Goodall, I. Todd, Combined atom probe tomography and TEM investigations of CoCrFeNi, CoCrFeNi-Pdx (x=0.5, 1.0, 1.5) And CoCrFeNi-Sn, Acta Phys. Pol. A. 128 (2015).

[5] W. Research, Mathematica 10.4, 10.4, Champaign, Illinios, 2016.

[6] F. Ren, K. Cao, J. Ren, A.A. Volinsky, T.H. Tran, B. Tian, Numerical Calculation of the Electron Density at the Wigner–Seitz Radius Based on the Thomas–Fermi–Dirac Equation, J. Comput. Theor. Nanosci. 11 (2014) 344–347. doi:10.1166/jctn.2014.3358.

[7] J.H. Rose, J. Ferrante, J.R. Smith, Universal Binding Energy Curves for Metals and Bimetallic Interfaces, Phys. Rev. Lett. 47 (1981) 675–678. doi:10.1103/PhysRevLett.47.675.

[a1] A.C. Larson, R.B. Von Dreele, GSAS General Structure Analysis System, Report LAUR 86-748, Los Alamos National Laboratory, Los Alamos, NM. (1986).

# 4. The Local Environment of Alloys

| | |
|---|---|
| Objective | To understand the underlying relationship between the electronic structure and phase presence in High-entropy Alloys. |
| Hypothesis | The Mulliken electronegativity scale of the first valence electron will enable discrimination between simple and complex phases due to the difference in metallic bonding between simple and complex phases. This difference can also be evidenced from the electron density. |
| Analysis Type | Analytical (80%), Experimental (20%) |
| Variables | Alloy Composition |
| Primary Result | Electronegativity, Electron density |
| Techniques | Arc-Melting & Casting, XRD, Numerical Analysis |

**Table of Contents**

**Symbols and Abbreviations**

| | |
|---|---|
| $\Delta X$ | Electronegativity difference |
| $\Delta X^*$ | Change in Miedema electronegativity |
| $\Delta X_{Allen}$ | Allen electronegativity difference |
| $\Delta S$ | Entropy of mixing |
| $a_0$ | Bohr radius |
| Å | Units Angstrom |
| $\hat{\sigma}$ | Standard deviation |
| $\delta$ | Atomic size difference |
| $\mu$ | Electronic chemical potential |
| $\varphi(x)$ | Thomas-Fermi-Dirac Function |
| BCC | Body-centred cubic |
| E | Energy |
| FCC | Face-centred cubic |
| HEA | High-entropy alloy |
| $n(x)$ | Electron density at x |
| $n_P$ | Averaged primary quantum number |
| $n_{WS}$ | Electron density at the Wigner-Seitz radius |
| N | Number of electrons |
| PCA | Principal component analysis |
| PDF | Pair distribution function |
| r | Radius |
| $r_{ws}$ | Wigner-Seitz radius |
| RK | Runge-Kutta |
| TFD | Thomas-Fermi-Dirac |
| V | Potential of the nuclei |
| VEC | Valence electron concentration |
| x | Normalised radius |
| $X_{Allen}$ | Allen electronegativity |
| $X_{Mulliken}$ | Mulliken electronegativity |
| $X_{Pauling}$ | Pauling electronegativity |

| | |
|---|---|
| Z | Atomic number |

**Tables of Figures**

## 4.1 Chapter Preface

Chapter 4 is split into two sections involving two separate analyses; section 4.2 covers the analysis of the relationship between enthalpy of mixing and various measures of electronegativity (Pauling, Allen, and Mulliken) High-entropy Alloy (HEA) parameters, while section 4.3 addresses the electron density analysis of HEAs simple and complex phases. The hypothesis tested in this chapter is as follows:

> *The Mulliken electronegativity scale of the first valence electron will enable discrimination between simple and complex phases due to the difference in metallic bonding between simple and complex phases. This difference can also be evidenced from the electron density, being representative of the electronic structure.*

In Section 4.2 the average electronegativity values of selected HEA compositions are considered for their ability in distinguishing and predicting simple/complex phase presence in HEAs. Electronegativity is expected to offer better discrimination as their point of reference will more accurately reflect the atomic environment; as mentioned in Section 1.3.2 of the Literature review these scales may be derived from properties of the free atoms such as their heats of formation, paired bond lengths, charge transfer properties etc. The Mulliken electronegativity may be able to better represent the metallic bonding nature of HEA compositions by taking the arithmetic mean of the first electron affinity and first ionisation energy, as the valence electrons in transition metals are dependent on many factors related to the electronic structure [10].

In Section 4.3 the electron densities of selected HEA compositions are probed for their ability in distinguishing and predicting simple/complex phase presence in HEAs. Complex phase presence in HEAs is often attributed to the addition of alloying elements which possess increased bond directionality (*c.f.* Section 1.4 in the Literature Review). Further evidence is given for charge redistribution in these phases, suggesting that their local environment is different from the simple phases, and that an analysis of the electron density at the Wigner-Seitz radius may allow for further discrimination.

It is the aim of this Chapter to explore the difference between discrimination of simple/complex phases determined through a semi-empirical method utilising averaged electronegativity values in Section 4.2, and through a simple approximation of the local

environment using the Thomas-Fermi-Dirac equations in Section 4.3. The results and increased understanding in this chapter are used to fuel the development of a strategy for alloy design.

## 4.2 Analysis of the relationship between High-entropy alloy parameters: Enthalpy of mixing and averaged electronegativities (Pauling, Allen, and Mulliken)

The effect of some empirical and thermodynamic parameters (enthalpy of mixing ($\Delta H$), electronegativity difference (ΔX), atomic size difference ($\delta$), entropy of mixing ($\Delta S$), and valence electron concentration (VEC)) on the presence of the simple phase was studied by Dominguez *et al.* [11] statistically utilising a principal component analysis (PCA), from which it was shown that the VEC and $\Delta H$ parameters could be used to distinguish between the presence of simple and complex structures in HEA compositions. It is of particular interest that the electronegativity parameter, defined as the ability of an atom to attract electrons towards itself, did not successfully discriminate between simple and complex phases in the PCA.

The electronegativity rule is an electrochemical effect employed to describe the electronic interactions between the constituent components of an alloy composition [12]. In a binary system this is evaluated by taking the difference in the Pauling electronegativity between the two constituent elements. An electronegativity difference of zero would imply that elements possess the same tendency to attract electrons and the electrons will be shared between both atoms, while a large electronegativity difference would imply that the resulting charge transfer is more favourable towards the formation of a compound phase.

As mentioned in Section 1.3.2 of the Literature Review, electronegativity scales may be broadly divided into either absolute scales, or Pauling-like scales. Absolute scales originate from Parr's 1934 [13] communication which showed that electronegativity analysed from the viewpoint of density functional theory is equivalent to the negative of $\mu$, the electronic chemical potential and this value is constant for any chemical system, atom, ion or molecule. The chemical potential may be defined by the function $= \frac{\partial E}{\partial N} V$, where E is the electronic energy, N is equivalent to the number of electrons, and V is the potential of the nuclei. It is further shown that the Mulliken electronegativity, the average of the ionisation energy and the electron affinity, is a good approximation of $\mu$, and that the Mulliken electronegativity is termed the 'absolute electronegativity' in reference to its near equality to this property, $-\mu$.

The electroneutrality principle introduced by Pauling [14] states that charge has to be transferred from the more electronegative to the less electronegative atom. This concept has been explored by Miedema [15] who reports > 96% accuracy in predicting the metallurgical behaviour of transition metal alloys in terms of the electronegativity difference and electron density difference at the Wigner-Seitz radius parameters. The motivation of this section is to therefore determine the influence of the mean Pauling, Allen, and Mulliken electronegativity parameters, at which electroneutrality should be reached theoretically, on the discrimination of simple FCC and BCC phase forming HEA compositions, and their applicability in compositional selection and alloy design.

### 4.2.1 Calculations: Cluster and probability density function analysis.

The dataset used in this study consists of 24 HEA compositions selected by considering their diffraction patterns (presenting one simple diffraction pattern of either FCC, BCC, or HCP type]) from literature showing the presence of a majority (>90%) phase consisting of simple FCC (9 compositions), simple BCC (10 compositions), and complex structures (4 compositions). Shown in Table 6, the values of the primary quantum number (n), the Pauling electronegativity ($X_{Pauling}$), Allen electronegativity ($X_{Allen}$), Mulliken electronegativity ($X_{Mulliken}$), enthalpy of mixing ($\Delta H$) and valence electron concentration (VEC) for each composition are determined from the weighted average of the respective composition's individual elemental alloying additions. Values of $X_{Mulliken}$ here are determined as the average of the first ionisation energy and electron affinity of the alloying element involved.

**Table 6.** Tabulated values of the for $X_{Pauling}$, $X_{Allen}$, and $X_{Mulliken}$ mean electronegativities of selected HEA compositions taken from literature, with their corresponding averaged primary quantum number, $n_P$, majority phase present, enthalpy of mixing, and valence electron concentration.

| Nominal composition | Group | n | $X_{Pauling}$ | $X_{Allen}$ | $X_{Mulliken}$ | $\Delta H$ | VEC | Ref |
|---|---|---|---|---|---|---|---|---|
| $Al_{0.17}Co_{0.17}Cr_{0.17}Fe_{0.17}Mo_{0.02}Ni_{0.17}$ | BCC (3d) | 3.2 | 1.49 | 1.46 | 3.28 | -12.13 | 4.52 | [a1] |
| $Al_{0.17}Co_{0.17}Cr_{0.17}Fe_{0.17}Ni_{0.17}Nb_{0.02}$ | BCC (3d) | 3.2 | 1.48 | 1.46 | 3.28 | -13.32 | 4.51 | [a2] |
| $Al_{0.27}$ $Co_{0.18}Cr_{0.18}Fe_{0.18}Ni_{0.18}$ | BCC (4d) | 3.7 | 1.75 | 1.73 | 3.82 | -12.32 | 5.13 | [a3] |
| $Al_{0.2}Nb_{0.2}Ta_{0.2}Ti_{0.2}V_{0.2}$ | BCC (4d) | 4.4 | 1.58 | 1.45 | 3.61 | -13.44 | 4.40 | [a4] |
| $Al_{0.11}Nb_{0.22}Ta_{0.22}Ti_{0.22}V_{0.22}$ | BCC (4d) | 3.7 | 1.29 | 1.18 | 2.99 | -8.40 | 3.73 | [a4] |
| $Nb_{0.25}Mo_{0.25}Ta_{0.25}W_{0.25}$ | BCC (5d) | 5.5 | 1.91 | 1.42 | 4.01 | -6.50 | 5.50 | [a5, a6] |
| $Al_{0.06}Nb_{0.23}Ta_{0.23}Ti_{0.23}V_{0.23}$ | BCC (5d) | 4.7 | 1.57 | 1.42 | 3.69 | -6.50 | 4.67 | [a4] |
| $Hf_{0.2}Nb_{0.2}Ta_{0.2}Ti_{0.2}Zr_{0.2}$ | BCC (5d) | 5.2 | 1.45 | 1.32 | 3.64 | 2.72 | 3.60 | [a6] |
| $Nb_{0.2}Mo_{0.2}Ta_{0.2}V_{0.2}W_{0.2}$ | BCC (5d) | 5.2 | 1.85 | 1.44 | 3.93 | -4.64 | 5.40 | [a6] |
| $Hf_{0.33}Nb_{0.33}Zr_{0.33}$ | BCC (5d) | 5.3 | 1.41 | 1.30 | 3.61 | 3.56 | 3.00 | [a7] |
| $Al_{0.06}Cr_{0.19}Fe_{0.19}Co_{0.19}Ni_{0.19}Cu_{0.19}$ | FCC (4d) | 3.7 | 1.82 | 1.79 | 4.12 | 0.16 | 6.77 | [a8] |
| $Al_{0.10}Cr_{0.18}Fe_{0.18}Co_{0.18}Ni_{0.18}Cu_{0.18}$ | FCC (4d) | 3.7 | 1.82 | 1.79 | 4.09 | -1.52 | 6.64 | [a8] |
| $Co_{0.25}Cr_{0.25}$ $Fe_{0.25}Ni_{0.25}$ | FCC (4d) | 4.0 | 1.82 | 1.79 | 4.10 | 6.25 | 6.00 | [a9, a10, a11] |
| $Cr_{0.23}Fe_{0.23}Co_{0.23}Ni_{0.23}Cu_{0.12}$ | FCC (4d) | 4.0 | 1.83 | 1.80 | 4.15 | 0.49 | 6.56 | [a9, a10] |
| $Co_{0.2}Cr_{0.2}$ $Fe_{0.2}Ni_{0.2}Pd_{0.2}$ | FCC (4d) | 4.2 | 1.90 | 1.75 | 4.17 | -5.60 | 6.80 | [a10, a11] |
| $Co_{0.2}Cr_{0.2}Fe_{0.2}$ $Mn_{0.2}Ni_{0.2}$ | FCC (4d) | 4.0 | 1.77 | 1.78 | 4.03 | -4.16 | 6.20 | [a12] |
| $Co_{0.23}Cr_{0.23}$ $Fe_{0.23}Ni_{0.23}Pd_{0.12}$ | FCC (4d) | 4.1 | 1.86 | 1.77 | 4.14 | -4.80 | 6.44 | [a9, a10] |
| $Co_{0.19}Cr_{0.19}Fe_{0.19}Ni_{0.19}Pd_{0.28}$ | FCC (4d) | 4.3 | 1.92 | 1.74 | 4.20 | -5.83 | 7.09 | [a9, a10] |
| $Cr_{0.13}$ $Cu_{0.25}Fe_{0.25}$ $Mn_{0.13}Ni_{0.25}$ | FCC (4d) | 4.0 | 1.81 | 1.81 | 4.16 | -17.5 | 7.25 | [a15] |
| $AlCoCrFeMo_{0.5}Ni$ | Complex | - | 1.81 | 1.73 | 3.93 | -11.21 | 5.45 | [a15] |
| CuTiVFeNiZrCo | Complex | - | 1.72 | 1.39 | 3.36 | -14.82 | 6.00 | [a8] |
| $CoCrFeNiCuAl_{0.5}V$ | Complex | - | 1.79 | 1.51 | 3.46 | -4.46 | 6.38 | [a16] |
| $CoCrFeNiCuAl_{0.5}V_{1.6}$ | Complex | - | 1.75 | 1.31 | 2.95 | -11.53 | 5.49 | [a16] |
| $Ti_{0.25}Mn_{0.25}Fe_{0.25}Ni_{0.25}$ | Complex | - | 1.71 | 1.70 | 3.90 | -16.55 | 7.25 | [a17] |

In addition to separating the 24 compositions by the majority phase present, they have been further partitioned according to their averaged primary quantum numbers rounded to integer values. These subdivided groups are illustrated in Table 1 as the BCC (3d), BCC (4d), BCC (5d), FCC (4d), and complex structures. The distribution of these compositions may be analysed utilising a Euclidean distance-based cluster analysis.

By designating the compositions belonging in each group as members of each cluster (here the clusters are denoted as BCC (3d), BCC (4d), BCC (5d), and FCC (4d)), the cluster centre may be determined by minimising the Euclidean distance between each composition within a group to a common arbitrary point that is defined as the cluster centre. The values of

these are shown in Table 6 listed together with the standard deviations of each cluster for values of $X_{Pauling}$, $X_{Allen}$, $X_{Mulliken}$, and VEC. Values of these results will be shown graphically and discussed individually in the following results and discussion section. The presence of complex phases within the cluster analysis were found to be independent of the simple phase partition. This result is in agreement with previous work in the VEC-ΔH plot [6], which will be shown later in this work to be similar to the X-ΔH plots. The analysis in this work will therefore focus on the separation between the FCC and BCC structures, and for ease of representation, complex structures will not be shown.

**Table 7.** Coordinates of cluster centres for BCC (3d), BCC (4d), BCC (5d), and FCC (4d) data calculated from HEA compositions listed in

Table **6** for for $X_{Pauling}$, $X_{Allen}$, and $X_{Mulliken}$ tabulated together with the calculated standard deviation of the samples. Cluster centre coordinates are obtained by minimising the Euclidean distance between the coordinates of each point in the $X - \Delta H$ biplot of identified clusters.

| Cluster | $X_{Pauling}$ | | $X_{Allen}$ | | $X_{Mulliken}$ | | VEC | |
|---|---|---|---|---|---|---|---|---|
| | $X \pm \hat{\sigma}$ | $\Delta H \pm \hat{\sigma}$ | $X \pm \hat{\sigma}$ | $\Delta H \pm \hat{\sigma}$ | $X \pm \hat{\sigma}$ | $\Delta H \pm \hat{\sigma}$ | $VEC \pm \hat{\sigma}$ | $\Delta H \pm \hat{\sigma}$ |
| **BCC (3d)** | 1.49 ± 0 | -12.75 ± 0.6 | 1.46 ± 0 | -12.56 ± 0.62 | 3.28 ± 0 | -12.76 ± 0.6 | 4.86 ± 0.34 | -12.77 ± 0.6 |
| **BCC (4d)** | 1.75 ± 0.28 | -12.32 ± 2.35 | 1.73 ± 0.36 | -12.32 ± 2.35 | 3.82 ± 0.49 | -12.32 ± 2.35 | 4.67 ± 0.63 | -12.07 ± 2.27 |
| **BCC (5d)** | 1.85 ± 0.24 | -4.64 ± 3.91 | 1.44 ± 0.06 | -4.64 ± 3.91 | 3.93 ± 0.19 | -4.64 ± 3.91 | 5.38 ± 0.96 | -3.29 ± 3.83 |
| **FCC (4d)** | 1.82 ± 0.05 | -1.65 ± 3.87 | 1.78 ± 0.02 | -1.77 ± 3.86 | 4.11 ± 0.05 | -1.87 ± 3.86 | 6.12 ± 0.55 | -2.93 ± 4 |

### 4.2.2 Cluster analysis of $\mathbf{VEC - \Delta H}$ plot

The result of the cluster analysis is first analysed as a biplot of VEC-ΔH in Figure 1(a). This biplot is the similar to the one presented by Dominguez et al. as a result of their PCA, and shows the two variables that best distinguish the simple FCC/BCC and complex phases from one another, out of all five empirical parameters that were analysed. It is emphasised again that each point on the left-most plot represents 1 of the 24 selected compositions, which have been partitioned into one of several groups/clusters. The highlighted zones on the plot show the results of the cluster analysis, while the secondary plot on the right is the result of another statistical analysis, the probability density function of the distribution of these identified clusters. These analyses are used to study the distribution of the HEA compositions within the subsequent biplots as a function of their classification to each cluster, the discussion of which will be elaborated later.

Figure 15 (a) shows a graphical representation of the cluster centres encompassing an area with two boundaries; The first boundary's limits are defined by the cluster standard deviation (see values of $\hat{\sigma}$ in Table 6), while the second boundary's limits are defined by the composition within the cluster possessing the largest difference in Euclidean distance from its centre. The resultant analysis shows a distinct overlap within the first cluster boundary between the simple FCC (4d) and BCC (5d) clusters. Additionally, the BCC (3d) cluster is found to be located within the BCC (4d) cluster, although minimal overlap between the second cluster boundary of BCC (4d) and BCC (5d).

Figure 15 (b) presents a smoothed pair density function (PDF) of the distribution of VEC of the HEA compositions using the KernelMixtureDistribution function included in the

Mathematica 10 package [8]. The kernel bandwidth, h for $X_{Pauling}$, $X_{Allen}$, $X_{Mulliken}$, and VEC was estimated using the mean of Silverman's normal distribution approximation [19], given by:

$$h = 1.06\,\hat{\sigma}\,n^{-0.2} \tag{1}$$

where $\hat{\sigma}$ is the standard deviation and n is the dataset length. h was determined to be of the following values for $X_{Pauling}$ (h: 0.21), $X_{Allen}$ (h: 0.15), $X_{Mulliken}$ (h: 0.25), and VEC (h: 0.88) respectively. Further information on the numerical analyses may be found in the Methods section. In the two-dimensional PDF landscape represented by Figure 15 (b), the PDF determined independently of $\Delta H$, the BCC (3d), BCC (4d), and BCC (5d) clusters exhibit significant overlap with each other, which is in agreement with Figure 15 (a). The positions of the cluster centres and standard deviations in Figure 15 (a) are mapped as to Figure 15 (b) according to their corresponding clusters, shown by the highlighted regions of the PDF curves. The location of the cluster centre is observed to be off-centre from the mean position of the smoothed histogram, showing the influence of $\Delta H$ in determining the cluster centres located in Figure 15 (a), and their influence on phase discrimination.

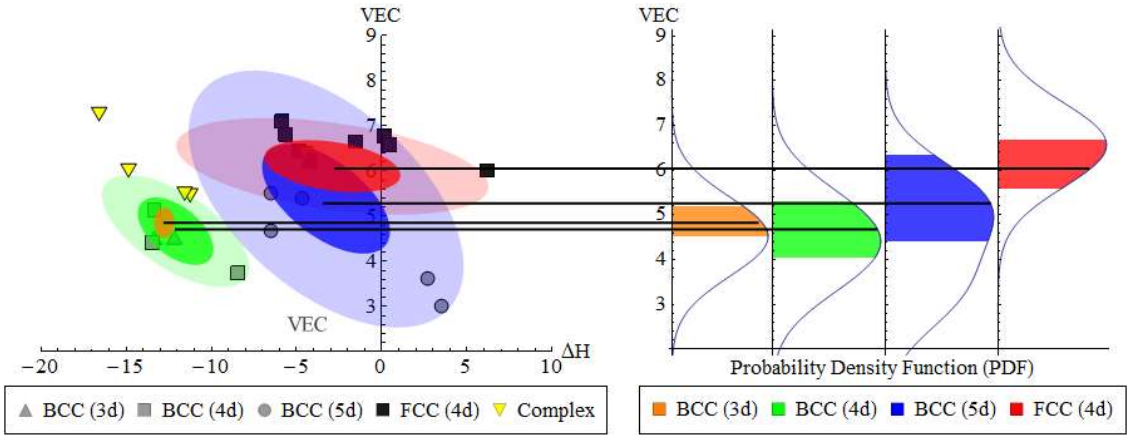


**Figure 15. (a)** Two-dimensional plot of $VEC - \Delta H$ following Dominguez et al.'s analysis with dark areas bounded, and **(b)** The associated Probability Density Function (PDF) for the VEC distribution of HEA compositions studied here.

The above analysis is performed by obtaining $\Delta H_{conf}$ values from the Miedema model using the interaction between the volumetric effect, chemical potential for electronic charge, and change in the electron density at the Wigner-Seitz boundary as a basis for evaluation [20]. The proportionality between neighbouring atoms may be given by [3]:

$$\Delta H \propto -P(\Delta X^*)^2 + Q\left(\Delta {n_{WS}}^{1/3}\right)^2 \quad (2)$$

where P and Q are constants related to combinations of metals depending on their valences [3], $\Delta X^*$ is Miedema's electronegativity difference and $\Delta n_{WS}^{1/3}$ is the difference in the electron density at the Wigner-Seitz boundary. Electronegativity is linked to the valence electrons of an atom, even such that the Allen electronegativity scale is defined as the average energy of the valence electrons of an atom at the ground state [10]. Previous studies have shown that the structure of a composition may be strongly related to the valence electron concentration, famously used to explain the stability FCC and BCC brass by Hume-Rothery [12], and shown to also apply to a wide variety of other structures, including HEAs [12,21,22]. The stability of these phases might be attributed to the dependence of the size changes on the electronic properties of the composition such as electronegativity and valence electron [23], which is in agreement with the two-dimensional plot of Dominguez *et al.* [11]. By making the simplification that $VEC \propto X$, the gradient of the $VEC - \Delta H$ can be written as:

$$\frac{\delta \overline{VEC}}{\delta \Delta H} = \frac{\delta VEC}{\delta\left(-P(\Delta X*)^2 + Q\Delta {n_{WS}}^{2/3}\right)} \quad (3)$$

The difference between the identified clusters of simple structures can then be determined to be the ratio between the rate of change of the valence electron concentration to the rate of change of the sum of Miedema's electronegativity difference and the electron density at the Wigner-Seitz radius as described in Eq. 2. The separation of the clusters between the simple FCC and BCC phases and their respective averaged primary quantum numbers can then be attributed to a different rate of change in $\delta\Delta H$. From Eq. 3, this may be attributed to a combination of 1. The change in the shielding effect between atom to atom in the case of an increased primary quantum number, reducing the attraction experienced between the valence electrons and the nucleus and hence $\Delta X*$; and 2. A difference in the bonding behaviour in the electronic structure reflected by the electron density.

The discrimination can thus be seen to be based on the behaviour of the electrons, from quantum-mechanical principles. The value of VEC by itself, can then be taken as a semi-empirical value reflecting the electronic structure that in combination with the ratio $\frac{\delta \overline{VEC}}{\delta \Delta H}$, allows discrimination of the simple structures. Although this 2-D plot shown in Figure 15

allows said discrimination, the resulting histogram analysis shown in Figure 15. (b) does not conform to expectation of the energy levels of these structures, as one might expect the overall energy of an atom to increase in tandem with its size. This may be attributed to the fact that VEC values, derived semi-empirically from the periodic table, may be very different from the exact electrons available for bonding at the quantum-mechanical level, due to interactions of the electronic structure.

As the change in Miedema's electronegativity parameter, $\Delta X^*$ is proportional to the change in Pauling electronegativity [3,15,23] which should be better able to reflect the electronic properties of an atom, it is proposed here that a relationship between $\overline{X} - \Delta H$ may give better partitioning of the simple/complex phases in HEAs. Figure 16 presents the cluster and PDF analysis performed for $\overline{X} - \Delta H$ for three different electronegativity scales, $X_{\text{Allen}}$, $X_{\text{Pauling}}$, and $X_{\text{Mulliken}}$.

### 4.2.3 Cluster analysis of $\overline{X} - \Delta H$ plots

Figure 16 (a) and (b) shows the similar cluster and PDF analysis performed to investigate the $\overline{X}_{\text{Pauling}} - \Delta H$ relationship. The simple/complex phase discrimination here is in good agreement with the two-dimensional plot of $VEC - \Delta H$ shown in Figure 15 (a). In comparison, while here a larger overlap between the FCC (4d) and BCC (5d) clusters is observed, the BCC (3d) cluster here is more distinctly distinguished from the BCC (4d) cluster, being located at the edge of the first boundary of the BCC (4d) cluster. From Figure 16 (b), the separation of $\overline{X}_{\text{Pauling}}$ values between the clusters with values $\overline{X}_{\text{BCC (3d)}}$: 1.49, $\overline{X}_{\text{BCC (4d)}}$: 1.75, $\overline{X}_{\text{BCC (5d)}}$: 1.85 are observed to be much more distinct when compared to the plot of $VEC - \Delta H$ shown in Figure 15 (a). The close overlap of the FCC (4d) and BCC (5d) cluster is also observed in Figure 16 (b) with $\overline{X}_{\text{FCC (4d)}}$: 1.82 and $\overline{X}_{\text{BCC (5d)}}$: 1.8.

Figure 2 (c) shows the cluster and PDF analysis performed for the $\overline{X}_{\text{Allen}} - \Delta H$ relationship, where a clear distinction between the FCC (4d) and BCC (4d) structure is observed. The spread of the BCC (4d) cluster is seen to be much larger in comparison to the BCC (3d), BCC (5d), and FCC (4d) clusters as evidenced by $\widehat{\sigma}_{\text{BCC (4d)}}$: 0.36, in comparison to $\widehat{\sigma}_{\text{BCC (3d)}}$: 0, $\widehat{\sigma}_{\text{BCC (5d)}}$: 0.06, and $\widehat{\sigma}_{\text{FCC (4d)}}$: 0.02. The locations of these cluster centres in ascending order are $\overline{X}_{\text{BCC (4d)}}$: 1.44, $\overline{X}_{\text{BCC (3d)}}$: 1.46, $\overline{X}_{\text{BCC (5d)}}$: 1.73, and $\overline{X}_{\text{FCC (4d)}}$: 1.78, reflecting a discrepency with the earlier $\overline{X}_{\text{Allen}} - \Delta H$ analysis, as the electronegativity, reflective of the

orbital energy, should scale with the mean atomic size. The PDF analysis in Figure 2 (d) demonstrates a similar pattern with the BCC (4d) distribution appearing to be more evenly distributed, due to the small sample size of the BCC (4d) cluster. The positions of the BCC (3d), BCC (4d) and BCC (5d) peaks in Figure 2 (d) are seen to be very close to one another, which shows good comparison with Figure 2 (b).

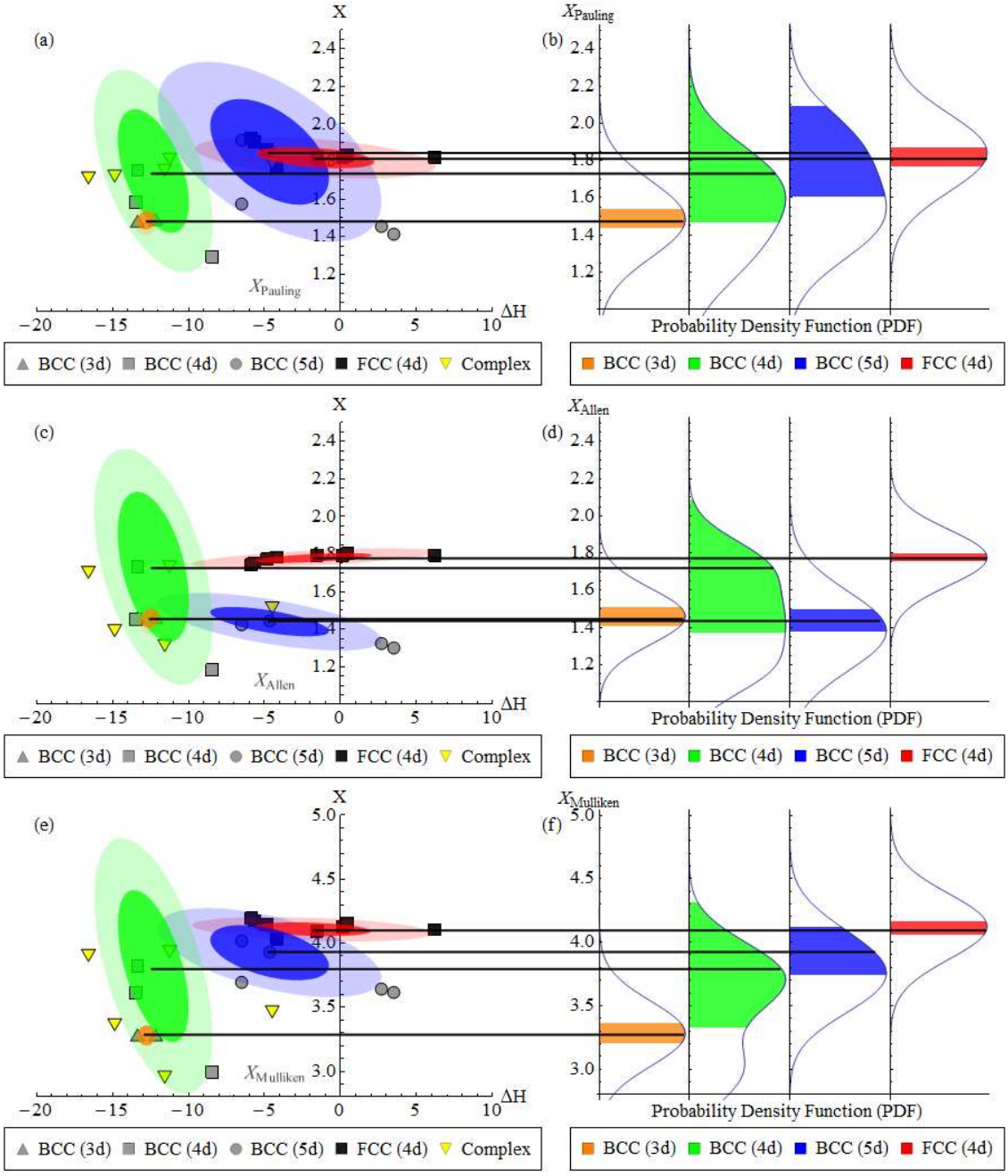


**Figure 16. (Left: a, c, e)** HEA distribution shown on biplots of electronegativity plotted against enthalpy of mixing for $X_{Pauling}$, $X_{Allen}$, and $X_{Mulliken}$ with dark bounded areas showing the extent of

standard deviation from the cluster centre and light bounded areas showing the maximum Euclidean distance between cluster centre and the outermost regions. **(Right: b, d, f)** Smoothed histogram plots for $X_{Pauling}$, $X_{Allen}$, and $X_{Mulliken}$ of BCC (3d), BCC (4d), BCC (5d), and FCC (4d) HEA alloy compositions following a Gaussian distribution.

Figure 16 (e) shows the analysis performed the $\overline{X}_{\mathrm{Mulliken}} - \Delta H$ relationship showing good identification of phases within the two-dimensional plot. The FCC (4d) and BCC (5d) clusters are observed to overlap at around $\Delta H = -5.5$. The cluster positions as shown in Figure 2 (f) are in ascending order are $\overline{X}_{\mathrm{BCC\ (3d)}}$: 3.28, $\overline{X}_{\mathrm{BCC\ (4d)}}$: 3.82, $\overline{X}_{\mathrm{BCC\ (5d)}}$: 3.93, and $\overline{X}_{\mathrm{FCC\ (4d)}}$: 4.11, showing a good relationship between electronegativity and mean orbital size. The location of the PDF peaks in Figure 16 (e) are similar to those from the cluster analysis in Figure 16 (d), in ascending order being BCC (3d), BCC (4d), BCC (5d), and FCC (4d).

In general, it is observed from the analyses in Figure 15 and Figure 16 taking into account not only the phase, but also the mean primary quantum number of the HEA compositions allows for better discrimination of these clusters within the associated two-dimensional plots as shown above. Furthermore, the values of $\overline{X}$ are observed to co-relate with the mean primary quantum number as may be expected from established relationships between electronegativity and orbital energy [24,25]. Of the three electronegativities explored here the distinction between all four clusters is based on the position of the maxima and found to be most distinct for the $\overline{X}_{\mathrm{Mulliken}} - \Delta H$ relationship.

### 4.2.4 Distribution of Complex Phases

The distribution of complex phases in Figure 15 and Figure 16 are found to generally lie outside the range of cluster values attributed to the presence of the simple FCC and BCC phases. In the plot of $VEC - \Delta H$, the CoCrFeNiCuAl0.5V composition at position ($\Delta H$: -4.46, VEC: 6.38) was located within the first boundary of the FCC (4d) and BCC (5d) cluster.

The $\overline{X}_{\mathrm{Pauling}} - \Delta H$ plot fares worse than the $VEC - \Delta H$ plot, showing $CoCrFeNiCuAl_{0.5}V$ ($\Delta H$: -11.53, $\overline{X}_{\mathrm{Pauling}}$: 1.79), and AlCoCrFeMo0.5Ni ($\Delta H$: -11.21, $\overline{X}_{\mathrm{Pauling}}$: 1.75) located within the first boundary of the BCC (4d) cluster, with the CoCrFeNiCuAl0.5V composition at position ($\Delta H$: -4.46, VEC: 1.79) also located within the first boundary of the FCC (4d) and BCC (5d) cluster. Whereas in the $\overline{X}_{\mathrm{Allen}} - \Delta H$ plot, only the AlCoCrFeMo0.5Ni composition ($\Delta H$: -

11.21, $\overline{\mathrm{X}}_{\mathrm{Allen}}$: 1.73) is found to be located within the first boundary, showing better discrimination between simple and complex phases within the cluster analysis.

For the $\overline{\mathrm{X}}_{\mathrm{Mulliken}} - \Delta\mathrm{H}$ plot, the complex phases are located outside the first boundary of the identified clusters, showing good separation between the simple and complex phases. No boundaries or separate clusters were able to be identified for the complex phases without significant overlap between the existing FCC (4d), BCC (3d), BCC (4d), and BCC (5d) clusters. The position of the complex phases were found in general to be dispersed throughout the 2-D plot in the analysis of Dominguez *et al.* [11], similar to those found in the analysis here. Pettifor's analysis of the Miedema enthalpy of mixing model shows that the ratio of $\Delta\mathrm{H}/(\Delta\mathrm{VEC})^2$ begins deviating from theoretical predictions between $4 < \mathrm{VEC} < 7$, which is regarded as a zone of complex phase presence in HEAs [15,26]. The non-conformation of the complex phase containing compositions may result from the increased bonding directionality exhibited by these phases [27,28], which may lead to a change in the electron density and charge transfer behaviour, hence leading to different overall scaling in the 2-D plots shown above.

### 4.2.5 Summary

The analysis performed in Sections 4.2.1 and 4.2.2 show that utilising the average electronegativity value of a HEA composition allows for discrimination between the simple HEA phases, with the best separation shown for $X_{Mulliken}$. However, complex phases are found to be interspaced between the zones of simple phase formation possessing no common trend. This is attributed to the change in charge redistribution between simple and complex phases [23,28,29], which is hypothesised to result from interactions in the electronic structure that may be analysed as a function of the electronic density. The next section will therefore aim to look at the changes in electron density as a function of simple and complex structure containing HEA compositions.

## 4.3 Electron Density Analysis of High-entropy Alloys Simple and Complex Phases

Principal component analysis of the atomic and thermodynamic parameters has largely differentiated simple and complex phases in a 2-dimensional plot of the valence electron concentration against the enthalpy of mixing [11]. As a) the valence electron parameter may be considered a quantum-mechanical parameter used as an indicator of the electronic

structure to predict phase stability [30–32] and b) the electronic structure of complex phases is not simple: e.g. some B2 phases are shown to possess increased directional bonding [15], and the Sigma phase shares some local structure properties with icosahedral glass [33], the study of the electronic structure of HEAs should therefore shed light on the competition between simple and complex phases. Furthermore, analysis of HEA simple/complex phase presence utilising various electronegativity scales performed in Section 4.2 shows good discrimination between the FCC and BCC simple phases, which may be further separated according to their principal quantum number. The absence of trend of the complex phases was hypothesised to be attributed to increased charge redistribution between their alloying components, leading to a change in the electron density at the Wigner-Seitz radius.

Motivated by this possibility and the lack of available knowledge on the electronic structures of HEAs, the electron density of some HEA compositions produced experimentally, and from literature is probed utilising the Runge-Kutta (RK) numerical solution of the Thomas-Fermi-Dirac (TFD) equation first presented by Ren et al. [9]. While the choice of numerical model may not provide full information on the electronic structure of these compositions, it meets the criteria of this work – that is to use a minimally complicated model to relate aspects of the electronic structure with experimentally determined phases present. Here, the results of the RK TFD solution are used not as a tool for phase prediction or justification, but instead as a numerical laboratory for additional insight.

### 4.3.1 Calculations: 4th order Runge-Kutta solution of the Thomas-Fermi-Dirac equation.

The TFD model is an expansion on Thomas' [34] and Fermi's [35] original work to account for the effect of electron exchange interactions to solve the many-electron problem. According to the TFD Model, the electron density at absolute zero is given by:

$$n(x) = \frac{Z}{4\pi\mu^3}\left[\varepsilon + \left(\frac{\varphi(x)}{x}\right)^{1/2}\right]^3 \quad (1)$$

where $\mu = a_0\left(\frac{9\pi^2}{128Z}\right)^{1/3}$, $\varphi(x)$ is the TFD function, $n(x)$ represents the electron density, $a_0$ is the Bohr radius, Z is the atomic number, $x$ is the normalised radius with $r = \mu\, x$, and $\varepsilon = \left(\frac{3}{32\pi^2}\right)^{1/3} Z^{-2/3}$ represents the electron exchange interaction term introduced by Dirac.

Following Ren *et al.* [9], the second-order differential expression of the TFD equation in Eq. (2) with associated boundary conditions in Eq. (3) & Eq. (4) for a non-isolated neutral atom.

$$\frac{d^2\varphi}{dx^2} = x\left[\left(\frac{\varphi(x)}{x}\right)^{1/2} + \varepsilon\right]^3 \quad (2)$$

$$\varphi(0) = 1 \quad (3)$$

$$\left(\frac{d\varphi}{dx}\right)_{x=x_0} = \frac{\varphi(x_0)}{x_0} \quad (4)$$

A semi-convergent expansion of Eq. 2 may then be written as:

$$\varphi(x) = 1 + a_n(x)^{n/2} + \ldots, \text{ up to n = 13} \quad (5)$$

where $a_n$ represents the coefficients of the expansion which may be obtained by inserting Eq. (5) into Eq. (2) and comparing coefficients of similar power exponents from both sides of the equation, with the exception of the coefficient $a_2$ which is defined as the initial slope of the TFD equation, where $a_2 = \varphi'(0)$. $a_2$ coefficients lie between -1.7 and -1.5 [36], and the numerical solution of the TFD equation in Eq. (2) is then obtained by determining the minimised electron density, *n(e*) for $a_2$ coefficients in this range, by solving Eq. (5) and its derivative utilising the fourth order RK method for a given atomic number, *Z*. $n(r_{ws})$ may then be selected from the determined TFD solution of each $a_2$ value through knowledge of the composition's the Wigner-Seitz radius, $r_{ws}$. For a known crystal structure, the $r_{ws}$ may be approximated from the mean volume, *V* per atom, *N* of the unit cell where each atom is considered to be spherical, hence leading to:

$$r_{ws} = \frac{3V}{4N\pi}^{1/3} \quad (6)$$

Selected HEA compositions with principal alloying components $Co_1Cr_1Fe_1Ni_1A_x$ with A = Pd, Ti, Al, and V (here denoted CCFN-$A_x$) from the literature have been selected and added with newer compositions. The samples made here are processed by arc-melting elements of at least 99.9% purity in a water-cooled copper hearth in a backfilled Ar atmosphere. 3 mm rods were cast via suction casting into a water-cooled copper hearth under similar conditions and the main phases present in the as-cast condition with their associated lattice parameters were determined through x-ray diffraction as described in the Methods section. Experimentally determined XRD patterns are presented in Figure 17 from which it is shown that the simple FCC phase is stable for the four-component CoCrFeNi system.

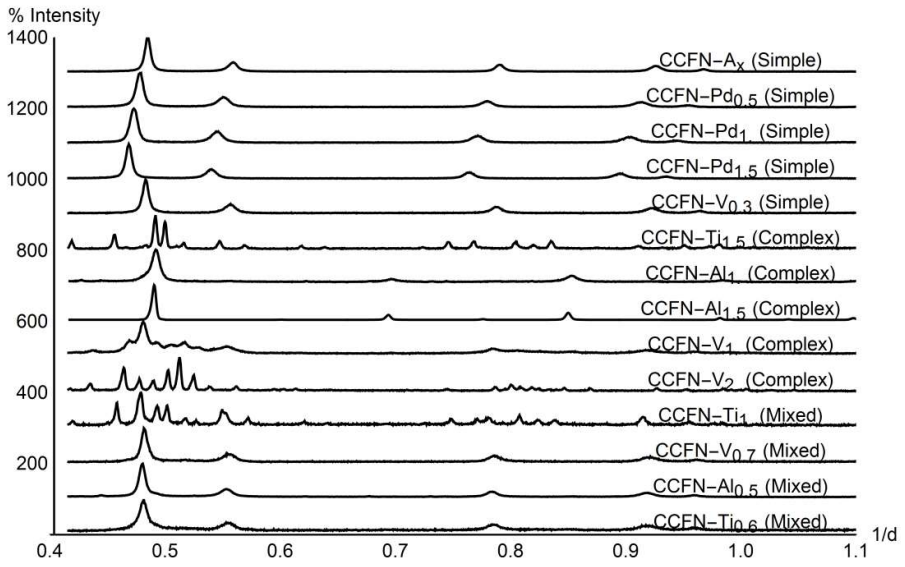


**Figure 17.** XRD patterns of $Co_1Cr_1Fe_1Ni_1A_x$ (denoted CCFN-$A_x$) where A = Al, Ti, V, Mn, and Pd with associated phase classifications as shown in Table 3.

Further addition of a fifth element to equimolar CCFN is observed to destabilise the FCC structure as the average atomic number, $Z_{avg}$ decreases; this is the case for CCFN-Ti, CCFN-Al, and CCFN-V. Conversely, an increase in $Z_{avg,}$ as in CCFN-Pd is observed to maintain the presence of the FCC phase. The results obtained here are consistent with the predictions and observations from the literature, where complex phases are observed to be present at intermediate valence electron values [37–40]. Lattice parameters and volume fractions for the observed majority phases are obtained via Rietveld refinement (*cf.* Appendix) and are used to estimate averaged $r_{ws}$ values from Eq. (6) by weighting according to the observed volume fractions, and are listed in Table 3; $r_{ws}$ values obtained thus are considered to be averaged values representing the electronic structure of the alloy composition. CCFN is calculated to have an $r_{ws}$ value of 1.387 Å, and further addition of a fifth element to the composition increases $r_{ws}$, with CCFN-$Pd_{1.0}$ at 1.430 Å; CCFN-$Ti_{1.0}$ at 1.422 Å; CCFN-$Al_{1.0}$ at 1.418 Å; and CCFN-$V_{1.0}$ at 1.411 Å. Values for other stochiometries may be found in Table 3. This increase is consistent, but not necessarily indicative of the severe lattice distortion effect alluded to by Tsai and Yeh [41] that should scale with the number of HEA components. The large increase in $r_{ws}$ for CCFN-Pd is thought to be caused by the larger size difference of Pd in comparison to the base four-component alloy.

The aforementioned numerical solution was programed utilising Mathematica 10.0 [8], following the steps outlined previously.

To confirm the accuracy of the model, $n(r_{ws})$ for elemental Cu and Fe were calculated by substituting $r_{ws}$ values obtained from atomic radii data. These values of $r_{ws}$ correspond to 1.413Å for Cu and 1.411Å for Fe respectively. Corresponding values of $n(r_{ws})$ are listed in parentheses for Cu ($2.926\times10^{29}m^{-3}$) and for Fe ($2.867\times10^{29}m^{-3}$) respectively. These values are in relatively good agreement with the previously calculated results [a18, a19] of Ren *et al.* [9] for Cu ($2.931\times10^{29}m^{-3}$) and Fe ($2.739\times10^{29}m^{-3}$), and are also within reasonable range of Ghosh *et al.'s* density functional approach, with Cu ($2.82\times10^{29}m^{-3}$) and Fe ($2.79\times10^{29}m^{-3}$) [a20].

**Table 8.** Tabulated HEA compositions selected for this study with references where applicable, phases present (FCC/BCC/C14/Sigma/Mixed), calculated Wigner-Seitz radius ($r_{ws}$), and electron density (*n(e)*).

*The lattice parameters from which $r_{ws}$ is approximated from for these compositions are taken from literature.

**The electron densities of these elements have been used to verify the accuracy of our calculations.

| Composition | Phase & classification | Ref. | $r_{ws}$ (Å) | *n(e)* ($\times 10^{29}$ $m^{-3}$) |
|---|---|---|---|---|
| CCFN | FCC (Simple) | This work | 1.387 | 3.43464 |
| CCFN-$Pd_{0.5}$ | FCC (Simple) | This work | 1.415 | 3.131 |
| CCFN-$Pd_{1.0}$ | FCC (Simple) | This work | 1.430 | 3.22017 |
| CCFN-$Pd_{1.5}$ | FCC (Simple) | This work | 1.450 | 2.97 |
| MnFeNiCo* | FCC (Simple) | [11] | 1.591 | 1.79266 |
| $CuCrFeNi_2Mn_2$* | FCC (Simple) | [43] | 1.420 | 3.03986 |
| $CuCr_2Fe_2Ni_2Mn_2$* | FCC (Simple) | [43] | 1.420 | 3.00415 |
| $Cu_2CrFe_2Ni_2Mn$* | FCC (Simple) | [43] | 1.420 | 3.21073 |
| CCFN-$V_{0.3}$ | FCC (Simple) | This work | 1.399 | 3.3334 |
| MnNbVTi* | BCC (Simple) | [11] | 1.546 | 2.1672 |
| MoFeCrTiW* | BCC (Simple) | [44] | 1.540 | 2.27894 |
| $AlCoCrFeNiTi_{0.5}$* | BCC (Simple) | [45] | 1.428 | 3.02415 |
| $AlCoCrFeNiTi_{1.0}$* | BCC (Simple) | [45] | 1.418 | 3.28204 |
| CCFN-$Ti_{1.5}$ | C14 (Complex) | This work | 1.518 | 2.11844 |
| MnFeNiTi* | C14 (Complex) | [11] | 1.430 | 2.7202 |
| CoCrFeNiCuTi* | C14 (Complex) | [46] | 1.516 | 2.16777 |
| $AlCoCrFeNiTi_{1.5}$* | C14 (Complex) | [45] | 1.516 | 2.17118 |
| CCFN-$Al_{1.0}$ | B2 (Complex) | This work | 1.418 | 2.90383 |
| CCFN-$Al_{1.5}$ | B2 (Complex) | This work | 1.427 | 2.82094 |
| CCFN-$V_{1.0}$ | Sigma (Complex) | This work | 1.411 | 2.84697 |
| CCFN-$V_{2.0}$ | Sigma (Complex) | This work | 1.422 | 2.78239 |
| $Al_{0.5}CoCrCuFeNiTi$* | Sigma (Complex) | [47] | 1.420 | 2.76524 |
| CCFN-$Ti_1$ | FCC/C14 (Mixed) | This work | 1.422 | 2.86675 |
| CCFN-$V_{0.7}$ | FCC/Sigma (Mixed) | This work | 1.403 | 2.94575 |
| CCFN-$Al_{0.5}$ | FCC/B2 (Mixed) | This work | 1.407 | 2.79962 |
| CoCrFeNiAlCu* | FCC/BCC (Mixed) | [48] | 1.430 | 2.88853 |
| CCFN-$Ti_{0.5}$ | FCC/C14 (Mixed) | This work | 1.411 | 2.95598 |
| $Ta_{34}Nb_{33}Hf_8Zr_{14}Ti_{11}$* | BCC (Simple 5d) | [49] | 1.654 | 1.94304 |
| NbMoTaW* | BCC (Simple 5d) | [50] | 1.586 | 2.47968 |
| TaNbHfZr* | BCC (Simple 5d) | [51] | 1.689 | 1.56364 |
| VNbMoTaW* | BCC (Simple 5d) | [52] | 1.569 | 2.57589 |

Utilising the results of the RK solution of the TFD equation, the electron density is obtained through Eq. (1). These values are listed in Table 8 and are shown graphically in Figure 18

with the primary phase observed experimentally. A full table containing values of the $a_2$ coefficient may be found in the appendix. It is observed that there appears to be a demarcation between HEA simple and complex phases, with the lines in Figure 18 acting as a guide to the eye. Simple phases are further observed to be separated depending on the mean primary quantum number of the constituent alloying components (differentiated as *4d*, and *5d* in Figure 18), as the electron density scales with $r_{ws}$ for HEAs with alloying components that are mainly from the same row of the periodic table, or have similar average primary quantum numbers due the increasing number of non-valence electrons (*c.f.* Table I). Current empirical approaches do not account for the influence of the average primary quantum number of the considered alloy though the effect may be mirrored in new ways of depicting data.

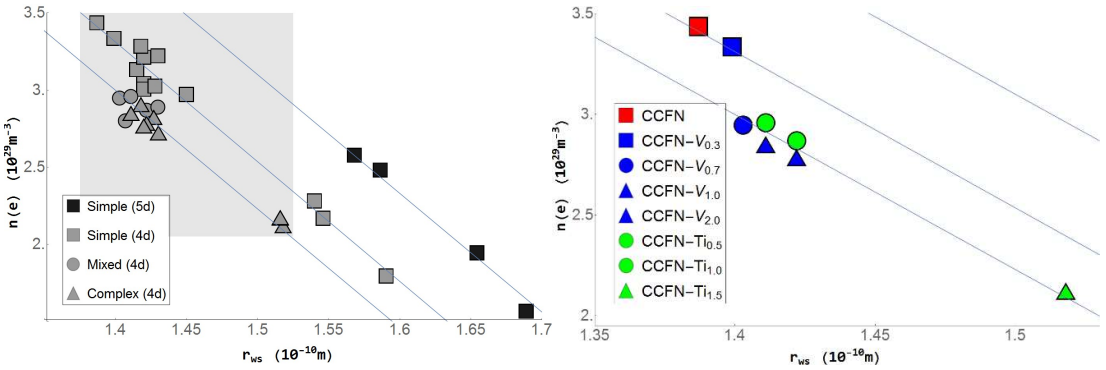


**Figure 18. (Left)** 2-dimensional plot of electron density against the Wigner-Seitz radius showing the separation of complex and simple phases; **(Right)** HEA compositions from the shaded zone in (Left) from the CCFN-$A_x$ family (A = V and Ti) are displayed. The square markers represent the simple phase, the circular markers represent a mixed phase (simple + complex), while the triangular markers represent a complex structure. It is observed that the electron density lowers immediately upon the precipitation of even minor amounts of a secondary complex structure, as characterised via XRD.

The demarcation between simple and complex phases is characterised by a downwards shift so that the electron density is lowered for any equivalent $r_{ws}$ value. This is illustrated in the inset of Figure 18 for both CCFN-V and CCFN-Ti HEA compositions where the occurrence of the complex phase is shown to correspond to a rapid lowering of the electron density, for both mixed and complex phase compositions, indicating the influence of the alloying addition in destabilising the electronic structure of the simple phase. The three areas shown

in Figure 18 each show a linear-like relationship with $r_{ws.}$ It must be emphasised that the regions observed are of dissimilar compositional content despite originating from the same row of the periodic table and thus the linear relationship may be considered to be content-independent; showing the electronic structure of complex phases to be distinguishable from simple phases within this two-dimensional plot.

Returning to Figure 18, the simple phase appears to be stabilised through alloying additions that are able to maintain a near-delocalised bandstructure near the Fermi energy. The complex phases are likely stabilised once the addition of alloying elements with covalent-like character are able to sufficiently distort the bandstructure [28]; thus leading to an immediate corresponding change in the electron density. Physically, an increase in interatomic spacing may allow for increased occupancy at interstitial sites as required, thus creating conditions for the formation of an energetically stable structure that may better reflect the state of the bandstructure. In this case, stability of HEA simple phases may possibly be achieved by maintaining the delocalisation of its electrons near its Fermi energy either through selection of non-directional alloying elements, or compensating for alloying elements that exhibit covalent-like character.

### 4.3.2 Summary

In conclusion, the electron densities of five-component HEA compositions based on the equimolar four-component CCFN composition have been analysed together with other HEA compositions from literature. This analysis shows the effective successful structural separation between simple and complex phases within a single two-dimensional map comparable to semi-empirical methods. Current results suggest that the influence of the average primary quantum number when utilising enthalpy of mixing values should be further examined to possibly distinguish 4d, 5d, and etc. compositions in predictions for HEA alloy design. Precipitation of complex phases is also observed to be linked to a change in electronic structure behaviour which varies from that of the simple phases. This could be useful for phase predictions when combined with an appropriate method for extrapolating the Wigner-Seitz radius for multi-principal component alloys. In closing, an in-depth study of the electronic structure would be instructive in facilitating the development of an efficient

alloy design strategy that accounts in toto all main contributions to the electronic structure for avoiding 'hot zones' of complex phase formation, as required.

## 4.4 Conclusions

The analysis in Sections 4.2 of this chapter have shown that the simple phase differentiation in a 2-D plot may more accurately reflect the electronic structure when values of VEC are replaced with those of the averaged electronegativity, $\overline{\mathrm{X}}_{\mathrm{Mulliken}}$. The distinction between the FCC and BCC simple phases, and the simple and complex phases are attributed to changes in the shielding of larger sized atoms for the former, and changes in bond directionality reflected in the electronic density at the Wigner-Seitz radius for the latter.

The analysis in Section 4.3 finds that a 2-D plot of Wigner-Seitz radius determined from experimental and literature-based lattice constants against the electronic density calculated from the Thomas-Fermi-Dirac shows a destabilisation of the electron density to lower values at any equivalent Wigner-Seitz radius as the complex phase is stabilised, satisfying the hypothesis presented in Section 4.2.

Both results show the dependence of both simple and complex structures on the electronic structure of the material that so far, cannot be fully represented on any 2-D plots studied here. Further investigation of the phase stability based on the electronic structure is necessary to shed further light on HEA structural stability.

## 4.5 References


[1] L.C. Allen, Electronegativity is the average one-electron energy of the valence-shell electrons in ground-state free atoms, J. Am. Chem. Soc. 111 (1989) 9003–9014. doi:10.1021/ja00207a003.

[2] L.A. Dominguez, R. Goodall, I. Todd, Prediction and validation of quaternary high entropy alloys using statistical approaches, Mater. Sci. Technol. 31 (2015) 1201–1206.

[3] U. Mizutani, Hume-Rothery rules for structurally complex alloy phases, CRC Press, Boca Raton, 2011.

[4] R.G. Parr, R.A. Donnelly, M. Levy, W.E. Palke, Electronegativity: The density functional viewpoint, J. Chem. Phys. 68 (1978) 3801. doi:10.1063/1.436185.

[5] L. Pauling, THE NATURE OF THE CHEMICAL BOND. IV. THE ENERGY OF SINGLE BONDS AND THE RELATIVE ELECTRONEGATIVITY OF ATOMS, J. Am. Chem. Soc. 54 (1932) 3570–3582. doi:10.1021/ja01348a011.

[6] A.R. Miedema, The electronegativity parameter for transition metals: Heat of formation and charge transfer in alloys, J. Common Met. 32 (1973) 117–136. doi:10.1016/0022-5088(73)90078-7.

[7] C.-C. Juan, C.-Y. Hsu, C.-W. Tsai, W.-R. Wang, T.-S. Sheu, J.-W. Yeh, S.-K. Chen, On microstructure and mechanical performance of AlCoCrFeMo0.5Nix high-entropy alloys, Intermetallics. 32 (2013) 401–407. doi:10.1016/j.intermet.2012.09.008.

[8] J.W. Yeh, S.K. Chen, S.J. Lin, J.Y. Gan, T.S. Chin, T.T. Shun, C.H. Tsau, S.Y. Chang, Nanostructured high-entropy alloys with multiple principal elements: Novel alloy design concepts and outcomes, Adv. Eng. Mater. 6 (2004) 299–303.

[9] M.-R. Chen, S.-J. Lin, J.-W. Yeh, M.-H. Chuang, S.-K. Chen, Y.-S. Huang, Effect of vanadium addition on the microstructure, hardness, and wear resistance of Al0.5CoCrCuFeNi high-entropy alloy, Metall. Mater. Trans. A. 37 (2006) 1363–1369. doi:10.1007/s11661-006-0081-3.

[10] W. Research, Mathematica 10.4, 10.4, Champaign, Illinios, 2016.

[11] B.W. Silverman, Density estimation for statistics and data analysis, Chapman & Hall/CRC, Boca Raton, 1998.

[12] H. Bakker, A. Miedema, Enthalpies in alloys: Miedemaṡ semi-empirical model, Trans Tech Publications, Uetikon-Zuerich, Switzerland ; Enfield, N.H, 1998.

[13] F.R. de Boer, ed., Cohesion in metals: transition metal alloys, 2., print, North Holland, Amsterdam, 1988.

[14] R.F. Berger, P.L. Walters, S. Lee, R. Hoffmann, Connecting the Chemical and Physical Viewpoints of What Determines Structure: From 1-D Chains to γ-Brasses, Chem. Rev. 111 (2011) 4522–4545. doi:10.1021/cr1001222.

[15] S. Guo, N. C, L. J, L.C. T, Effect of valence electron concentration on stability of fcc or bcc phase in high entropy alloys, J. Appl. Phys. 109 (2011) 10.

[16] T. Rajasekharan, V. Seshubai, Charge transfer on the metallic atom-pair bond, and the crystal structures adopted by intermetallic compounds, Acta Crystallogr. A. 68 (2012) 156–165. doi:10.1107/S0108767311044151.

[17] C.-G. Zhan, J.A. Nichols, D.A. Dixon, Ionization Potential, Electron Affinity, Electronegativity, Hardness, and Electron Excitation Energy: Molecular Properties from Density Functional Theory Orbital Energies, J. Phys. Chem. A. 107 (2003) 4184–4195. doi:10.1021/jp0225774.
[18] R.G. Pearson, Absolute electronegativity and hardness correlated with molecular orbital theory, Proc. Natl. Acad. Sci. 83 (1986) 8440–8441. doi:10.1073/pnas.83.22.8440.
[19] D.G. Pettifor, A Quantum Mechanical Critique of the Miedema Rules for Alloy Formation, Solid State Phys. 40 (1987) 43–92.
[20] A. Savin, R. Nesper, S. Wengert, T.F. Fässler, ELF: The Electron Localization Function, Angew. Chem. Int. Ed. Engl. 36 (1997) 1808–1832. doi:10.1002/anie.199718081.
[21] M.E. Eberhart, The metallic bond: Elastic properties, Acta Mater. 44 (1996) 2495–2504. doi:10.1016/1359-6454(95)00347-9.
[22] B. Silvi, C. Gatti, Direct Space Representation of the Metallic Bond, J. Phys. Chem. A. 104 (2000) 947–953. doi:10.1021/jp992784c.
[23] A. Paxton, M. Methfessel, D.G. Pettifor, A bandstructure view of the Hume-Rothery electron phases, Proc. R. Soc. A. 453 (1997) 1493.
[24] D. Nguyen-Manh, A. Paxton, D.G. Pettifor, A. Pasturel, On the phase stability of transition metal trialuminide compounds, Intermetallics. 3 (1995) 9–14.
[25] D.G. Pettifor, The structures of binary compounds. I. Phenomenological structure maps, J. Phys. C Solid State Phys. 19 (1986) 285–313. doi:10.1088/0022-3719/19/3/002.
[26] S.I. Simdyankin, S.N. Taraskin, M. Dzugutov, S.R. Elliott, Vibrational properties of the one-component σ phase, Phys. Rev. B. 62 (2000) 3223–3231. doi:10.1103/PhysRevB.62.3223.
[27] F. Ren, K. Cao, J. Ren, A.A. Volinsky, T.H. Tran, B. Tian, Numerical Calculation of the Electron Density at the Wigner–Seitz Radius Based on the Thomas–Fermi–Dirac Equation, J. Comput. Theor. Nanosci. 11 (2014) 344–347. doi:10.1166/jctn.2014.3358.
[28] L.H. Thomas, The calculation of atomic fields, Math. Proc. Camb. Philos. Soc. 23 (1927) 542. doi:10.1017/S0305004100011683.
[29] E. Fermi, Un metodo statistico per la determinazione di alcune priorieta dell'atome, Rend Accad Naz Lincei. 6 (1927) 32.
[30] N. Metropolis, J.R. Reitz, Solutions of the Fermi-Thomas-Dirac Equation, J. Chem. Phys. 19 (1951) 555. doi:10.1063/1.1748292.
[31] G.A. Salishchev, M.A. Tikhonovsky, D.G. Shaysultanov, N.D. Stepanov, A.V. Kuznetsov, I.V. Kolodiy, A.S. Tortika, O.N. Senkov, Effect of Mn and V on structure and mechanical properties of high-entropy alloys based on CoCrFeNi system, J. Alloys Compd. 591 (2014) 11–21. doi:10.1016/j.jallcom.2013.12.210.
[32] N.D. Stepanov, D.G. Shaysultanov, G.A. Salishchev, M.A. Tikhonovsky, E.E. Oleynik, A.S. Tortika, O.N. Senkov, Effect of V content on microstructure and mechanical properties of the CoCrFeMnNiVx high entropy alloys, J. Alloys Compd. 628 (2015) 170–185. doi:10.1016/j.jallcom.2014.12.157.

[33] H.P. Chou, Y.S. Chang, S.K. Chen, J.W. Yeh, Microstructure, thermophysical and electrical properties in Al x CoCrFeNi (0 ≤ x ≤2) high-entropy alloys, Mater. Sci. Eng. B. 163 (2009) 184–189.
[34] T.T. Shun, L.Y. Chang, M.H. Shiu, Microstructures and mechanical properties of multiprincipal component CoCrFeNiTix alloys, Mater. Sci. Eng. A. 556 (2012) 170–174.
[35] M.-H. Tsai, J.-W. Yeh, High-Entropy Alloys: A Critical Review, Mater. Res. Lett. 2 (2014) 107–123. doi:10.1080/21663831.2014.912690.
[36] P. Politzer, R.G. Parr, D.R. Murphy, Approximate determination of Wigner-Seitz radii from free-atom wave functions, Phys. Rev. B. 31 (1985) 6809–6810. doi:10.1103/PhysRevB.31.6809.
[37] B. Ren, Z.X. Liu, B. Cai, M.X. Wang, L. Shi, Aging behavior of a CuCr2Fe2NiMn high-entropy alloy, Mater. Des. 33 (2012) 121–126. doi:10.1016/j.matdes.2011.07.005.
[38] B. Zheng, Q.B. Liu, L.Y. Zhang, Microstructure and Properties of MoFeCrTiW High-Entropy Alloy Coating Prepared by Laser Cladding, Adv. Mater. Res. 820 (2013) 63–66. doi:10.4028/www.scientific.net/AMR.820.63.
[39] Y.J. Zhou, Y. Zhang, Y.L. Wang, G.L. Chen, Solid solution alloys of AlCoCrFeNiTi x with excellent room-temperature mechanical properties, Appl. Phys. Lett. 90 (2007) 181904. doi:10.1063/1.2734517.
[40] X.F. Wang, Y. Zhang, Y. Qiao, G.L. Chen, Novel microstructure and properties of multicomponent CoCrCuFeNiTix alloys, Intermetallics. 15 (2007) 357–362. doi:10.1016/j.intermet.2006.08.005.
[41] M.-R. Chen, S.-J. Lin, J.-W. Yeh, S.-K. Chen, Y.-S. Huang, C.-P. Tu, Microstructure and Properties of Al0.5CoCrCuFeNiTix (x=0–2.0) High-Entropy Alloys, Mater. Trans. 47 (2006) 1395–1401. doi:10.2320/matertrans.47.1395.
[42] L. Xie, P. Brault, A.-L. Thomann, J.-M. Bauchire, AlCoCrCuFeNi high entropy alloy cluster growth and annealing on silicon: A classical molecular dynamics simulation study, Appl. Surf. Sci. 285 (2013) 810–816. doi:10.1016/j.apsusc.2013.08.133.
[43] P. Koželj, S. Vrtnik, A. Jelen, S. Jazbec, Z. Jagličić, S. Maiti, M. Feuerbacher, W. Steurer, J. Dolinšek, Discovery of a Superconducting High-Entropy Alloy, Phys. Rev. Lett. 113 (2014). doi:10.1103/PhysRevLett.113.107001.
[44] Y. Zou, S. Maiti, W. Steurer, R. Spolenak, Size-dependent plasticity in an Nb25Mo25Ta25W25 refractory high-entropy alloy, Acta Mater. 65 (2014) 85–97. doi:10.1016/j.actamat.2013.11.049.
[45] S. Maiti, W. Steurer, Structural-disorder and its effect on mechanical properties in single-phase TaNbHfZr high-entropy alloy, Acta Mater. 106 (2016) 87–97. doi:10.1016/j.actamat.2016.01.018.
[46] O.N. Senkov, G.B. Wilks, J.M. Scott, D.B. Miracle, Mechanical properties of Nb25Mo25Ta25W25 and V20Nb20Mo20Ta20W20 refractory high entropy alloys, Intermetallics. 19 (2011) 698–706. doi:10.1016/j.intermet.2011.01.004.

[a1] J.M. Zhu, H.F. Zhang, H.M. Fu, A.M. Wang, H. Li, Z.Q. Hu, Microstructures and compressive properties of multicomponent AlCoCrCuFeNiMox alloys, J. Alloys Compd. 497 (2010) 52–56. doi:10.1016/j.jallcom.2010.03.074.
[a2] S.G. Ma, Y. Zhang, Effect of Nb addition on the microstructure and properties of AlCoCrFeNi high-entropy alloy, Mater. Sci. Eng. A. 532 (2012) 480–486. doi:10.1016/j.msea.2011.10.110.
[a3] H.P. Chou, Y.S. Chang, S.K. Chen, J.W. Yeh, Microstructure, thermophysical and electrical properties in Al x CoCrFeNi (0 ≤ x ≤2) high-entropy alloys, Mater. Sci. Eng. B. 163 (2009) 184–189.
[a4] X. Yang, Y. Zhang, P.K. Liaw, Microstructure and Compressive Properties of NbTiVTaAlx High Entropy Alloys, Procedia Eng. 36 (2012) 292–298. doi:10.1016/j.proeng.2012.03.043.
[a5] H. Yao, J.-W. Qiao, M. Gao, J. Hawk, S.-G. Ma, H. Zhou, MoNbTaV Medium-Entropy Alloy, Entropy. 18 (2016) 189. doi:10.3390/e18050189.
[a6] O.N. Senkov, G.B. Wilks, J.M. Scott, D.B. Miracle, Mechanical properties of Nb25Mo25Ta25W25 and V20Nb20Mo20Ta20W20 refractory high entropy alloys, Intermetallics. 19 (2011) 698–706. doi:10.1016/j.intermet.2011.01.004.
[a7] T. Nagase, S. Anada, P.D. Rack, J.H. Noh, H. Yasuda, H. Mori, T. Egami, Electron-irradiation-induced structural change in Zr–Hf–Nb alloy, Intermetallics. 26 (2012) 122–130. doi:10.1016/j.intermet.2012.02.015.
[a8] J.W. Yeh, S.K. Chen, S.J. Lin, J.Y. Gan, T.S. Chin, T.T. Shun, C.H. Tsau, S.Y. Chang, Nanostructured high-entropy alloys with multiple principal elements: Novel alloy design concepts and outcomes, Adv. Eng. Mater. 6 (2004) 299–303.
[a9] Z. Leong, J.S. Wróbel, S.L. Dudarev, R. Goodall, I. Todd, D. Nguyen-Manh, The Effect of Electronic Structure on the Phases Present in High Entropy Alloys, Sci. Rep. 7 (2017) 39803. doi:10.1038/srep39803.
[a10] U. Dahlborg, J. Cornide, M. Calvo-Dahlborg, T.C. Hansen, A. Fitch, Z. Leong, S. Chambreland, R. Goodall, Structure of some CoCrFeNi and CoCrFeNiPd multicomponent HEA alloys by diffraction techniques, J. Alloys Compd. 681 (2016) 330–341. doi:10.1016/j.jallcom.2016.04.248.
[a11] M.S. Lucas, L. Mauger, J. Munoz, Y. Xiao, A.O. Sheets, S.L. Sematin, Magnetic and vibrational properties of high-entropy alloys, J. Appl. Phys. 109 (2011) 7
[a12] B. Cantor, I.T.H. Chang, P. Knight, A.J.B. Vincent, Microstructural development in equiatomic multicomponent alloys, Materials Science and Engineering A, Phys. Rev. B Condens. Matter. 375–377 (2004) 213–218.
[a13] B. Ren, Z.X. Liu, B. Cai, M.X. Wang, L. Shi, Aging behavior of a CuCr2Fe2NiMn high-entropy alloy, Mater. Des. 33 (2012) 121–126. doi:10.1016/j.matdes.2011.07.005.
[a14] B. Ren, Z.X. Liu, D.M. Li, L. Shi, B. Cai, M.X. Wang, Effect of elemental interaction on microstructure of CuCrFeNiMn high entropy alloy system, J. Alloys Compd. 493 (2010) 148–153. doi:10.1016/j.jallcom.2009.12.183.
[a15] C.-C. Juan, C.-Y. Hsu, C.-W. Tsai, W.-R. Wang, T.-S. Sheu, J.-W. Yeh, S.-K. Chen, On microstructure and mechanical performance of AlCoCrFeMo0.5Nix high-entropy alloys, Intermetallics. 32 (2013) 401–407. doi:10.1016/j.intermet.2012.09.008.
[a16] M.-R. Chen, S.-J. Lin, J.-W. Yeh, M.-H. Chuang, S.-K. Chen, Y.-S. Huang, Effect of vanadium addition on the microstructure, hardness, and wear resistance of Al0.5CoCrCuFeNi high-entropy alloy, Metall. Mater. Trans. A. 37 (2006) 1363–1369. doi:10.1007/s11661-006-0081-3.

[a17] L.A. Dominguez, R. Goodall, I. Todd, Prediction and validation of quaternary high entropy alloys using statistical approaches, Mater. Sci. Technol. 31 (2015) 1201–1206.
[a18] P. Politzer, R.G. Parr, D.R. Murphy, Approximate determination of Wigner-Seitz radii from free-atom wave functions, Phys. Rev. B. 31 (1985) 6809–6810. doi:10.1103/PhysRevB.31.6809.
[a19] C. Ke, Calculation of the Electron Density on the Surface of Atoms and Research of Internal Stress in Films Based on Cheng's Theory, Henan University of Science and Technology, 2011.
[a20] A.K. Ghosh, S. Chakraborty, A. Manna, Density Functional Approach for Metals. The Matheiss Prescription, Phys. Status Solidi B. 118 (1983) 373–379. doi:10.1002/pssb.2221180143.

# 5. The Effect of Electronic Structure on the Phases Present in HEAs

| | |
|---|---|
| Objective | To understand the underlying relationship between the electronic structure and phase presence in High-entropy Alloys. |
| Hypothesis | The Mulliken electronegativity scale of the first valence electron will enable discrimination between simple and complex phases due to the difference in metallic bonding between simple and complex phases. This difference can also be evidenced from the electron density. |
| Analysis Type | Analytical (80%), Experimental (20%) |
| Variables | Alloy Composition |
| Primary Result | Electronegativity, Electron density |
| Techniques | Arc-Melting & Casting, XRD, Numerical Analysis |

## Table of Contents

## Symbols and Abbreviations

| | |
|---|---|
| $\Delta E^{(1-2)}$ | Energy difference between structures 1 and 2 |
| BCC | Body-centred cubic |
| $D^{\uparrow}(\varepsilon)$ | Spin-polarised total DOS per atom for electrons for spin-up |
| $D^{\downarrow}(\varepsilon)$ | Spin-polarised total DOS per atom for electrons for spin-down |
| DFT | Density function theory |
| DOS | Density of states |
| $\varepsilon_F$ | Fermi energy |
| FCC | Face-centred cubic |
| HEA | High-entropy alloy |
| $I_{eff}$ | Effective Stoner parameter |
| $m_{av}$ | Average magnetic moment |
| *n* | Valence electron concentration, quantum-mechanics based |
| RBA | Rigid-band approximation |
| SQS | Special quasirandom structure |
| VEC | Valence electron concentration, semi-empirical |
| XRD | X-ray Diffraction |

## Table of Figures

## 5.1 Chapter Preface

Continuing from the previous chapter where effects of the electronic structure were found to influence phase stability, Chapter 5 delves deeper into the electronic structure aspect of HEAs and its influence on the structural stability. To access such information, the Density Functional Theory (DFT) formalism [53] can be used, such as in investigating enthalpies [54] and entropies [55] of formation for HEAs within spin-polarised electronic structure calculations. Full electronic structure calculations are not easily performed on a composition to composition basis, as the various structural parameters of the ground state must be first determined, and calculations must be performed for each prospective composition regardless of stoichiometry.

One simplification of the DFT approach is the Rigid Band Approximation (RBA) as described in the Literature Review, originally proposed for non-magnetic metallic alloys, which assumes that the energy difference between two phases is given entirely by the difference in band-structure energy [30,31,56,57]. This allows the investigation of A-B HEAs where A is the base alloy composition and B is the varying alloy addition. This technique allows the competing structures to be analysed across the entire A-$B_x$ range; here magnetic compositions of CoCrFeNi-Ax (here denoted CCFN-$A_x$) where A: Al, Pd, V, and Ti are investigated. The RBA predictions are validated with XRD characterisation, showing good agreement between experimental and theoretical predictions in the phase structures present, and providing increased accuracy in predicting the phase transitions of these compositions over those of the semi-empirical methods. The RBA models are simple enough to readily interpret the available experimental data, while powerful enough to predict correctly the new stable phase in a multicomponent system, while taking into account the electronic structure.

A combined modelling and experimental approach is thus proposed in this chapter, by generalising a RBA model for magnetic systems and taking electronic structure effects into account in prediction of the phase most likely to be found in multicomponent alloys. It is found that the VEC parameter is able to serve as a good predictor of simple-complex transitions when the s, p, and d valence electrons are accounted for. Therefore, the RBA model can be used as a simple but relatively accurate method based on electronic structure calculations for phase stability prediction in HEAs, in particular in the understanding and

design of a new HEA system, CoFeNiV, where the structural transition with varying levels of constituent elements is predicted, as a function of the valence electron concentration, *n* obtained from the integrated spin-polarised density of states.

## 5.2 Rigid Band Approximation of High Entropy Alloys

Adapted from Zhaoyuan Leong, Jan S. Wróbel, Sergei L. Dudarev, Russell Goodall, Iain Todd, Duc Nguyen-Manh, "**The Effect of Electronic Structure on the Phases Present in High-Entropy Alloys**", Nature Scientific Reports, *Awaiting editor decision.*

In order to better understand, and improve on, the phase discrimination found in 2-dimensional plots of the empirical models [11], the simple-complex phase transition of a number of 5-component HEA alloys based on the equiatomic CoCrFeNi (CCFN) composition is investigated through X-Ray Diffraction (XRD) characterisation. The compositions are compared to predictions from the RBA approach, in particular of the transition between phases that occurs with changing stoichiometry. The original RBA approach [31,58,59] is generalised to include the effects of magnetism using the Stoner model [60–62], as this affects the change in energy between two phases (particularly since the constituent metals Co, Cr, Fe, and Ni already exhibit magnetic behaviour; other CoCrFeNi-type alloys have also been reported for their magnetic properties [55,63–65]).

### 5.2.1 Experimental Identification of Phases Adopted by CoCrFeNi-type Compositions

20 HEA compositions based on $CoCrFeNiA_X$, where A = Pd, Al, V, and Ti (henceforth denoted as CCFN-Pdx, CCFN-Alx, CCFN-Vx, and CCFN-Tix) with nominal compositions given in Table 1 were made. The amount of each alloying addition was selected to explore the transition between simple (FCC and BCC) and complex (B2, Sigma and C14) phases. The analysis of CCFN-Ax compositions has been extended beyond those previously reported to identify the accuracy of the RBA predicted phase stability in terms of the relative behaviour of the electronic densities of states. Further compositions from the novel CoFeNiVx system (henceforth denoted CoFN-Vx) were also prepared in order to validate the use of the RBA model for unknown compositions against experimental data. The compositional variations are tabulated in Table 1.

**Table 9.** High Entropy Alloy compositions with their respective nominal compositions, indexed phases and lattice constants, and VEC values.

*These new stoichiometric compositions have been selected to extend the data on the CCFN-A (A = Pd, V, Al, and Ti) compositional families selected for this work.

| Composition | Nominal Composition | Indexed Phase | Lattice Parameter (Å) +/- 0.01 Å | VEC | Reference |
|---|---|---|---|---|---|
| **CCFN** | CoCrFeNi | FCC | $a$ = 3.56 | 8.25 | [7,22,65] |
| **CCFN-Pd$_{0.5}$** | $(CoCrFeNi)_{0.89}Pd_{0.11}$ | FCC | $a$ = 3.62 | 8.44 | [65] |
| **CCFN-Pd$_{1.0}$** | $(CoCrFeNi)_{0.80}Pd_{0.20}$ | FCC | $a$ = 3.66 | 8.60 | [65] |
| **CCFN-Pd$_{1.5}$** | $(CoCrFeNi)_{0.73}Pd_{0.27}$ | FCC | $a$ = 3.71 | 8.73 | This Work* |
| **CCFN-Al$_{0.5}$** | $(CoCrFeNi)_{0.89}Al_{0.11}$ | FCC | $a$ = 3.60 | 7.67 | [39,66] |
| | | BCC | $a$ = 2.87 | | |
| **CCFN-Al$_{1.0}$** | $(CoCrFeNi)_{0.80}Al_{0.20}$ | BCC | $a$ = 2.88 | 7.20 | [39,66] |
| **CCFN-Al$_{1.5}$** | $(CoCrFeNi)_{0.73}Al_{0.27}$ | BCC | $a$ = 2.88 | 6.81 | [39,66] |
| | | B2 | $a$ = 2.82 | | |
| **CCFN-Al$_{3.0}$** | $(CoCrFeNi)_{0.57}Al_{0.43}$ | B2 | $a$ = 2.89 | 6.00 | This Work* |
| **CCFN-V$_{0.3}$** | $(CoCrFeNi)_{0.93}Al_{0.07}$ | FCC | $a$ = 3.58 | 8.02 | This Work* |
| **CCFN-V$_{0.7}$** | $(CoCrFeNi)_{0.85}V_{0.15}$ | FCC | $a$ = 3.59 | 7.77 | This Work* |
| | | Sigma | $a$ = 8.78, $c$ = 4.60 | | |
| **CCFN-V$_{1.0}$** | $(CoCrFeNi)_{0.80}V_{0.20}$ | FCC | $a$ = 3.61 | 7.60 | [37] |
| | | Sigma | $a$ = 8.79, $c$ = 4.58 | | |
| **CCFN-V$_{2.0}$** | $(CoCrFeNi)_{0.67}V_{0.33}$ | Sigma | $a$ = 8.87, $c$ = 4.59 | 7.17 | This Work* |
| **CoFN-V$_{1.0}$** | $(CoFeNi)_{0.75}V_{0.25}$ | FCC | $a$ = 3.59 | 8.00 | This Work* |
| **CoFN-V$_{1.5}$** | $(CoFeNi)_{0.67}V_{0.33}$ | FCC | $a$ = 3.61 | 7.67 | This Work* |
| **CoFN-V$_{2.0}$** | $(CoFeNi)_{0.60}V_{0.40}$ | Sigma | $a$ = 9.04, $c$ = 4.68 | 7.40 | This Work* |
| **CCFN-Ti$_{0.4}$** | $(CoCrFeNi)_{0.91}Ti_{0.09}$ | FCC | $a$ = 3.59 | 7.86 | This Work* |
| **CCFN-Ti$_{0.6}$** | $(CoCrFeNi)_{0.87}Ti_{0.13}$ | FCC | $a$ = 3.61 | 7.70 | This Work* |

| | | | | | |
|---|---|---|---|---|---|
| **CCFN-Ti$_{1.0}$** | $(CoCrFeNi)_{0.80}Ti_{0.20}$ | C14 | $a$ = 4.79, $c$ = 7.76 | 7.40 | [40] |
| | | FCC | $a$ = 3.64 | | |
| **CCFN-Ti$_{1.5}$** | $(CoCrFeNi)_{0.73}Ti_{0.27}$ | C14 | $a$ = 4.77, c = 7.74 | 7.09 | This Work* |
| **CCFN-Ti$_{2.0}$** | $(CoCrFeNi)_{0.67}Ti_{0.33}$ | C14 | $a$ = 4.81, $c$ = 7.82 | 6.83 | This Work* |
| | | BCC | $a$ = 2.98 | | |

To analyse the phases adopted by these compositions, XRD characterisation experiments were performed on samples. The XRD patterns show that, within detection limits, the FCC phase is present for compositions CCFN-Pd0.5, CCFN-Pd1.0, and CCFN-Pd1.5. New compositions CoFN-V1.0, CoFN-V1.5 and CoFN-V2.0 were also synthesised to consider the phase stability resulting from the removal of Cr from the CCFN-Vx family. For the CCFN-Alx family the FCC phase is maintained for CCFN-Al0.5 with some small amounts of BCC/B2 formation. The BCC phase is fully adopted at the CCFN-Al1.0 composition the BCC/B2 phase at CCFN-Al3.0. Similarly, the CCFN-Vx family is FCC-stable at the smaller V additions of CCFN-V0.5 and CCFN-V0.8 with some secondary phase formation for larger V additions. A mixed FCC-Sigma phase is observed for CCFN-V1.0 and the composition fully adopts the Sigma phase by CCFN-V2.0. The phase formation and Rietveld refined lattice parameters are summarised in Table 9; where increasing amounts of Pd, Al, and V are added to CCFN there is an associated increase in the lattice parameter. The empirical VEC used in the analysis of the alloy compositions are obtained from the weighted average of the electrons accommodated in the s, p, d orbitals of the alloy's constituent elements [22].

The phase discrimination as a 2-dimensional plot of the enthalpy of mixing against VEC was first presented by Dominguez *et al.* [14] where a single BCC phase forms for 3 < VEC < 6, a single FCC phase forms for 8 < VEC < 11, and complex phases form for 6 < VEC < 8. The experimental results show that the compositions of complex phases (*c.f.* Table 1) indeed possess values in the intermediate range of 6 < VEC < 7.8. However, when considering the phase stability of complex structures in specific compositions, the cubic B2 presence in CCFN-Alx compositions determined experimentally is observed fully only from VEC $\leq$ 6.81; the tetragonal Sigma phase presence in the CCFN-Vx compositions at VEC $\leq$ 7.77; and the hexagonal C14 phase presence in CCFN-Tix compositions is only observed at VEC $\leq$ 7.4.

These observations highlight the behaviours that result from the dependence of electronic structure for the different complex phases as a function of elemental alloy additions. The RBA method employed in this study allows investigation of the relative structural stability of CCFN (CCFN-Ax) as a function of the exact valence electron concentration, n which is, in turn obtained from the integration of density of states (*c.f.* equation (2) below).

### 5.2.2 RBA Phase Stability as a Function of Valence Electron Concentration

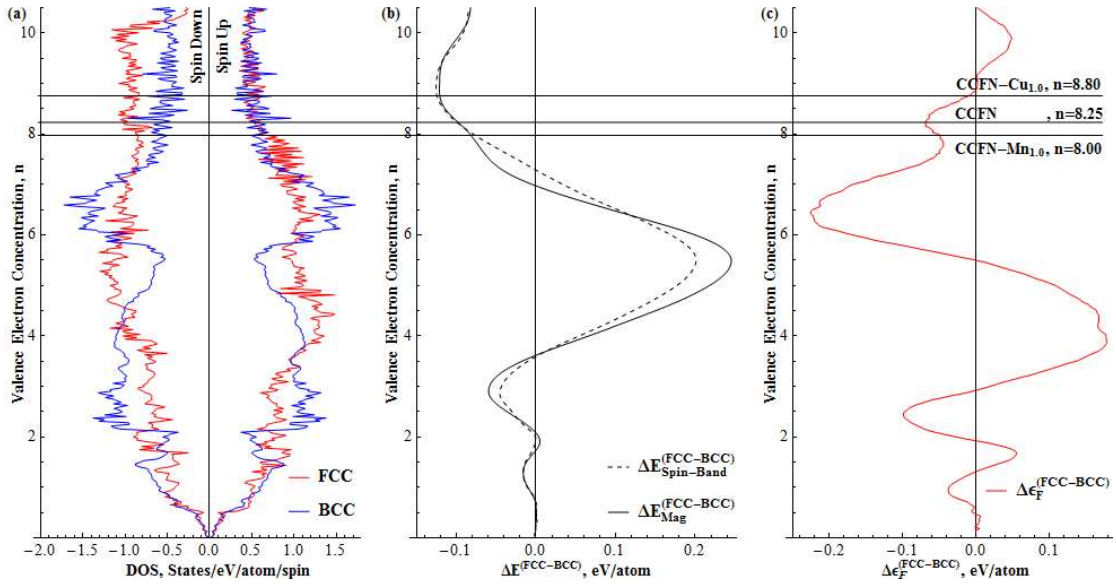


**Figure 19. (a)** Spin-polarised density of states of FCC and BCC 32-atom Special Quasi-Random Structure (SQS) CCFN and; **(b)** Spin-polarised band energy difference between FCC and BCC CCFN (i) Without double-counting Stoner corrections, (ii) With Stoner Correction and; **(c)** The Fermi energy difference between the FCC and BCC structure (*c.f.* equation (4)).

Within DFT, the total energy difference between two structures (1 and 2) at a fixed volume for an investigated alloy can be decomposed into two contributions [31,67,68]:

$$\Delta E^{(1-2)} = \Delta E_B^{(1-2)} + \Delta E_{e-e}^{(1-2)} \quad (1)$$

where the first contribution represents the change in band energy between two structures, and the second contribution arises from the structural energy difference in electrostatic and electron-electron interactions. By using the RBA/frozen potential approach [67,68] the energy difference between two non-magnetic phases can be simply approximated from comparing the band-structure energy difference using the same frozen potential for the two structures at a fixed volume. This approximation is valid to the first order not only for an

elemental metal but also for metallic alloys where the second contribution is considered to be small [30,31,56,57]. In order to analyse the phase stability of alloys for a wide range of concentrations the energy difference can be presented as a function of n. The latter can be in turn determined from the integration of total electronic density of states (DOS) per atom up to the Fermi energy.

For magnetic alloys, such as CCFN-based HEAs investigated in this work, applying the Stoner model to the RBA allows the band energy difference to be decomposed to contributions from the spin-polarised band energy and the double-counting contributions arising from magnetic interactions [60,61]. In this case, the value of valence electron concentration, n, can be obtained from the integration of spin-polarised total DOS per atom as

$$n = \int_{-\infty}^{\varepsilon_F} D^{\uparrow}(\varepsilon)d\varepsilon + \int_{-\infty}^{\varepsilon_F} D^{\downarrow}(\varepsilon)d\varepsilon = n\uparrow + n\downarrow \quad (2)$$

where $D^{\uparrow}(\varepsilon)$ and $D^{\downarrow}(\varepsilon)$ are the spin-polarised total DOS per atom for electrons with spin-up and spin-down, respectively, and $\varepsilon_F$ is the Fermi energy.

An exact application of the Stoner model requires the knowledge of magnetic moments of all atoms in the system but it can be simplified through using an effective Stoner parameter, $I_{eff}$. The latter one is defined as the exchange splitting of the on-site energies of electrons with spin-up and spin-down due to average atomic magnetic moment, $m_{av}$, which can be obtained from the non-magnetic total DOS and the value of the average atomic magnetic moment of the entire simulation cell. The energy difference between any two magnetic structures can be thus written as:

$$\Delta E_{Mag}^{(1-2)} \approx \Delta E_{Spin-Band}^{(1-2)} + \frac{1}{4}\left[I_{eff}^{(1)} m_{av}^{2\,(1)} - I_{eff}^{(2)} m_{av}^{2\,(2)}\right] \quad (3)$$

where the first term is related to the spin-polarised band energy difference obtained from the total DOS per atom and per electron spin and the second term is the double-counting contribution coming from magnetic interactions. As shown in Table SI in the Appendix, the energy differences calculated with a knowledge of magnetic moments of all atoms in the system and those obtained using average magnetic moments and effective Stoner parameters are in a quantitative agreement and in line with the results obtained using the

LMTO code [69]. Thus, for the RBA analysis of stability of other CCFN-based alloys the simplified method based on the effective Stoner parameter will be applied. The derivation of the RBA for magnetic systems using the Stoner model can be found in the Appendix [see equations (I-V)]. Fig. 19 (a) shows the spin-polarised DOS of disordered simple FCC and BCC phases calculated utilising a Special Quasi-random Structure (SQS) [70,71] generated Co8Cr8Fe8Ni8 structure representing the CCFN composition, which is used for the RBA analysis. Fig. 19 (b) shows the resulting FCC-BCC band energy difference of CCFN alloys calculated with and without Stoner corrections as a function of n.

From Fig. 19 (b) it is observed that the FCC phase for the CCFN composition is stabilised in the region of $n > 6.97$ according to the RBA prediction from equation (3). The FCC stable zone reported by Dominguez et al.'s PCA analysis was found to lie between $8 < VEC < 11$ [11]; this difference is expected as we have not considered the stability of complex phases in the CCFN composition. The compositions CCFN-Mn and CCFN-Cu with $n = 8$ and $n = 8.8$ respectively, lie within the FCC-stable region; this RBA prediction is in agreement with experimental determination of their respective structure [72]. According to Fig. 1(b), the simple BCC phase would be stabilised within the region of $3.75 < n < 6.97$. Extension of our RBA analysis to the experimental observation for BCC HEAs containing 4d and 5d BCC transition metals (TMs) previously reported such as WNbMoTa [73,74] with VEC = 5.5, and TiVMnNb [11] with VEC = 5.25 agrees with the RBA model as both fall within the BCC-stable region.

Below we apply the RBA model for studying the structural-stability competition between simple phases (FCC and BCC) and different complex phases within four CCFN-Ax alloys (A=Pd, Al, V and Ti).

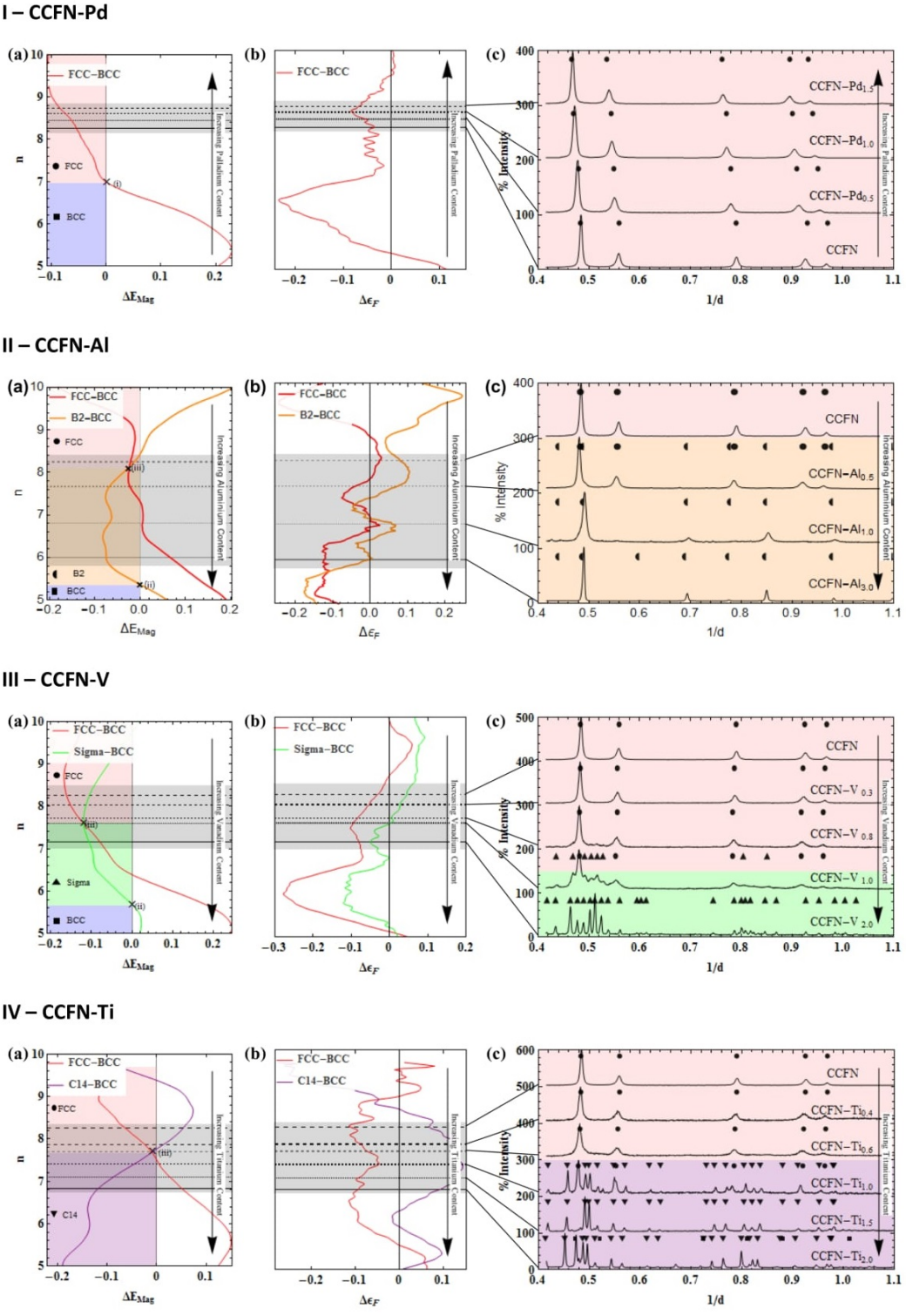


**Figure 20.** Predictions and experimental results for several alloy systems, I – CCFN-Pd, II – CCFN-Al, III –CCFN-V, and IV – CCFN-Ti, showing for each, the change in phase stability with increasing 5$^{th}$ element content through (a) VEC, *n*, against the band energy difference, (b) The Fermi Energy difference as defined in equation (4) below, and (c) Its associated XRD patterns.

Fig. 20(I-IV) shows the results of theoretical and experimental investigation of phase stability of several 5-component CCFN-based alloy systems. In each case the fifth element was chosen in such a way that it represents different type of alloying element. In the CCFN-Pd alloys shown in Fig. 20I, palladium is a 4d-transition metal element located on a different row of the periodic table in comparison to the other four elements (Cr, Co, Fe and Ni; 3d transition metals). Accordingly, the results from the RBA model comparing the energy difference between FCC and BCC structures in CCFN-Pd alloys, shown in Fig. 2I, are slightly different to those for CCFN alloys displayed in Fig. 19. The RBA results for structural energy differences between the simple phases (FCC and BCC) and B2 phase in CCFN-Al alloys are shown in Fig 2II, where Al is a sp-metal from outside the transition metal series. Finally for CCFN-V and CCFN-Ti alloys, where both V and Ti are in the same 3d transition metal series, there is competition between simple and complex phases in term of the Sigma and C14 structures; the RBA model results are shown in Figs. 2III and 2IV, respectively. The energy differences between complex phases (B2, Sigma or C14) and the BCC phase calculated using RBA as a function of *n* are shown in Figs. 2I-IV(a). The relationship between the calculated total energy difference of two competitive structures (Eq. 3) and the plots of Fermi energy differences, $\Delta \varepsilon_F$ shown in Figs. 2I-IV(b) will be explained later in the "*Discussion*" section. The corresponding XRD patterns for CCFN and the four CCFN-$A_X$ HEAs are presented in Figs. 2I-IV(c). The XRD peaks were attributed to different considered phases: FCC, BCC, B2, Sigma and C14. In order to compare the theoretical RBA results and the experimental data, the valence electron concentration values *n* calculated within the RBA model for a chosen measured alloy composition are indicated on Figs. 20I-IV(a) and Figs. 20I-IV(b) by lines of the same pattern as in the XRD results in Figs. 20I-IV(c).

The FCC-BCC energy difference for CCFN-$Pd_x$ HEA obtained using the RBA method shows that the increase of *n*, associated with the increasing additions of Pd stabilises the FCC phase, see Fig. 20I(a). Moreover, the region of stability of single FCC phase contains not only the CCFN and CCFN-$Pd_x$ HEA compositions but it can be extended to *n* = 7. The experimental XRD results for corresponding valence electron concentration values, *n* confirm the RBA prediction for the CCFN-$Pd_x$ HEA since all of the patterns are indexed as the FCC phase. The experimental results also show an increase in the FCC lattice parameter with the increasing

concentration of Pd, wich is in agreement with the most recent fully-relaxed DFT calculations [5].

Fig. 20II displays the results for RBA analysis for CCFN-$Al_x$ where *x* = 0, 0.5, 1.0, and 1.5. The B2 phase is also considered as there is shown to be a high enthalpy of formation of the B2 structure between FeAl, CoAl, NiAl[75]. Moving down Figures 20II (a), (b), and (c) represents an increase in aluminium content according to corresponding *n* values, and the existence of the B2 phase for CCFN-$Al_{1.0}$ (*n* =7.2) and CCFN-$Al_{3.0}$ (*n* = 6.81) is confirmed through XRD verification which is also in accordance with the literature[39,66] while CCFN-$Al_{0.5}$ (*n* = 7.67) retains the FCC phase.

In Fig. 20III, for CCFN-$V_x$ where *x* = 0, 0.3, 0.8, 1.0, and 2.0, we include consideration of the complex Sigma phase, shown in binary FeCr and FeV phase diagrams [76]. The valence electron concentration value n is decreased with increasing V addition. By comparing Fig. 20III (a) and Fig. 20III (c), an excellent agreement of predicted stable phase as a function of n, from single FCC to complex Sigma phase from $\Delta E_{Mag}$ values is found with experimental results, in accordance with literature [37].

In Fig. 20IV, for CCFN-$Ti_x$ where *x* = 0, 0.4, 0.6, 1.0, and 1.5, the C14 phase is additionally considered as this intermetallic structure is related to the $CoTi_2$, $CrTi_2$, and $TiCr_2$ complex phase forming binary compounds[76]. The inclusion of Ti and the related C14 complex phase into the RBA analysis destabilises the BCC phase much further below *n* = 5.5 than in the previously considered cases of Pd, Al and V alloying. XRD results show that the CCFN-Ti undergoes a transition from the FCC to C14 phase between CCFN-$Ti_{0.6}$ (*n*=7.70) and CCFN-$Ti_{1.0}$ (n=7.40); the CCFN-$Ti_{1.0}$ (n=7.40), CCFN-$Ti_{1.5}$ (n=7.09), and CCFN-$Ti_{2.0}$ (*n*=6.83) phases have been indexed as FCC-C14, C14, and C14-BCC respectively. The structural trend in changes of phase stability between FCC, C14 and BCC will be discussed in the next section.

Generally, present predictions of phase stability as a function of *n* using the RBA analysis have been found to give a reasonable match when compared to the outputs from our XRD analysis. Lowering of the *n* value within families of HEAs causes a change in stability from a FCC single phase to complex phases (B2, Sigma and C14) back to a BCC single phase. Formation of complex phases is observed to occur at the transition between FCC-BCC stability, located near *n* = 7 as observed in Fig. 1 for the CCFN alloys. This prediction based

on electronic structure calculations is in line with Gao's empirical rules [77] where complex phase formation is observed at intermediate n values between 6.5 and 7.5.

### 5.2.3 Electronic Origin of Phase Stability for Complex Phases in HEA.

In order to understand the structural trend from simple to complex phase in CCFN-$A_x$ HEAs investigated in the previous section, we begin to analyse the phase stability of CCFN-$Al_x$ (where $x$ = 0.5, 1.0, and 3.0) within the RBA model in predicting transition from the FCC to the B2 phase. It is worth emphasising again that the RBA has been used successfully to investigate the structural trend of intermetallic compounds and complex Hume-Rothery phases in transitional metal aluminides known as *spd electron phases* [31,56]. Here the hybridisation effect between sp-valence electrons of Al with the d-orbitals of transition metals (TM) plays a crucial role in structural stability trends and their physical properties. In the case of HEA CCFN-$Al_x$, a similar effect can be seen from the construction of frozen-potential approximation for Al and TM atoms (Cr, Co, Fe, Ni) to the electronic structure calculations within the RBA model for different SQS structures. It is well-known from both experimental and DFT data that among the B2 compounds formed between Al and TMs, the B2-AlNi phase has the strongest negative enthalpy of formation [75]. The B2 phase can be built, therefore, from an ordered structure with four Al, Ni, Fe, Co atoms where Al-Ni pairs are dominant at nearest neighbour distance in the BCC-like structure.

Fig. 2IIa shows the B2-BCC structural energy difference calculated from the RBA model plotted together with the FCC-BCC difference as a function of $n$. It is found from the RBA calculations that the competition between FCC and B2 phases starts at valence electron concentration, $n \approx 8$ Comparing with the present experimental data for HEA CCFN-$Al_{0.5}$ ($n$ = 7.67) indicating the existence of FCC peaks in XRD (Fig.IIc), it appears that the RBA model could overestimate the stability of the B2 phase. However, in comparison with a new HEA composition, $AlCoCrFeNi_{2.1}$, where the corresponding valence electron concentration, $n$ = 7.70, the experimental observation [78] of an FCC/B2 dual-phase constitution not only validates our theoretical prediction but also demonstrates that the formation of B2 phase is strongly correlated with the short-range chemical order between Al and the excess composition of Ni transition metals in the HEAs.

The phase stability trends between the FCC phase and intermetallic phase C14 for the CCFN-$Ti_x$ compositions in Fig. 2IV also deserve further analysis. From Table 9, we observe a change in experimentally determined phase stabilities from CCFN-$Ti_{1.0}$, CCFN-$Ti_{1.5}$ and CCFN-$Ti_{2.0}$ as a mixture of FCC-C14, to C14, and finally a BCC-C14 mixture, respectively. By comparing the theoretical results displayed between Fig. 20IV and Fig. 19, it is found that the CCFN-$Ti_{1.0}$ composition with *n* = 7.40 is located within the CCFN FCC stable region while the CCFN-$Ti_{2.0}$ composition with *n* = 6.83 is below the CCFN FCC-BCC nodal point at *n* = 7.26. The CCFN-$Ti_{0.5}$ composition with *n* = 7.09 lies closest to the FCC-BCC nodal point where $\Delta E_{Mag} = 0$, suggesting that complex phases form at these points, which is in line with the analysis performed by Dominguez *et al.* [11] where the stability was found to range from the simple FCC phase (high VEC values), to the complex phase (medium VEC values), to the simple BCC phase (low VEC values), which follows a similar trend to *n* in this analysis.

### 5.2.4 Relative Structural Stability and their Fermi Energy Difference, $\Delta \varepsilon_F$.

The relative structural stability between two phases within the RBA model is defined by comparing the spin-polarised band-structure energy difference in equation (3) as a function of the number of valence electron, *n*, determined from equation (2). The origin of the structural stability within the RBA model can be further analysed in terms of the change in Fermi energy [30,31]. The latter one can be defined as the first derivative of the band energy difference of two competing structures with respect to the change in *n*:

$$\Delta \varepsilon_F^{(1-2)} = \frac{\partial\left(\Delta E_{Mag}^{(1-2)}\right)}{\partial n} \tag{4}$$

From equation (4) it follows that the extremal of the energy difference, $\Delta E_{Mag}$ occurs for the number of electrons at which the two Fermi energies are equal, i.e. $\Delta \varepsilon_F^{(1-2)} = 0$. The latter condition is important because it would correspond to the stationary points where the second phase becomes the most stable one in comparison to the first phase [30,31]. For the CCFN case shown in Fig. 1, $\Delta \varepsilon_F^{(FCC-BCC)} = 0$ at *n* = 5.5 where $\Delta E_{Mag}^{(FCC-BCC)}$ is maximal and the BCC phase exhibits the largest stability with respect to the FCC phase, see Figs. 19(b) and 19(c). Applying the criterion (4) for CCFN-$Pd_x$ HEA the maximum difference between FCC and BCC phase is predicted at *n* = 9.4 where $\Delta \varepsilon_F = 0$ as can be seen in Fig. 20I(b). For that number of *n* the FCC phase the most stable one in comparison with the BCC phase.

Fig. 20II (b) shows $\Delta\varepsilon_F$ plots calculated from energy difference $\Delta E_{Mag}$ for both FCC and B2 phases in CCFN-$Al_x$ HEA in reference to the BCC phase. The maximum $\Delta E_{Mag}$ between the FCC-BCC phases is at *n* = 7.8 which in turn corresponds to $\Delta\varepsilon_F = 0$, but the former is not the most stable structure since $\Delta E_{Mag}$ of the B2-BCC phases is lower than that of FCC-BCC phases at this value, as shown in Fig. 20II (a). The plot for $\Delta\varepsilon_F$ as a function of *n* for B2-BCC phases shows that there are two zero values at *n* = 6.4 and 7.4 where the B2 phase could be the most stable. The differentiation of both phases with XRD in the present study cannot be certain due to the low intensity of the obtained peaks, but B2 formation appears to begin from CCFN-$Al_{0.5}$ onwards at *n* = 7.67 and continues in CCFN-$Al_{1.0}$ at *n* = 7.2 and CCFN-$Al_{1.5}$ at *n* = 6.81. This is in line with the determined value of *n* = 7.4 where the Fermi energy difference between B2 and BCC is equal to zero. It is worth mentioning again that by looking at general competition between FCC, B2 and BCC phases the criterion $\Delta\varepsilon_F = 0$ strongly supports the experimental observation of dual FCC/B2 phases observed in $AlCoCrFeNi_{2.1}$ with the value *n*=7.7 which is located in between the FCC stable phase (*n*=7.8) and the B2 stable phase (*n*=7.4).

For CCFN-V from Fig. 20III (b) it appears that for maximum stability of the Sigma phase with respect to the BCC phase two zero values for $\Delta\varepsilon_F$ at *n* = 7.65 and *n* = 6.65 are observed. From XRD results it is evident that the Sigma phase is dominant between CCFN-$V_{1.0}$ and CCFN-$V_{2.0}$ (*n* = 7.6 and *n* = 7.16 respectively), and CoFN-$V_{1.5}$ and CoFN-$V_{2.0}$ (*n* = 7.67 and *n* = 7.4, respectively). This is also close to the predicted value of the most stable Sigma at *n* = 7.65.

According to Fig. 20IV (b) for the CCFN-Ti family, the prediction of the stationary point of $\Delta\varepsilon_F = 0$ from the FCC-BCC plot corresponding to the most stable FCC point lies at *n* = 9.0. The stationary point for the C14-BCC plot is located at *n* = 6.4 where the C14 phase is the most stable one. The C14 phase is not observed as a stable structure for CCFN-$Ti_{0.4}$ at *n* = 7.85 and CCFN-$Ti_{0.6}$ at *n* = 7.7 because from Fig 2IV (a) $\Delta E_{Mag}$ of the FCC-BCC plot is lower than the C14-BCC one for *n* ≥ 7.69. It is possible that C14 phases may exist in small quantities and further precipitation is being supressed by the high cooling rate as a result of the synthesis method used in this work.

Thus, beside the case of CCFN-$Pd_x$ HEA where the FCC phase is the most stable one for all n values (see Fig. 2I(b)), the above analysis using the criterion $\Delta \varepsilon_F = 0$ allows compositions to be predicted in CCFN-$Al_x$, CCFN-$V_x$, CCFN-$Ti_x$ HEAs that stabilise the complex phases and therefore possesses the ability to develop simple/complex phase combinations.

### 5.2.5 RBA versus Experimental observation of HEA Phase Stability as a Function of n

Fig. 21 illustrates a comparison of the experimentally-determined phase present and quantum-mechanical RBA-determined stable phase for each HEA family with different values of *n*. The first row for each HEA family represents the former as determined from $\Delta E_{Mag}$ while the indicated (bold, underline) regions show the points at which $\Delta \varepsilon_F = 0$ where the indicated phase is the most stable. It is shown that the agreement between experimental and RBA results is very satisfactory. In the case of CCFN-$Al_x$, the present experimental XRD results of the BCC phase in the range of Al concentration between 0.5 (*n*=7.67) and 1.0 (*n*=7.2) show that these BCC alloys are strongly disordered, whereas the Al-Ni short range chemical-order alloys present within the RBA model are more in favour of the B2 phase. The experimental observation of the dual FCC/B2 phases in the Ni-rich HEA of $AlCoCrFeNi_{2.1}$ (*n*=7.70) has confirmed the validity of RBA prediction. In general, it is observed that the simple FCC phase is present at $n > 8$, the complex phases are present between $6 < n < 8$, and the simple BCC phase at $n < 6$. This variation in phase stability as a function of n supports the simple two dimensional plot presented by Dominguez *et al.* [11] and Guo *et al.* [22]. In particular, the empirical VEC parameter used in all previous studies has a strong relationship with the quantum-mechanical value *n* from electronic-structure calculations.

| Family | Method | 5.0 - | 5.5 - | 6.0 - | 6.5 - | 7.0 - | 7.5 - | 8.0 - | 8.5 - | 9.0 |
|---|---|---|---|---|---|---|---|---|---|---|
| **CCFN** | Exp. | | | | | | | | FCC* | |
| | RBA | BCC | **BCC** | BCC | BCC | BCC | BCC | FCC | **FCC** | FCC |
| **CCFN-Pd** | Exp. | | | | | | | | FCC*[65] | FCC*[65] |
| | RBA | **BCC** | BCC | BCC | BCC | BCC | FCC | FCC | FCC | **FCC** |
| **CCFN-Al** | Exp. | | | | B2*[39,66] | B2*[39,66] | B2*[39,66] | FCC* FCC/B2[78] | | |
| | RBA | BCC | B2 | B2 | B2 | **B2** | B2 | B2 | FCC | FCC |
| **CCFN-V** | Exp. | | | | | σ* | σ*[37] | FCC* | | |
| | RBA | BCC | BCC | σ | σ | σ | **σ** | FCC | FCC | **FCC** |
| **CoFN-V** | Exp. | | | | | σ* | FCC* | FCC* | | |
| | RBA | BCC | BCC | σ | σ | σ | **σ** | FCC | FCC | **FCC** |
| **CCFN-Ti** | Exp. | | | | C14* | C14*[40] | FCC* | | | |
| | RBA | C14 | C14 | **C14** | C14 | C14 | FCC | FCC | FCC | **FCC** |

**Figure 21.** Phases present via XRD (Red) as a function of regions of valence electron concentration and predicted via $\Delta E_{Mag}$ (Black) and $\Delta \varepsilon_F = 0$ (**Bold, Underlined**) as a function of regions *n*. Both VEC and *n* are considered equivalent here, showing good interchangeability between both. While $\Delta E_{Mag}$ predicts the relative stability of different phases (*c.f.* equation (3)), $\Delta \varepsilon_F = 0$ represents the criterion point at which the considered phase is the most stable one (*c.f.* equation (4)). * indicates experiments performed in this work, while a superscript number indicates that the composition is found in the corresponding reference from the literature possessing the indicated structure.

Fig. 3 illustrates a comparison of the experimentally-determined phase present and quantum-mechanical RBA-determined stable phase for each HEA family with different values of *n*. The first row for each HEA family represents the former, while the latter is determined from $\Delta E_{Mag}$ with the indicated (bolded, underlined) regions showing the points at which $\Delta \varepsilon_F = 0$, where the indicated phase is the most stable. It is shown that the agreement between experimental and RBA results is very satisfactory. In the case of CCFN-$Al_x$, the present experimental XRD results of the BCC phase in the range of Al concentration between 0.5 (*n*=7.67) and 1.0 (*n*=7.2) shows that these BCC alloys are strongly disordered, whereas the Al-Ni short range chemical-order alloys present within the RBA model are more in favour of the B2 phase. The experimental observation of the dual FCC/B2 phases in the Ni-rich HEA of $AlCoCrFeNi_{2.1}$ (*n*=7.70) has confirmed the validity of RBA prediction. In

general, it is observed that the simple FCC phase is present at $n > 8$, the complex phases are present between $6 < n < 8$, and the simple BCC phase at $n < 6$. This variation in phase stability as a function of n supports the simple two dimensional plot presented by Dominguez *et al.*[14] and Guo *et al.* [22]. In particular, the empirical VEC parameter used in all previous studies has a strong relationship with the quantum-mechanical value *n* from electronic-structure calculations.

It is apparent from Fig. 20 and summarised in Fig. 21 that performed in conjunction, analysis of $\Delta E_{Mag}$ and $\Delta \varepsilon_F$ results allows for deeper understanding of phase stabilities, although for rough predictions $\Delta E_{Mag}$ alone is enough to give relatively accurate results for the compositions tested in this work. A comparison of $\Delta E_{Mag}$ and $\Delta \varepsilon_F$ with *n* values for the tested compositional families show that in terms of phase stability, *n* at which the simple FCC phase transition is located is dependent on the chemical bonding nature of the alloying element to CCFN.

The results of the RBA analysis suggest that empirical VEC values have a strong connection to the values of *n* calculated from electronic spin-polarised DOS (Eq. 2) and that the accuracy of predictions in alloy design can be improved as long as electronic structure effects at the quantum scale are accounted for. In light of the dependency on the electronic structure, the increased accuracy with which HEA complex phases may be determined is not surprising. As Miedema's empirical rule for the enthalpy of mixing, ΔH, has been found to be inconsistent with quantum mechanics principles [26,79], the ability of the two-dimensional plot shown by Dominguez *et al.* [11] to distinguish between components may arise from the deviation in the ratio between the enthalpy of mixing and the difference in the number of valence electrons squared from Miedema's model. The latter quantity $\Delta H / (\Delta n)^2$ has been shown [79] to start deviating from theoretical predictions between $4 < V < 7$, which is regarded as zones of complex phase presence in HEAs.

These factors may be accounted for by utilising the RBA technique presented in this chapter. As shown in Fig. 2 and Fig. 3, $\Delta E_{Mag}$ values may be used to approximate, to a good degree of accuracy, the phases present in any particular stoichiometric composition within a preselected CCFN family (here family refers to all elemental alloying components comprising the composition), as a function of *n*.

### 5.2.6 Structural Stability of New HEAs: The CoFeNi-$V_x$ family

The above hypothesis is tested through the removal of Cr from CCFN-$V_x$ to form the CoFeNi-$V_x$ (here denoted as CoFN-$V_x$) alloys and the subsequent analysis of its phase stabilities utilising the RBA method as a function of a change in vanadium addition. To achieve this the CCFN FCC-BCC RBA analysis is modified to include the consideration of the Sigma phase due to strong enthalpies of mixing of FeCr and FeV for the Sigma phase as in the case of CCFN-$V_x$. No explicit consideration is necessary as Co, Cr, Fe, Ni, and V are located on the same row of the periodic table.

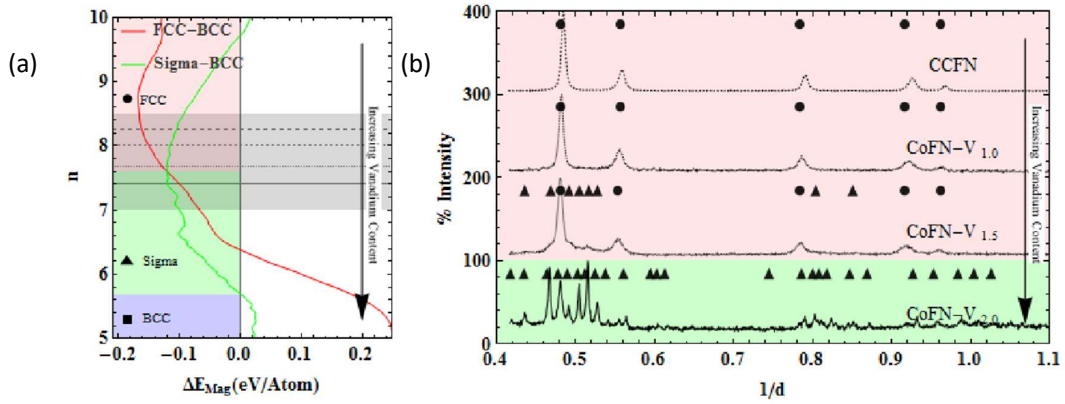


**Figure 22.** Transition of FCC to Sigma phase stability in CoFN-V (a) As a function of increasing Vanadium content represented by n, and (b) Its associated XRD Patterns.

Fig. 422 indicates the analysis of the CoFN-$V_x$ composition, in terms of *n*. The RBA analysis described in Fig. 2(III) for the relative structural energy between FCC-BCC and FCC-Sigma phases in CCFN-$V_x$ is adapted for investigation of the new HEAs. Removal of Cr has the effect of shifting *n* values to higher regions, with the effect of destabilising the Sigma structure. This shift in *n* to the region of FCC stability may be attributed to the Fermi surface nesting in HEAs with or without Cr which can stabilise a complex phase [80]. For equiatomic CoFN-$V_{1.0}$ at $n$ = 8 observed from Fig. 4 (a) that the FCC phase is stabilised as compared to the presence of Sigma phase previously considered at equiatomic CCFN-$V_{1.0}$ with $n$ = 7.6. In Fig. 4 (b) experimental XRD patterns verify the prediction of CoFN-$V_{1.0}$ and subsequent compositions, CoFN-$V_{1.5}$ (FCC phase at $n$ = 7.67) and CoFN-$V_{2.0}$ (Sigma phase at $n$ = 7.40) predicted within the RBA model, indicating that the VEC values in Table 1 are in good agreement with *n* and that the RBA method therefore can be used as a valid tool for phase prediction, by taking into consideration the chemical bonding of the alloying species.

The power of the RBA model when used in conjunction with *n* in predicting complex phase formation in HEAs makes it suitable for the design of new HEA compositions. The relative phase stability as a function of *n* may be analysed for equiatomic compositions of designated multi-component alloys with four or more elements. As formation of the complex phase is identified to occur around the nodal points of FCC-BCC energy difference where $\Delta E_{Mag} = 0$ (*c.f.* Fig. 2), the generalisation of the RBA approach would require a starting alloy composition that is a known simple phase (FCC/BCC) such as CCFN (FCC), CCFN-Pd (FCC), CCFN-Mn (FCC), WNbMoTa (BCC), or TiVMnNb (BCC), that is to be modified by changing its stoichiometry, or by further alloying additions to the composition. It is preferable for the initial structure to be FCC-type as it is less complicated to obtain the self-consistent charge density from a close-packed structure as an input frozen potential for the RBA, as compared to a more complex structure. The secondary phase chosen for consideration will depend on the alloying additions to the composition and the enthalpies of mixing of the phases which may either be analysed directly or obtained from literature.

## 5.3 Chapter Summary

In this chapter the RBA approach which gives a full description of the influence of electronic structure effects on phase formation in HEAs has been applied, and the predictions were compared to experimental results. The main findings are as follows:

- The RBA model proves successful to access information on phases present in multicomponent HEAs as a result of macro alloying of the CCFN composition. Formation of complex phases is found to coincide with the transition between FCC and BCC, being the lower energy structures at intermediate values of the valence electron concentration, *n* determined from integration of spin-polarised DOS for the magnetic HEAs.
- Values of *n* for which complex phases are found have been predicted with more precision for specific alloy systems and validated experimentally: Sigma phase for CCFN-$V_x$ ($n < 7.6$), B2 for CCFN-$Al_x$ ($n < 8.1$) and C14 phase for CCFN-$Ti_x$ ($n < 7.7$).
- The RBA scheme is successful at predicting the complex Sigma phase found in the previously unreported CoFN-$V_x$ composition ($n \leq 7.6$) and allow the prediction of other complex intermetallic phases in new alloy compositions as a function of *n*.

The results generally show that the phase stability and transition can be accurately described when the electronic structure of the composition is taken into account. Application of the RBA method greatly simplifies the modelling of prospective calculations while giving accurate results, but is limited to analyses of A-$B_x$ compositions. The results emphasise the need for a robust and fairly accurate predictive scheme that takes into account quantum mechanical effects that can be used to determine compositions of interest that can then be further investigated using computer-intensive ab-initio methods.

## 5.4 References


[1] D.B. Miracle, O.N. Senkov, A critical review of high entropy alloys and related concepts, Acta Mater. 122 (2017) 448–511. doi:10.1016/j.actamat.2016.08.081.

[2] E.J. Pickering, R. Munoz-Moreno, H.J. Stone, N.G. Jones, Precipitation in the equiatomic high-entropy alloy CrMnFeCoNi, Scr. Mater. 113 (2016).

[3] F.R. de Boer, ed., Cohesion in metals: transition metal alloys, 2., print, North Holland, Amsterdam, 1988.

[4] U. Dahlborg, J. Cornide, M. Calvo-Dahlborg, T.C. Hansen, Z. Leong, L.A. Dominguez, S. Chambreland, A. Cunliffe, R. Goodall, I. Todd, Crystalline structures of some high entropy alloys obtained by neutron and x-ray diffraction, Acta Phys. Pol. A. 128 (2015).

[5] M. Calvo-Dahlborg, J. Cornide, Tobola, D. Nguyen Manh, J.S. Wróbel, J. Juraszek, S. Jouen, U. Dahlborg, Effect of Pd on structural and magnetic properties of high entropy CoCrFeNiPd alloys. In preparation, (2016).

[6] J. Cornide, U. Dahlborg, Z. Leong, L.A. Dominguez, J. Juraszek, S. Jouen, T. Hansen, R. Wunderlich, S. Chambreland, I. Todd, R. Goodall, M. Calvo-Dahlborg, Structure and Properties of Some CoCrFeNi-Based High Entropy Alloys, in: TMS2015 Supplemental Proceedings, 2015.

[7] J. Cornide, M. Calvo-Dahlborg, S. Chambreland, L.A. Dominguez, Z. Leong, U. Dahlborg, A. Cunliffe, R. Goodall, I. Todd, Combined atom probe tomography and TEM investigations of CoCrFeNi, CoCrFeNi-Pdx (x=0.5, 1.0, 1.5) And CoCrFeNi-Sn, Acta Phys. Pol. A. 128 (2015).

[8] W. Research, Mathematica 10.4, 10.4, Champaign, Illinios, 2016.

[9] F. Ren, K. Cao, J. Ren, A.A. Volinsky, T.H. Tran, B. Tian, Numerical Calculation of the Electron Density at the Wigner–Seitz Radius Based on the Thomas–Fermi–Dirac Equation, J. Comput. Theor. Nanosci. 11 (2014) 344–347. doi:10.1166/jctn.2014.3358.

[10] L.C. Allen, Electronegativity is the average one-electron energy of the valence-shell electrons in ground-state free atoms, J. Am. Chem. Soc. 111 (1989) 9003–9014. doi:10.1021/ja00207a003.

[11] L.A. Dominguez, R. Goodall, I. Todd, Prediction and validation of quaternary high entropy alloys using statistical approaches, Mater. Sci. Technol. 31 (2015) 1201–1206.

[12] U. Mizutani, Hume-Rothery rules for structurally complex alloy phases, CRC Press, Boca Raton, 2011.

[13] R.G. Parr, R.A. Donnelly, M. Levy, W.E. Palke, Electronegativity: The density functional viewpoint, J. Chem. Phys. 68 (1978) 3801. doi:10.1063/1.436185.

[14] L. Pauling, THE NATURE OF THE CHEMICAL BOND. IV. THE ENERGY OF SINGLE BONDS AND THE RELATIVE ELECTRONEGATIVITY OF ATOMS, J. Am. Chem. Soc. 54 (1932) 3570–3582. doi:10.1021/ja01348a011.

[15] A.R. Miedema, The electronegativity parameter for transition metals: Heat of formation and charge transfer in alloys, J. Common Met. 32 (1973) 117–136. doi:10.1016/0022-5088(73)90078-7.

[16] C.-C. Juan, C.-Y. Hsu, C.-W. Tsai, W.-R. Wang, T.-S. Sheu, J.-W. Yeh, S.-K. Chen, On microstructure and mechanical performance of AlCoCrFeMo0.5Nix high-entropy alloys, Intermetallics. 32 (2013) 401–407. doi:10.1016/j.intermet.2012.09.008.

[17] J.W. Yeh, S.K. Chen, S.J. Lin, J.Y. Gan, T.S. Chin, T.T. Shun, C.H. Tsau, S.Y. Chang, Nanostructured high-entropy alloys with multiple principal elements: Novel alloy design concepts and outcomes, Adv. Eng. Mater. 6 (2004) 299–303.

[18] M.-R. Chen, S.-J. Lin, J.-W. Yeh, M.-H. Chuang, S.-K. Chen, Y.-S. Huang, Effect of vanadium addition on the microstructure, hardness, and wear resistance of Al0.5CoCrCuFeNi high-entropy alloy, Metall. Mater. Trans. A. 37 (2006) 1363–1369. doi:10.1007/s11661-006-0081-3.

[19] B.W. Silverman, Density estimation for statistics and data analysis, Chapman & Hall/CRC, Boca Raton, 1998.

[20] H. Bakker, A. Miedema, Enthalpies in alloys: Miedemaś semi-empirical model, Trans Tech Publications, Uetikon-Zuerich, Switzerland ; Enfield, N.H, 1998.

[21] R.F. Berger, P.L. Walters, S. Lee, R. Hoffmann, Connecting the Chemical and Physical Viewpoints of What Determines Structure: From 1-D Chains to γ-Brasses, Chem. Rev. 111 (2011) 4522–4545. doi:10.1021/cr1001222.
[22] S. Guo, N. C, L. J, L.C. T, Effect of valence electron concentration on stability of fcc or bcc phase in high entropy alloys, J. Appl. Phys. 109 (2011) 10.
[23] T. Rajasekharan, V. Seshubai, Charge transfer on the metallic atom-pair bond, and the crystal structures adopted by intermetallic compounds, Acta Crystallogr. A. 68 (2012) 156–165. doi:10.1107/S0108767311044151.
[24] C.-G. Zhan, J.A. Nichols, D.A. Dixon, Ionization Potential, Electron Affinity, Electronegativity, Hardness, and Electron Excitation Energy: Molecular Properties from Density Functional Theory Orbital Energies, J. Phys. Chem. A. 107 (2003) 4184–4195. doi:10.1021/jp0225774.
[25] R.G. Pearson, Absolute electronegativity and hardness correlated with molecular orbital theory, Proc. Natl. Acad. Sci. 83 (1986) 8440–8441. doi:10.1073/pnas.83.22.8440.
[26] D.G. Pettifor, A Quantum Mechanical Critique of the Miedema Rules for Alloy Formation, Solid State Phys. 40 (1987) 43–92.
[27] A. Savin, R. Nesper, S. Wengert, T.F. Fässler, ELF: The Electron Localization Function, Angew. Chem. Int. Ed. Engl. 36 (1997) 1808–1832. doi:10.1002/anie.199718081.
[28] M.E. Eberhart, The metallic bond: Elastic properties, Acta Mater. 44 (1996) 2495–2504. doi:10.1016/1359-6454(95)00347-9.
[29] B. Silvi, C. Gatti, Direct Space Representation of the Metallic Bond, J. Phys. Chem. A. 104 (2000) 947–953. doi:10.1021/jp992784c.
[30] A. Paxton, M. Methfessel, D.G. Pettifor, A bandstructure view of the Hume-Rothery electron phases, Proc. R. Soc. A. 453 (1997) 1493.
[31] D. Nguyen-Manh, A. Paxton, D.G. Pettifor, A. Pasturel, On the phase stability of transition metal trialuminide compounds, Intermetallics. 3 (1995) 9–14.
[32] D.G. Pettifor, The structures of binary compounds. I. Phenomenological structure maps, J. Phys. C Solid State Phys. 19 (1986) 285–313. doi:10.1088/0022-3719/19/3/002.
[33] S.I. Simdyankin, S.N. Taraskin, M. Dzugutov, S.R. Elliott, Vibrational properties of the one-component σ phase, Phys. Rev. B. 62 (2000) 3223–3231. doi:10.1103/PhysRevB.62.3223.
[34] L.H. Thomas, The calculation of atomic fields, Math. Proc. Camb. Philos. Soc. 23 (1927) 542. doi:10.1017/S0305004100011683.
[35] E. Fermi, Un metodo statistico per la determinazione di alcune priorieta dell'atome, Rend Accad Naz Lincei. 6 (1927) 32.
[36] N. Metropolis, J.R. Reitz, Solutions of the Fermi-Thomas-Dirac Equation, J. Chem. Phys. 19 (1951) 555. doi:10.1063/1.1748292.
[37] G.A. Salishchev, M.A. Tikhonovsky, D.G. Shaysultanov, N.D. Stepanov, A.V. Kuznetsov, I.V. Kolodiy, A.S. Tortika, O.N. Senkov, Effect of Mn and V on structure and mechanical properties of high-entropy alloys based on CoCrFeNi system, J. Alloys Compd. 591 (2014) 11–21. doi:10.1016/j.jallcom.2013.12.210.
[38] N.D. Stepanov, D.G. Shaysultanov, G.A. Salishchev, M.A. Tikhonovsky, E.E. Oleynik, A.S. Tortika, O.N. Senkov, Effect of V content on microstructure and mechanical properties of the CoCrFeMnNiVx high entropy alloys, J. Alloys Compd. 628 (2015) 170–185. doi:10.1016/j.jallcom.2014.12.157.
[39] H.P. Chou, Y.S. Chang, S.K. Chen, J.W. Yeh, Microstructure, thermophysical and electrical properties in Al x CoCrFeNi (0 ≤ x ≤2) high-entropy alloys, Mater. Sci. Eng. B. 163 (2009) 184–189.
[40] T.T. Shun, L.Y. Chang, M.H. Shiu, Microstructures and mechanical properties of multiprincipal component CoCrFeNiTix alloys, Mater. Sci. Eng. A. 556 (2012) 170–174.
[41] M.-H. Tsai, J.-W. Yeh, High-Entropy Alloys: A Critical Review, Mater. Res. Lett. 2 (2014) 107–123. doi:10.1080/21663831.2014.912690.

[42] P. Politzer, R.G. Parr, D.R. Murphy, Approximate determination of Wigner-Seitz radii from free-atom wave functions, Phys. Rev. B. 31 (1985) 6809–6810. doi:10.1103/PhysRevB.31.6809.
[43] B. Ren, Z.X. Liu, B. Cai, M.X. Wang, L. Shi, Aging behavior of a CuCr2Fe2NiMn high-entropy alloy, Mater. Des. 33 (2012) 121–126. doi:10.1016/j.matdes.2011.07.005.
[44] B. Zheng, Q.B. Liu, L.Y. Zhang, Microstructure and Properties of MoFeCrTiW High-Entropy Alloy Coating Prepared by Laser Cladding, Adv. Mater. Res. 820 (2013) 63–66. doi:10.4028/www.scientific.net/AMR.820.63.
[45] Y.J. Zhou, Y. Zhang, Y.L. Wang, G.L. Chen, Solid solution alloys of AlCoCrFeNiTi x with excellent room-temperature mechanical properties, Appl. Phys. Lett. 90 (2007) 181904. doi:10.1063/1.2734517.
[46] X.F. Wang, Y. Zhang, Y. Qiao, G.L. Chen, Novel microstructure and properties of multicomponent CoCrCuFeNiTix alloys, Intermetallics. 15 (2007) 357–362. doi:10.1016/j.intermet.2006.08.005.
[47] M.-R. Chen, S.-J. Lin, J.-W. Yeh, S.-K. Chen, Y.-S. Huang, C.-P. Tu, Microstructure and Properties of Al0.5CoCrCuFeNiTix (x=0–2.0) High-Entropy Alloys, Mater. Trans. 47 (2006) 1395–1401. doi:10.2320/matertrans.47.1395.
[48] L. Xie, P. Brault, A.-L. Thomann, J.-M. Bauchire, AlCoCrCuFeNi high entropy alloy cluster growth and annealing on silicon: A classical molecular dynamics simulation study, Appl. Surf. Sci. 285 (2013) 810–816. doi:10.1016/j.apsusc.2013.08.133.
[49] P. Koželj, S. Vrtnik, A. Jelen, S. Jazbec, Z. Jagličić, S. Maiti, M. Feuerbacher, W. Steurer, J. Dolinšek, Discovery of a Superconducting High-Entropy Alloy, Phys. Rev. Lett. 113 (2014). doi:10.1103/PhysRevLett.113.107001.
[50] Y. Zou, S. Maiti, W. Steurer, R. Spolenak, Size-dependent plasticity in an Nb25Mo25Ta25W25 refractory high-entropy alloy, Acta Mater. 65 (2014) 85–97. doi:10.1016/j.actamat.2013.11.049.
[51] S. Maiti, W. Steurer, Structural-disorder and its effect on mechanical properties in single-phase TaNbHfZr high-entropy alloy, Acta Mater. 106 (2016) 87–97. doi:10.1016/j.actamat.2016.01.018.
[52] O.N. Senkov, G.B. Wilks, J.M. Scott, D.B. Miracle, Mechanical properties of Nb25Mo25Ta25W25 and V20Nb20Mo20Ta20W20 refractory high entropy alloys, Intermetallics. 19 (2011) 698–706. doi:10.1016/j.intermet.2011.01.004.
[53] W. Kohn, L.J. Sham, Self-Consistent Equations Including Exchange and Correlation Effects, Phys. Rev. 140 (1965) A1133–A1138.
[54] M.C. Troparevsky, J.R. Morris, P.R.C. Kent, A.R. Lupini, G.M. Stocks, Criteria for Predicting the Formation of Single-Phase High-Entropy Alloys, Phys. Rev. X. 5 (2015). doi:10.1103/PhysRevX.5.011041.
[55] F. Kormann, D. Ma, D.D. Belyea, M.S. Lucas, C.W. Miller, B. Grabowski, H.F. Sluiter, “Treasure maps” for magnetic high-entropy-alloys from theory and experiment, Appl. Phys. Lett. 107 (2015).
[56] G. Trambly de Laissardière, D. Nguyen-Manh, D. Mayou, Electronic structure of complex Hume-Rothery phases and quasicrystals in transition metal aluminides, Prog. Mater. Sci. 50 (2005) 679–788. doi:10.1016/j.pmatsci.2005.01.001.
[57] D. Nguyen-Manh, V. Vitek, A.P. Horsfield, Environmental dependence of bonding: A challenge for modelling of intermetallics and fusion materials, Prog. Mater. Sci. 52 (2007) 52.
[58] S. Raimes, The rigid-band model, J. Phys. Radium. 23 (1962) 639–643. doi:10.1051/jphysrad:019620023010063901.
[59] E.A. Stern, Rigid-Band Model of Alloys, Phys. Rev. 157 (1967) 544–551. doi:10.1103/PhysRev.157.544.
[60] G. Liu, D. Nguyen-Manh, B.G. Liu, D.G. Pettifor, Magnetic properties of point defects in iron within the tight-binding-bond Stoner model, Phys. Rev. B. 71 (2005) 174115.

[61] D. Nguyen-Manh, S.L. Dudarev, Model many-body Stoner Hamiltonian for binary FeCr alloys, Phys. Rev. B. 80 (2009) 104440.
[62] S.L. Dudarev, P.M. Derlet, Interatomic potentials for materials with interacting electrons, J. Comput.-Aided Mater. Des. 14 (2008) 129.
[63] J.S. Wróbel, D. Nguyen-Manh, M.Y. Lavrentiev, M. Muzyk, S.L. Dudarev, Phase stability of ternary fcc and bcc Fe-Cr-Ni alloys, Phys. Rev. B. 91 (2015) 021408.
[64] C. Niu, A.J. Zaddach, A.A. Oni, X. Sang, J.W. Hurt, J.M. LeBeau, C.C. Koch, D.L. Irving, Spin-driven ordering of Cr in the equiatomic high entropy alloy NiFeCrCo, Appl. Phys. Lett. 106 (2015) 161906. doi:10.1063/1.4918996.
[65] M.S. Lucas, L. Mauger, J. Munoz, Y. Xiao, A.O. Sheets, S.L. Sematin, Magnetic and vibrational properties of high-entropy alloys, J. Appl. Phys. 109 (2011) 7.
[66] W.R. Wang, W.L. Wang, S.C. Wang, Y.C. Tsai, C.H. Lai, J.W. Yeh, Effects of Al addition on the microstructure and mechanical property of AlxCoCrFeNi high-entropy alloys, Intermetallics. 26 (2012) 44–51.
[67] D.G. Pettifor, Pressure-cell boundary relation and application to transition-metal equation of state, Commun. Theor. Phys. 1 (1977).
[68] O.K. Andersen, H.L. Skriver, H. Nohl, B.J. Johansson, Electronic structure of transition metal compounds; ground-state properties of the 3d-monoxides in the atomic sphere approximation, Pure Appl. Chem. 52 (1980) 93.
[69] G. Krier, O. Jepsen, A. Burkhardt, O.J. Andersen, The TB-LMTO-ASA program, Max-Planck-Institute für Festkörperforschung, 1994.
[70] A. Zunger, S. Wei, L. Ferreira, J. Bernard, Special quasirandom structures, Phys. Rev. Lett. 65 (1990).
[71] A.V. de Walle, T. P, J.M. de, O.D. L, A. M, D. A, S. D, W. Y, C. L, L. Z, C. M, Efficient stochastic generation of special quasirandom structures, Calphad - Comput. Coupling Phase Diagr. Thermochem. 42 (2013) 13–18.
[72] B. Cantor, I.T.H. Chang, P. Knight, A.J.B. Vincent, Microstructural development in equiatomic multicomponent alloys, Materials Science and Engineering A, Phys. Rev. B Condens. Matter. 375–377 (2004) 213–218.
[73] O.N. Senkov, G.B. Wilks, D.B. Miracle, C.P. Chuang, P.K. Liaw, Refractory high-entropy alloys, Intermetallics. 18 (2010) 1758–1765.
[74] I. Toda-Caraballo, J.S. Wróbel, S.L. Dudarev, D. Nguyen-Manh, P.E.J. Rivera-Diaz-del-Castillo, Interatomic spacing distribution in multicomponent alloys, Acta Mater. 97 (2015).
[75] D. Nguyen-Manh, D.G. Pettifor, Electronic structure, phase stability, and elastic moduli of AB transition metal aluminides, Intermetallics. 7 (1999).
[76] P. Villars, H. Okamoto, K. Cenzual, eds., ASM Alloy Phase Diagrams Database, ASM International, Materials Park, OH, 2006. http://www1.asminternational.org/AsmEnterprise/APD.
[77] Y. Zhang, Z.P. Lu, S.G. Ma, P.K. Liaw, Z. Tang, Y.Q. Cheng, M.C. Gao, Guidelines in predicting phase formation of high-entropy alloys, MRS Commun. 4 (2014) 57–62. doi:10.1557/mrc.2014.11.
[78] Y. Lu, Y. Dong, S. Guo, L. Jiang, H. Kang, T. Wang, B. Wen, Z. Wang, J. Jie, Z. Cao, H. Ruan, T. Li, A Promising New Class of High-Temperature Alloys: Eutectic High-Entropy Alloys, Sci. Rep. 4 (2014) 6200. doi:10.1038/srep06200.
[79] D.G. Pettifor, Theory of the Heats of Formation of Transition-Metal Alloys, Phys. Rev. Lett. 42 (1978) 846.
[80] G.M. Stocks, W.A. Shelton, D.M. Nicholson, F.J. Pinski, B. Ginatempo, A. Barbieri, B.L. Györffy, D.D. Johnson, J.B. Staunton, P.E.A. Turchi, M. Sluiter, Ordered Intermetallics — Physical Metallurgy and Mechanical Behaviour, in: C.T. Liu, R.W. Cahn, G. Sauthoff (Eds.), Springer Netherlands, Dordrecht, 1992: pp. 15–36. http://dx.doi.org/10.1007/978-94-011-2534-5_2.

[81] S. Lee, R. Hoffmann, Bcc and Fcc Transition Metals and Alloys: A Central Role for the Jahn−Teller Effect in Explaining Their Ideal and Distorted Structures, J. Am. Chem. Soc. 124 (2002) 4811–4823. doi:10.1021/ja0114557.
[82] J.C. Slater, Atomic Shielding Constants, Phys. Rev. 36 (1930) 57–64. doi:10.1103/PhysRev.36.57.
[83] E. Clementi, D.L. Raimondi, Atomic Screening Constants from SCF Functions, J. Chem. Phys. 38 (1963) 2686. doi:10.1063/1.1733573.
[84] J.H. Rose, J. Ferrante, J.R. Smith, Universal Binding Energy Curves for Metals and Bimetallic Interfaces, Phys. Rev. Lett. 47 (1981) 675–678. doi:10.1103/PhysRevLett.47.675.
[85] C. Zener, Analytic Atomic Wave Functions, Phys. Rev. 36 (1930) 51–56. doi:10.1103/PhysRev.36.51.
[86] M.S. Lucas, D. Belyea, C. Bauer, N. Bryant, E. Michel, Z. Turgut, S.O. Leontsev, J. Horwath, S.L. Semiatin, M.E. McHenry, C.W. Miller, Thermomagnetic analysis of FeCoCrxNi alloys: Magnetic entropy of high-entropy alloys, J. Appl. Phys. 113 (2013) 17A923. doi:10.1063/1.4798340.
[87] C. Kittel, Introduction to solid state physics, 8th ed, Wiley, Hoboken, NJ, 2005.
[88] K.-Y. Tsai, M.-H. Tsai, J.-W. Yeh, Sluggish diffusion in Co–Cr–Fe–Mn–Ni high-entropy alloys, Acta Mater. 61 (2013) 4887–4897. doi:10.1016/j.actamat.2013.04.058.
[89] B. Cantor, Multicomponent and High Entropy Alloys, Entropy. 16–19 (2014) 4749–4768.
[90] Y.-F. Kao, S.-K. Chen, T.-J. Chen, P.-C. Chu, J.-W. Yeh, S.-J. Lin, Electrical, magnetic, and Hall properties of AlxCoCrFeNi high-entropy alloys, J. Alloys Compd. 509 (2011) 1607–1614. doi:10.1016/j.jallcom.2010.10.210.
[91] W. Hume-Rothery, R.E. Smallman, C.W. Haworth, The Structure of Metals and Alloys, The Institute of Metals, Carlton House Terrace, London SW1Y 5DB, UK, 1988.
[92] D.G. Pettifor, Individual orbital contributions to the SCF virial in homonuclear diatomic molecules, J. Chem. Phys. 69 (1978) 2930.
[93] H.J. Jones, Concentrated solid solutions of normal metals, 23 (1962) Journal de Physique et le Radium.
[94] N. Christensen, O. Gunnarsson, O. Jepsen, O.J. Andersen, Local spin density theory for ferro- and antiferromagnetic materials, J. Phys. C. 8 (1988).

# 6. Tetragonal distortion of simple phases

"The interest I have to believe a thing is no proof that such a thing exists."
— Voltaire

| | |
|---|---|
| Objective | To explore alternative methods of predicting structural presence within multi-component alloys by simplifying the problem where applicable, while still retaining key concepts from quantum mechanics. |
| Hypothesis | The FCC, BCC and complex structures can be represented as a type of distorted tetragonal structure. The d-orbitals can be mapped out to real space from reciprocal space onto this distorted structure, allowing the energy of the structure to be quantified and different structures to be compared. |
| Analysis Type | Analytical (80%), Experimental (20%) |
| Variables | Alloy Composition, Alloy Structure, Valence Electron Concentration |
| Primary Result | Prediction of Stable Structures in HEAs |
| Techniques | Arc-Melting & Casting, XRD, Numerical Analysis |

## Table of Contents

## Symbols and Abbreviations

| | |
|---|---|
| $\delta r$ | Change in radius |
| $\delta r^+$ | Positive change in radius |
| $\delta r^-$ | Negative change in radius |
| $\delta r_{Dist.}$ | Change in radius resulting from a distorted tetragonal structure |
| $\delta r_d(d)$ | Normalised distance between the occupied d-orbital from $r_m$ |
| $\Delta D$ | Difference is the distance between the maximum and minimum distortion of the tetragonal structure from $r_m$ |
| $l$ | Effective quantum number |
| $\lambda$ | Thomas-Fermi screening length |
| $\varphi_{Slater}$ | Slater wavefunction |
| Å | Angstrom symbol |
| $\mathcal{H}$ | Hamiltonian |
| BCC | Body-centred cubic |
| BCT | Body-centred tetragonal |
| $e$ | Electron rest charge |
| $e_i$ | Energy of the quantised energy level |
| $g_i$ | Degeneracy of the energy level, $i$ |
| $E_{avg}$ | Average energy of a system of particles |
| $\overline{E_{del}}$ | Mean delocalisation of energy |
| $E_{ee}$ | Electron-electron interaction energy |
| $E_{en}$ | Electron-nucleus interaction energy |
| $E_K$ | Kinetic energy |
| $E_{Dist.}$ | Energy of the distorted tetragonal structure |
| $E_{Orbital}$ | Orbital energy |
| $\Delta E^X_{r_m}$ | Change in energy at $r_m$ for an atom X |
| $E_{Rose}$ | Potential energy of the valence electrons calculated using a modified Rose binding energy equation |
| $E_{Spin}$ | Energy associated with a change in spin satisfying the Pauli exclusion principle |
| $E_T$ | Total energy |

| | |
|---|---|
| $F_{FD}$ | Fermi-Dirac distribution |
| FCC | Face-centred cubic |
| $k_B$ | Boltzmann constant |
| $N_d$ | Number of d-electrons |
| $n$ | Valence electron concentration |
| $n_Q$ | Primary quantum number |
| $n(r_{ws})$ | Electron density at the Wigner-Seitz radius |
| r | Radius |
| $r_m$ | Fictitious mean radius |
| s | Screening constant |
| $\mu$ | Chemical potential |
| $V(r)$ | Potential energy at distance r |
| Z | Atomic number |

## Table of Figures

## 6.1 Chapter Preface

The structure of Chapter 6 can be loosely defined as a step-by-step presentation of the construction of a method to obtain the energy of a structural system (whether FCC, BCC or complex structures), and its application to the prediction of various phases of alloys of transition elements. The FCC, BCC, and complex structures are represented here by a distorted tetragonal system with different $c/a$ ratios of its axis. The hypotheses and subsequent corollaries gathered from the conclusions of the previous chapters are used extensively in the formulation of this prediction scheme.

The hypothesis tested in this chapter is:

> *The FCC, BCC and complex structures can be represented as a type of distorted tetragonal structure. Therefore, if the d-orbitals can be mapped out to real space from reciprocal space onto this distorted structure, the stability of the structures can be studied as a function of the filling of the d-orbitals.*

The verification is made with comparison to physical systems and the literature, where applicable, in order to confirm the accuracy and validity of the assumptions and corresponding results.

In Section 6.2.4, the stable structures of elemental Fe and Ni are predicted to verify the method; while in Section 6.2.5 a Fermi distribution is applied in order to demonstrate the interplay between the stability of Fe FCC and BCC allotropes as a function of temperature.

In Section 6.2.6, the FCC-BCC stability curve (*cf.* Figure 30) generated is compared to the RBA method described in Chapter 5, and also the Tight-Binding method used by Lee and Hoffman [81]. The incorporation of complex structures into this stability curve results in Figure 31 in Section 6.2.7, which is compared to the semi-empirical model as summarised utilising PCA described by Dominguez *et al.* [11].

Finally, in Section 6.28 the method is simplified and used to predict the structure of various CoCrFeNi-$A_x$ systems (where A = Al, Ti, V, Mo, and Pd), and CoCrFe-$V_x$, CoCrFe-$Ti_x$, and CoFeNi-$V_x$ systems. The predictions are confronted with the results of experimental XRD characterisation, and where applicable, predictions from the RBA model used in Chapter 5.

It is the aim of this Chapter to explore alternative methods of describing structural presence within multi-component alloys by simplifying the problem where applicable, while still retaining concepts from quantum mechanics. In doing so, the method described here will provide a strategy for a first-pass 'filter' of potentially good alloy compositions as a function of stoichiometry so that more advanced and accurate strategies can be employed to further study the system, such as robust ab-initio calculations.

The results of these compositions are in good agreement with their equivalent comparisons, and the final chapter will describe how the stability values described here can be applied to estimate some mechanical and functional properties of HEA compositions.

## 6.2 Experiment/Calculations

### 6.2.1 Distorted tetragonal cell: Construction of cell

From previous chapters, the simple structures present at valence electron concentration values $n > 7$, and $n < 6.5$ and the complex structures found between $6.5 < n < 7$ [11,22] are attributed to changes in the electronic structure. The different behaviour of complex structures from simple structures from the average electronegativity and electron density analyses in Chapter 4 suggests that some destabilisation mechanism occurs in the $6.5 < n < 7$ range, and that this mechanism is responsible for the stabilisation of the simple phases. To investigate the mechanism by which the energy levels of the simple FCC and BCC phases are kept constant, the body-centred tetragonal (BCT) structure is selected for analysis in this chapter. The FCC phase may be represented simply by a body-centred tetragonal (BCT) phase with $c/a = \left(\sqrt{2}\right)^1$, while the BCC phase is represented by a BCT phase with $c/a = \left(\sqrt{2}\right)^0$.

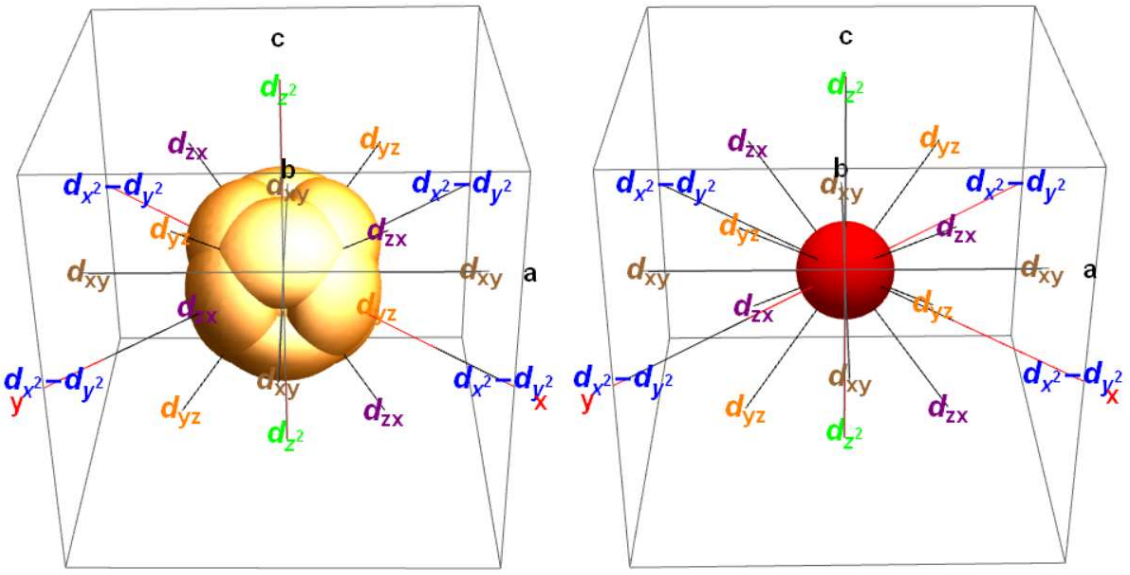


**Figure 23.1. (Left)** The figure shows the 5 d-orbitals combined, with the directions of the d-orbitals mapped into 3-d space. **(Right)** The directions of the d-orbitals are mapped into a tetragonal unit cell, with the d-orbital x and y axes shifted by 45° (relative to the a and b axes, which represent the unit cell axes), to bring the direction of the d-orbitals in line with the nearest neighbours. The nearest neighbours are not shown for clarity, but can be seen in Figure 23.2.

A $2 \times 2 \times 2$ supercell of both structures is constructed to obtain values of the interatomic distances between the nearest neighbours. The d-orbitals are the primary contributors to bonding in transition metals, and their preferred axes be mapped into the unit cell (*cf.* Table 10 for further explanation later in the chapter) by considering the structure only in its real-space coordinates as hard spheres. Figure 23.1 shows how these orbitals may be mapped onto a tetragonal unit cell by shifting the x and y axes by 45°. It is useful to emphasise that the d-orbitals are mapped to the neighbouring atoms to consider the effects of the d-orbital to d-orbital bonding (since when the unit cell is expanded into a supercell, the orbitals of each atom are assumed bond with each neighbour in the directions presented here).

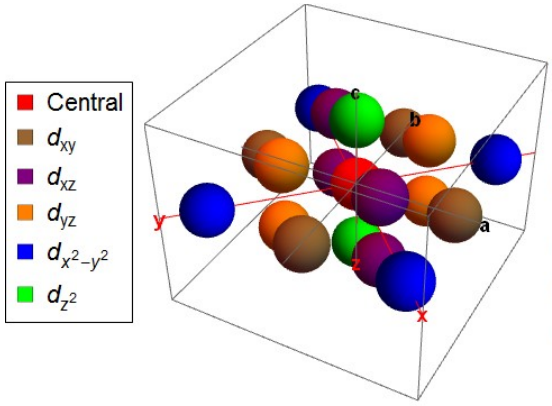


| d-orbital | Distance |
|---|---|
| $d_{x^2-y^2}$ | $\sqrt{2}$ |
| $d_{z^2}$ | $\frac{1}{\sqrt{2}}$ |
| $d_{xy}$ | 1 |
| $d_{xz}$ | 0.790569 |
| $d_{yz}$ | 0.790569 |

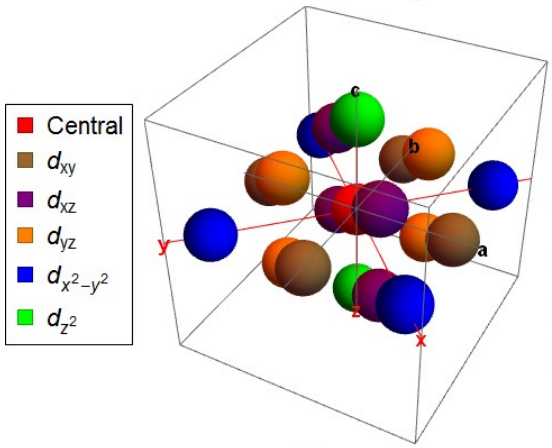


| d-orbital | Distance |
|---|---|
| $d_{x^2-y^2}$ | $\sqrt{2}$ |
| $d_{z^2}$ | 1 |
| $d_{xy}$ | 1 |
| $d_{xz}$ | 0.866025 |
| $d_{yz}$ | 0.866025 |

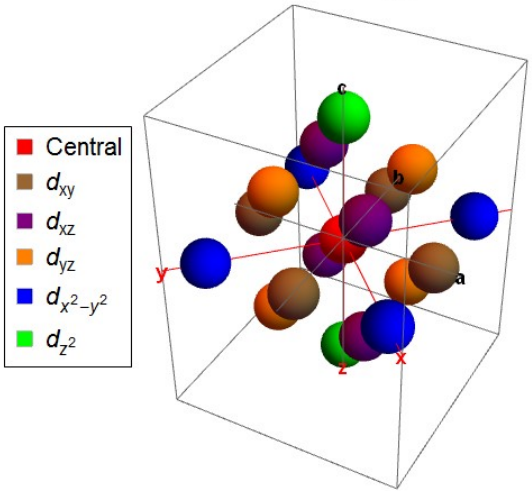


| d-orbital | Distance |
|---|---|
| $d_{x^2-y^2}$ | $\sqrt{2}$ |
| $d_{z^2}$ | $\sqrt{2}$ |
| $d_{xy}$ | 1 |
| $d_{xz}$ | 1. |
| $d_{yz}$ | 1. |

**Figure 23.2.** Atoms in a 2 x 2 x 2 tetragonal structure around a central atom, highlighted according to their assigned d-orbitals. The x-y-z and a-b-c axes are indicated in the figure for the ratios $\left(\sqrt{2}\right)^{-1}$, $\left(\sqrt{2}\right)^{0}$, and $\left(\sqrt{2}\right)^{1}$. (Bottom) The distance between the atoms in each assigned d-orbital are tabulated.

Figure 23 shows the selected closest neighbour atoms corresponding to several distorted BCT lattices with $c/a = \left(\sqrt{2}\right)^{-1}, \left(\sqrt{2}\right)^{0}, and\ \left(\sqrt{2}\right)^{1}$. As shown in Figure 23.2 (a), the x and y

directions are located at 45° to the a and b axis, while the z axis is defined as parallel to the c axis. The corresponding $d_{xy}$, $d_{yz}$, $d_{xz}$, $d_{x2-y2}$, and $d_{z2}$ orbitals have been labelled accordingly.

Since the average kinetic energy remains constant for a fixed temperature, changes in interatomic distance may be attributed to a change in only the potential energy, it is assumed here that the interatomic distance between the central atom and each denoted d-orbital is proportional to the change in bond energy. For purposes of this analysis we consider the electrons within a fixed 'frame' – that is, they are approximated as possessing directionality, occupying certain regions as per the spherical harmonics of Schrodinger's equation (*cf.* Chapter 2.8). The interatomic distances are normalised against the $d_{x^2-y^2}$ interatomic distance and presented in Figure 1 (d, e, f). At $c/a = \left(\sqrt{2}\right)^1$, presented in Figure 23.2 (f) the $d_{xy}, d_{xz}, and\ d_{yz}$ orbitals are observed to be $1/\sqrt{2}$ of the interatomic distance between the $d_{x2+y2}\ and\ d_{z2}$ orbitals. As the d-orbitals do not possess a similar interatomic distance, it may argued that the d-orbitals have been lifted from their five-fold degeneracy in the ground state, which will be located between the energy levels of the $d_{xy}, d_{xz}, and\ d_{yz}$, and $d_{x2+y2}\ and\ d_{z2}$ orbitals, within the $c/a = \left(\sqrt{2}\right)^1$ (FCC) distorted BCT structure. In order to proceed with analysis of the relative energy levels of the undistorted tetragonal lattice, the interatomic distance corresponding to the fivefold degenerate ground state must be defined.

Before the fivefold degenerate ground state is discussed in the following section, the cross-sections of the real d-orbitals are calculated and shown by substituting the radial part of the Schrodinger equation for a Slater-type orbital [82], using Clementi's constants [83], (*cf.* Table 10). Here, the distortion of the various d-orbitals to a less spherical shape is assumed to be an indication of reduced metallic character due to increased probability of orbital overlap between neighbouring atoms, and therefore increased bonding directionality. To obtain representative values of the different c/a ratios, the radius pertaining to each d-orbital is multiplied by the separation found from the previous analysis of the distorted tetragonal cell, as shown in Figure 23.2. The cross-sections across the yz and xz planes were observed to be similar and as such, only the cross-sections across the yz=xz and xy planes are shown below.

**Table 10.** Cross-sections along the x-y and y-z axis of the d-orbitals with different z/x ratios to represent the c/a ratios $(\sqrt{2})^{-1}$, $(\sqrt{2})^{0}$, and $(\sqrt{2})^{1}$ in a tetragonal structure. The shape of the d-orbitals are calculated using a Slater-type orbital [82] (*cf.* Eq. 2 below) using Clementi's constants [83] for the radial part of the Schrodinger equation. The y-z cross-section is equivalent to the x-z cross-section as the axis is constrained so that x=y.

| c/a | yz = xz | xy |
|---|---|---|
| $(\sqrt{2})^{-1}$ **(0.71)** | 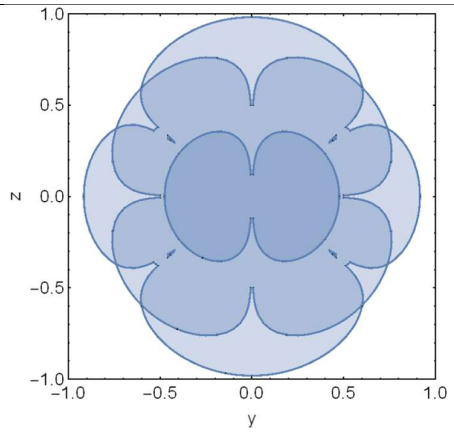  | 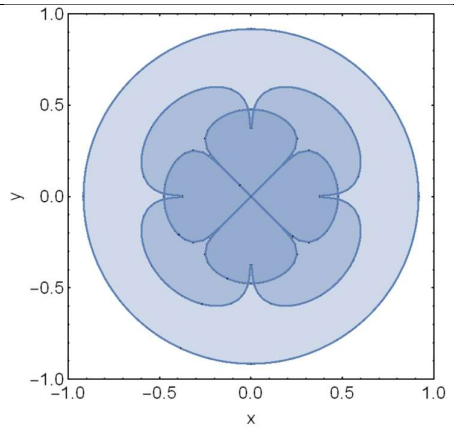  |
| $(\sqrt{2})^{0}$ **(1.00)** | 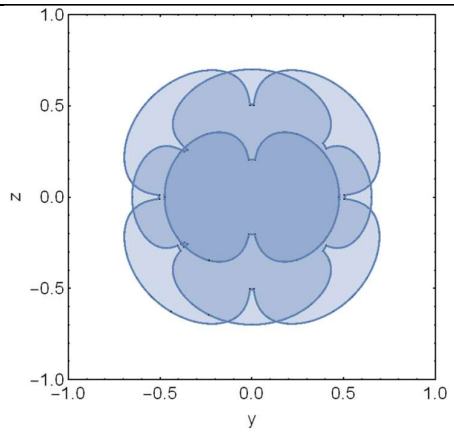  | 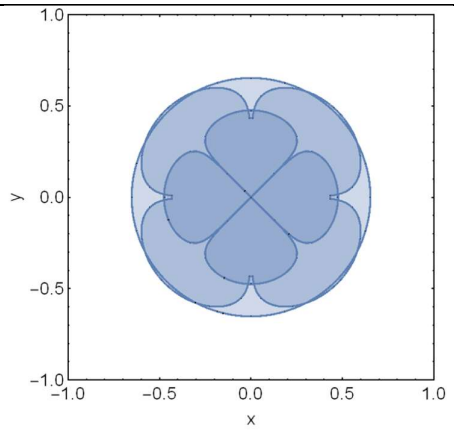  |
| $(\sqrt{2})^{1}$ **(1.41)** | 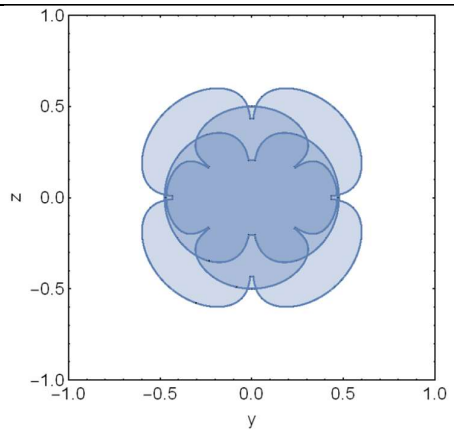  | 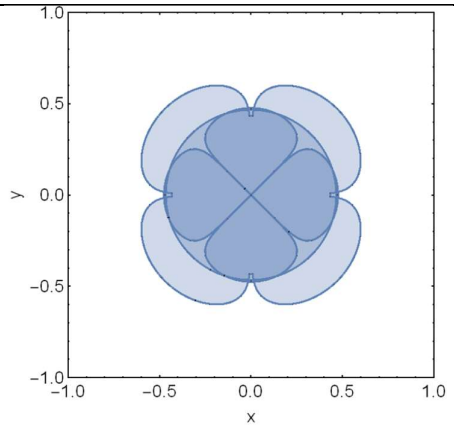  |

The cross-sections corresponding to the $c/a = \left(\sqrt{2}\right)^{0}$ and $\left(\sqrt{2}\right)^{1}$ ratios are found to be approximately spherical in nature (*cf.* Figure 24). Figure 24 presents a graph of the ratio of displacement between the radial distance between the xy and yz cross-sections. It is observed that between $0 < \theta < \frac{\pi}{4}$, the xy cross-section is observed to experience a large displacement along the z-axis. In contrast, when changing from a ratio of $c/a = \left(\sqrt{2}\right)^{1}$ to $c/a = \left(\sqrt{2}\right)^{0}$ the displacement between both the xy and yz cross-sections only rises above 5% between $0 < \theta < \frac{\pi}{8}$. The analysis performed here offers good agreement with the agreed properties of the more delocalised nature of the simple FCC and BCC structures, represented by the $c/a = \left(\sqrt{2}\right)^{1}$ and $c/a = \left(\sqrt{2}\right)^{0}$ ratios. The analysis suggests that a tetragonal distortion with $c/a = \left(\sqrt{2}\right)^{-1}$ possesses significant directional bonding in comparison to the other ratios, although this cannot be directly attributed to complex structures, such as how the FCC and BCC structures are represented by the other $c/a$ ratios. In the following sections, the discussion will first consider the possible phase presence of FCC and BCC structures in HEAs, as a function of a distorted tetragonal structure, before dealing with the justification of the $c/a = \left(\sqrt{2}\right)^{-1}$ representation of the complex structure.

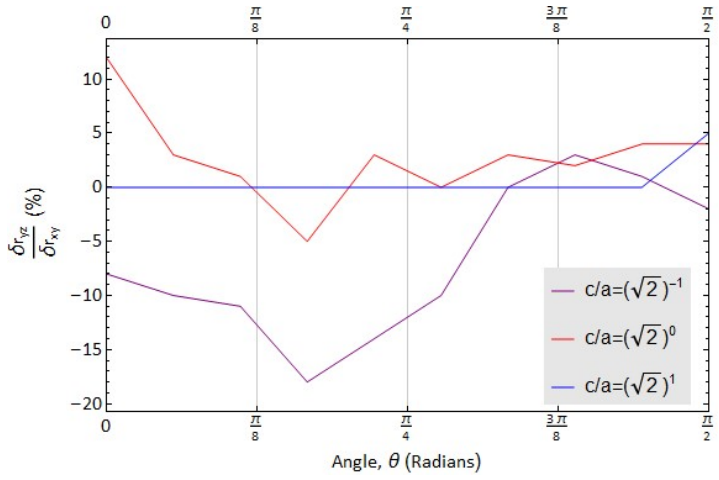


**Figure 24.** Ratio between the radius of the first quartile of the yz cross-section to the radius of the first quartile of the xy cross-section. For the $c/a = -\left(\sqrt{2}\right)^{-1}$ ratio, between $0 < \theta < \frac{\pi}{4}$, the xy cross-section is observed to experience a large displacement along the z-axis. In contrast, when changing from a ratio of $c/a = \left(\sqrt{2}\right)^{1}$ to $c/a = \left(\sqrt{2}\right)^{0}$ the displacement between both the xy and yz cross-sections only rise above 5% between $0 < \theta < \frac{\pi}{8}$.

### 6.2.2 Searching for the fivefold degenerate energy

The Ni FCC structure is used as the representative of simple transition metal structure in searching for the theoretical non-distorted energy. A simple 2-D potential plot of the energy against the radius is employed to determine the non-distorted energy. Figure 25 below shows the 4s and 3d orbital interatomic energies of Ni as a function of its radius, calculated using a modified version of the method of *Rose et al.* [84] with the general form:

$$E_{Rose} = -E_{Orbital}\,(1 + \beta\,\alpha^{*})e^{-\beta\,\alpha^{*}} \tag{1}$$

where $\beta$ is a fitting constant where $\beta = 1.16$ [84], $\alpha^{*} = \frac{2(r-r_m)}{\lambda}$ where $\lambda$ is the Thomas-Fermi screening length $\lambda = \left(\frac{9\pi}{4}\right)^{1/3}\left(\frac{4\pi\,\varphi_{Slater}(r_m)}{3}\right)^{1/6}$, $r$ is the radius and $r_m$ is the mean radius at which $\frac{d\varphi(r)^2}{dr} = 0$. The final parameters are related to orbital wavefunctions which here, are approximated from a Slater-type orbitals [82]; $E_{Orbital}$ is the orbital energy of the 4s and 3d orbitals which is the integral of $\varphi_{Slater}(r)$, the radial part of the Scrodinger wavefunction represented by a non-normalised Slater-type orbital given by the general form:

$$\varphi_{Sl} \quad (4s + 3d) = \sum_{4s+3d} r^{n_Q - 1} e^{-\frac{Z-s}{n_Q} r} \tag{2}$$

where $s$ is the atomic screening constant, $r$ is the radius, $Z$ is the atomic number, and $n_Q$ is the primary quantum number. The atomic screening constants are obtained from Clementi [83] where the effective atomic number, $l = Z - s$. The first and second neighbours as found in the previous section may be written as a function of Ni first nearest neighbour, $n1_{Ni}$, where $d_{xy}, d_{xz}, and\ d_{yz} = n1_{Ni}$, and $d_{x2+y2}\ and\ d_{z2} = \sqrt{2}\,n1_{Ni}$.

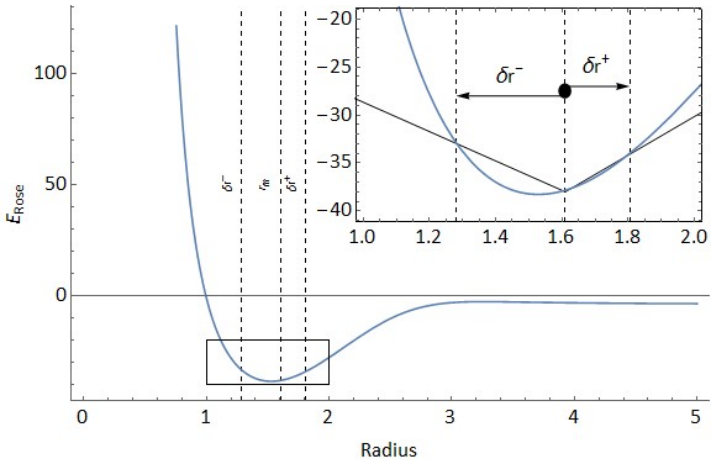


**Figure 25.** Plot of the potential for the valence electrons of FCC Ni. The energy-radius relationship here is obtained using a modified Rose binding energy equation [84] of FCC Ni's 4s and 3d valence orbitals (*cf.* Eq. 1). (Inset) Zoom-in to the change in radius, $\delta r^-$ and $\delta r^+$ from $r_m$ that is equivalent to the change in energy (*cf.* Eq. 3)

Consequently, as the Ni FCC cell possesses a lattice parameter of 3.6 Å, the first nearest neighbour distance may be calculated as $n1_{Ni} = \frac{3.6\ \text{Å}}{2\sqrt{2}} = 1.28\ \text{Å}$, and $n2_{Ni} = \sqrt{2}\, n1_{Ni} = 1.81\ \text{Å}$. These distances correspond to the predetermined distances between the atoms in each assigned d-orbital for a value of $\text{c/a} = \left(\sqrt{2}\right)^1$. The interatomic distance corresponding to the fivefold degenerate ground state, which may be considered to be a fictitious mean ratio, $r_m$ is located between $n1_{Ni} < r_m < n2_{Ni}$. The exact location is determined here as the point at which the sum of the change in energy between $r_m$ and the distorted d-orbitals is equivalent to zero and may be computed by considering the gradient of the potential shown in Figure 25. Mathematically, the first derivative of the potential with respect to change in radius, $\delta r$ can be solved for all increases ($\delta r^+$) and decreases ($\delta r^-$) to $r_m$. Here, the equation to be solved is:

$$\frac{\delta\, E^{3d}_{Rose}(n1_{Ni} - r_m)}{\delta r}(\delta r^-) = \frac{\delta\, E^{3d}_{Rose}(r_m - n2_{Ni})}{\delta r}(\,\delta r^+) \tag{3}$$

Solving for the above equation where $n1_{Ni} = 1.28$, and $n2_{Ni} = 1.80$ returns $r_m = 1.61$. These values are illustrated graphically in the inset of Figure 25. The difference in magnitude between $\delta r^-$ and $\delta r^+$ is attributed to the shape of the potential, where the slope of a negative displacement from $r_m$ is steeper than that of a corresponding positive

displacement. As a result, when normalised against the total displacement, $\delta r^- + \delta r^+$, the values $\delta r^- \cong 0.63\ (\delta r^- + \delta r^+)$ and $\delta r^+ \cong 0.37\ (\delta r^- + \delta r^+)$.

### 6.2.3 Distorted tetragonal cell: Effect of different c/a ratios

The d-orbitals from Figure 1 can now be analysed in terms of the theoretical fivefold degenerate energy, $r_m$ . For a FCC structure, the equivalent distorted BCT cell is at $c/a = \sqrt{2^1}$. The interatomic distances between the $d_{xy}, d_{xz}, d_{yz}, d_{x^2+y^2}\ and\ d_{z^2}$ orbitals can be shown as a function of $r_m$. Figure 26 (c) shows the BCT $c/a = \sqrt{2^1}$ cell where the red line denotes the undistorted energy determined from values of $\delta r^-$ and $\delta r^+$. From the earlier analysis, the normalised distance between the $d_{xy}, d_{xz}, \text{and } d_{yz}$ orbitals and $r_m$ is taken as $\approx \delta r^- = -0.6$ and $d_{x2+y2}\ and\ d_{z2}$ as $\delta r^+ \approx 0.4$. This is represented in Figure 26 as $\delta r^- \approx -\frac{0.18}{(0.12+0.18)}$ and $\delta r^+ \approx \frac{0.12}{(0.12+0.18)}$, respectively. The convention of the signs used represents either an increase (+) or a decrease in interatomic distance from $r_m$ (-).

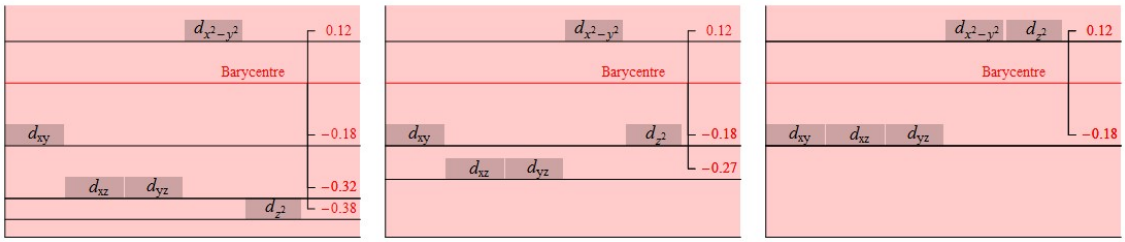


**Figure 26.** Normalised distance of the d-orbitals from determined value of $r_m$ for different ratios of (a) BCT $c/a = \sqrt{2^{-1}}$; (b) BCT $c/a = \sqrt{2^0}$; and (c) BCT $c/a = \sqrt{2^1}$

A contraction of the $c/a$ ratio affects the interatomic distance of the bonds along the length of the z axis, leading to a corresponding contraction in the interatomic distances of the d orbitals. At $c/a = \sqrt{2^0}$ it can be determined that as a consequence of the $c/a$ distortion the earlier degeneracy = 3 of $d_{xy}, d_{xz}, and\ d_{yz}$ orbitals and degeneracy = 2 of $d_{x^2+y^2}\ and\ d_{z^2}$ orbitals have been lifted so that the $d_{xz}, and\ d_{yz}$ interatomic distances have decreased, with respect to the $d_{xy}$ orbital. The ratio between the interatomic distances of the $d_{x^2-y^2}\ and\ d_{xy}$ orbitals (*c.f.* Figure 23.2) have remained unchanged, where $\frac{d_{x^2-y^2}}{d_{xy}} = \sqrt{2}$ and the relative position of $r_m$ with respect to these orbitals is expected to remain unchanged. Therefore, the normalised interatomic distance between the d-orbitals and $r_m$

for a distortion to $c/a = \sqrt{2}^{0}$ is -0.27 for $d_{xy}\ and\ d_{yz}$, -0.18 for $d_{xy}\ and\ d_{z2}$, and 0.12 for $d_{x2-y2}$.

Utilising a similar distorted tetragonal analysis, a contraction of the z axis so that $c/a = \sqrt{2}^{-1}$ leads to further breaking of the 2/2/1 d-orbital degeneracy at $c/a = \sqrt{2}^{0}$ so that the normalised interatomic distance between the d-orbitals and $r_m$ are now -0.38 for $d_{z2}$, -0.32 for $d_{xz}\ and\ d_{yz}$, -0.18 for $d_{xy}$, and 0.12 for $d_{x2-y2}$.

### 6.2.4 Distorted tetragonal cell: Energy levels

The energy of the distorted tetragonal cells may then be evaluated by invoking the Aufbau principle and the Pauli exclusion principle so that the most stable occupancy of the d-orbitals is obtained. In general, the energy of a many-electron system orbiting a nucleus consists of nucleus energy and the electron energy. The Born-Oppenheimer principle allows the energy of the nucleus to be separated into its nuclear and electronic components and as such the general form of the electronic energy may be written as (*c.f.* Chapter 2):

$$E_T = E_K + E_{en} + E_{ee} \tag{4}$$

where $E_K$ is the kinetic energy, $E_{en}$ is the electron-nucleus interaction energy, $E_{ee}$ is the electron-electron interaction energy. The total energy, $E_T$ may be obtained through several methods. In the following analysis the total energy that is, the energy required to remove all the atoms surrounding the nucleus to an infinite distance is given by [82,85]:

$$E_T(N) = \mathcal{H}(N) = \sum_{i=1}^{N=Z} -\left(\frac{Z-s}{n_Q}\right)^2 \tag{5}$$

where Z is the atomic number, s is the Clementi shielding constant [83], and $n_Q$ is the primary quantum number. In the model of the distorted tetragonal cell described here, the energy of the distorted cell is a function of the interaction between an energy change cause by a shift in interatomic distance and the energy associated with a change in spin satisfying the Pauli exclusion principle, $\Delta E_{Spin}$. It follows that the tetragonal distortion leads to a corresponding change in the potential energy of the electron so that:

$$V(r) = \frac{N_d\, e^2}{r} \tag{6}$$

Applying the Laplacian gives:

$$\nabla^2 V(r) = 4\,\pi e^2\, N_d\, dr \tag{7}$$

Since for $E_T(N)$, $\delta r(d) = 0$, the energy associated with the distortion from $r_m$, $E_{Dist.}$ is then:

$$E_{Dist.}(\delta r_{Dist.}, N_d) = \sum_{i=1}^{d_{1,2,3\ldots5}} (4\,\pi\,)(N_d\,)(\delta r_d(d))(\Delta D)\; + \sum_{i=1}^{N(\uparrow\downarrow)} \Delta E_{Spin}(N_d) \tag{8}$$

where $E_{Dist.}$ is given in terms of the $c/a$ orbital distortion, $\delta r_{Dist.}$ and the number of d electrons, $N_d$; the first term is the total energy given by the occupancy of each d-orbital ( $d_{1,2,3\ldots5} = d_{xy}, d_{xz}, d_{yz}, d_{x2+y2}\; and\; d_{z2}$ ) satisfying the Aufbau principle and Pauli exclusion principle with each orbital possessing energy $E_T(r_m, N).\,\delta r_{d.}$ where $\delta r_d(d)$ is the normalised distance between the occupied d-orbital from $r_m$. The second term arises from the energy required to change the sign of the electron spin to satisfy the Pauli exclusion principle. For easier calculation, $\delta r_{Dist.}$ is normalised so that $\frac{\delta r_{Dist.}}{\Delta D} = C$, where $\Delta D$ is the difference is the distance between the maximum and minimum distortion of the tetragonal structure from $r_m$ as determined in Figure 26, and C is a constant related to the ratio of the distortion of an orbital to $\Delta D$.

For 3d-block transition metal possessing 10 d-electrons, satisfying the Aufbau principle will lead to the condition where the energy of the fully filled distorted cell will be equivalent to the energy at $r_m$, i.e. where the total change in energy required to change the sign of the electron spin to satisfy the Pauli exclusion principle is equivalent to the sum of the change in energy required to distort the tetragonal structure by $\delta r_{Dist.} = C\;\Delta D$. Mathematically:

$$E_{Dist.}(\delta r_{Dist.}, 10) \approx E_T(10) \tag{9}$$

By substituting values for C from Figure 26, $E_T(10)$ for a tetragonal cell with $c/a = \sqrt{2}^1$ corresponding to an FCC structure is calculated:

$$4\,\pi[(6)(-0.6)(\Delta D) + (4)(0.4)(\Delta D)] + 5\;\Delta E_{Spin} = E_T(10) \tag{10}$$

Whereas for a tetragonal cell with $c/a = \sqrt{2}^0$ corresponding to a BCC structure,

$$4\,\pi[(4)(-0.5)(\Delta D) + (4)(-0.3)(\Delta D) + (2)(0.2)(\Delta D)] + 5\;\Delta E_{Spin} = \; E_T(10) \tag{11}$$

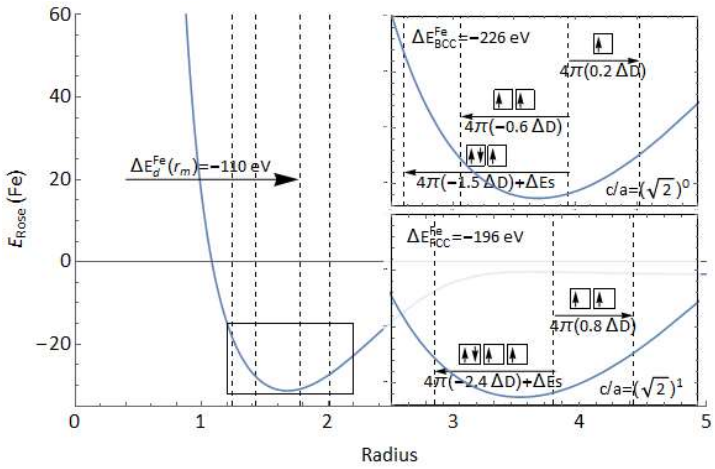


**Figure 27.** Plot of the potential for the valence electrons of Fe obtained using a modified Rose binding energy equation [84] of Fe's 4s and 3d valence orbitals (*cf.* Eq. 1), with the value for the energy at $r_m$, $\Delta E_{r_m}^{Fe}$ indicated. (Inset: Top) Zoom-in to the electron occupancy of the hypothesised distorted d=orbitals for the BCC structure where c/$a = \left(\sqrt{2}\right)^0$ ; and (Inset: Bottom) Zoom-in to the electron occupancy of the hypothesised distorted d-orbitals for the FCC structure where $/a = \left(\sqrt{2}\right)^1$.

Therefore, solving for Ni at $N_d = 10$, the following is obtained:

$$\Delta E_{Spin}^{Ni-FC}\ (N_d) = 43.28\ eV,\ \Delta E_{Spin}^{Ni-B}\ \ (N_d) = 76.22\ eV \tag{12}$$

While solving for Fe at $N_d = 10$, the values are:

$$\Delta E_{Spin}^{Fe-F}\ \ (N_d) = 35.98\ eV,\ \Delta E_{Spin}^{Fe-BC}\ (N_d) = 63.15\ eV \tag{13}$$

It must first be noted that these values in eV cannot be considered to be the exact energy values of the system studied as the full potential is not used, and no attempt was made to solve any of the equations central to quantum mechanics to obtain the ground-state energies. The values here may, however, be used as a comparison of the relative stability of the structures in a distorted tetragonal system. Values of $\Delta E_{Spin}^{Ni-BCC}$, and $\Delta E_{Spin}^{Fe-F}$ are considered unphysical as the Ni and Fe system does not adopt these phases at the ground state. These approximated $E_{Spin}$ values are still, however, in agreement with the empirical parameters predicted by Dominguez *et al.* [11] where the FCC structure is present at $7 < VEC < 10$ and the BCC structure is present at $5 < VEC < 7$ since the spin energies for FCC are lower than that for the BCC at $N_d = 10$, and hence in terms of stability $\Delta E_{Spin}^{FCC}(N_d)$

>$\Delta E_{Spin}^{BCC}(N_d)$. Figure 27 shows the energy-radius curve for Fe, $E_{Rose}(Fe)$ and the various energy levels of the d-orbitals are indicated with the dashed lines. As all approximated values of $E_{Spin} > \Delta E_{r_m}^{Fe}$, in fulfilling the Aufbau principle all available d-orbitals must be filled with an electron before the Pauli principle is invoked. In calculating the physical example of Fe with 6 d-electrons $N_d$=6, the inset of Figure 27 (Top), presents the electron occupancy for $c/a = \left(\sqrt{2}\right)^0$ representing the BCC structure and Figure 27 (Bottom), presents the electron occupancy for $c/a = \left(\sqrt{2}\right)^1$ representing the FCC structure. At $N_d$=10, $\Delta E_d^{Fe}(10) = \Delta E_{r_m}^{Fe} = -110\ eV$, as discussed earlier. However, for $\Delta E_{BCC}^{Fe}(6)$ the energy levels are seen to lower to $\Delta E_{BCC}^{Fe}(6) = -266\ eV$. A corresponding decrease is found for $\Delta E_{FCC}^{Fe}(6) = -196\ eV$. Of these, $\Delta E_{BCC}^{Fe}(6)$ is lower in energy and therefore the more stable structure at $N_d$=6 for Fe. This is the correct physical structure for Fe at 0 K.

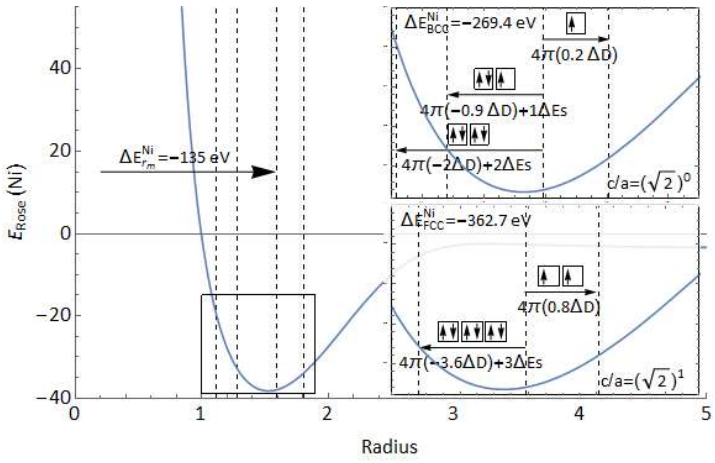


**Figure 28.** Plot of the potential for the valence electron of Ni obtained using a modified Rose binding energy equation [84] of Ni's 4s and 3d valence orbitals (*cf.* Eq. 1), with the value for the energy at $r_m$, $\Delta E_{r_m}^{Fe}$ indicated. (Inset: Top) Zoom-in to the electron occupancy of the hypothesised distorted d-orbitals for the BCC structure where $/a = \left(\sqrt{2}\right)^0$ ; and (Inset: Bottom) Zoom-in to the electron occupancy of the hypothesised distorted d-orbitals for the FCC structure where $c/a = \left(\sqrt{2}\right)^1$.

Figure 28 shows a similar analysis for the physical Ni system, with $N_d$=8, displaying the energy-radius curve for Ni, $E_{Rose}(Ni)$ and the various energy levels corresponding to the d-orbitals indicated again with dashed lines. For Ni, $\Delta E_{r_m}^{Ni} = -135\ eV$, and obtained values of $\Delta E_{BCC}^{Ni}(8) = -269.4\ eV$ and $\Delta E_{FCC}^{Fe}(8) = -362.7\ eV$, showing that the lower energy value of $\Delta E_{FCC}^{Fe}$ is responsible for the stability of the FCC structure at 0 K for Ni.

### 6.2.5 Distorted tetragonal cell: Allotrope of Fe (BCC->FCC)

The analyses performed in the preceding sections are performed on a system at 0K. As a system increases in temperature, the average energy, $E_{avg} = k_B\, T$ according to the equipartition theorem where $k_B$the Boltzmann constant, and T is is the temperature in Kelvin. An increase in temperature therefore leads to a corresponding increase in $E_{avg}$. The distribution of a system of identical fermions that can be distinguished may be described using Fermi-Dirac statistics which take the form of:

$$F_{FD} = \frac{1}{e^{E/(k_B\, T)}+1} \tag{14}$$

where $F_{FD}$ denotes the Fermi-Dirac distribution, $E$ denotes a general energy term, $k$ the Boltzmann constant, and $T$ the temperature in Kelvin. However, $F_{FD}$ does not account for the energy sensitivity of the degenerate $d_{xy}, d_{xz}, d_{yz}, d_{x2+y2}, or\ d_{z2}$ orbitals that is dependent on the potential of the d-orbital.

An increase in temperature in the system leads to a change in the distribution of the electrons represented by $F_{FD}$. As a result, the mean radius of the d-orbital electrons may be shifted to a different energy level. This change in radius is shown graphically in Figure 29 and may be given by:

$$r(E + \delta E) = r(E) + r(\delta E) \tag{15}$$

Assuming continuous stability of the distorted tetragonal lattice, the relative position of the degenerate energy orbitals must be constrained such that for $c/a = \left(\sqrt{2}\right)^1$ representing the FCC structure, the radius of the lowest energy orbital corresponds to the nearest neighbour distance, $n1$, the next lowest orbital corresponds $(1.41)(n1)$ as determined from the early analysis of the distorted tetragonal cell. Similarly, for $c/a = \left(\sqrt{2}\right)^0$ representing the BCC structure the radius of the d-orbitals correspond to the nearest neighbour distance, $n1$, for the lowest energy d-orbital, $n1/0.87$, and $1.41(n1/0.87)$ for the highest energy level corresponds. The change in energy can only therefore result in a limited distortion of the radius, $\delta r$ depending on the existing energy level of the d-orbital at a radius, $r$ which satisfies the wavefunction, $\varphi$, given by Schrodinger's equation. Therefore the sensitivity of the change in energy is:

$$A_{n1}\,\frac{E(r+\delta r)}{E(r)} = A_{n1}\left(\frac{E(r)}{E(r)} + \frac{\delta E(\delta r)}{E(r)}\right) = A_{n1}\left(1 + \frac{\delta E(\delta r)}{E(r)}\right) \tag{16}$$

where $A_i$ is a constant related to the first nearest neighbour distance. When $E(r) \gg E(\delta r)$, $1 + \frac{E(\delta r)}{E(r)} \approx e^{\frac{E(\delta r)}{E(r)}}$ and therefore:

$$\frac{\overline{E_{del}}}{A_{n1}} = e^{\frac{1}{n_i}\sum_i \frac{E(\delta r)}{E(r)}} \tag{17}$$

where $\overline{E_{del}}$ represents the mean delocalisation of energy that is attributed to a state, $i$, where $i = FCC\ or\ BCC$, and $n_i$ represents the number of energy levels in the system $i$; i.e. $n_{FCC} = 2$ and $n_{BCC} = 3$. The probability of finding an electron is then reduced by this averaged delocalisation of energy such that:

$$F_{FD} = \frac{A_{n1}}{\left(e^{\frac{E-(k_B\,T)(Log(\overline{E_{del}}))}{(k_B\,T)}}\right)+e^{-(Log(\overline{E_{del}})}} \tag{18}$$

where $(k_B\,T)(Log(\overline{E_{del}}) = \frac{k_B\,T}{n_i}\sum_i \frac{E(\delta r)}{E(r)}$ is the rate of change of the average delocalisation of energy of a state, $i$, to the temperature, $T$.

Since $\left(e^{\frac{E-(k_B\,T)(Log(\overline{E_{del}}))}{(k_B\,T)}}\right)\left(\frac{1}{e^{-(Log(\overline{E_{del}})}}\right)$ reduces to $e^{E/(k_B\,T)}$, Equation 18 may be re-written for a trial FCC system with phase X as:

$$F_{FD}^{X} = \frac{(A_{n1})(\overline{E_{del}})}{(e^{E/(k_B\,T)})+1} = \frac{(A_{n1})\left(\overline{E_{del}}^{X}\right)}{\left(e^{\Delta E_{Fe}^{X}/(k_B\,T)}\right)+1} \tag{19}$$

Combining the two equations, the stability between the BCC structure demonstrated by a distorted tetragonal cell, $c/a = \left(\sqrt{2}\right)^0$ and the FCC structure represented by a distorted tetragonal cell, $c/a = \left(\sqrt{2}\right)^1$ of a trial Fe system may therefore be given by:

$$F_{FD}^{BCC-FCC}(Fe) = A_{n1Fe}\left(F_{FD}^{BCC}(Fe) - F_{FD}^{FCC}(Fe)\right), \tag{20}$$

$$F_{FD}^{BCC-FCC}(Fe) = A_{n1Fe}\left(\frac{\overline{E_{del}}^{BCC}}{e^{\Delta E_{Fe}^{BCC}/(k_B\,T)}+1} - \frac{\overline{E_{del}}^{FCC}}{e^{\Delta E_{Fe}^{FCC}/(k_B\,T)}+1}\right) \tag{21}$$

Interestingly, the general form of $F_{FD}$ described here using the Fermi-Dirac distribution (*cf.* Equation 19) can be compared with the microcanonical ensemble of the Fermi-Dirac distribution:

$$F_{FD} = \frac{g_i}{e^{(e_i-\mu)/(k_B T)}+1} \tag{22}$$

where $g_i$ is the degeneracy of the energy level, $i$; $e_i$ is the energy of the quantised energy level, and $\mu$ is the chemical potential. The difference between the microcanonical ensemble form of the Fermi-Dirac distribution and $F_{FD}^{X}$ used in this analysis is that $\overline{E_{del}}$ is estimated through a perturbation of the radius of each of the degenerate energy levels of the corresponding distorted tetragonal structure corresponding to the FCC and BCC structures as a function of the first nearest neighbour distance given by the constant $A_{n1}$, rather than being a directly calculated value. The relationship between each $d_{xy}, d_{xz}, d_{yz}, d_{x2+y2}\ and\ d_{z2}$ orbital energy level and $A_{n1}$ is obtained from analysis in the preceding sections.

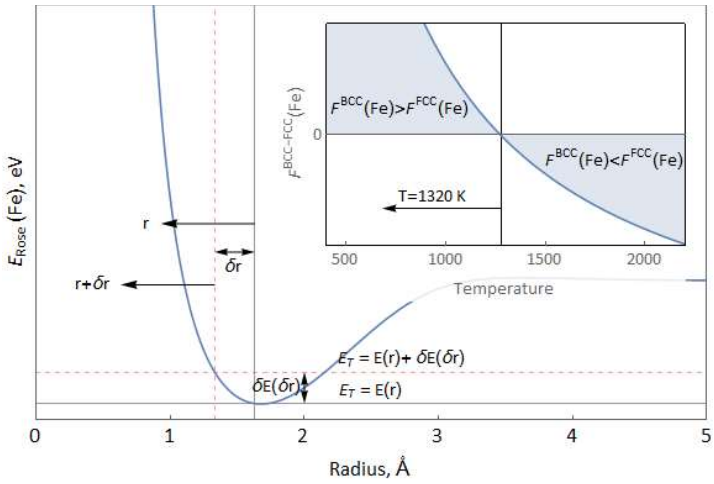


**Figure 29.** Plot of the potential for the valence electron of Fe obtained using a modified Rose binding energy equation [84] of Ni's 4s and 3d valence orbitals (*cf.* Eq. 1). The black line illustrates the total energy at a radius r, $E_T = E(r)$ while the dotted red line illustrates the perturbation of the radius by $\delta r$ so that $E_T = E(r) + \delta r$. (Inset) Plot of $F_{FD}^{FCC-BCC}(Fe)$ as a function of temperature showing the BCC phase stabilised at T < 1320K, and the FCC phase stabilised at T > 1320K.

Figure 29 shows the change in energy as a function of a perturbation of the radius, $r$ to $r + \delta r$. The inset of Figure 29 shows a plot of the earlier derived $F_{FD}^{BCC-FCC}(Fe)$ equation as a function of the temperature, $T$ in Kelvin. It is only possible for $F_{FD}^{BCC-FCC}(Fe) > 0$

when $F_{FD}^{BCC} > F_{FD}^{FCC}$ and conversely, for for $F_{FD}^{BCC-FCC}(Fe) < 0$ when $F_{FD}^{BCC} < F_{FD}^{FCC}$. As shown in the inset the transition between both phases occurs when the occupancy rate of both states are equivalent to one another, $F_{FD}^{BCC} = F_{FD}^{FCC}$, at which $T = 1320K = 1047°C$, which is in reasonable agreement with the transition temperature to austenite Fe at $912°C$.

### 6.2.6 General stability between the FCC and BCC structures as a function of the d-electron number

In the above sections, it has been demonstrated that in the comparison of the energies of the FCC and BCC phases as a function of a distorted tetragonal structure with different $c/a$ ratios, the BCC structure is stable at 0K for Fe, and the FCC structure is stable at 0 K for Ni. The average delocalisation of energy of the d-orbitals has been shown to be obtainable through a perturbation of $E_{Rose}$, predicting a FCC to BCC transition value for Fe (1320 K) that is in good agreement with the experimental value (1180K).

In this section, the distorted tetragonal structure analysis is employed to attempt to distinguish between FCC and BCC phase stability as a function of the d-electron count. The energy difference between both phases is:

$$E_{Dist.}^{FCC-BCC} = E_{Dist.}^{FCC}(\delta r_{Dist.}, N_d) - E_{Dis\ .}^{BCC}(\delta r_{Dist.}, N_d) \tag{23}$$

As the spin-orbit contribution is unique for each number of d-electrons, $N_d = 1, 2, 3 \ldots 10$, the second term, $\sum_{i=1}^{N(\uparrow\downarrow)} \Delta E_{Spin}(N_d)$ from $E_{Dist.}^{FCC}$ and $E_{Dist.}^{BCC}$ (*cf.* Eq. 8) cancel out, and the Eq. 23 can be written as:

$$E_{Dist.}^{FCC-B} \quad (N_d) = (4\,\pi\,) \begin{pmatrix} \sum_{i=1}^{d_{1,2,3\ldots5}} \left(\frac{N_d.\delta r_d(d)}{\Delta D^{BCC}}\right)(\Delta E^{FCC}) \\ -\sum_{i=1}^{d_{1,2,3\ldots5}} (N_d\,) \left(\frac{N_d.\delta r_d(d)}{\Delta D^{FCC}}\right)(\Delta E^{BCC}) \end{pmatrix} \tag{24}$$

Referring to the results of Chapter 4, simple and complex HEA phases were found to be separated in a two-dimensional plot of the electron density and the Wigner-Seitz radius. The Hohenberg-Kohn theorems state that the total energy of any system acting under an external potential may be described as a function of its electron density. As the simple phases are found in the previous analysis to scale with the Wigner-Seitz radius irrespective of FCC or BCC structure, we can write:

$$\frac{\Delta E_T^{BCC}}{\Delta E_T^{FCC}} \approx \frac{n(r)^{BCC}}{n(r)^{FCC}} = \frac{N^{BCC}}{N^{FCC}} \frac{V(\delta r^{FCC})}{V(\delta r^{BCC})} \tag{25}$$

By assuming that the number of electrons remains constant, the ratio of the total energy of the BCC structure to the FCC structure, as shown in Eq. 25, can simply be taken as the cube of the ratio between the nearest neighbour distance of the FCC and BCC structure obtained from analysis of the distorted tetragonal structure. For $c/a = \left(\sqrt{2}\right)^0$ these values correspond to $n1_{BCC} = r$ and $n2_{BCC} = \left(\frac{2}{3}\right)^{1/3} r$. Hence $\Delta E_T^{BCC}$ may be written in terms of $\Delta E_T^{FCC}$:

$$\Delta E_T^{BCC} \approx \frac{2}{3} \Delta E_T^{FCC} \tag{26}$$

and Equation 24 is now:

$$E_{Dist.}^{FCC-BCC}(N_d) = (4\,\pi) \begin{pmatrix} \sum_{i=1}^{d_{1,2,3\ldots5}} (N_d) \left(\frac{\delta r_d(d)}{\Delta D^{BCC}}\right) (\Delta E^{BCC}) \\ -\sum_{i=1}^{d_{1,2,3\ldots5}} (N_d) \left(\frac{\delta r_d(d)}{\Delta D^{FCC}}\right) (\frac{2}{3} \Delta E_T^{FCC}) \end{pmatrix} \tag{27}$$

The Aufbau and Pauling principles are then employed to determine the filling of the d-orbitals, allowing $E_{Dist.}^{FCC-B}$ to be shown as a function of the number of valence electrons. Figure 30 presents a plot of $E_{Dist.}^{FCC-B}$ against $N_d$ where $E_{Dist.(3d)}^{FCC-BCC}$ is shown by the black, dashed line. This is similar in magnitude to $E_{Dist.(3d\,4s)}^{FCC-BCC}$ but diverges past $N_d = 8$. The $E_{Dist.(3d)}^{FCC-BCC}$ curve shows that the BCC phase represented by $c/a = \left(\sqrt{2}\right)^0$ is stable between roughly $4 < N_d < 7$ and $N_d > 8.5$; while the FCC phase represented by a tetragonal distortion of $\left(\sqrt{2}\right)^1$ is stable between $N_d < 4$ and $7 < N_d < 8.5$. Comparison between these predicted values and $E_{Spin-band}^{FCC-B}$ obtained through the Rigid Band Approximation performed in Chapter 5 is acceptable, up to $N_d = 8$ whereby $E_{Dist.(3d)}^{FCC-BCC}$ diverges into the BCC-stable region. This prediction by $E_{Dist.(3d)}^{FCC-BCC}$ is unphysical as known compositions such as Ni $(N_d = 8)$, Cu $(N_d = 9)$, and Ag $(N_d = 9)$ possess the FCC structure at room temperature. Furthermore, HEA compositions such as CoCrFeNiPd [65,86] $(N_d = 8.25)$ and its stochiometries possess the FCC phase as well. One reason for the deviation may be the s-d orbital hybridisation that occurs. It is well-known that Cu, despite possessing fewer electrons than required to obtain a closed-shell structure for the s and d orbitals, possesses a d10 configuration; which is not exclusive to Cu but applies to Group 11 of the periodic

table. A reasonable hypothesis is that the increase in energy from d-orbital filling favours a hybridised 3d-4s orbital to decrease the total energy of the system. This hypothesis is consistent with this study, which argues that splitting of orbitals can be mapped onto the closest neighbours in a distorted tetragonal structure and can affect the overall energy of the system, leading to the energetical preference of one structure over another.

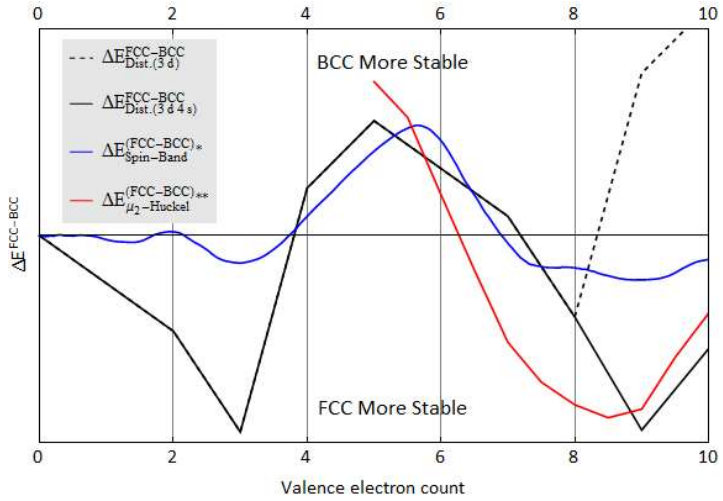


**Figure 30.** Plot of the FCC-BCC energy difference calculated using a 3d distorted tetragonal structure, $E_{Dist.(3d)}^{FCC-BCC}$; 4s 3d distorted tetragonal structure, $E_{Dist.(3d\ 4s)}^{FCC-BCC}$; using the RBA methodology from Chapter 4, $E_{Spin-Band}^{FCC-B}$; and adapted from Lee and Hoffman's tight binding model [81], $E_{\mu 2-Hu}^{FCC-BCC}$ .

A naïve approximation to simulating this criterion is to allow for an additional energy level between $\delta r_d(min)$ and $r_m$ for two additional electrons, which will cause a decrease in energy, stabilising the system. In Figure 30, $E_{Dist.(3d\ 4s)}^{FCC-BCC}$, the black solid line represents this approximation, where the application of this correction brings the deviation of $E_{Dist.(3d)}^{FCC-BCC}$ for $N_d > 8.5$ back to agreement with experimental results, and the predicted zones of FCC and BCC stability as determined from Dominguez *et al.'s* work [11]. It is observed from the $E_{Dist.(3d\ 4s)}^{FCC-BCC}$ curve that the FCC structure is found to be stable up to $VEC = 7.2$ while the BCC structure is stable between $3.8 < VEC < 7.2$. In comparison to the RBA-derived curve, $E_{Spin-Ban}^{FCC-BCC}$ shown also in Figure 30, the FCC structure is found to be stable up to $VEC = 7$ while the BCC structure is stable between $3.8 < VEC < 7$. Both analyses of the FCC-BCC stability are comparable and are in good agreement with one another.

As discussed in Chapter 5, the RBA model calculates the structural stability utilising ab-initio methods where the atomic positions can be constrained to a periodic lattice group, based on Bloch's theorem [87], to obtain the electronic band structure from which the total energies of the structure can be obtained. The RBA generates the FCC-BCC stability curve by assuming that the energy curves and density of states of a solvent metal do not change on alloying [58,59]. In this method, it is approximated that on alloying, the effect of the solute metal is to modify the occupancy of the electrons in the electronic band structure, so changing the Fermi surface and filling of the density of states to a new equilibrium energy. In this way, the structural stability between the FCC and BCC simple structures can be obtained by subtracting the energy curves from one another, and represented simply as a function of the averaged number of electrons present in the periodic lattice group, or some representation thereof such as a disordered structure generated using the Special Quasirandom Structure method (SQS) [70].

In contrast, the distorted tetragonal method described and presented in this chapter considers the structure as a function of an axial distortion of a tetragonal lattice. This distortion leads to a change in the corresponding energy levels of the d-orbitals that are mapped onto the tetragonal lattice in real space, so modifying the energy occupancy from an undistorted tetragonal structure where $a = b = c$, thus changing the fivefold degeneracy of the d-orbital. The energy level of a distorted structure as a function of the number of d-electrons is then dependent on the Aufbau and Pauling principles as a function of the spin and occupancy energies. The structural stability is then obtained by subtracting the energy levels of distorted structures representing the FCC and BCC structures.

It can be seen that stability values derived from both the RBA and distorted tetragonal methods are dependent on obtaining the difference in the energy levels of the competing structures. While the RBA method searches for the electronic energy difference based on the changing occupancy at the density of states, the distorted tetragonal method obtains the energy difference by making an *a posteriori* determination of the relationship between the degree of distortion of a tetragonal structure and the phase present as a function of possible d-orbital degeneracy. This relationship is then used to predict phase presence for all future compositions as a function of the valence electron concentration. Although theoretical analysis from quantum mechanical principles on this d-orbital degeneracy is not

performed here, comparison between both methods and their good agreement strengthens the value of the assumptions made in the construction of the distorted tetragonal structure approach.

Furthermore, a similar approach was reported by Lee and Hoffman [81], who suggest that the FCC-BCC competition in transition metals may be described by a Jahn-Teller like distortion, similar to that exhibited by molecular compounds. They construct an energy function to test this hypothesis using an ab-initio tight-binding method. For comparison, in Figure 30 the red line represents the results of this energy difference, $E_{\mu 2-Huckel}^{FCC-BCC}$. The minimum of $E_{\mu 2-Huckel}^{FCC-BCC}$ is observed to be at $VEC = 8.5$ while the maximum is observed to be at $VEC = 5$ while the transition where $E_{\mu 2-Huckel}^{FCC-BCC} = 0$ is observed at $VEC = 6.2$. $E_{Dist.(3d\ 4s)}^{FCC-BCC}$ shows the minimum to be at $VEC = 9$, the maximum to be at $VEC = 5$, and the transition point to be at $VEC = 7.2$. Overall, the results of $E_{\mu 2-Huckel}^{FCC-BCC}$ are in excellent agreement with $E_{Dist.(3d\ 4s)}^{FCC-BCC}$ where it is emphasised again that the energy difference is approximated from the interatomic distance between neighbouring atoms of the distorted tetragonal structure, allowing for faster 'back of the envelope' type solutions that can be employed for alloy design.

### 6.2.7 Extension of theory to predict HEA systems

In the earlier sections, a methodology to describe the FCC and BCC structure in terms of a distorted tetragonal structure was developed and described. Following that, the method was used to analyse the stability of Fe and Ni at 0K, and furthermore predict the FCC-BCC transition between two allotropes of Fe. All predictions were found to be well-grounded in reality. The method was then further generalised to describe the FCC-BCC phase stability as a function of the number of d-electrons, which was shown to be in agreement with the earlier chapters utilising the Thomas-Fermi-Dirac model and the Rigid-Band Approximation, while also being in agreement with predictions from literature [11,81]. In this section, a method for predictions of the stable phases of HEA alloys and some of their properties will be developed and discussed.

While in the previous sections the FCC and BCC structures have been shown to be successfully represented by the distorted tetragonal lattice, complex structures have not yet been analysed within this context. The complex phase is defined here as an intermediate

energy transition through the cusp of FCC-BCC stability following the analysis of Dominguez *et al.* [11] and the Rigid Band analysis from earlier chapters; within the context of the distorted tetragonal structure as determined earlier from the deviation from spherical symmetry in Table 10 and quantified in Figure 24, the ansatz is that the complex phase may be taken to be represented by the ratio $c/a = \left(\sqrt{2}\right)^{-1} \approx 0.71$.

By using a similar analysis as that performed in section 4.2.3, this ansatz is tested and confronted with the results presented by Dominguez e*t al.* [11]. The normalised interatomic distance between the d-orbitals and $r_m$ are now are now -0.23 for $d_{xz}\ and\ d_{yz}$, -0.18 for $d_{xy}$, -0.04 for $d_{z2}$, and 0.12 for $d_{x2-y2}$.

To obtain the stability values for a $E_{Dist.}^{Complex-BC}\ (N_d)$ analysis, it is necessary to identify the energy ratio between the complex and BCC structure, $\frac{\Delta E_T^{Complex}}{\Delta E_T^{BCC}}$. From the results of Chapter 4, the electron density at the Wigner-Seitz radius, $n(r_{ws})$ of complex and simple systems is shown to vary with each other as a result of the electron density analysis using the Thomas-Fermi-Dirac approximation. Analysis of $n(r_{ws})$ values obtained from the 4th order Runge-Kutta solution of the Thomas-Fermi-Dirac formula in Chapter 2 shows that $n(r_{ws})$ decreases by $\frac{3.0-2.6}{3.0} = 0.13.\ \Delta E_T^{Compl}$ is then given as:

$$\frac{\Delta E_T^{BCC}}{\Delta E_T^{Complex}} = (1 - 0.13) \tag{28}$$

$$\Delta E_T^{Complex} \approx 1.15\ \Delta E_T^{BCC} \tag{29}$$

The resulting plot is given as:

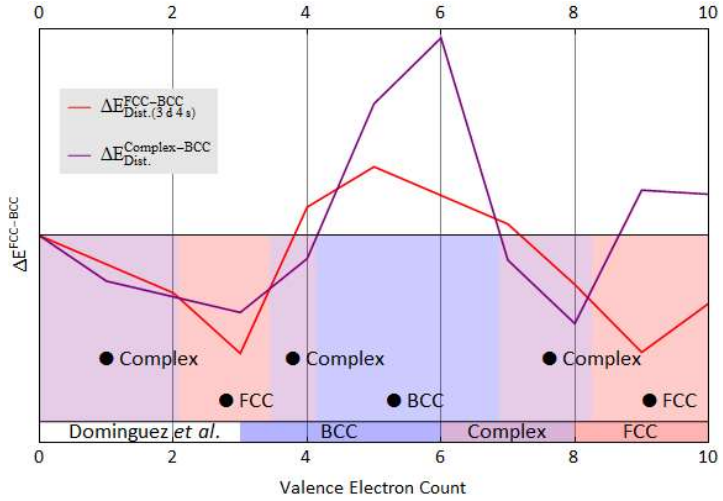


**Figure 31.** Plot of $\Delta E^{FCC-BC}_{Dist.\ (3d\ 4s)}$ and $\Delta E^{Complex-BCC}_{Dist.\ (3d\ 4s)}$ as a function of the valence electron concentration. Regions of phase stability are highlighted for simple FCC phases (Red), complex phases (Purple), and simple BCC phases (Blue). The phase stabilities as predicted by Dominguez *et al.* [11] are included at the bottom of the graph, for comparison.

Figure 31 shows the resulting plot of $E^{Complex-BC}_{Dist.}$, where $E^{Complex}_{Dist.}$ is represented by a tetragonal distortion with $c/a = \left(\sqrt{2}\right)^{-1}$. The most stable phase in this analysis is identified as the one with the lowest energy; when both curves are in the positive region for any value of VEC, in that region the BCC structure is considered to be more stable. When any of the curves are in the negative region, the more stable phase is dependent upon the more negative value between the FCC and Complex structures, represented by $E^{FCC-BCC}_{Dist.}$ and $E^{Complex-BCC}_{Dist.}$. The results of this analysis are shown in Figure 31 where the red-shaded region represents the FCC structure, the purple-shaded region represents the Complex structure(s), and the blue-shaded region represents the BCC structure. The bottom of the graph shows stability regions as determined from Dominguez *et al.'s* principal component analysis [11]. The stability regions as predicted from Figure 31 show the FCC-stable region to be located between $8.25 < VEC < 10$, the complex-stable region between $6.88 < VEC < 8.25$, and the BCC stable region between $4.15 < VEC < 6.88$, while stability at lower regions are not discussed as for most cases of HEAs and other alloys the VEC values are not that low, and the results from Dominguez *et al.* does not offer a similar opportunity for comparison. The predicted stability regions by Dominguez *et al.* lie between $8 < VEC < 10$

for the FCC structure, $6 < VEC < 8$ for complex structures, and $3 < VEC < 6$ for the BCC structure.

In general, results obtained from both methods are comparable with one another, other than a discrepancy in stability regions around $VEC \approx 1$, which is more than the estimated error values of the distorted tetragonal analysis of $\pm\frac{1}{2}$ electron. This difference may be attributed to the different synthesis methods performed by reported compositions in the literature, as the microstructure and phase present in HEAs are considered to be dependent on the cooling rate [2,4]. Moreover, as considered in Chapter 4, the overall accuracy of the RBA method to the 2-D VEC-$\Delta H$ plot from the PCA method stems from the fact that the valence electron concentration is unable to accurately represent the energies within the electronic structure, attributed to the occupancy levels of the valence orbitals e.g. 3d, 4d, 4f orbitals that will modify stability regions as a function of VEC. This has been shown in the analyses of average electronegativity and electron density in the Chapter 4. Therefore, stability values obtained from the PCA method therefore may not offer distinction of energy values of the valence orbitals, not due to weakness of the method, but instead attributed to the statistical noise resulting from grouping all HEA compositions together.

The discussion of the distorted tetragonal method up to this point has been generalised so that the energy values do not have to be explicitly considered, for ease of calculation. However, later inclusion of the energy values are expected shift stability values accordingly. While this analysis gives generally reasonable results with regards to the more stable phase, as mentioned earlier, the specificity of these predictions with regards to specific alloy compositions are lacking. In calculating $E_{Dist.}^{FCC-BCC}$ and $E_{Dist.}^{Complex-BCC}$, the energies between the considered FCC, BCC, and Complex structures were considered to be equal and therefore cancelled each other out within Eq. 26. In reality, the energy of these structures at specific valence electron concentrations are unique to each composition, as a function of their individual alloying elements and interactions. In order to make useful predictions for any particular composition so that their structures can be known with reasonable certainty *prior to any experimental work*, the approach must be modified to account for the structural energies. From Eq. 27:

$$E_{Dist.}^{X-Y}(N_d) = (4\,\pi)\begin{pmatrix} \sum_{i=1}^{d_{1,2,3\ldots5}} \left(\frac{N_d.\delta r_d(d)}{\Delta D^X}\right)(\Delta E^X) - \\ \sum_{i=1}^{d_{1,2,3\ldots5}} (N_d)\left(\frac{N_d.\delta r_d(d)}{\Delta D^Y}\right)(\Delta E^Y) \end{pmatrix} \quad (30)$$

To account for the non-physical values of treating $\Delta E^X = \Delta E^Y$, let $\Delta E^X = A\,\Delta E^Y$ and separate $E_{Dist.}$ into two parts so that $E_{Dist.}^{X} = S^X(N_d).\Delta E^X$. This modification is similar to the treatment used earlier to perform analysis of $E_{Dist.}^{FCC-BCC}$ and $E_{Dist.}^{Complex-BCC}$.

$$E_{Dist.}^{X-Y}(N_d) = \Delta E^Y\left(S^X(N_d).A\ - S^Y(N_d)\right) \quad (31)$$

The right-hand side of $E_{Dist.}^{X-Y}(N_d)$ takes the form of the equations from the earlier analysis of $E_{Dist.}^{FCC-B}$ and $E_{Dist.}^{Complex-BCC}$, the difference being that previously $\Delta E^X\ and\ \Delta E^Y$ cancelled each other out. $\left(S^X(N_d).A\ - S^Y(N_d)\right)$ can be further simplified by considering the relationship as Boltzman-type distribution where:

$$\frac{F^X}{F^Y} = \frac{e^{S^X(N_d).A}}{e^{S^Y(N_d)}} \quad (32)$$

As $VEC = 10 \rightarrow 0$, the stable structures go from $FCC \rightarrow Complex \rightarrow BCC$. The most stable point of $S^{FCC}(N_d)$ can therefore be used as a point of reference to simplify the above formula. Figure 32 shows interpolated values of $S^{FCC}(N_d)$ and its derivative, $S^{FCC\prime}(N_d)$ performed on Mathematica using the built-in integration command. It is found that between $8.25 < VEC < 10$ where the FCC structure is considered stable, the inflection point of $S^{FCC}(N_d) = E_{Dist.}^{FCC-B}\ \ (N_d)$, $S^{FCC\prime}(N_d) = 0$ lies at $VEC = 9, \text{or}\ N_d = 7$ if it is assumed that there are two electrons in the s-orbitals, which is the point where the FCC structure can be considered most stable.

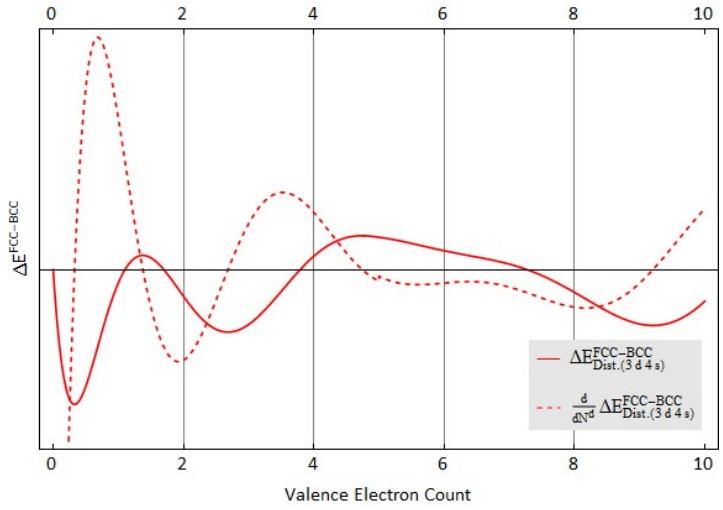


**Figure 32.** Plot of the FCC-BCC energy difference calculate for the 4s 3d distorted tetragonal structure, $\Delta E_{Dist.\ (3d\ 4s)}^{Complex-BCC}$ shown as a Red solid line, and its derivative $\frac{\delta}{\delta\ N_d}\Delta E_{Dist.\ (3d\ 4s)}^{Complex-BC}$ .

Equation 32 is rewritten as a function of $N_d$ so that:

$$\frac{F^X}{F^Y} = C + \frac{e^7}{e^{N_d}} \tag{33}$$

where C is a fitting constant to account for the approximation $S^X(N_d) \approx C + N_d$. The averaged electronegativity analysis from Chapter 4 showed that the energy of a composition can be reasonably well approximated by the Mulliken electronegativity, $X_{Mulliken}$. Let $\Delta E^Y \approx E_F \approx \frac{I+A}{2}$ where I is the first ionisation potential and A is the first electron affinity, and therefore Eq. 31 transforms into:

$$E_{Dist.}^{X-Y}(N_d) = C + X_{Mulliken}\, e^{7-N^d} \tag{34}$$

where $C = -11$. The above equation can now be used as a naïve prediction method to distinguish between the phases present in some compositions of HEAs as a function of only $X_{Mulliken}$ and $N^d$. A demonstration of the use of the above equation is shown in Figure 33, where an additional transition element is added the four-component CoCrFeNi to form an equimolar composition, here denoted as CCFN-A. $X_{Mulliken}$ and $N^d$ values are obtained by obtaining a weighted average of the compositions, according to their stoichiometry.

| CCFN (−2.3) | 3 | 4 | 5 | 6 | 7 | 8 | 9 | 10 | 11 | 12 | 13 |
|---|---|---|---|---|---|---|---|---|---|---|---|
| 3 | | | | | | | | | | | Al (17.9) |
| 4 | Sc (12.92) | Ti (8.67) | V (5.25) | Cr (N/A) | Mn (−0.06) | Fe (N/A) | Co (N/A) | Ni (N/A) | Cu (−6.8) | Zn (−6.8) | |
| 5 | Y (12.79) | Zr (8.74) | Nb (2.43) | Mo (0.05) | Tc (N/A) | Ru (−3.2) | Rh (−4.8) | Pd (−6.8) | Ag (−6.8) | Cd (−7.7) | |
| 6 | | Hf (8.68) | Ta (5.5) | W (2.77) | Re (0.09) | Os (−1.6) | Ir (−3.1) | Pt (−5.64) | Au (−6.6) | Hg (N/A) | |

**Figure 33.** Pseudo-stability values of FCC and non-FCC structures for equimolar CCFN-A compositions, $E_{Dist.}^{FCC-X}$ for transition elements in the periodic table. Positive values (highlighted in purple) denote the preferred presence of simple/complex non-FCC structures while negative values (highlighted in red) denote the preferred presence of the simple FCC structure. Values close to $E_{Dist.}^{X-FC} = 0$ are likely to posesss mixed phases (highlighted in orange), with the proportion of FCC/non-FCC phases being dependent on the degree of positive/negative value of $E_{Dist.}^{X-FCC}$.

From Figure 33 it may be determined that the compositions CCFN* [4,5,5,6], CCFN-Mn* [88,89], CCFN-Cu* [4], CCFN-Zn, CCFN-Ru*, CCFN-Rh*, CCFN-Pd*, CCFN-Ag, CCFN-Cd**, CCFN-Os**, CCFN-Ir**, CCFN-Pt, and CCFN-Au are considered to be FCC stable. Of the 12 compositions identified here, CCFN-Cd, CCFN-Os, and CCFN-Ir denoted by (**), are considered too toxic to synthesise without the use of special equipment. Of the remaining compositions, 5 compositions denoted with an (*) have been synthesised and confirmed to possess a close-packed structure. Of these, CCFN-Rh and CCFN-Re have been found to possess a HCP close-packed structure, while the remaining possesses the FCC structure. Of the untested compositions, CCFN-Zn possesses an extremely low vapour-pressure and is not easily synthesised, in CCFN-Ag silver is widely considered to be an immiscible alloy due to its high binary enthalpy of mixing values with respect to CCFN, and the cost involving the synthesis of CCFN-Pt and CCFN-Au have prevented any experiments from being run. Electron affinity data for Tc and Hg were not available for any calculations for those calculations.

Of the compositions with values close to $E_{Dist.}^{X-FCC} = 0$, CCFN-Mn is a well-known composition with the FCC structure that is also thought to possess the Sigma phase on heat treatment [2]. Equimolar CCFN-Mo was found to possess a complex phase that was not fully

indexed, while equimolar CCFN-Re was synthesised and is expected to possess a mixed structure containing a HCP phase with another unidentified structure.

In terms of the compositions possessing positive values, these are found to be CCFN-Sc**, CCFN-Ti* [4], CCFN-V*, CCFN-Y**, CCFN-Zr*, CCFN-Hf, CCFN-Ta, CCFN-W, and CCFN-Al* [39]. From the listed compositions, CCFN-Ti, CCFN-V, and CCFN-Al denoted with an (*) are found to possess complex phases of C14 Laves, Sigma, and B2, respectively. Synthesis of CCFN-Sc and CCFN-Y, denoted by (**) was considered unviable due to its levels of moderate toxicity, while synthesis of CCFN-Ta and CCFN-W was attempted but no conclusive results/analysis were obtained due to the large disparity between the melting temperature of W and Ta to the base CCFN alloy components. Synthesised compositions are discussed with respect to different stoichiometries in the following section.

### 6.2.8 Application of the method: Predicting stoichiometric phase presence in HEA compositional families

In Figure 34, the tetragonal distortion model is applied to predict the relative stability of the FCC phase in the well-studied CCFN-$Al_x$ system [4–6,66,90] (here referred to as the CCFN-Al family). The analysis in Figure 34 is divided into three sections, where Figure 34. (a) shows Eq. 33 applied to the CCFN-Al stability where negative-values mean that the FCC phase is more likely to be present (and hence, stable), while positive-values mean that the FCC structure is less likely to be present. For convenience, zones where the FCC structure is considered to be more stable are shaded in Red, while zones where the FCC structure is less stable are shaded in green, and these zones are delineated as a function of x addition in a $(CoCrFeNi)_{4+x}$-$A_x$ composition (here denoted as CCFN-$A_x$ following the conventions in HEA literature), with A = Al in this instance. Figure 34. (b) shows the XRD traces for selected compositions within the CCFN-Al family, following the procedures outlined in the Methods section. The XRD patterns presented in terms of the percentage intensity and in units of the reciprocal space vector, $\frac{1}{d}$, are shown next to their corresponding positions to Figure 34. (a); and are also colour-coded according to the phase determined to be present via XRD with red representing the FCC structure and green representing all other structures. For convenience, the full XRD analysis of the compositions are not discussed here, for the reader may refer to appendix X for analysis on the XRD structure characterisation and lattice parameters via Rietveld refinement. Figure 34. (c) shows the zoomed-in XRD traces between

$0.45 < \frac{1}{d} < 0.6$ where the change in peak structure, whether peak asymmetry or intensity is shown to demonstrate the presence of non-FCC structures.

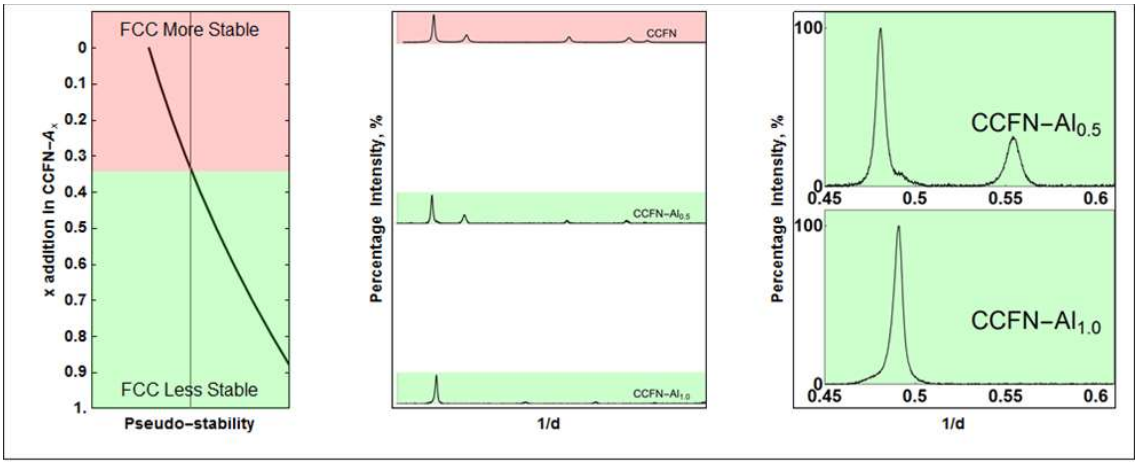


**Figure 34.** Prediction of the different stoichiometry of the CCFN-Al family with experimental verification (XRD).

The analysis in Figure 34. (a) shows that for the CCFN-$Al_x$ family, the FCC structure will be more stable at $x < 0.35$. The compositions CCFN, CCFN-$Al_{0.5}$, and CCFN-$Al_{1.0}$ were synthesised into 3 mm rods as described in the methods section, following that the samples were prepared for XRD analysis and the obtained patterns were analysed as described also in the methods section. CCFN-$Al_{0.5}$ is observed to possess the FCC structure. The <111> peak has an asymmetrical shoulder on the right side of the peak, that is thought to be attributed to the formation of a B2 structure due to the high enthalpy of formation of this structure between FeAl, CoAl, NiAl [75] pairs. The CCFN-$Al_{1.0}$ structure, however, is characterised as a BCC structure, due to the absence of characteristic peaks attributed to the B2 structure. The presence of a secondary structure in CCFN-$Al_{0.5}$ classifies it as being no longer FCC-stable. When the asymmetry of CCFN-$Al_{0.5}$ is reduced to a sum of two peaks, the position of the secondary peak is found to be similar to the position of the <110> BCC peak in CCFN-$Al_{1.0}$ and as such both CCFN-$Al_{0.5}$ and CCFN-$Al_{1.0}$ are classified as compositions where the FCC structure is considered to be less stable. The predicted structural presence in Figure 34. (a) is found to be validated by the XRD characterisation shown in Figure 34. (b); the predictions and experimental characterisation are also found to be in good agreement with the literature.

Earlier predictions using the RBA model predict the FCC-BCC/B2 transition to be at $VEC = 8.1$ which corresponds to $x = 0.2$, which is at a lower value compared to the prediction made in Figure 34. (a) where the transition point is observed at $x = 0.35$. The low intensity peaks corresponding to the secondary structure present in CCFN-$Al_{0.5}$ in Figure 34. (c) suggests that the transition point lies near the $x = 0.5$ point, in which case the prediction in Figure 34. (a) offers better accuracy in prediction the transition point of the CCFN-$Al_{0.5}$ family. As discussed in the earlier chapter, this discrepancy may be attributed to the construction of the Special Quasirandom Structure (SQS) used as input for the RBA analysis, rather than being indicative of the accuracy of the method.

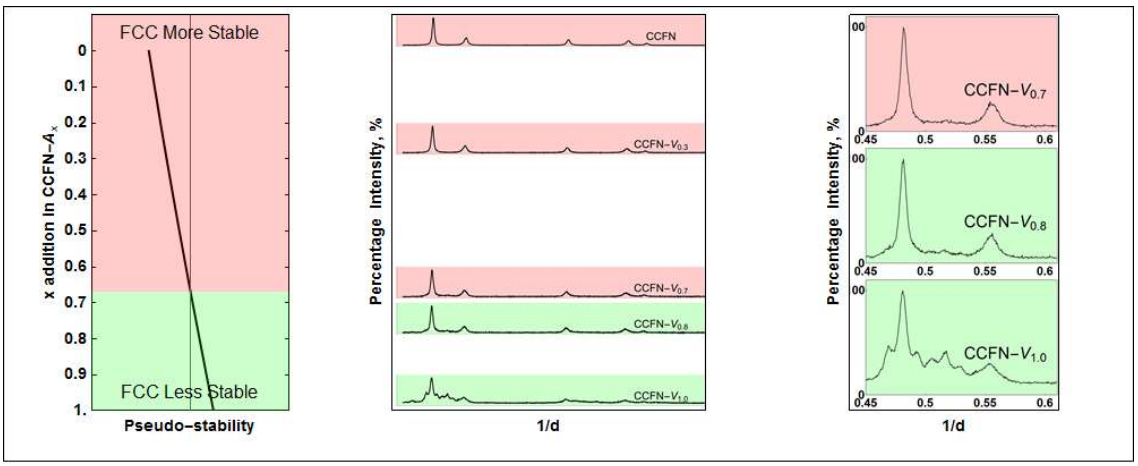


**Figure 35.** Prediction of the different stoichiometry of the CCFN-V family with experimental verification (XRD).

A similar analysis to that performed in Figure 34 is done for the CCFN-$V_x$ family here in Figure 35. The transition point between stoichiometries where the FCC structure structures is considered to be more stable and where the FCC structure is considered to be less stable is found to be at $x = 0.68$. This structure is expected to be the complex Sigma phase as determined from binary FeCr and FeV phase diagrams [76]. Compositions of CCFN-V, CCFN-$V_{0.3}$, CCFN-$V_{0.7}$, CCFN-$V_{0.8}$, and CCFN-$V_{1.0}$ were synthesised and analysed using the same methods as in the analysis of the CCFN-$Al_x$ family and are shown in Figure 35. (b). The onset of precipitation of a secondary non-FCC structure cannot be determined with 100% certainty due to the low resolution of the Mo source used in the XRD analysis, however, the presence of low-intensity peaks at CCFN-$V_{0.8}$ at $\frac{1}{d} = 0.47$ and $\frac{1}{d} = 0.52$ (*cf.* Figure 35. (c)) which are not observed in CCFN-$V_{0.7}$ suggests that the onset of secondary structure

formation lies between CCFN-$V_{0.7}$ and CCFN-$V_{0.8}$, which is in good agreement with the predictions made from Figure 35. (a). CCFN-$V_{1.0}$ has been characterised showing the Sigma complex structure, which is as expected from the FeCr and FeV binary phase diagrams [76]. In Figure 35. (c), the position of the Sigma structure peaks are in good agreement with the location of the low-intensity secondary structure peaks found in CCFN-$V_{0.8}$. In general, the results of the analysis show that the predictions are in good agreement with the experimental characterisation, and consistent with the results presented in literature [37].

Earlier predictions using the RBA model predict the FCC-Sigma transition to be at $VEC = 7.6$ which corresponds to $x = 1.0$, where the Sigma trace is observed to be the majority structure only observed for CCFN-$V_{1.0}$ (*cf.* Figure 35. (c)). It must be clarified that the difference between the predictions made through the RBA and the distorted tetragonal method is that the latter appears predicts the onset of the formation of the Sigma phase (*cf.* Figure 35. (a)).

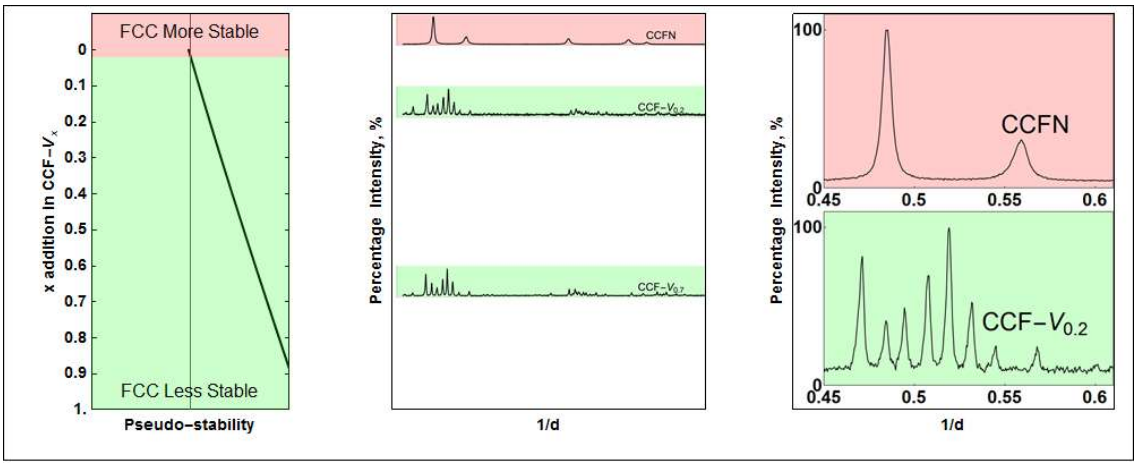


**Figure 36.** Removal of Ni from CCFN-V to form CoCrFe-$V_x$ (CCF-V) and prediction of its stability with experimental verification (XRD).

Following the streamlined semi-empirical rules reported by Dominguez *et al.* [11] using a Principal Component Analysis (PCA), the coordinates of a composition in a two-dimensional plot of the enthalpy of mixing ($\Delta H$) and the valence electron concentration (VEC) indicates the structural stability of a HEA composition. The conditions for the FCC stable zone reported by Dominguez *et al.'s* PCA analysis that must be met are for 8 < VEC < 11 and $\Delta H > -5$. For a new test composition where the removal of Ni from the equimolar CCFN-$V_{1.0}$ composition to form equimolar CoCrFe-$V_{1.0}$ (here denoted CCF-$V_{1.0}$), $\Delta H$ is lowered from

-6.08 kJ/mol to -7.25 kJ/mol while the valence electron concentration is reduced from $VEC = 7.6$ to $VEC = 7$ which does not meet the conditions for formation of a simple FCC structure. The composition CCF-$V_{0.2}$ possesses $\Delta H = -4.02$ and $VEC = 7.5$, suggesting that the complex phase will be present at this composition as well. Figure 36. (a) shows the analysis for the CFN-$V_x$ family from which it is determined that the CCN-$V_x$ composition prefers to adopt a non-FCC phase at all values of x, which is in agreement with the trends in Figure 31 describing $\Delta E^{FCC-BCC}_{Dist.\ (3d\ 4s)}$ and $\Delta E^{Complex-BC}_{Dist.\ (3d\ 4s)}$ as a function of the VEC. This is further confirmed in the XRD characterisation of CCF-$V_{0.2}$ and CCF-$V_{0.7}$ in Figure 36. (b) both of which have been identified as the Sigma phase which is as expected from the FeCr and FeV binary phase diagrams [76], and shows good agreement with the semi-empirical rules.

As the alloying elements in the CFN-$V_x$ family are from the same section of the periodic table as CCFN-$V_x$, its predictions generated using the RBA method can be used for a similar analysis. This earlier analysis predict the FCC-Sigma transition to be at $VEC = 7.6$ which corresponds to $x = 0.1$, which is good accordance with the results predicted using the distorted tetragonal structure method shown in Figure 36. (a). The composition CCF-$V_{0.2}$ is indexed to possess the Sigma structure as a majority structure; and it may be reasonably noted that similar to the its prediction of the CCFN-$V_x$ family, the RBA method overestimates the FCC to non-FCC transition point here also.

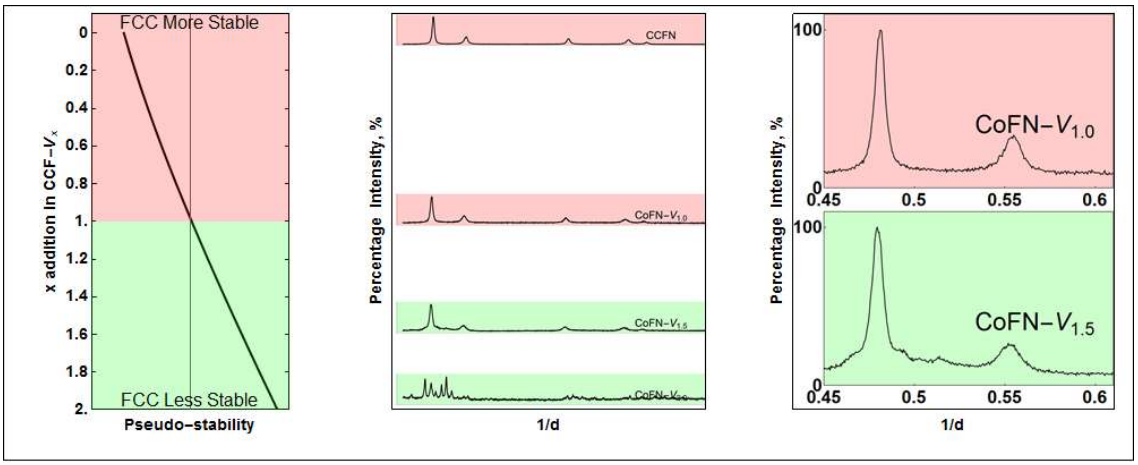


**Figure 37.** Removal of Cr from CCFN-V to form CoFeNi-$V_x$ (CoFN-V) and prediction of its stability with experimental verification (XRD).

In Chapter 4 a CoFeNi-$V_x$ (here denoted CoFN-$V_x$) system was developed using the RBA method through removal of Cr from the CCFN-$V_x$ system. As mentioned previously, Cr is expected to contribute to stability of the Sigma phase from binary FeCr contributions [76]. Additionally, Cr may contribute to nesting at the Fermi surface that leads to directional bonding which stabilises the complex phase [80]. In Figure 37. (a) the CoFN-$V_x$ system is analysed, and the transition point between stoichiometries where the FCC structure is more stable and where other phases are more stable lies at $x = 1$. The experimental characterisation of synthesised compositions from the CoFN-$V_x$ system is shown in Figure 37. (b) for CoFN-$V_{1.0}$, CoFN-$V_{1.5}$, and CoFN-$V_{2.0}$. Figure 37. (c) shows the XRD patterns of CoFN-$V_{1.0}$ and CoFN-$V_{1.5}$ from $0.45 < \frac{1}{d} < 0.6$ where in contrast to CoFN-$V_{1.0}$ which is determined to be a FCC structure, the CoFN-$V_{1.5}$ pattern is observed to possess low intensity peaks signalling the precipitation of a secondary phase. The FCC to non-FCC transition determined experimentally lies between $1 < x < 1.5$, from which it may be determined that the prediction in Figure 37. (a) has underestimated the FCC to non-FCC transition of the system.

The RBA model predicts the FCC-Sigma transition to be at $VEC = 7.6$ which corresponds to $x = 1.5$, which is in excellent agreement with the experimental validation in Figure 37. (b), but contradicts the prediction shown in Figure 37. (a) where the transition point is predicted to be $x = 1$. It is interesting that the while predictions concerning the FCC to non-FCC transition points in the previous two V-containing families of CCFN-$V_x$ and CCF-$V_x$ were overestimated in comparison to the tetragonal distorted structure method, here in the CoFN-$V_x$ family the transition point is accurately represented. As the CCFN system was used as a point of reference to obtain the constant $C$ in Eq. 33, the inaccuracy could result from electronic interaction effects arising from the removal of Cr such as its spin density wave effect, which cannot be accounted for by the method used here, which uses only the Mulliken electronegativity and the VEC to represent electronic structure effects. The influence of Fermi surface nesting on the constant $C$ will need to be further investigated to improve accuracy of this method.

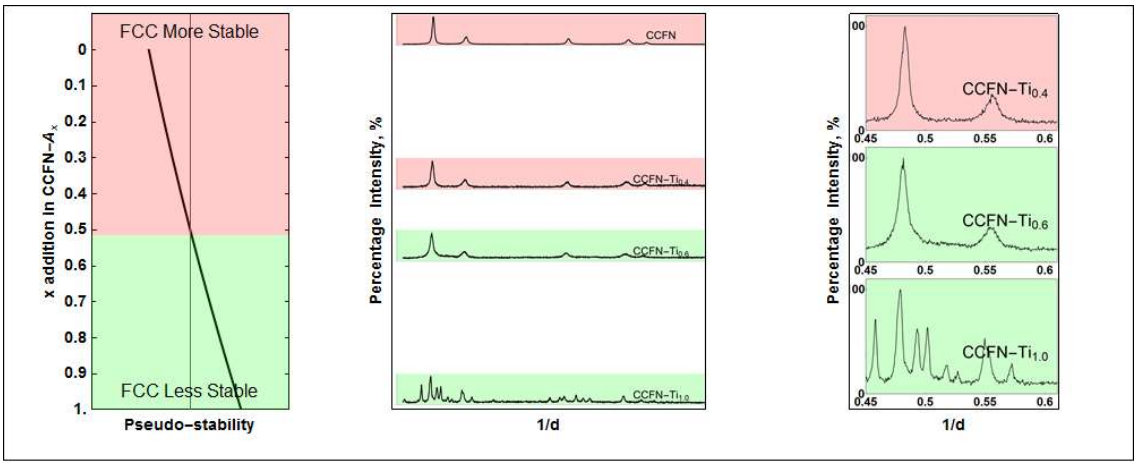


**Figure 38.** Prediction of the different stoichiometry of the CCFN-Ti family with experimental verification (XRD).

The known CCFN-$Ti_x$ family [40] is next investigated using the distorted tetragonal structure method Figure 38. (a) presents this analysis where the transition point between the FCC and non-FCC structure is located at $x = 0.5$. Figure 38. (b) shows the graph of the synthesised CCFN-$Ti_x$ compositions for CCFN-$Ti_{0.4}$, CCFN-$Ti_{0.6}$, and CCFN-$Ti_{1.0}$. CCFN-$Ti_{0.4}$ and CCFN-$Ti_{0.6}$ are found to possess a FCC structure while CCFN-$Ti_{1.0}$ possesses the C14 Laves structure. In Figure 38. (c) the CCFN-$Ti_{0.4}$ pattern is indexed as a FCC structure and the <111> peak is observed to be fairly symmetrical, while the CCFN-$Ti_{0.6}$ pattern although also indexed as a FCC structure possesses several low intensity peaks that are related to the presence of a secondary non-FCC structure. The low intensities make it difficult to characterise the secondary structure, but it is expected to be the C14 Laves phase, as indexed in CCFN-$Ti_{1.0}$. In total, the characterisation of the CCFN-$Ti_x$ samples are in good agreement with the prediction in Figure 38. (a).

Earlier predictions using the RBA model predict the FCC-C14 transition to be at $VEC = 7.55$ which corresponds to $x = 0.6$, which is very close to the prediction in Figure 38. (a) which corresponds to $x = 0.51$. The XRD patterns in Figure 38. (c) show the zoom-in of the XRD patterns for the compositions CCFN-$Ti_{0.4}$, CCFN-$Ti_{0.6}$, and CCFN-$Ti_{1.5}$. The increase in asymmetry of the <111> peak in CCFN-$Ti_{0.4}$ and CCFN-$Ti_{0.6}$ can be seen in the right shoulder of the peak, which represents low-intensity peaks corresponding to a secondary structure, as mentioned earlier. Consequently, the RBA method appears to overestimate the FCC to non-FCC transition point of the CCFN-$Ti_x$ family.

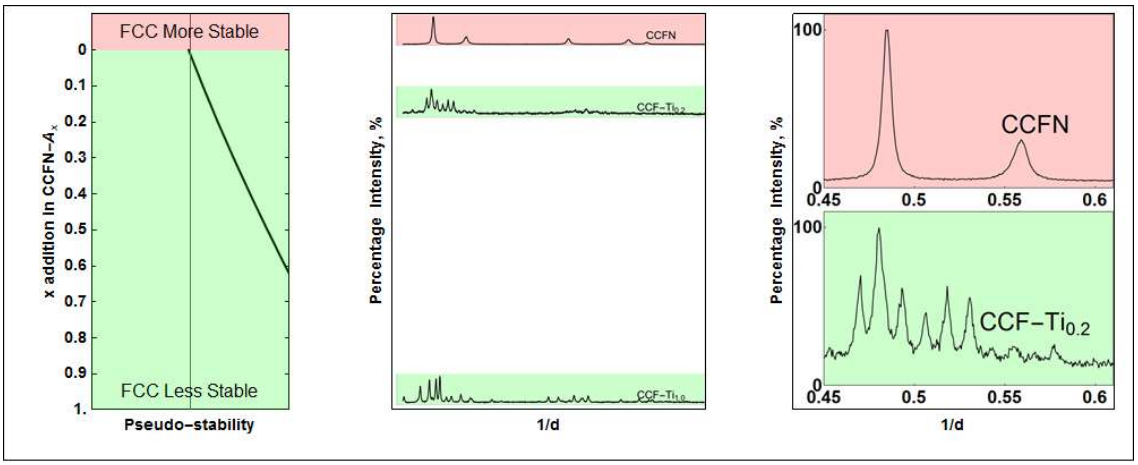


**Figure 39.** Prediction of the different stoichiometry of the CCF-Ti family with experimental verification (XRD).

Similar to the analysis of the CCF-$V_x$ family as presented in Figure 36, the removal of Ni form CCFN-$Ti_x$ to form a CoCrFe-$Ti_x$ type composition (here denoted CCF-$Ti_x$) is analysed here to test the robustness of the predictive scheme. Figure 39. (a) presents the stability of the FCC structure and non-FCC structures generated using the distorted tetragonal structure model. Compared to V which possesses $VEC = 5$, Ti possesses $VEC = 4$, which leads to a further destabilisation of the FCC structure, towards the zones where the complex phases and BCC phases are stable, according to the semi-empirical rules [11,91]. In Figure 39. (a) it is observed that for the entire stoichiometric range of CCF-$Ti_x$ the FCC structure is not considered to be stable. The XRD patterns of two synthesised compositions belonging to the CCF-$Ti_x$ family, CCF-$Ti_{0.2}$ and CCF-$Ti_{1.0}$ are shown in Figure 39. (b) where the structure consists of a majority C14 Laves phase similar to the CCFN-$Ti_x$ family, and other unidentified peaks that may belong to one or more structures. The CCF-$Ti_{0.2}$ pattern contains no peaks that can be indexed to the FCC structure and is considered as a complex phase containing composition. (*cf.* Figure 39. (c)), while for CCF-$Ti_{1.0}$ the observed structure is also a mixture of the Laves C14 structure and some other unindexed peaks due to the complexity of the system.

Similar to the previous, the alloying components belonging to the CCF-$Ti_x$ family are comparable to the CCFN-$Ti_x$ family and as such the earlier analysis of the latter using the RBA method may be used to also analyse the phase stability of the CCF-$Ti_x$ family compositions. From the RBA method it is observed that the FCC-C14 transition point lies at

$VEC = 7.7$, which is an unphysical value for the CCF-$Ti_x$ family as the CoCrFe (here denoted CCF) composition without any Ti addition possesses $VEC = 7.67$. As such, it is expected that all additions of Ti to the CCF structure would further stabilise the Laves C14 structure, which is in accordance with the predictions made in Figure 39. (a). Overall, for the CCF-$Ti_x$ system, predictions made using the distorted tetragonal structure model are in excellent agreement with experiments, and also the analysis using the RBA model.

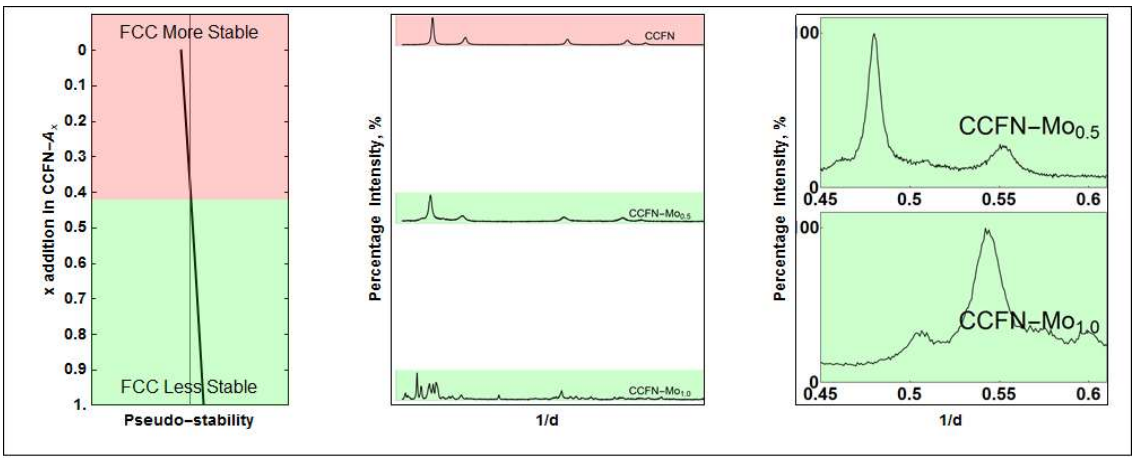


**Figure 40.** Prediction of the different stoichiometry of the CCFN-Mo family with experimental verification (XRD).

Previous analyses of CCFN-$A_x$ type HEA compositions were performed, where A represents selected 3d transition metal elements. It is worth mentioning again that the approximation of the distorted tetragonal structure described in this chapter makes predictions as a function of the Mulliken electronegativity and VEC. From the conclusion of the analysis of the averaged electronegativity and electron density in Chapter 4, it was shown that the energy levels of HEA compositions, and indeed any alloy composition is sensitive to the primary quantum number of the alloying elements, as this directly reflects the occupancy of the valence orbital, and hence the orbital energy. It is therefore of interest to test the method on transition metal elements possessing different primary quantum numbers.

In Figure 40, the stability of the FCC and non-FCC structures are analysed for Mo addition to the equimolar CCFN composition, here referred to as the CCFN-$Mo_x$ family. The complex structure in the CCFN-$Mo_x$ family, if any, is expected to be the rhombohedral Mu phase that is associated with FeMo and FeCrMo phase diagrams [76]. Figure 40. (a) shows the resulting analysis where the FCC to non-FCC transition point is located at $x = 0.42$. Figure 40. (b)

shows the analysis of synthesised CCFN-$Mo_{0.5}$ and CCFN-$Mo_{1.5}$ compositions. The CCFN-$Mo_{0.5}$ composition is indexed to have a majority phase consisting of the FCC structure; low intensity peaks are found at $\frac{1}{d} = 0.47$ and $\frac{1}{d} = 0.51$ for this composition (*cf.* Figure 40. (c)) that show the possible presence of a secondary structure. The pattern cannot be fully indexed due to the low noise-to-signal ratio associated with the instrument. The CCFN-$Mo_{1.0}$ composition in Figure 40. (c) is not fully indexed due to the complexity of the phase. The FCC and non-FCC transition point determined experimentally will occur at slightly below $x = 0.5$, which is in good agreement with the prediction in Figure 40. (a).

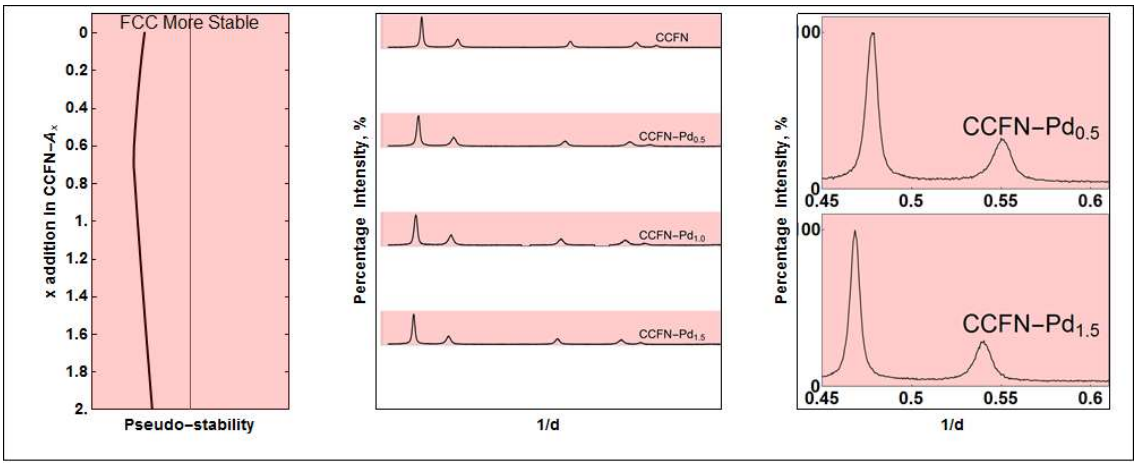


**Figure 41.** Prediction of the different stoichiometry of the CCFN-Pd family with experimental verification (XRD).

Similarly, the above analysis for 4d type transition metals is extended for Pd addition to the equimolar CCFN composition to form the CCFN-$Pd_x$ composition. In Figure 41. (a) it is shown that the FCC structure is stable for all values of $x$ up to $x = 2.0$. The XRD analysis of synthesised CCFN-$Pd_{0.5}$, CCFN-$Pd_{1.0}$, and CCFN-$Pd_{1.5}$ is shown in Figure 41. (b), where all of the indexed phases are determined to be of the FCC structure. The zoom-in of the XRD patterns in Figure 41. (c), show no traces of low-intensity peaks related to the presence of a secondary structure. The determination of the structures present in these phases is in good agreement with the prediction in Figure 41. (a).

## 6.3 Conclusions

In conclusion:

- A method to describe the energy levels of FCC, BCC and Complex structures based on a distorted tetragonal structure has been developed and described in this Chapter. The method has been verified by correctly predicting the structural stability of Ni and Fe at 0K. Furthermore, adapting the method to a Fermi-Dirac distribution demonstrates the capability in describing the FCC-BCC transition of Fe allotrope as a function of temperature.
- The distorted tetragonal method was generalised to describe the stability of FCC, BCC, and complex structures as a function of the valence electron concentration. Comparison of the generated FCC-BCC and complex-BCC curves with Lee and Hoffman's tight-binding method [81] and Dominguez *et al.'s* semi-empirical based PCA method verified the accuracy of the method and indirectly the applicability of the assumptions employed in its construction.
- To develop a simplistic but robust model for HEA prediction, the generalised model is approximated so that it may be described as a function of the Fermi energy and a exponential-type probability function. Several HEA compositions of type CCFN-$A_x$ where A is some transition metal or post-transition metal such as Al are synthesised and the method is used to predict their stabilities. Predictions using the RBA method are used as comparison and the results are very close with one another, and in some cases offers better accuracy. The influence of some quantum effects such as Fermi surface nesting are not adequately described, and further work needs to be undertaken for refinement. However, the overall error of the 8 compositional families tested, conservatively, is < 5.25%, where $error = \left[\left(\frac{0.2}{2}\right)\left(\frac{1}{8}\right) + \left(\frac{0.5}{12}\right)\right] 100\%$, which is reasonable.

The key achievement of this chapter is that a method for prediction of alloy stabilities have been developed and further simplified so that predictions for entire ranges of stoichiometries can be performed quickly in spreadsheet-based software such as MS Excel. Once key compositional stoichiometries are identified, more computationally expensive ab-initio methods with increased accuracy may be used to further confirm the selection and improve the alloy design process.

## 6.4 References


[1] D.B. Miracle, O.N. Senkov, A critical review of high entropy alloys and related concepts, Acta Mater. 122 (2017) 448–511. doi:10.1016/j.actamat.2016.08.081.

[2] E.J. Pickering, R. Munoz-Moreno, H.J. Stone, N.G. Jones, Precipitation in the equiatomic high-entropy alloy CrMnFeCoNi, Scr. Mater. 113 (2016).

[3] F.R. de Boer, ed., Cohesion in metals: transition metal alloys, 2., print, North Holland, Amsterdam, 1988.

[4] U. Dahlborg, J. Cornide, M. Calvo-Dahlborg, T.C. Hansen, Z. Leong, L.A. Dominguez, S. Chambreland, A. Cunliffe, R. Goodall, I. Todd, Crystalline structures of some high entropy alloys obtained by neutron and x-ray diffraction, Acta Phys. Pol. A. 128 (2015).

[5] M. Calvo-Dahlborg, J. Cornide, Tobola, D. Nguyen Manh, J.S. Wróbel, J. Juraszek, S. Jouen, U. Dahlborg, Effect of Pd on structural and magnetic properties of high entropy CoCrFeNiPd alloys. In preparation, (2016).

[6] J. Cornide, U. Dahlborg, Z. Leong, L.A. Dominguez, J. Juraszek, S. Jouen, T. Hansen, R. Wunderlich, S. Chambreland, I. Todd, R. Goodall, M. Calvo-Dahlborg, Structure and Properties of Some CoCrFeNi-Based High Entropy Alloys, in: TMS2015 Supplemental Proceedings, 2015.

[7] J. Cornide, M. Calvo-Dahlborg, S. Chambreland, L.A. Dominguez, Z. Leong, U. Dahlborg, A. Cunliffe, R. Goodall, I. Todd, Combined atom probe tomography and TEM investigations of CoCrFeNi, CoCrFeNi-Pdx (x=0.5, 1.0, 1.5) And CoCrFeNi-Sn, Acta Phys. Pol. A. 128 (2015).

[8] W. Research, Mathematica 10.4, 10.4, Champaign, Illinios, 2016.

[9] F. Ren, K. Cao, J. Ren, A.A. Volinsky, T.H. Tran, B. Tian, Numerical Calculation of the Electron Density at the Wigner–Seitz Radius Based on the Thomas–Fermi–Dirac Equation, J. Comput. Theor. Nanosci. 11 (2014) 344–347. doi:10.1166/jctn.2014.3358.

[10] L.C. Allen, Electronegativity is the average one-electron energy of the valence-shell electrons in ground-state free atoms, J. Am. Chem. Soc. 111 (1989) 9003–9014. doi:10.1021/ja00207a003.

[11] L.A. Dominguez, R. Goodall, I. Todd, Prediction and validation of quaternary high entropy alloys using statistical approaches, Mater. Sci. Technol. 31 (2015) 1201–1206.

[12] U. Mizutani, Hume-Rothery rules for structurally complex alloy phases, CRC Press, Boca Raton, 2011.

[13] R.G. Parr, R.A. Donnelly, M. Levy, W.E. Palke, Electronegativity: The density functional viewpoint, J. Chem. Phys. 68 (1978) 3801. doi:10.1063/1.436185.

[14] L. Pauling, THE NATURE OF THE CHEMICAL BOND. IV. THE ENERGY OF SINGLE BONDS AND THE RELATIVE ELECTRONEGATIVITY OF ATOMS, J. Am. Chem. Soc. 54 (1932) 3570–3582. doi:10.1021/ja01348a011.

[15] A.R. Miedema, The electronegativity parameter for transition metals: Heat of formation and charge transfer in alloys, J. Common Met. 32 (1973) 117–136. doi:10.1016/0022-5088(73)90078-7.

[16] C.-C. Juan, C.-Y. Hsu, C.-W. Tsai, W.-R. Wang, T.-S. Sheu, J.-W. Yeh, S.-K. Chen, On microstructure and mechanical performance of AlCoCrFeMo0.5Nix high-entropy alloys, Intermetallics. 32 (2013) 401–407. doi:10.1016/j.intermet.2012.09.008.

[17] J.W. Yeh, S.K. Chen, S.J. Lin, J.Y. Gan, T.S. Chin, T.T. Shun, C.H. Tsau, S.Y. Chang, Nanostructured high-entropy alloys with multiple principal elements: Novel alloy design concepts and outcomes, Adv. Eng. Mater. 6 (2004) 299–303.

[18] M.-R. Chen, S.-J. Lin, J.-W. Yeh, M.-H. Chuang, S.-K. Chen, Y.-S. Huang, Effect of vanadium addition on the microstructure, hardness, and wear resistance of Al0.5CoCrCuFeNi high-entropy alloy, Metall. Mater. Trans. A. 37 (2006) 1363–1369. doi:10.1007/s11661-006-0081-3.

[19] B.W. Silverman, Density estimation for statistics and data analysis, Chapman & Hall/CRC, Boca Raton, 1998.

[20] H. Bakker, A. Miedema, Enthalpies in alloys: Miedemaś semi-empirical model, Trans Tech Publications, Uetikon-Zuerich, Switzerland ; Enfield, N.H, 1998.

[21] R.F. Berger, P.L. Walters, S. Lee, R. Hoffmann, Connecting the Chemical and Physical Viewpoints of What Determines Structure: From 1-D Chains to γ-Brasses, Chem. Rev. 111 (2011) 4522–4545. doi:10.1021/cr1001222.
[22] S. Guo, N. C, L. J, L.C. T, Effect of valence electron concentration on stability of fcc or bcc phase in high entropy alloys, J. Appl. Phys. 109 (2011) 10.
[23] T. Rajasekharan, V. Seshubai, Charge transfer on the metallic atom-pair bond, and the crystal structures adopted by intermetallic compounds, Acta Crystallogr. A. 68 (2012) 156–165. doi:10.1107/S0108767311044151.
[24] C.-G. Zhan, J.A. Nichols, D.A. Dixon, Ionization Potential, Electron Affinity, Electronegativity, Hardness, and Electron Excitation Energy: Molecular Properties from Density Functional Theory Orbital Energies, J. Phys. Chem. A. 107 (2003) 4184–4195. doi:10.1021/jp0225774.
[25] R.G. Pearson, Absolute electronegativity and hardness correlated with molecular orbital theory, Proc. Natl. Acad. Sci. 83 (1986) 8440–8441. doi:10.1073/pnas.83.22.8440.
[26] D.G. Pettifor, A Quantum Mechanical Critique of the Miedema Rules for Alloy Formation, Solid State Phys. 40 (1987) 43–92.
[27] A. Savin, R. Nesper, S. Wengert, T.F. Fässler, ELF: The Electron Localization Function, Angew. Chem. Int. Ed. Engl. 36 (1997) 1808–1832. doi:10.1002/anie.199718081.
[28] M.E. Eberhart, The metallic bond: Elastic properties, Acta Mater. 44 (1996) 2495–2504. doi:10.1016/1359-6454(95)00347-9.
[29] B. Silvi, C. Gatti, Direct Space Representation of the Metallic Bond, J. Phys. Chem. A. 104 (2000) 947–953. doi:10.1021/jp992784c.
[30] A. Paxton, M. Methfessel, D.G. Pettifor, A bandstructure view of the Hume-Rothery electron phases, Proc. R. Soc. A. 453 (1997) 1493.
[31] D. Nguyen-Manh, A. Paxton, D.G. Pettifor, A. Pasturel, On the phase stability of transition metal trialuminide compounds, Intermetallics. 3 (1995) 9–14.
[32] D.G. Pettifor, The structures of binary compounds. I. Phenomenological structure maps, J. Phys. C Solid State Phys. 19 (1986) 285–313. doi:10.1088/0022-3719/19/3/002.
[33] S.I. Simdyankin, S.N. Taraskin, M. Dzugutov, S.R. Elliott, Vibrational properties of the one-component σ phase, Phys. Rev. B. 62 (2000) 3223–3231. doi:10.1103/PhysRevB.62.3223.
[34] L.H. Thomas, The calculation of atomic fields, Math. Proc. Camb. Philos. Soc. 23 (1927) 542. doi:10.1017/S0305004100011683.
[35] E. Fermi, Un metodo statistico per la determinazione di alcune priorieta dell'atome, Rend Accad Naz Lincei. 6 (1927) 32.
[36] N. Metropolis, J.R. Reitz, Solutions of the Fermi-Thomas-Dirac Equation, J. Chem. Phys. 19 (1951) 555. doi:10.1063/1.1748292.
[37] G.A. Salishchev, M.A. Tikhonovsky, D.G. Shaysultanov, N.D. Stepanov, A.V. Kuznetsov, I.V. Kolodiy, A.S. Tortika, O.N. Senkov, Effect of Mn and V on structure and mechanical properties of high-entropy alloys based on CoCrFeNi system, J. Alloys Compd. 591 (2014) 11–21. doi:10.1016/j.jallcom.2013.12.210.
[38] N.D. Stepanov, D.G. Shaysultanov, G.A. Salishchev, M.A. Tikhonovsky, E.E. Oleynik, A.S. Tortika, O.N. Senkov, Effect of V content on microstructure and mechanical properties of the CoCrFeMnNiVx high entropy alloys, J. Alloys Compd. 628 (2015) 170–185. doi:10.1016/j.jallcom.2014.12.157.
[39] H.P. Chou, Y.S. Chang, S.K. Chen, J.W. Yeh, Microstructure, thermophysical and electrical properties in Al x CoCrFeNi (0 ≤ x ≤2) high-entropy alloys, Mater. Sci. Eng. B. 163 (2009) 184–189.
[40] T.T. Shun, L.Y. Chang, M.H. Shiu, Microstructures and mechanical properties of multiprincipal component CoCrFeNiTix alloys, Mater. Sci. Eng. A. 556 (2012) 170–174.
[41] M.-H. Tsai, J.-W. Yeh, High-Entropy Alloys: A Critical Review, Mater. Res. Lett. 2 (2014) 107–123. doi:10.1080/21663831.2014.912690.

[42] P. Politzer, R.G. Parr, D.R. Murphy, Approximate determination of Wigner-Seitz radii from free-atom wave functions, Phys. Rev. B. 31 (1985) 6809–6810. doi:10.1103/PhysRevB.31.6809.
[43] B. Ren, Z.X. Liu, B. Cai, M.X. Wang, L. Shi, Aging behavior of a CuCr2Fe2NiMn high-entropy alloy, Mater. Des. 33 (2012) 121–126. doi:10.1016/j.matdes.2011.07.005.
[44] B. Zheng, Q.B. Liu, L.Y. Zhang, Microstructure and Properties of MoFeCrTiW High-Entropy Alloy Coating Prepared by Laser Cladding, Adv. Mater. Res. 820 (2013) 63–66. doi:10.4028/www.scientific.net/AMR.820.63.
[45] Y.J. Zhou, Y. Zhang, Y.L. Wang, G.L. Chen, Solid solution alloys of AlCoCrFeNiTi x with excellent room-temperature mechanical properties, Appl. Phys. Lett. 90 (2007) 181904. doi:10.1063/1.2734517.
[46] X.F. Wang, Y. Zhang, Y. Qiao, G.L. Chen, Novel microstructure and properties of multicomponent CoCrCuFeNiTix alloys, Intermetallics. 15 (2007) 357–362. doi:10.1016/j.intermet.2006.08.005.
[47] M.-R. Chen, S.-J. Lin, J.-W. Yeh, S.-K. Chen, Y.-S. Huang, C.-P. Tu, Microstructure and Properties of Al0.5CoCrCuFeNiTix (x=0–2.0) High-Entropy Alloys, Mater. Trans. 47 (2006) 1395–1401. doi:10.2320/matertrans.47.1395.
[48] L. Xie, P. Brault, A.-L. Thomann, J.-M. Bauchire, AlCoCrCuFeNi high entropy alloy cluster growth and annealing on silicon: A classical molecular dynamics simulation study, Appl. Surf. Sci. 285 (2013) 810–816. doi:10.1016/j.apsusc.2013.08.133.
[49] P. Koželj, S. Vrtnik, A. Jelen, S. Jazbec, Z. Jagličić, S. Maiti, M. Feuerbacher, W. Steurer, J. Dolinšek, Discovery of a Superconducting High-Entropy Alloy, Phys. Rev. Lett. 113 (2014). doi:10.1103/PhysRevLett.113.107001.
[50] Y. Zou, S. Maiti, W. Steurer, R. Spolenak, Size-dependent plasticity in an Nb25Mo25Ta25W25 refractory high-entropy alloy, Acta Mater. 65 (2014) 85–97. doi:10.1016/j.actamat.2013.11.049.
[51] S. Maiti, W. Steurer, Structural-disorder and its effect on mechanical properties in single-phase TaNbHfZr high-entropy alloy, Acta Mater. 106 (2016) 87–97. doi:10.1016/j.actamat.2016.01.018.
[52] O.N. Senkov, G.B. Wilks, J.M. Scott, D.B. Miracle, Mechanical properties of Nb25Mo25Ta25W25 and V20Nb20Mo20Ta20W20 refractory high entropy alloys, Intermetallics. 19 (2011) 698–706. doi:10.1016/j.intermet.2011.01.004.
[53] W. Kohn, L.J. Sham, Self-Consistent Equations Including Exchange and Correlation Effects, Phys. Rev. 140 (1965) A1133–A1138.
[54] M.C. Troparevsky, J.R. Morris, P.R.C. Kent, A.R. Lupini, G.M. Stocks, Criteria for Predicting the Formation of Single-Phase High-Entropy Alloys, Phys. Rev. X. 5 (2015). doi:10.1103/PhysRevX.5.011041.
[55] F. Kormann, D. Ma, D.D. Belyea, M.S. Lucas, C.W. Miller, B. Grabowski, H.F. Sluiter, “Treasure maps” for magnetic high-entropy-alloys from theory and experiment, Appl. Phys. Lett. 107 (2015).
[56] G. Trambly de Laissardière, D. Nguyen-Manh, D. Mayou, Electronic structure of complex Hume-Rothery phases and quasicrystals in transition metal aluminides, Prog. Mater. Sci. 50 (2005) 679–788. doi:10.1016/j.pmatsci.2005.01.001.
[57] D. Nguyen-Manh, V. Vitek, A.P. Horsfield, Environmental dependence of bonding: A challenge for modelling of intermetallics and fusion materials, Prog. Mater. Sci. 52 (2007) 52.
[58] S. Raimes, The rigid-band model, J. Phys. Radium. 23 (1962) 639–643. doi:10.1051/jphysrad:019620023010063901.
[59] E.A. Stern, Rigid-Band Model of Alloys, Phys. Rev. 157 (1967) 544–551. doi:10.1103/PhysRev.157.544.
[60] G. Liu, D. Nguyen-Manh, B.G. Liu, D.G. Pettifor, Magnetic properties of point defects in iron within the tight-binding-bond Stoner model, Phys. Rev. B. 71 (2005) 174115.

[61] D. Nguyen-Manh, S.L. Dudarev, Model many-body Stoner Hamiltonian for binary FeCr alloys, Phys. Rev. B. 80 (2009) 104440.
[62] S.L. Dudarev, P.M. Derlet, Interatomic potentials for materials with interacting electrons, J. Comput.-Aided Mater. Des. 14 (2008) 129.
[63] J.S. Wróbel, D. Nguyen-Manh, M.Y. Lavrentiev, M. Muzyk, S.L. Dudarev, Phase stability of ternary fcc and bcc Fe-Cr-Ni alloys, Phys. Rev. B. 91 (2015) 021408.
[64] C. Niu, A.J. Zaddach, A.A. Oni, X. Sang, J.W. Hurt, J.M. LeBeau, C.C. Koch, D.L. Irving, Spin-driven ordering of Cr in the equiatomic high entropy alloy NiFeCrCo, Appl. Phys. Lett. 106 (2015) 161906. doi:10.1063/1.4918996.
[65] M.S. Lucas, L. Mauger, J. Munoz, Y. Xiao, A.O. Sheets, S.L. Sematin, Magnetic and vibrational properties of high-entropy alloys, J. Appl. Phys. 109 (2011) 7.
[66] W.R. Wang, W.L. Wang, S.C. Wang, Y.C. Tsai, C.H. Lai, J.W. Yeh, Effects of Al addition on the microstructure and mechanical property of AlxCoCrFeNi high-entropy alloys, Intermetallics. 26 (2012) 44–51.
[67] D.G. Pettifor, Pressure-cell boundary relation and application to transition-metal equation of state, Commun. Theor. Phys. 1 (1977).
[68] O.K. Andersen, H.L. Skriver, H. Nohl, B.J. Johansson, Electronic structure of transition metal compounds; ground-state properties of the 3d-monoxides in the atomic sphere approximation, Pure Appl. Chem. 52 (1980) 93.
[69] G. Krier, O. Jepsen, A. Burkhardt, O.J. Andersen, The TB-LMTO-ASA program, Max-Planck-Institute für Festkörperforschung, 1994.
[70] A. Zunger, S. Wei, L. Ferreira, J. Bernard, Special quasirandom structures, Phys. Rev. Lett. 65 (1990).
[71] A.V. de Walle, T. P, J.M. de, O.D. L, A. M, D. A, S. D, W. Y, C. L, L. Z, C. M, Efficient stochastic generation of special quasirandom structures, Calphad - Comput. Coupling Phase Diagr. Thermochem. 42 (2013) 13–18.
[72] B. Cantor, I.T.H. Chang, P. Knight, A.J.B. Vincent, Microstructural development in equiatomic multicomponent alloys, Materials Science and Engineering A, Phys. Rev. B Condens. Matter. 375–377 (2004) 213–218.
[73] O.N. Senkov, G.B. Wilks, D.B. Miracle, C.P. Chuang, P.K. Liaw, Refractory high-entropy alloys, Intermetallics. 18 (2010) 1758–1765.
[74] I. Toda-Caraballo, J.S. Wróbel, S.L. Dudarev, D. Nguyen-Manh, P.E.J. Rivera-Diaz-del-Castillo, Interatomic spacing distribution in multicomponent alloys, Acta Mater. 97 (2015).
[75] D. Nguyen-Manh, D.G. Pettifor, Electronic structure, phase stability, and elastic moduli of AB transition metal aluminides, Intermetallics. 7 (1999).
[76] P. Villars, H. Okamoto, K. Cenzual, eds., ASM Alloy Phase Diagrams Database, ASM International, Materials Park, OH, 2006. http://www1.asminternational.org/AsmEnterprise/APD.
[77] Y. Zhang, Z.P. Lu, S.G. Ma, P.K. Liaw, Z. Tang, Y.Q. Cheng, M.C. Gao, Guidelines in predicting phase formation of high-entropy alloys, MRS Commun. 4 (2014) 57–62. doi:10.1557/mrc.2014.11.
[78] Y. Lu, Y. Dong, S. Guo, L. Jiang, H. Kang, T. Wang, B. Wen, Z. Wang, J. Jie, Z. Cao, H. Ruan, T. Li, A Promising New Class of High-Temperature Alloys: Eutectic High-Entropy Alloys, Sci. Rep. 4 (2014) 6200. doi:10.1038/srep06200.
[79] D.G. Pettifor, Theory of the Heats of Formation of Transition-Metal Alloys, Phys. Rev. Lett. 42 (1978) 846.
[80] G.M. Stocks, W.A. Shelton, D.M. Nicholson, F.J. Pinski, B. Ginatempo, A. Barbieri, B.L. Györffy, D.D. Johnson, J.B. Staunton, P.E.A. Turchi, M. Sluiter, Ordered Intermetallics — Physical Metallurgy and Mechanical Behaviour, in: C.T. Liu, R.W. Cahn, G. Sauthoff (Eds.), Springer Netherlands, Dordrecht, 1992: pp. 15–36. http://dx.doi.org/10.1007/978-94-011-2534-5_2.

[81] S. Lee, R. Hoffmann, Bcc and Fcc Transition Metals and Alloys: A Central Role for the Jahn−Teller Effect in Explaining Their Ideal and Distorted Structures, J. Am. Chem. Soc. 124 (2002) 4811–4823. doi:10.1021/ja0114557.
[82] J.C. Slater, Atomic Shielding Constants, Phys. Rev. 36 (1930) 57–64. doi:10.1103/PhysRev.36.57.
[83] E. Clementi, D.L. Raimondi, Atomic Screening Constants from SCF Functions, J. Chem. Phys. 38 (1963) 2686. doi:10.1063/1.1733573.
[84] J.H. Rose, J. Ferrante, J.R. Smith, Universal Binding Energy Curves for Metals and Bimetallic Interfaces, Phys. Rev. Lett. 47 (1981) 675–678. doi:10.1103/PhysRevLett.47.675.
[85] C. Zener, Analytic Atomic Wave Functions, Phys. Rev. 36 (1930) 51–56. doi:10.1103/PhysRev.36.51.
[86] M.S. Lucas, D. Belyea, C. Bauer, N. Bryant, E. Michel, Z. Turgut, S.O. Leontsev, J. Horwath, S.L. Semiatin, M.E. McHenry, C.W. Miller, Thermomagnetic analysis of FeCoCrxNi alloys: Magnetic entropy of high-entropy alloys, J. Appl. Phys. 113 (2013) 17A923. doi:10.1063/1.4798340.
[87] C. Kittel, Introduction to solid state physics, 8th ed, Wiley, Hoboken, NJ, 2005.
[88] K.-Y. Tsai, M.-H. Tsai, J.-W. Yeh, Sluggish diffusion in Co–Cr–Fe–Mn–Ni high-entropy alloys, Acta Mater. 61 (2013) 4887–4897. doi:10.1016/j.actamat.2013.04.058.
[89] B. Cantor, Multicomponent and High Entropy Alloys, Entropy. 16–19 (2014) 4749–4768.
[90] Y.-F. Kao, S.-K. Chen, T.-J. Chen, P.-C. Chu, J.-W. Yeh, S.-J. Lin, Electrical, magnetic, and Hall properties of AlxCoCrFeNi high-entropy alloys, J. Alloys Compd. 509 (2011) 1607–1614. doi:10.1016/j.jallcom.2010.10.210.
[91] W. Hume-Rothery, R.E. Smallman, C.W. Haworth, The Structure of Metals and Alloys, The Institute of Metals, Carlton House Terrace, London SW1Y 5DB, UK, 1988.
[92] D.G. Pettifor, Individual orbital contributions to the SCF virial in homonuclear diatomic molecules, J. Chem. Phys. 69 (1978) 2930.
[93] H.J. Jones, Concentrated solid solutions of normal metals, 23 (1962) Journal de Physique et le Radium.
[94] N. Christensen, O. Gunnarsson, O. Jepsen, O.J. Andersen, Local spin density theory for ferro- and antiferromagnetic materials, J. Phys. C. 8 (1988).

# 7. Designing hardfacing HEAs with $E_{Dist.}^{X}$

**Design of Experiment**

Objective: To use the semi-empirical methods developed in previous chapters for the design of new alloy compositions.

Hypothesis: The presence of both simple and complex phases possesses a strong influence on the mechanical properties of HEA composition. Values of $E_{Dist.}^{X-BCC}$ have been successfully used to predict the simple to complex phase transitions in HEAs and is expected to co-relate with the mechanical properties, and leveraged upon as a strategy for alloy design.

Exp. Type: Data mining, Verification

Primary Var.: Alloy Composition; as a function of (Enthalpy of Mixing & $E_{PSEUDO}$)

Constant Var.: Pressure, Temperature

Primary Result: XRD characterisation, Vickers hardness, Elastic modulus, Yield strength

Techniques: Compression Testing, Arc-Melting & Casting

## Table of Contents

## Symbols and Abbreviations

| | |
|---|---|
| Å | Units Angstrom |
| $\Delta G$ | Gibbs free energy per unit area for formation of the secondary phase |
| $\Delta H$ | Change in enthalpy of mixing |
| $\Delta n$ | Change in the valence electron concertation |
| $\gamma$ | Surface energy between the matrix/secondary phase |
| $\gamma_0$ | Surface energy between grain boundaries before the nucleation of any secondary phase |
| $\mu$ | Chemical potential of the system |
| $\mu_0$ | Chemical potential at the standard rate of the vacancy |
| $\phi_{strain}$ | Dilatational strain energy |
| $\sigma_{Yield}$ | Yield stress |
| a | Actual activity of the old solid solution phase |
| $a_e$ | Equilibrium activity of the old solid solution phase |
| A | Electron affinity |
| $C_{11,c}$, $C_{12,c}$, and $C_{44,c}$ | Elastic constants of the strain cluster |
| $C_{11,m}$, $C_{12,m}$, and $C_{44,m}$ | Elastic constants of the strain matrix |
| $E_{Dist.}$ | Energy associated with a distorted tetragonal structure |
| $E_{eff}$ | Effective driving force for nucleation |
| $E_y$ | Young's modulus |
| I | Ionisation energy |
| k | Boltzmann constant |
| N | Units Newton |
| Pa | Units Pascal |
| T | Temperature in Kelvin |
| $v_c$ | Poisson's ratio for the strain cluster |
| $v_m$ | Poisson's ratio for the strain matrix |
| $V_c$ | Volumes per molecule for the strain cluster |
| $V_m$ | Volumes per molecule for the strain matrix |

## Table of Figures

## 7.1 Chapter Preface

In the previous chapters, the structural stability of HEAs was shown the be strongly influenced by the alloy composition's electronic structure, where 2-D plots of these parameters are sufficient to separate out the various simple and complex phases from one another, thereby providing a means to determine the possibility of a structure being present in any given composition. Ab-initio calculations performed using the Rigid Band Approximation (RBA) was employed to probe the electronic structure in further detail, as a function of the valence electron concentration. It was found that the RBA was sufficient to describe HEA alloys of a perturbed CoCrFeNi (here denoted CCFN) structure with some elemental addition A, to form CCFN-$A_x$. The success of the predictive results was limited by the fact that the potential of the starting composition (here, CCFN) must be determined with high accuracy, and the difficulty of determining the various parameters of an unknown composition, as discussed in the literature review. A simplified method for determining structural stability that attempts to naively describe the quantum mechanical Aufbau and Pauli principles using a distorted tetragonal structure as a reference point was developed in Chapter 5 and discussed.

In Chapter 6, the distorted tetragonal structure method is used to develop a strategy for designing a new alloy composition using as an example the hard-facing of combustion engine valves.

## 7.2 Design of alloy replacement for Stellite coating in hardfacing applications

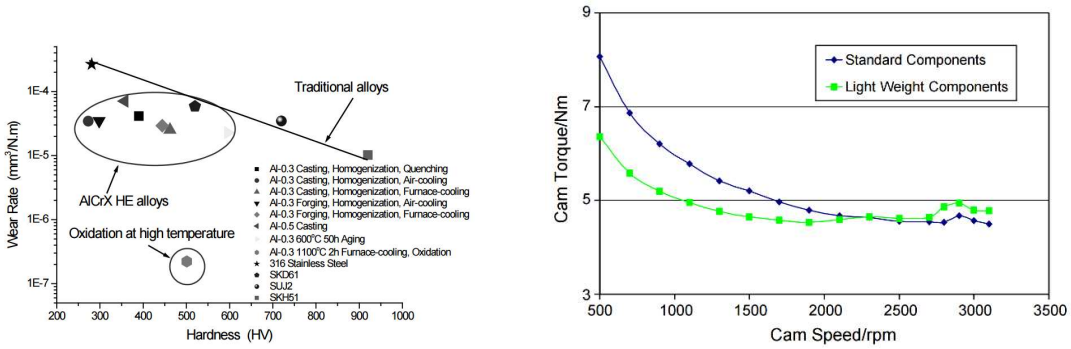


**Figure 42. (a)** Comparison of wear-resistance and hardness between some multicomponent alloys and traditional alloys [1]. **(b)** Effect of lightweighting of components on cam speed [2].

Providing a hard face for components exposed to wear in combustion engines is desirable so that lighter materials that may not have the prerequisite mechanical properties and corrosion resistance may be used. The use of these lightweight materials may increase the potential revolution per minute (rpm) of an engine, leading to higher specific power (horsepower/litre), and hence increased fuel efficiency [2,3], reducing emissions. This is shown in Figure 1. (b), where light weight components reduce torque at maximum engine speed up to 2,000 rpm, at which most engines are driven, and can contribute noticeable fuel savings.

In a valve as an example of such as component the key materials challenge is to obtain a good degree of toughness and corrosion resistance. In high volume production, X45CrSi9-3 Martensitic steel [4] is used as a valve material, while the hard-facing properties of the valve head are enhanced with a coating; the surface treatment can either be a nitriding process, or a coating may be applied such as the $Co_{64}Cr_{30}W_5C_1$ composition, with the commercial name Stellite-6. The Stellite 6 coating is often used in engines that run on unleaded fuel, so that durability can be enhanced in the absence of Pb lubrication from leaded fuel.

Al and Cr containing HEA compositions possess increased wear and corrosion resistance (*cf.* Figure 1) [1]. Research on the CoCrFeNi-Al composition has shown that the proportion of B2 intermetallic phases can be controlled as a function of the stoichiometry to achieve targeted mechanical properties by controlling the Al and Cr additions as shown in Chapters 4 and 5. Comparable hardness and yield strengths to Stellite 6 may thus be achieved by tuning the

stoichiometry, or through additional alloying additions. Possible precipitation of the B2 phase at increased temperatures may alleviate issues with thermal loading at increased engine temperatures. Another advantage of HEAs is that the thermal stability of its main phase renders it relatively insensitive to production conditions, reducing production costs by allowing larger tolerances for cooling rate and heat treatments in production.

Since corrosion is an electrochemical process the structure of the system has less influence on the corrosion properties. The corrosion resistance is a function of the alloying components and selection of potential alloy stoichiometries will have to take this into account. The remaining two key parameters, the degree of toughness and resistance to wear must first be related to $E_{Dist.}^{X-BC}$ values for further application into alloy design of a Stellite replacement.

## 7.3 Analysis of variation of yield stress to $E_{Dist.}^{X-FCC}$

As discussed in the Literature Review, recent advances in HEAs [5–8] report that the microstructures of HEAs are not, in fact, of a single phase but may instead contain multiple simple phases, complex phases (here all non-simple phases are called complex phases), or a mixture of both, showing a thermodynamically non-ideal nature which may be considered to originate from strain and chemical interactions between chemical species during the mixing process. The mixing of atoms in a structure leads to lattice strain when atoms of significantly different sizes are exchanged, leading to increased volume per atom values and excess enthalpies of mixing [9]. Despite this, it is notable that the lattice parameters of co-existing simple phases are very similar to each other [6–8]. Many of these mixed simple phase HEAs demonstrate attractive mechanical properties for engineering such as the ductility of the CoCrFeNi composition [10], the high fracture toughness of CoCrFeNiMn at low temperatures [11], and the thermal stability of CoCrFeNiCu [12,13]. Engineering these properties for use will require correlating the bulk mechanical properties of a composition to its possible phases, which remain a challenge due to the thermodynamic and kinetic complexity [14].

To illustrate, the four-component equiatomic CoCrFeNi composition (here denoted CCFN) HEA which has been extensively studied within the past 10 years is considered here for simplicity to possess a FCC simple phase [6–8,15]. Addition of a fifth element into a

composition to form CCFN-$A_x$ will either 1) maintain the simple FCC phase, 2) destabilise the simple FCC phase into a complex phase or combination of phases, or 3) destabilise the simple FCC phase into a BCC phase [16] depending the relative miscibility of additional alloying components. Although the relative stability of these CCFN-X compositions may be estimated from HEA empirical parameters (atomic size mixing, electronegativity), thermodynamic (enthalpy of mixing, configurational entropy) [17], their mechanical properties may only be empirically estimated by taking the weighted average of the hardness of the constituent phases, which must first be determined experimentally [15], and may be affected by composition.

In alloying, the inclusion of elements with large atomic size difference is thought to contribute a large strain energy leading to formation of regions of solid immiscibility that reduces the free energy of the system [18]. The increasing volume density of atoms in HEAs with higher number of components is associated with strain fields within their structures [15]. This dilatational strain field may be expressed only in terms of the elastic modulus and Poisson's ratio of the matrix and the substitutional element [9]. Through the Voigt average, this may be expressed in terms of the elastic constants $C_{11}$, $C_{12}$, and $C_{44}$. This change is analysed with $E_{Dist.}^{X-F}$ to determine if a link between phase structure and strain energy is present, and more importantly, how the combination of phases present and their mechanical properties may correspond to $E_{Dist.}^{X-FCC}$ and therefore provide a parameter to aid in the alloy design for hard-facing applications.

### 7.3.1 XRD characterisation of selected CCFN-$A_x$ compositions

For this investigation, HEA compositions CCFN, CCFN-$V_{0.3}$, CCFN-$V_{0.7}$, CCFN-$Ti_{0.4}$, CCFN-$Ti_{0.6}$, CCFN-$Al_{0.5}$, CCFN-$Pd_{0.5}$, CCFN-$Pd_{1.0}$, and CCFN-$Pd_{1.5}$ as listed in Table 11 are selected as they have been reported to lie within the stoichiometry range where the simple FCC phase is present as a majority phase, allowing subsequent Rietveld refinement to be simplified. Their stoichiometric compositions are listed in Figure 43. The samples are synthesised and characterised via XRD following the steps outlined in the methods section; synthesised 3 mm rods were further sectioned so that the length to diameter ratio of the rods was 2.0 +/- 0.1 (6 mm) following ASTM E9-89A standards for compression testing as mentioned in the methods section. Testing is performed on a Zwick/Roell Z050 compression testing machine utilising a 50 kN load cell under a strain rate of 2 x $10^{-4}s^{-1}$.

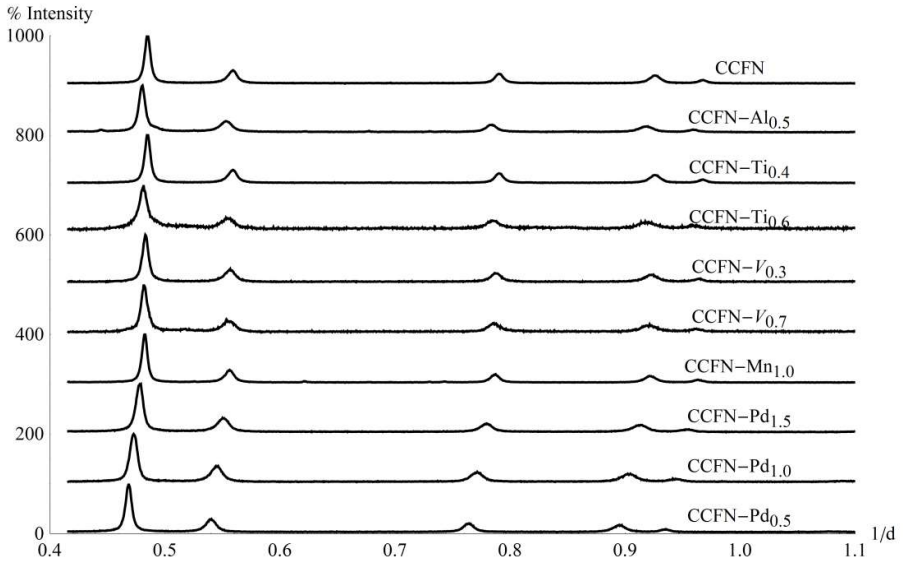


**Figure 43.** XRD patterns of FCC CCFN-X (X: Al, Ti, V, Mn, and Pd)

XRD patterns of the as-cast compositions show that the majority phase is of the simple FCC phase, which is in good agreement with the literature [7,19,20]. The lattice parameters are obtained from a Rietveld refinement of the data and are tabulated in Table 11. It is observed that in general, alloying additions to the CCFN structure expand the FCC lattice. The magnitude of the lattice expansion is, in turn dependent on the atomic radius of the elemental addition. Pd addition to CCFN causes the lattice constant to vary the most, from 3.55 to 3.62, 3.66, and 3.69 Å, for compositions CCFN-$Pd_{0.5}$, CCFN-$Pd_{1.0}$, and CCFN-$Pd_{1.5}$ respectively (*c.f.* Table 11). In contrast, additions of V, Ti, and Al only expand the lattice to

3.58, 3.59, and 3.60 Å for CCFN-$V_{0.3}$, CCFN-$Ti_{0.6}$, and CCFN-$Al_{0.5}$ respectively. Further additions of V, Ti, and Al expands the FCC lattice minimally past these values as complex phase precipitation steadily increases in tandem with these elemental additions [21,22].

The <111> peak of compositions CCFN-$Al_{0.5}$, CCFN-$Ti_{0.6}$, and CCFN-$V_{0.7}$ are observed to be asymmetric on the right shoulder of the peak, suggesting possible precipitation of a secondary phase. This is in accordance with $E_{Dist.}^{X-BCC}$ values for CCFN-$Al_{0.5}$, CCFN-$Ti_{0.6}$, and CCFN-$V_{0.7}$ which are positive and suggest the presence of non-FCC structures. As Al, Ti and V are B2, Laves C14, and Sigma phase stabilisers respectively from both binary phase diagrams sources [23] as well as experimental characterisation [6–8,15,20,22,24], the secondary phase is regarded as a complex phase, which is in agreement with the experimental characterisation here. $E_{Dist.}^{X-BCC}$ values corresponding to $E_{Dist.}^{X-BCC}(CCFN - Al_{0.5}) = 2.59$, $E_{Dist.}^{X-BCC}(CCFN - Ti_{0.6}) = 0.92$, and $E_{Dist.}^{X-BCC}(CCFN - V_{0.7}) = 0.21$ are at the cusp of the FCC/non-FCC transition where the onset of secondary phase presence begins.

**Table 11.** Compositions tested in the study, and their determined values for the lattice parameter, $a_{exp}$ (Å); dilatational strain value, $\phi_{strain}$; enthalpy of mixing, $\Delta H$ (kJ/mol); and valence electron concentration, VEC; and tetragonal distortion energy, $E_{Dist.}^{X-BCC}$.

| | **Nominal Composition** | **$a_{exp}$ (Å)** | **$\phi_{strain}$** | **$\Delta H$ (kJ/mol)** | **VEC** | **$E_{Dist.}^{X-BCC}$** |
|---|---|---|---|---|---|---|
| **CCFN** | $Co_{25}Cr_{25}Fe_{25}Ni_{25}$ | 3.55 | N/a | -3.75 | 8.25 | -4.20 |
| **CCFN-$Al_{0.5}$** | $Co_{22}Cr_{22}Fe_{22}Ni_{22}Al_{11}$ | 3.60 | 7.292 | -9.98 | 7.67 | 2.59 |
| **CCFN-$Ti_{0.4}$** | $Co_{23}Cr_{23}Fe_{23}Ni_{23}Ti_{09}$ | 3.59 | 4.306 | -9.43 | 7.86 | -0.96 |
| **CCFN-$Ti_{0.6}$** | $Co_{22}Cr_{22}Fe_{22}Ni_{22}Ti_{13}$ | 3.59 | 5.277 | -9.77 | 7.70 | 0.92 |
| **CCFN-$V_{0.3}$** | $Co_{23}C3_{23}Fe_{23}Ni_{23}V_{07}$ | 3.58 | 2.398 | -6.21 | 8.02 | -2.43 |
| **CCFN-$V_{0.7}$** | $Co_{21}Cr_{21}Fe_{21}Ni_{21}V_{15}$ | 3.59 | 5.725 | -8.32 | 7.77 | 0.21 |
| **CCFN-$Mn_{1.0}$** | $Co_{20}Cr_{20}Fe_{20}Ni_{20}Mn_{20}$ | 3.59 | 13.74 | -4.16 | 8 | -2.01 |
| **CCFN-$Pd_{0.5}$** | $Co_{22}Cr_{22}Fe_{22}Ni_{22}Pd_{11}$ | 3.62 | 26.79 | -5.02 | 8.44 | -6.37 |
| **CCFN-$Pd_{1.0}$** | $Co_{20}Cr_{20}Fe_{20}Ni_{20}Pd_{20}$ | 3.66 | 65.14 | -5.81 | 8.6 | -5.91 |
| **CCFN-$Pd_{1.5}$** | $Co_{18}Cr_{18}Fe_{18}Ni_{18}Pd_{27}$ | 3.69 | 110.0 | -5.98 | 8.78 | -6.41 |

### 7.3.2 Mechanical properties of selected CCFN-$A_x$ compositions

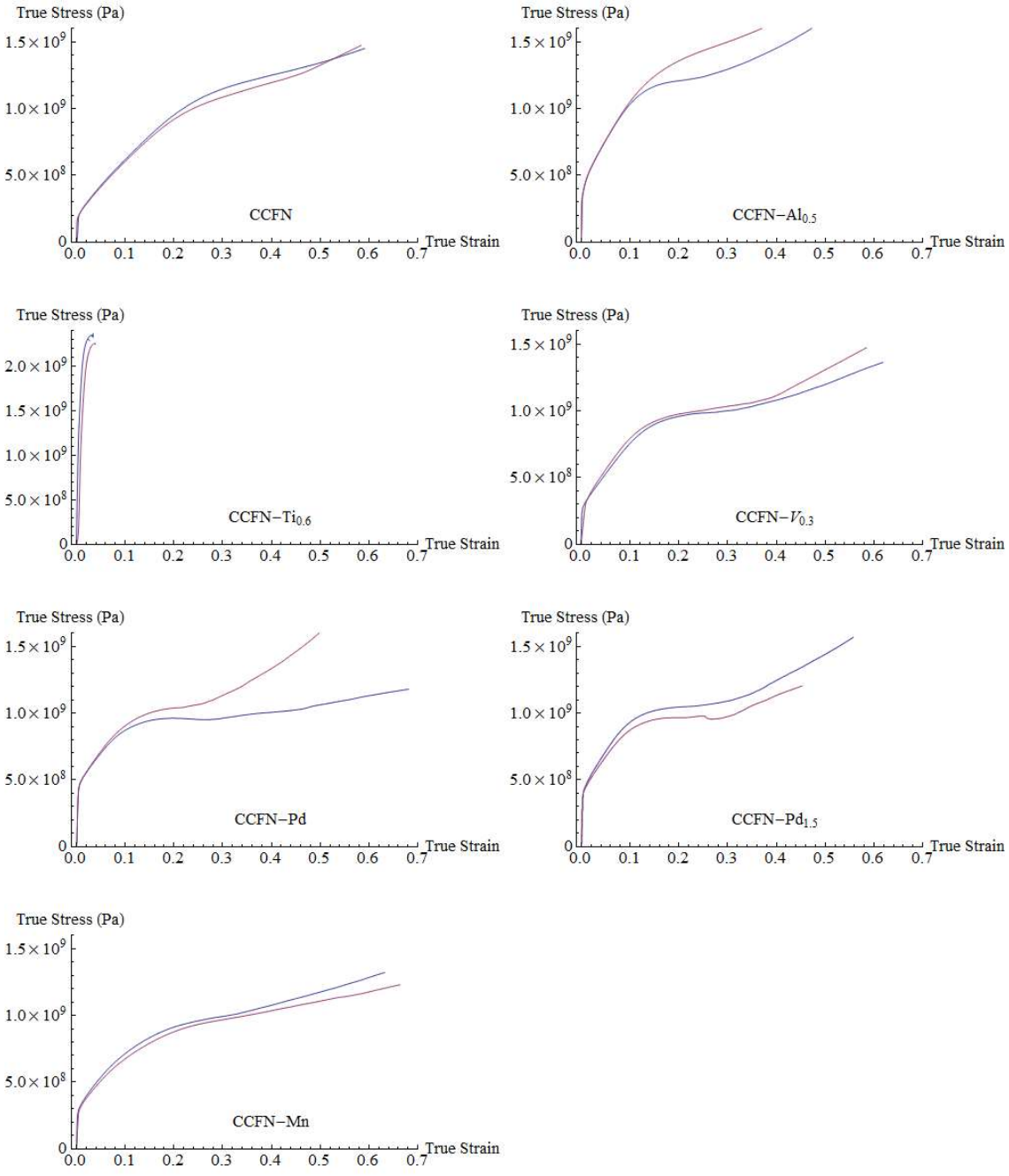


**Figure 44.** Compression testing results of CCFN, CCFN-$Al_{0.5}$, CCFN-$V_{0.3}$, CCFN-Mn and CCFN-Pd HEA compositions with two repeats.

For the CCFN, CCFN-$Al_{0.5}$, CCFN-$Ti_{0.6}$, CCFN-$V_{0.3}$, CCFN-Mn, and CCFN-Pd compositions, two compression testing samples were prepared each. The obtained results were corrected for

the machine compliance and Figure 44 presents the compression testing results of all CCFN-X (X: Al, Ti, V, Mn, and Pd) investigated in this communication.

Calculation of the errors can be found in the Appendix. A visual inspection of Figure 44 shows that the repeats are in good agreement with one another. The elastic modulus and 0.2% yield stress of the compositions were determined from the initial gradient of the compression test curves. The results are shown below in Table 12.

**Table 12.** 0.2% Yield Strength (MPa), Experimental Young Modulus (GPa), and Young Modulus (GPa) values from literature where applicable for the selected composition.

| Composition | 0.2% $\sigma_{Yield}$ (MPa) | $E_y$ Exp. (GPa) | $E_y$ Lit. (GPa) | Ref |
|---|---|---|---|---|
| CCFN | 190 | 100 | 171 | [11] |
| CCFN-$Al_{0.6}$ | 360 | 266 | 250 | [16] |
| CCFN-$Ti_{0.6}$ | 1600 | 264 | N/A | N/A |
| CCFN-$V_{0.3}$ | 290 | 160 | N/A | N/A |
| CCFN-Mn | 280 | 105 | 137 | [25] |
| CCFN-Pd | 240 | 150 | N/A | N/A |
| CCFN-$Pd_{1.5}$ | 382 | 155 | N/A | N/A |

The experimental repeats are found to be in good agreement with one another. The experimentally determined elastic modulus of CCFN, CCFN-$Al_{0.6}$, and CCFN-$Mn_{1.0}$ were found to be in reasonably good agreement with previously determined elastic moduli. Of the determined 0.2% yield strengths, CCFN-Ti0.6 (1600 MPa) is observed to possess the highest, followed by CCFN-$Pd_{1.5}$ (382 MPa), CCFN-$Al_{0.6}$ (360 MPa), CCFN-$V_{0.3}$ (290 MPa), CCFN-Mn (280 MPa), CCFN-Pd (240 MPa), and CCFN (190 MPa). Furthermore from Figure 44 it can be seen that CCFN-$Ti_{0.6}$ has experienced brittle failure while CCFN-$Al_{0.6}$, CCFN-$V_{0.3}$, CCFN-Mn, CCFN-$Pd_{1.5}$, and CCFN-Pd experienced ductile fracture. These observations appear to be in good agreement with the XRD results where complex phase precipitation is expected in the CCFN-$Al_{0.6}$ and CCFN-$Ti_{0.6}$ compositions.

### 7.3.3 Dilatational strain analysis as a function of the enthalpy of mixing

The effects of the possible presence of strain within a HEA structure can be considered to be two-fold: 1) higher strain energy, $\phi_{\mathrm{strain}}$ increases the barrier for dislocation movement and hence affects mechanical properties [26], and 2) Heterogenous nucleation of a secondary

phase is only possible when the driving force for nucleation, dU is greater than the dilatational strain, $\phi_{\text{strain}}$ affecting the formation of complex phases [27]. The strain energy per atom in a cluster for an initially unstrained matrix is given by:

$$\phi_{strain} = \frac{(V_m - V_c)^2 E_{Y,c} E_{Y,m}}{3V_c\left[2(1-2v_c)E_{Y,m} + (1+v_m)E_{Y,c}\right]} \quad (1)$$

where $V_m$ and $V_c$ are the volumes per molecule for the matrix and the cluster respectively, $E_{Y,m}$ and $E_{Y,c}$ are the Young's modulus for the matrix and the cluster respectively, and $v_m$ and $v_c$ are the Poisson's ratio for the matrix and the cluster respectively. The Voigt average [28], where it is assumed that a homogenous strain is present in the structure for cubic structures is taken so that the elastic strain energy, $\phi_{strain}$ can be expressed as a function of the elastic constants $C_{11}$, $C_{12}$, and $C_{44}$:

$$\phi_{strain} = \frac{(V_m - V_c)^2 (C_{11,m} - C_{12,m} - 3C_{44,m})(2C_{11,c} + 2C_{12,c})}{3V_c\left[4C_{11,m} - 4C_{12,m} + 12C_{44,m} + 5C_{11,c} + 10C_{12,c}\right]} \quad (2)$$

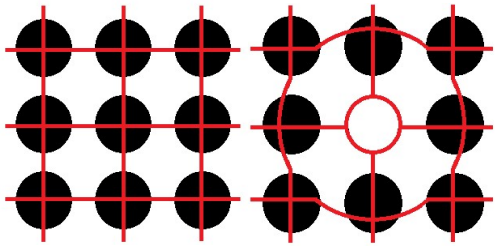

**Figure 45.** Dilational strain induced by the substitution of a single atom.

where $C_{11,m}$, $C_{12,m}$, and $C_{44,m}$ are the elastic constants of the matrix and $C_{11,c}$, $C_{12,c}$, and $C_{44,c}$ are the elastic constants of the matrix. As the equimolar CCFN composition has been previously determined to mainly consist of the simple FCC phase [6–8], a naïve simplification of the alloying process may be taken. The substitution of a CCFN matrix with some foreign element, X, is considered, and characterised by an associated $\phi_{strain}$ value due to elastic constant and volume mismatch between the matrix and the cluster. The dilational strain induced by the substitution of a single atom is illustrated in Figure 45 through eq. 2, the change in strain energy by the modification of the CCFN composition with some alloying element, A to form CCFN-$A_x$.

**Table 13.** Elastic constants of the four-component CCFN composition and elemental V, Al, and Ti in their stable phases at standard conditions, obtained from literature.

| | $C_{11}$ (MPa) | $C_{12}$ (MPa) | $C_{44}$ (MPa) | Ref |
|---|---|---|---|---|
| **CCFN** | 238 | 151 | 168 | [29,30] |
| **Al** | 162 | 92 | 47 | [30,31] |
| **Ti** | 107 | 61 | 29 | [30,32] |
| **V** | 237 | 122 | 48 | [30,33] |
| **Mn** | 257 | 272 | 105 | [30] |
| **Pd** | 198 | 156 | 70 | [30] |

Rietveld refined lattice parameters listed in Table 11 are substituted into Eq. 2 to obtain the dilational strain energy induced by addition of an alloying element into the CCFN matrix, $\phi_{strain}^{exp}$ where it is observed that for compositions whose alloying additions only show the simple phase to be present, CCFN-$Mn_{1.0}$ (19.74), CCFN-$Pd_{0.5}$ (26.79), CCFN-$Pd_{1.0}$ (65.14), and CCFN-$Pd_{1.5}$ (110.0), are observed to possess higher $\phi_{strain}^{exp}$ values as compared to CCFN-$V_{0.3}$ (4.71), CCFN-$V_{0.7}$ (7.90), CCFN-$Ti_{0.4}$ (3.59), CCFN-$Ti_{0.6}$ (6.99), and CCFN-$Al_{0.5}$ (8.64) which adopt a majority complex phase structure at higher values of V, Ti, or Al addition [20]. This may be attributed to the fact that increased strain energy increases the energy associated with the compositional fluctuations within the solid solution and is known to reduce the driving force for nucleation from a strained matrix [27].

### 7.3.4 Comparison of $\Delta H$ and $E_{Dist.}^{X-BCC}$ to describe variation in $\phi_{strain}$ values

A plot of the strain energy and the enthalpy of mixing is presented in Figure 46 (Left) where enthalpy of mixing values are obtained from the Miedema model, which evaluates the interaction between a volumetric effect, the chemical potential for electronic charge, and the change in the electron density at the Wigner-Seitz boundary [34]. The strain energy associated with the bending and stretching of bonds is thought to play a role in determining the mixing enthalpy of the system [9] and as the strain energy is attributed mainly to the volumetric difference, the observed deviation between the two groups whose alloying addition stabilise the simple phase (Mn and Pd) and destabilise the simple phase (Al, Ti, and V) may be attributed to a change in the electron density and electronegativity difference. The partition between simple and complex phases in this 2-dimensional plot is in line with

previous investigations which have shown the dependence of simple/complex phase presence on the electron density [35], and the values of $\Delta H$ at which these phases are stabilised [17]. The onset of complex phase formation is characterised by immediate destabilisation of the electronic structure by increased bonding directionality as discussed in Chapter 3 may be linked to the ability of the structure to accommodate strain in the system.

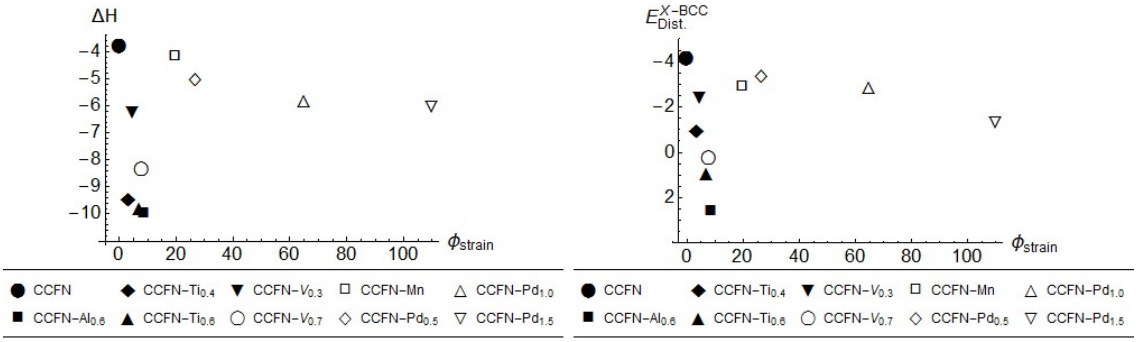


**Figure 46. (Left).** Plot of the strain energy and the enthalpy of mixing; **(Right)** Plot of the strain energy against $E_{Dist.}^{X-BCC}$.

Figure 46 (Right) displays a plot of the strain energy against $E_{Dist.}^{X-BCC}$. While a rigorous comparison of $E_{Dist.}^{X-FCC}$ and $\Delta H$ is not performed in this chapter as the aim is to obtain a correlation between $E_{Dist.}^{X-FC}$ and compositional mechanical properties, the graphical comparison in Figure 46 shows a correlation between both when $E_{Dist.}^{X-FCC}$ values are reversed. The similarity between $E_{Dist.}^{X-FCC}$ and $\Delta H$ may be attributed to the use of an electronegativity scale which is equivalent to the chemical potential at 0 K to represent both functions. As mentioned in Chapter 4, the ratio between the enthalpy of mixing and the difference in the number of valence electrons squared, $\Delta H / (\Delta n)^2$ from Miedema's model has been shown [36] to start deviating from theoretical predictions between $4 < n < 7$, which is regarded as a zone of complex phase presence in HEAs. This limit of *n* is similar to the cut-off point for FCC formation determined using the distorted tetragonal model discussed in Chapter 5. A graphical comparison of Figure 46 (Left) and Figure 46 (Right) shows that the dispersion of the points possesses increased linearity in the 2-D plot of Figure 46 (Right) in comparison with Figure 46 (Left). The accuracy of each function with respect to the ability to represent $\phi_{strain}$, or their exact co-dependence cannot be determined from just the graphical comparison, but merely indicates that both functions

may be representative of one another. In any case, in further discussion, for predictive purposes for all observed trends, $\Delta H$ values can be substituted for by $E_{Dist.}^{X-FCC}$ values.

### 7.3.5 Effect of $\phi_{strain}$ on complex phase presence and mechanical properties

The driving force for nucleation of a secondary phase from a matrix is, as mentioned previously, partly dependent on the strain energy of the system with the effective driving force for nucleation of this secondary phase defined as:

$$E_{eff} = -(\Delta\mu - \phi_{strain}^{exp}) \quad (3)$$

where $\Delta\mu = kT\ Log(\frac{a}{a_e})$ and $a$ and $a_e$ are the actual and equilibrium activity of the old solid solution phase, and $k$ and $T$ are the Boltzmann constant and temperature, respectively. The above equation covers the decay of solids through condensation of 'atomic vacancies' arising from the old phase dissolved in them and is valid for all instances where $a > a_e$. This condensation leads to the appearance of macroscopic cavities i.e. the new phase in the solid. The activity, $a$ is defined by:

$$\mu = \mu_0 + RT\ Log(a) \quad (4)$$

where $\mu$ and $\mu_0$ are defined as the chemical potential of the system and chemical potential at the standard rate of the vacancy, and $R$ and $T$ are the gas constant and the temperature, respectively. For a dilute solution, the activity may be approximated as its molar concentration; moreover it may be approximated that at equilibrium, $a_e \approx M_{CCFN} \approx 1$. Eq. 3 therefore transforms to:

$$E_{eff} = -(\frac{\mu-\mu_0}{N} - \phi_{strain}^{exp}) \quad (5)$$

where the chemical potential may be taken as the rule-of-mixtures Mulliken electronegativity of the composition of the matrix, and the cluster to be:

$$u \approx -\chi_{Mulliken} \approx \sum_i(-\frac{I+A}{2})_i x_i \quad (6)$$

where $I$ and $A$ are the first ionisation energy and electron affinity respectively and $i$ represents the total number of components in the alloy system and therefore $\Delta\mu$ transforms into:

$$\Delta\mu = \frac{\sum_{i_{CCFN}}(-\frac{I+A}{2})_{i_{CCFN}} x_{i_{CCFN}} - \sum_{i_{CCFN-A}}(-\frac{I+A}{2})_{i_{CCFN}} \quad x_{i_{CCFN-A}})}{N} \tag{7}$$

By substituting Eq. 7 into Eq. 3, the effective driving force may be determined. It therefore follows that for nucleation to proceed the condition $\Delta\mu > \phi_{strain}$ must be fulfilled so that $E_{eff} < 0$. In Eq. 7, the driving force for nucleation is dependent upon the chemical potential and its magnitude relative to $\phi_{strain}$. Values for $E_{eff}$ are determined from known ionisation energies and electron affinities using a weighted average for each composition, with each stoichiometry being assumed to be a random solid solution.

From the results it is observed that compositions containing simple-phase stabilising alloying additions, CCFN-$Mn_{1.0}$ (12.12), CCFN-$Pd_{0.5}$ (29.61), CCFN-$Pd_{1.0}$ (70.2), and CCFN-$Pd_{1.5}$ (117.2) are larger than those containing complex-phase alloying additions: CCFN-$V_{0.3}$ (2.31), CCFN-$V_{0.7}$ (2.79), CCFN-$Ti_{0.4}$ (0.73), CCFN-$Ti_{0.6}$ (0.79), and CCFN-$Al_{0.5}$ (1.33). Although no secondary phases are observed in these samples, a plot of $E_{eff}/\phi_{strain}^{exp}$ against $\Delta H$ as shown in Fig. 46 (b) shows that the effective driving force for nucleation, $E_{eff}$ normalised to the strain energy, $\phi_{strain}$ decreases as $\Delta H$ decreases into more negative regions, towards regions of complex phase formation [17], showing that the $\Delta\mu > \phi_{strain}$ condition may be reached with increasing alloying additions of Ti, V, or Al. The reduced strain energy of Ti, V, and Al containing compositions may be caused by changes in energy caused by phase transformation in the solid solutions with more negative $\Delta H$ values due to increased ordering. The formation of complex phases would modify the total energy balance at the interface between the matrix and the secondary phase for incoherent alloying additions, which may be expressed as:

$$\gamma = \gamma_0 + \Delta G \tag{8}$$

where $\gamma$ is the surface energy between the matrix/secondary phase, $\gamma_0$is surface energy between grain boundaries before the nucleation of any secondary phase. $\Delta G$ is regarded as the Gibbs free energy per unit area for formation of the secondary phase. Since $\Delta G$ is negative, the surface energy is reduced by the formation of a complex phase. Negative enthalpy of mixing values may thus provide a pathway for strain reduction for compositions containing complex-phase stabilising elements.

The inability for formation of a complex phase as a mechanism for strain reduction is reflected in the increasing strain energy that is consistent for all FCC simple phases (CCFN-Mn and CCFN-Pd). Due to the increased strain energy, system with such characteristics may exhibit regions of solid immiscibility where the free energy is reduced by separation of the composition into regions that possess compositions closer to the unalloyed state; this may explain the degrees of separation that have been observed for some compositions where multiple simple phases appear that are enriched with particular elemental combinations [5–8]. It may be inferred that the addition of anisotropic alloying elements leads to increased directional bonding, and may reduce the total free energy through the formation of complex structures that can reduce the surface energy in the structure (*cf.* Eq. 8). As change in bond anisotropy affects the elastic anisotropy of the structure [37], the precipitation of complex phases leads to deleterious effects on the bulk mechanical properties [15]. As shown in Figure 47 the elastic modulus of compositions possessing the simple structure are less sensitive to an equivalent reduction in strain energy as compared to compositions possessing complex structure(s). As a result, complex phase(s) containing compositions possess higher elastic modulus and yield stress for any equivalent value of elastic strain.

One concern is that the strain energy presented in this chapter is derived by utilising the CoCrFeNi composition as the matrix element, with the assumption that the composition is a solid solution that is thermodynamically near-ideal. This is a simplification as the composition is considered to contain multiple similar simple FCC phases but appears to provide good properties in comparison to all other HEA CCFN-X compositions presented [6–8]. The relationship between the elastic modulus and calculated dilatational strain values are shown in Figure 47 below. As expected, the elastic modulus appears to decrease with $\phi_{strain}$ following a similar trend with the $\Delta H - \phi_{strain}^{exp}$ relationship, whereby the elastic modulus of complex phase stabilised compositions such as CCFN-$V_{0.3}$ and CCFN-$Al_{0.6}$ are observed to increase much more rapidly as compared to simple phase stabilised compositions such as CCFN-Mn and CCFN-Pd.

From an electronic perspective, complex phase stabilised HEA compositions are reported to possess lower electron densities compared to simple phase stabilise HEA compositions at any particular Wigner-Seitz radius, suggesting the possibility of chemical bonding of increased covalent nature and fewer electrons delocalised around the Wigner-Seitz radius

[38] and is associated with reduced dislocation generations and a smaller dislocation core size [39] leading to reduced mobility for dislocations [40], thus an increased number of dislocations may be accumulated in each slip plane [41]. This leads to an increase in strength [42], which is observed in Figure 47 in comparison with the simple phase where the elastic modulus increases at a much slower rate.

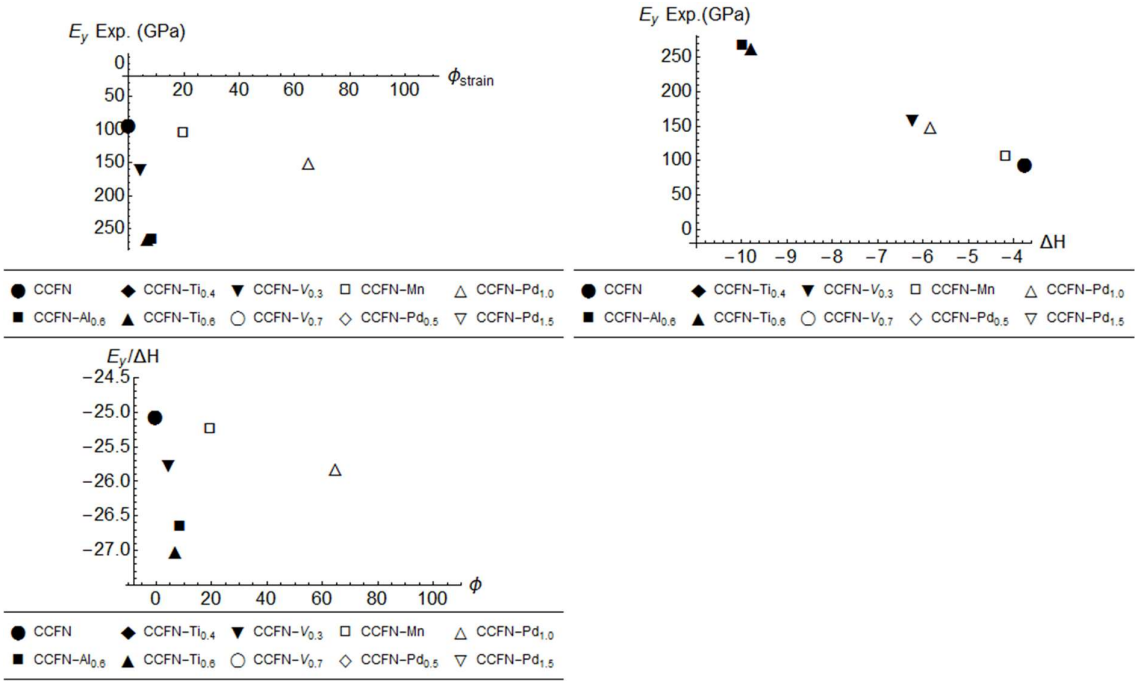


**Figure 47.** Clockwise from top-left: **(a)** Plot of the elastic modulus against the calculated strain energy of CCFN, CCFN-Al, CCFN-$Ti_{0.6}$, CCFN-Mn, and CCFN-Pd showing a separation between complex-phase and simple phase stabilising additions; **(b)** A plot of the elastic modulus of the previous compositions against their enthalpy of mixing values, showing the relationship between them, and; **(c)** For comparison with; (b) a plot of the enthalpy of mixing against the calculated strain energy showing also the separation between complex and simple phase containing HEAs.

From Figure 47 comparing the top and the bottom figure shows that the enthalpy of mixing appears to be linked to the changes in the elastic modulus, which is in good agreement with Christian who reports that the strain energy is associated with the mixing enthalpy of the system [9]. From Eq. 2 it may be seen that the strain energy is derived from both the elastic anisotropy mismatch and volume mismatch between the CCFN matrix and the alloying addition, and that both may be thought to influence structural stability of the resulting HEA composition; these parameters are similar to previous methods which employ the atomic

radius as a means of determining structural stability, following Hume-Rothery rules [17,43]. The ability to distinguish between compositions that will eventually lead to simple and complex phase presence with even small amounts of alloying additions is demonstrated in the 2-dimensional plots of $\Delta H - \phi_{strain}^{exp}$ and $E_y - \phi_{strain}^{exp}$. This separation is in good agreement with the results presented in a previous communication where addition of alloying components which stabilise the complex phase is immediately preceded by a decrease in the electron density for any equivalent Wigner-Seitz radius.

By plotting $E_y - \Delta H$ it may be seen from Figure 47b that for the five-component HEA compositions studied here, experimentally determined $E_y$ scales well with $\Delta H$ with:

$$\Delta H = -0.0376\ E_y$$

with $E_y$ written in units of GPa for the CCFN-X compositions tested in this paper. The identical trends observed in both $\Delta H - \phi_{strain}^{exp}$ and $E_y - \phi_{strain}^{exp}$ curves establish that the enthalpy of mixing may be used to determine roughly the elastic modulus of a given HEA system despite the observed influence of the alloying addition on the dilatational strain.

### 7.3.5 Section summary

In summary, in this study it has been determined that:

1. Predictive trends involving enthalpy of mixing values may be substituted for by values of $E_{Dist.}^{X-FCC}$.
2. Negative enthalpy of mixing values may provide a pathway for strain reduction for compositions containing complex-phase stabilising elements through the precipitation of complex phases that lower the interfacial energy.
3. A separation between compositions that stabilise the simple phase and the complex phase is shown here suggesting that the effect of alloying addition on mechanical properties is dependent only on the dilatational strain.
4. The enthalpy of mixing is shown to be useable as an empirical parameter to predict the elastic modulus of the CCFN-X (X: Al, Ti, V, Mn, and Pd) HEA compositions that have been investigated in this study. These values do not give any indication of the ductility of the compositions, and further analysis of the dilatational strain with

regards to ductility would be required to correctly sift out HEA compositions that may be used during the alloy design process.

## 7.4 Strategy for alloy design

From previous discussion, it is shown that values of $E_{Dist.}^{X}$ scale with the elastic modulus. This scaling is reflected in the analysis of the dilatational strain where the precipitation of a complex phase is thought to modify the total energy balance at the interface between the matrix and the secondary phase for incoherent alloying additions, which has the effect of reducing the surface energy by the formation of a complex phase, lowering the overall total energy. The similarity to $E_{Dist.}^{X}$ is attributed to the treatment taken in derivation of $E_{Dist.}^{X}$, where the total energy is considered as a function of the interatomic distance between the neighbours in a modified distorted tetragonal cell.

In order to facilitate the design of a replacement alloy composition for Stellite-6, a prediction scheme for the desired mechanical properties to be obtained from a HEA composition must be developed. Due to the lack of tensile test data for HEA compositions in the literature, hardness values are substituted instead. Hardness values could be used as an indication of the elastic modulus as long as the ratio of contribution of the elasticity and plasticity of the material to its overall strength remains similar [44] (a rather coarse assumption). In Table 5 several HEA compositions and their associated hardness values in Vickers hardness (Hv) are tabulated together with the corresponding structure present, and value of $E_{Dist.}^{X}$. The column Ref. indicates the reference of the particular composition and its associated hardness values and phase present. (*) indicates that the hardness values for the denoted compositions have been approximated from the yield strengths obtained from Section 6.4.2 using the relationship $Hv \approx \frac{\sigma_Y}{0.3}$, while (**) indicates new compositions that have been synthesized following the guidelines as described in the Methods section and hardness tested to verify the model.

### 7.4.1 Populating data table to obtain trends of $E_{Dist.}^{FCC}$ with Vickers hardness (HV)

**Table 14.** List of selected HEA compositions and their associated values of hardness values in Vickers hardness (Hv), structures present, and calculated values of $E_{Dist.}^{X}$. References are indiciated where appropriated as well.

| Composition | Hardness (HV) | Structure | $E_{Dist.}^{FCC}$ | $E_{Dist.}^{BCC}$ | $E_{Dist.}^{COMPLEX}$ | Ref. |
|---|---|---|---|---|---|---|
| **FeNiCrCuCo** | 286.00 | FCC | -6.82 | | | [45] |
| **$AlCo_{0.5}CrCuFeNi$** | 473.00 | SIMPLE | -6.62 | | | [46] |
| **$CoCrFeNi\text{-}Pd_{1.5}$** | 344.44 | FCC | -6.41 | | | * |
| **CoCrFeNi-Pd** | 333.33 | FCC | -5.91 | | | * |
| **CoCrFeNiCu** | 219.00 | FCC | -5.91 | | | ** |
| **$CoCrCuFeNiAl_{0.5}$** | 150.00 | FCC | -5.89 | | | [47] |
| **$Al_{0.5}CoCrCuFeNi$** | 208.00 | FCC | -5.14 | | | [46] |
| **$CoCrCuFeNiAl_{0.5}$** | 200.00 | FCC | -4.59 | | | [44] |
| **CoCrFeNi** | 232.00 | FCC | -4.24 | | | ** |
| **CoCrFeNi** | 222.22 | FCC | -4.24 | | | * |
| **CoCrNiCu** | 300.00 | FCC | -4.04 | | | ** |
| **FeNiCrCuAl** | 342.00 | SIMPLE | -3.77 | | | [45] |
| **$CoCrFeNiCuAl_{0.5}V_{0.2}$** | 200.00 | FCC | -3.71 | | | [24] |
| **$AlCoCr_{0.5}CuFeNi$** | 367.00 | SIMPLE | -3.32 | | | [43] |
| **AlCoCrCuFeNi** | 420.00 | SIMPLE | -3.14 | | | [43] |
| **$CoCrFeNiCuAl_{0.5}V_{0.4}$** | 225.00 | FCC | -2.91 | | | [45] |
| **CoCrFeNi-Mn** | 255.56 | FCC | -2.90 | | | * |
| **$CoCrFeNi\text{-}V_{0.3}$** | 355.56 | FCC | -2.44 | | | * |
| **$CoCrFeNiCuAl_{0.5}V_{0.6}$** | 325.00 | SIMPLE | -1.99 | | | [45] |
| **$AlCoCrCuFe_{0.5}Ni$** | 418.00 | SIMPLE | -1.87 | | | [43] |

| | | | | | | |
|---|---|---|---|---|---|---|
| **$Co_{64}Cr_{30}W_5C_1$** | 413.00 | FCC | -1.72 | | | [48] |
| **$CoCrFeNiCuAl_{0.5}V_{0.8}$** | 450.00 | COMPLEX | -1.09 | | | [45] |
| **$AlCoCrCuFeNi_{0.5}$** | 423.00 | SIMPLE | -0.18 | | | [43] |
| **$CoCrCuFeNiAl_{1.0}$** | 400.00 | SIMPLE | -0.07 | | | [44] |
| **$AlCoCrCu_{0.5}FeNi$** | 458.00 | BCC | 0.84 | | | [43] |
| **FeNiCrCuMn** | 296.00 | SIMPLE | 5.50 | | | [42] |
| **$Co_{16}Cr_{16}Fe_{16}Al_{16}Ni_{36}$** | 440.00 | BCC | | 2.89 | | [44] |
| **$CoCrCuFeNiAl_{1.5}$** | 500.00 | BCC | | 6.05 | | [44] |
| **CuTiVFeNiZr** | 590.00 | N/A | | 13.44 | | [49] |
| **$CoCrCuFeNiAl_{2.0}$** | 550.00 | BCC | | 14.05 | | [44] |
| **$CoCrCuFeNiAl_{2.5}$** | 600.00 | BCC | | 23.84 | | [44] |
| **$CoCrCuFeNiAl_{3.0}$** | 670.00 | BCC | | 35.54 | | [44] |
| **MoTiVFeNiZr** | 740.00 | N/A | | 44.31 | | [46] |
| **AlTiVFeNiZrCoCr** | 780.00 | N/A | | 55.67 | | [46] |
| **AlTiVFeNiZrCo** | 790.00 | N/A | | 65.12 | | [46] |
| **AlTiVFeNiZr** | 800.00 | N/A | | 111.86 | | [46] |
| **$Cr_{20}Fe_{30}Mo_{35}Cu_{15}$** | 500.00 | COMPLEX | | | -0.66 | ** |
| **$CoCrFeNiCuAl_{0.5}V$** | 650.00 | COMPLEX | | | -0.07 | [45] |
| **CoCrFeNi -$Ti_{0.6}$** | 586.67 | COMPLEX | | | 0.91 | * |
| **$CoCrFeNiCuAl_{0.5}V_{1.2}$** | 575.00 | COMPLEX | | | 0.93 | [45] |
| **$AlCoCrFe_{2.0}Mo_{0.5}Ni$** | 660.00 | COMPLEX | | | 1.44 | [50] |
| **$CoCrFeNiCuAl_{0.5}V_{1.4}$** | 580.00 | COMPLEX | | | 1.89 | [45] |
| **$CoCrFeNiCuAl_{0.5}V_{1.6}$** | 590.00 | COMPLEX | | | 2.93 | [24] |
| **$Co_{25}Cr_{25}Cu_{15}Ni_{15}Al_{20}$** | 610.00 | N/A | | | 3.57 | ** |

| | | | | | | |
|---|---|---|---|---|---|---|
| **$AlCoCrFe_{1.5}Mo_{0.5}Ni$** | 650.00 | COMPLEX | | | 3.86 | [50] |
| **$CoCrFeNiCuAl0.5V_{1.8}$** | 595.00 | COMPLEX | | | 4.05 | [45] |
| **$CoCrFeNi\text{-}Al_{0.6}$** | 591.11 | B2 | | | 4.33 | * |
| **$CoCrFeNiCuAl_{0.5}V_{2.0}$** | 590.00 | BCC | | | 5.10 | [24] |
| **FeNiCrCoZr** | 566.00 | COMPLEX | | | 5.18 | [42] |
| **$AlCoCrFeMo_{0.5}Ni$** | 725.00 | COMPLEX | | | 7.52 | [46] |
| **CuTiVFeNiZrCo** | 630.00 | N/A | | | 8.08 | [49] |
| **CuTiVFeNiZrCoCr** | 680.00 | N/A | | | 8.91 | [49] |
| **$AlCoCrFe_{0.5}Mo_{0.5}Ni$** | 750.00 | COMPLEX | | | 12.65 | [46] |
| **MoTiVFeNiZrCo** | 790.00 | N/A | | | 27.41 | [49] |

The following figure, Figure 48, shows a graphical plot of the data shown in Table 5, where the compositions have been separated depending on the respective structure as determined from the corresponding references in literature, or from experimental XRD characterisation. The construction of the approximated $E_{Dist.}^{X}$ values plotted against $HV$ show a competition between the HEA complex phases and simple BCC phase in achievable values of hardness. It is observed from the 2-D plot that when the condition $E_{Dist.}^{X} > 0$ is reached, the achievable hardness of a HEA composition is dependent on the stabilisation of either the simple BCC structure, or of complex structures. This deviation in achievable hardness as a function of $E_{Dist.}^{X}$ may originate from the proportion of contribution of the elasticity and plasticity of the phase to the overall mechanical properties [44]. The formation of complex phases leads to a reduction in plasticity, which can be explained by the increase in bond directionality on formation of complex phases which is consistent with the analyses and the intermediate conclusions drawn thus far in the thesis. With an increase in bond directionality, the lattice distortion induced by the presence of a particular dislocation is enhanced, increasing the minimum stresses required for dislocation motion [51].

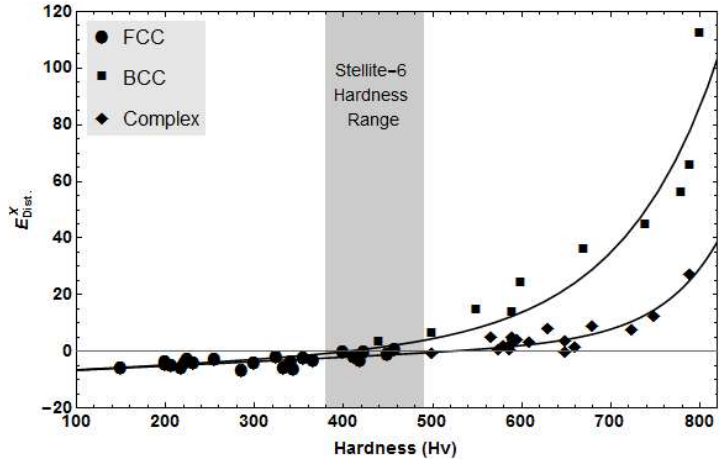


**Figure 48.** 2-D plot of $E^X_{Dist.}$against Vickers hardness (HV) values, showing the dependence of HEA hardness on the phase present. As discussed in Chapter 5, $E^X_{Dist.}$ values are able to indicate the relative stability of FCC and non-FCC structures; the divergence in the plot indicates the difference in properties exhibited by the BCC and complex structures. The hardness range attributed to the Stellite-6 composition is indicate in the plot, as well.

As mentioned earlier, $\sigma_Y$ values of CCFN-type compositions (in this section denoted by its full name, keeping with the naming convention of similar HEA compositions found in the literature search) CoCrFeNi, CoCrFeNi-$Pd_{1.0}$, CoCrFeNi-$Pd_{1.5}$, CoCrFeNi-Mn, CoCrFeNi-$V_{0.3}$, CoCrFeNi-$Ti_{0.6}$, and CoCrFeNi-$Al_{0.6}$ have been converted into Vickers hardness through the relationship $HV \approx \frac{\sigma_Y}{0.3}$. Converted hardness values are observed to conform to the plotted trends very well, as shown in Figure 48. The trends are further tested through the synthesis of several HEA compositions selected to test the capabilities of the 2-D plot for the design of alloy compositions with specific hardness and to verify the trends in the 2-D plot in Figure 48. The selected compositions are Cu-based HEAs which have been reported to offer good thermal stability [13], and Al-based HEAs which also offer good oxidisation resistance at high temperatures [1,22]. The selected compositions are CoCrFeNi, CoCrFeNiCu, CoCrNiCu, CoCrFeNi$Ti_{0.6}$, $Cr_{20}Fe_{30}Mo_{35}Cu_{15}$, and $Co_{25}Cr_{25}Cu_{15}Ni_{15}Al_{20}$. The measured hardness of these compositions is found to correspond well to the trend outlined in Figure 48, corresponding 232, 219, 300, 500, and 610 Hv respectively. The replacement of Co and Ni in the CoCrFeNiCu composition with Mo to form $Cr_{20}Fe_{30}Mo_{35}Cu_{15}$ changes $E^X_{Dist.}$. from -5.91 to -0.66, destabilizing the FCC structure and has the effect of increasing the hardness from 219 to 500 Hv; while the addition of Al to CoCrNiCu to form $Co_{25}Cr_{25}Cu_{15}Ni_{15}Al_{20}$ also destablises

the FCC structure to a greater degree than previously, from $E_{Dist.}^{X} = -4.04$ to $E_{Dist.}^{X} = 3.57$ leading to a greater corresponding increase in hardness from 300 Hv to 610 Hv. A similar comparison for the substitution of Fe with Al in $Co_{25}Cr_{25}Cu_{15}Ni_{15}Al_{20}$ to form equimolar CoCrFeNiCu shows a reduction from $E_{Dist.}^{X} = 3.57$ to $E_{Dist.}^{X} = -5.91$, leading to a greater corresponding decrease in hardness from 610 Hv to 219 Hv. The lower hardness in comparison to the CoCrNiCu composition is in agreement with the lower $E_{Dist.}^{X}$value of -5.91.

Initial investigations into the 2-D plot in Figure 48 strongly suggest that a HEA alloy design strategy to tune the hardness may be executed by taking a known FCC structure (beginning at the left edge of the plot) and tuning the stoichiometry to achieve an increase in hardness (moving to the right edge of the plot) to a range based on Figure 48. This strategy will allow several potential compositions to be shortlisted for in-depth testing for potential applications. In the following discussion the hardness corresponding to Stellite-6 will be identified.

The data points in Figure 48 are fitted following an exponential type equation of the general form:

$$E_{Dist.}^{X} = A + B_1 . e^{B_2 . Hv}$$

where the left-hand side of the equation, $A = A_1 + A_2 . Hv$ is related to the linear part of the equation representing HEA compositions where the simple FCC structure is present, where the fitting constants are determined to be $A_1 = -8.17$ and $A_2 = 1.5\times10^{-2}$. The right-hand side of the equation given by $B_1 . e^{B_2 . Hv}$ is related to the divergence of plastic to elastic contribution to influence of the hardness values, as a result of the presence of either the simple BCC structure or the complex structures. For a divergence to compositions where the simple BCC structure is considered present the fitting constants take the values $B_1^{BCC} = 49\times10^{-3}$ and $B_2^{BCC} = 0.929\times10^{-2}$; while for a divergence to compositions where the complex structures are considered present the fitting constants take the values $B_1^{Complex} = 0.1\times10^{-3}$ and $B_2^{Complex} = 1.55\times10^{-2}$.

The hardness range of Stellite-6 ($Co_{64}Cr_{30}W_5C_1$), highlighted in red in Table 5 is between 380 – 490 HV [48] and is shown in Figure 48. The region of desired hardness values corresponds

to a transition point between the FCC structure and non-FCC structures. As the hardness difference between the two groups of the simple BCC structure and the complex structures are only beginning to diverge from one another in this region, mixed structures containing a combination of the simple FCC and BCC structures, as well as complex structures may be considered as long as they meet threshold values of $E_{Dist.}^{X}$. Of the six compositions synthesised earlier, the $Co_{25}Cr_{25}Cu_{15}Ni_{15}Al_{20}$ is selected to be modified as the addition of Cr, Cu, Ni, and Al is believed to enhance to corrosion-resistance properties of the end compositions; while tuning of the amount of Al addition allows control over the presence of secondary phases to modify the existing mechanical properties of the FCC structure that is predicted to be stabilised in CoCrCuNi following the distorted tetragonal structure method with $E_{Dist.}^{X} = 4.04$.

To achieve a targeted hardness value of 450 HV, the threshold value determined from the fitting equation is $E_{Dist.}^{BCC} = 1.86$ for a composition where simple BCC-type structures are stabilised, and $E_{Dist.}^{Complex} = -1.22$ for a composition where complex structures are present. A new stoichiometry from the $Co_{25}Cr_{25}Cu_{15}Ni_{15}Al_{20}$ composition can be obtained using a genetic algorithm to fine-tune the desired stoichiometry so that the previously stated conditions $E_{Dist.}^{BCC} = 1.86$ and $E_{Dist.}^{Complex} = -1.22$ are achieved.

### 7.4.3 Proposed alloy compositions and cost projection of raw materials

The list of compositions in Table 6 show the tuning of the compositions as a result of the substitution of alloying elements and stoichiometry, while the Stellite-6 composition in Table 6 is used as a reference point, while subsequent compositions indicate the process of refinement of the alloy compositions. The equimolar $Co_{20}Cr_{20}Cu_{20}Ni_{20}Fe_{20}$ composition was first synthesised due to reported good thermal stability properties associated with this composition [13]. However, the hardness value of 300 Hv is considered to be outside the range of Stellite-6 to be considered as a viable replacement and as such an alternative composition where Fe is replaced by Al to form a $Co_{25}Cr_{25}Cu_{15}Ni_{15}Al_{20}$ multi-component alloy composition was synthesised also. Al is included as an alloying element due to its resistance to oxidation [1,22,47,49] and ability to harden the structure through the formation of B2 structures, which may be expected from the Al-Ni binary phase diagram [23] and negative enthalpy of mixing value [52]. Although the obtained hardness value of $Co_{25}Cr_{25}Cu_{15}Ni_{15}Al_{20}$,

at 610 Hv is too high to be considered as a replacement for Stellite-6, the higher hardness value offer scope for optimisation of the alloy stoichiometry.

**Table 15.** Cost reduction of proposed compositions and their associated hardness values. (*) indicates the hardness of the newly proposed compositions that will be discussed in the following section (*cf.* Table 7).

| Composition | $/100 g | Cost Reduction (%) | $E^{X}_{Dist.}$ | Hardness (Hv) |
|---|---|---|---|---|
| **Stellite-6** | 24.23 | N/A | -0.33 | 435 |
| **$Co_{20}Cr_{20}Cu_{20}Ni_{20}Fe_{20}$** | 15.14 | 38 | -5.89 | 300 |
| **$Co_{25}Cr_{25}Cu_{15}Ni_{15}Al_{20}$** | 18.87 | 22 | 3.57 | 610 |
| **$Co_{16}Cr_{13}Cu_{18}Ni_{28}Al_{25}$** | 14.96 | 38 | 1.86 | 542* |
| **$Co_{22}Cr_{14}Cu_{18}Ni_{26}Al_{20}$** | 15.65 | 35 | -1.23 | 426* |

New stoichiometries satisfying the conditions can be obtained using a random sampling method by employing the evolutionary algorithm included in the Microsoft Excel solver plugin. Two new stoichiometries of the $Co_{25}Cr_{25}Cu_{15}Ni_{15}Al_{20}$ composition are computed so that they match the conditions $E^{BCC}_{Dist.} = 1.86$ and $E^{Complex}_{Dist.} = -1.22$ and are shown in Table 6 above, and are found to be $Co_{16}Cr_{13}Cu_{18}Ni_{28}Al_{25}$ with $E^{X}_{Dist.} = 1.86$ and $Co_{22}Cr_{14}Cu_{18}Ni_{26}Al_{20}$ with $E^{X}_{Dist.} = -1.23$.

Early projections show a good reduction in cost per 100 g ($/100 g) of 38% and 35% in comparison to Stellite-6, due to the reduction in Co and Cr content.

### 7.4.4 Mechanical properties of alloy compositions

**Table 16.** Hardness values for the trial compositions $Co_{16}Cr_{13}Cu_{18}Ni_{28}Al_{25}$ and $Co_{22}Cr_{14}Cu_{18}Ni_{26}Al_{20}$ proposed in Section 6.4.2. Ten indentations are performed and the averaged hardness values are indicated. The second proposed composition $Co_{22}Cr_{14}Cu_{18}Ni_{26}Al_{20}$ achieved the targeted hardness values and is selected for further studies.

| | 1 | 2 | 3 | 4 | 5 | 6 | 7 | 8 | 9 | 10 | Average (Hv) |
|---|---|---|---|---|---|---|---|---|---|---|---|
| **$Co_{16}Cr_{13}Cu_{18}Ni_{28}Al_{25}$** | 530.3 | 524.7 | 558.9 | 536.0 | 508.3 | 541.8 | 541.8 | 547.7 | 566.0 | 559.8 | 541.5 ± 15% |
| **$Co_{22}Cr_{14}Cu_{18}Ni_{26}Al_{20}$** | 463.6 | 454.5 | 408.7 | 428.6 | 397.5 | 428.6 | 437.0 | 420.5 | 420.5 | 404.9 | 426.4 ± 15% |

The hardness values for the proposed compositions $Co_{22}Cr_{14}Cu_{18}Ni_{26}Al_{20}$ and $Co_{16}Cr_{13}Cu_{18}Ni_{28}Al_{25}$ in Table 6 of Section 6.5.2 are obtained from as-cast compositions of dimensions 15 mm x 10 mm x 2 mm following the synthesis methods outlined in the methods section. 10 repeats were taken and the average hardness value for $Co_{16}Cr_{13}Cu_{18}Ni_{28}Al_{25}$ was determined to be 541.5 Hv, while the average hardness value for $Co_{22}Cr_{14}Cu_{18}Ni_{26}Al_{20}$ was determined to be 426.4 Hv. Since the $Co_{16}Cr_{13}Cu_{18}Ni_{28}Al_{25}$ composition possesses $E^{X}_{Dist.} = 1.86$ and the Al-Co and Al-Ni binary pairs suggest the presence of decagonal AlCo-type and B2 AlNi-type intermetallic compounds, this suggests that the hardness of the system diverges to the curve where complex phases are considered present. Substituting $E^{X}_{Dist.}$ into the fitted equation with the assumption that the system diverges to the complex structure curve predicts a hardness value of 593 Hv, which is in reasonable agreement with the experimental value of 541.5 Hv, which is within the error range of 12%. Conversely, the $Co_{22}Cr_{14}Cu_{18}Ni_{26}Al_{20}$ composition possesses $E^{X}_{Dist.} = -1.23$ and is expected to retain a FCC structure. Substituting $E^{X}_{Dist.}$ into the fitted equation with the assumption that the system remains at the curve at which BCC structures are present predicts a hardness value of 393 Hv, which is in reasonable agreement with the experimental value of 426.4 Hv, and also lies within the error range. The hardness values for both compositions appears to be consistently underestimated by $\approx 8\%$, suggesting that the error encountered is a systematic error. The verification of the hardness values of both compositions show the possibility of the $E^{X}_{Dist.} - \mathrm{Hardness}$ plot as a tool for alloy design. The second proposed composition $Co_{22}Cr_{14}Cu_{18}Ni_{26}Al_{20}$ achieved the targeted hardness values within the 400-500 Hv range, which is expected to possess a dual FCC-BCC structure and was selected for further investigation.

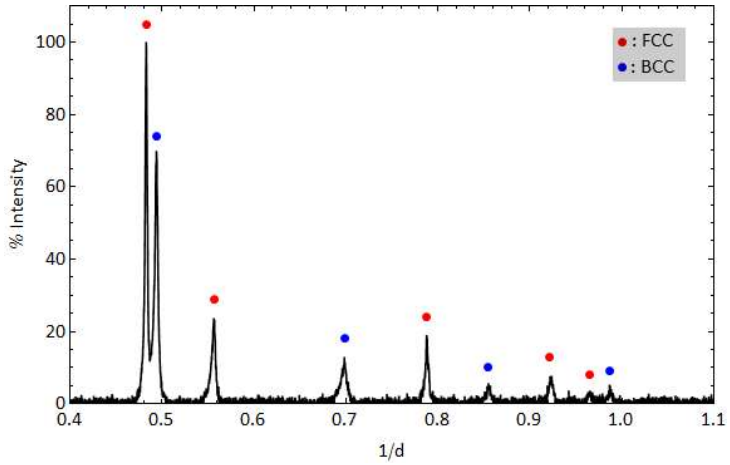


**Figure 49.** XRD pattern of $Co_{22}Cr_{14}Cu_{18}Ni_{26}Al_{20}$. The XRD pattern is found to consist of FCC and BCC peaks (demarked by red spherical markers and blue spherical markers, respectively), with the lattice parameters determined to be 3.59 Å for the FCC structure, and 2.87 Å for the FCC structure.

XRD characterisation of the phases present was performed following the methodology outlined in Chapter 2. Figure 49 shows the XRD patterns for the shortlisted composition $Co_{22}Cr_{14}Cu_{18}Ni_{26}Al_{20}$, which was indexed and found to contain peaks that are attributed to the FCC and BCC simple structures. The peaks corresponding to the FCC and BCC simple structures are indicated in Figure 49 with red spherical markers for the FCC structure and blue spherical markers for the BCC structure. The lattice parameters for both phases were determned to be 3.59 Å for the FCC structure, and 2.87 Å for the FCC structure, respectively. One issue with the XRD characterisation is that, as mentioned in Chapter 4, for Al-Co and Al-Ni containing compounds, the B2 phase may form due to interactions between these species [23]. The characterisation technique used here provides insufficient resolution and signal-to-noise ratio to differentiate between the BCC and B2 structure. However, comparison of the results from the hardness test to the 2-D $E_{Dist.}^{X} - \mathrm{Hardness}$ plot places the composition on the FCC -> BCC trendline, suggesting that the BCC structure is present rather than the B2 structure. Confirmation of this would require more advanced characterisation techniques.

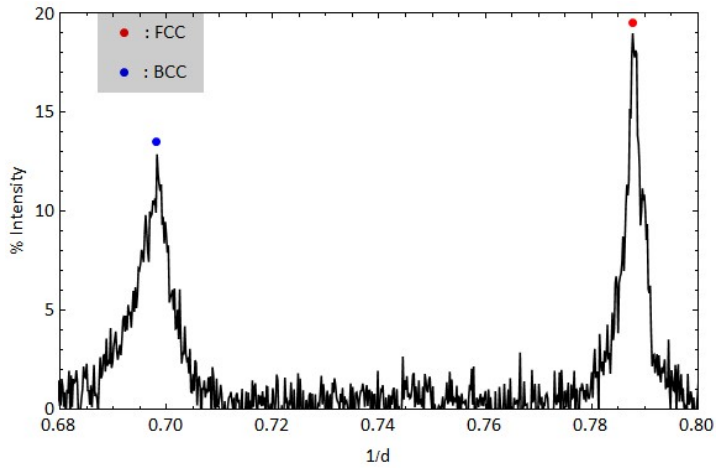


**Figure 50.** Zoom-in of the <2 0 0> BCC and <2 2 0> FCC peaks in the obtained XRD patterns showing peak asymmetry.

Cu may be regarded as a generally immiscible alloying addition; it possesses a positive enthalpy of mixing when in Cu-Co, Cu-Cr, and Co-Ni pairs, possessing only a negative enthalpy of mixing in Cu-Al. This may be indicative of a preference for segregation, which is observed in other Cu-containing HEA compositions. A visual inspection of the <2 0 0> BCC and <2 2 0> FCC peaks shows asymmetry in both BCC and FCC peaks. To try and confirm the possibility of a two-phase HEA, additional SEM characterisations were performed.

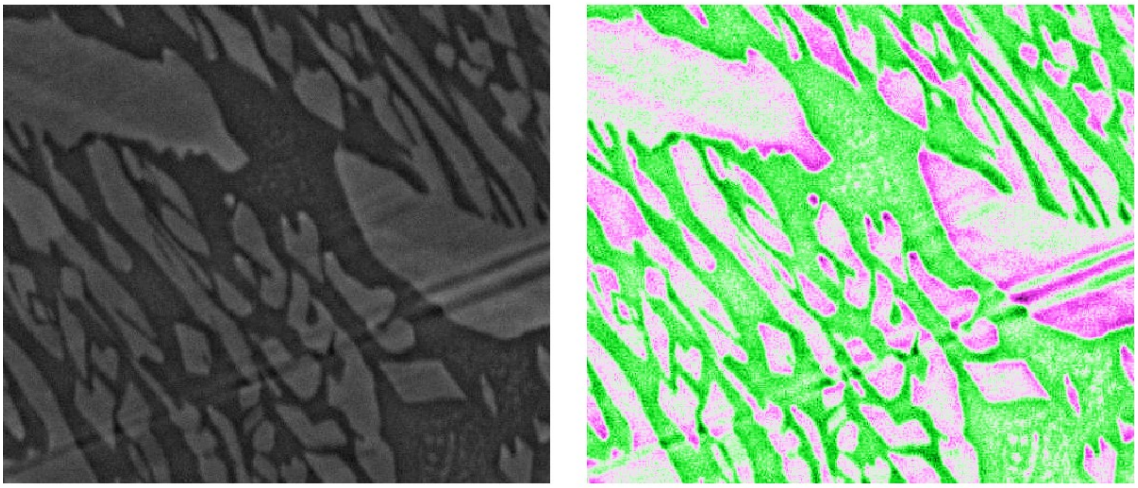

**Figure 51.** SEM characterisation micrographs. **(Left)** 20,000× magnification of the $Co_{22}Cr_{14}Cu_{18}Ni_{26}Al_{20}$ composition. **(Right)** False-colouring of the 20,000× magnification micrograph.

Figure 51 shows a 20,000× magnification of the $Co_{22}Cr_{14}Cu_{18}Ni_{26}Al_{20}$ composition showing primarily an island-like structure embedded in a matrix. False-colouring the micrograph (*c.f.* Figure 51 – Right) suggests that the edges of the grains possesses a different composition from the centre of the grains. Similarly, this behaviour is also noted in the matrix itself. Closer towards the grain boundaries, an enrichening of the matrix composition may be observed. Based also on the analysis of the false-colouring, it is seen that the composition of the small precipitations in the matrix are comparable to the grains (white-pink).

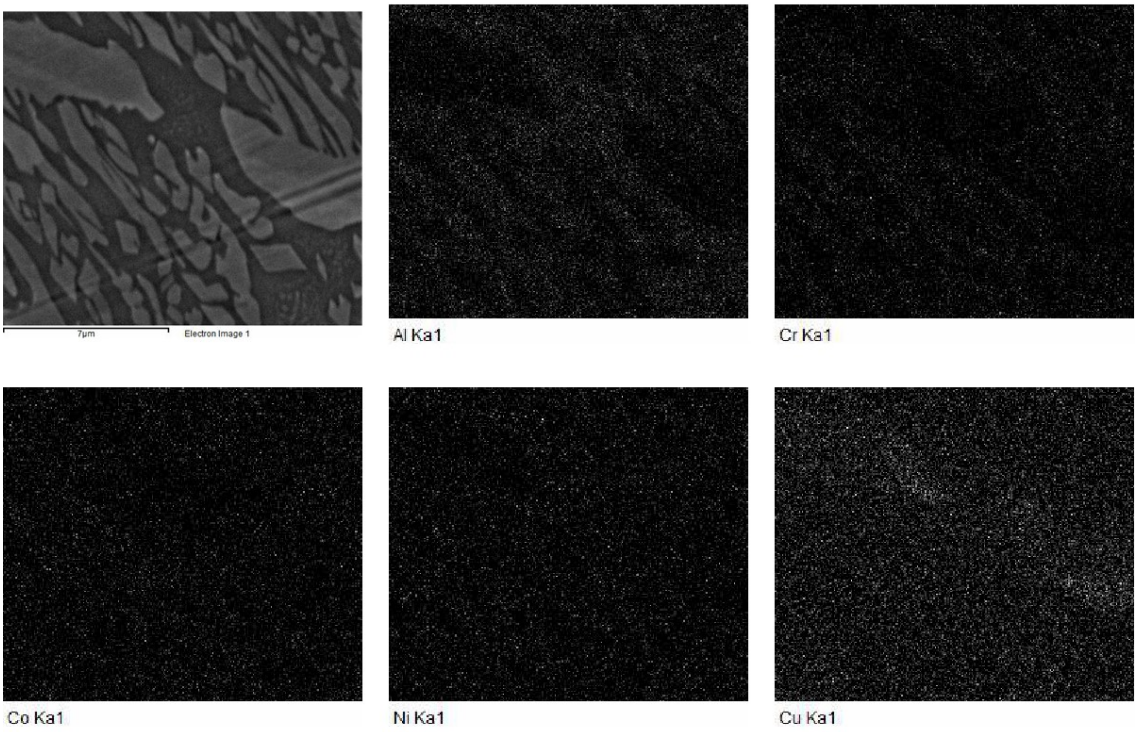


**Figure 52**. EDS analysis of a the $Co_{22}Cr_{14}Cu_{18}Ni_{26}Al_{20}$ composition at 20,000× magnification.

To try and co-relate the composition to the micrograph, an EDS analysis was also performed. From the analysis in Figure 52 is may be observed that the grains appear to be Cu-enriched, while the matrix appears to be Al-enriched; from this it may be hypothesised that the matrix represents the BCC phase, whilst the island-like grain structures represents the FCC phase. From the analysis in Figures 51 and 52, no obvious segregations are observed and the composition appears to adopt only two phases, although it is seen that enrichment of the microstructure exists. This may be the contribution to the XRD peak asymmetry, although higher characterisation tests will have to be performed to confirm this.

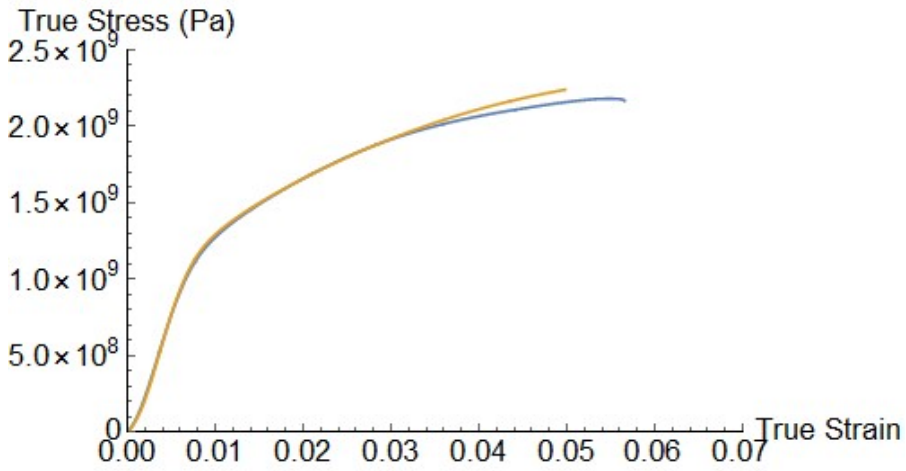


**Figure 53.** Compression test of the $Co_{22}Cr_{14}Cu_{18}Ni_{26}Al_{20}$ composition, with $\sigma_{Yield}$ of 1,243 MPa and a Young's Modulus of 184 MPa.

The mechanical properties of the $Co_{22}Cr_{14}Cu_{18}Ni_{26}Al_{20}$ composition was characterised via compression testing as outlined in the Methods section, Chapter 2. Figure 53 displays the true stress-true strain curve for the new HEA composition. Both tests show good repeatability with one another, and the yield stress, $\sigma_{Yield}$ is determined to be 1,243 MPa, while the elastic modulus, $E_Y$ was found to be 184 MPa.

**Table 17.** Summary of the mechanical properties of the shortlisted $Co_{22}Cr_{14}Cu_{18}Ni_{26}Al_{20}$ composition in comparison to the Stellte-6 composition.

| **Composition** | **Yield Stress, $\sigma_{Yield}$ (MPa)** | **Elastic Modulus, $E_Y$ (GPa)** | **Hardness (Hv)** | **H/$E_Y$ (HV/GPa)** | **Ref.** |
|---|---|---|---|---|---|
| **Stellite-6** | 750 | 209 | 435 | 2.08 | [53] |
| **$Co_{22}Cr_{14}Cu_{18}Ni_{26}Al_{20}$** | 1,243± 12% | 184± 12% | 426.4 ± 15% | 2.32 | Exp. |

A comparison with the mechanical properties of the Stellite-6 composition is shown in Table 17 where the mechanical properties of Stellite-6 were obtained from Kennametal [53] where $\sigma_{Yield}$ of the $Co_{22}Cr_{14}Cu_{18}Ni_{26}Al_{20}$ was found to be 65% higher in comparison to Stellite-6. On the other hand, the value $E_Y$ (209 GPa vs. 184 GPa) and Vickers hardness (435 HV vs 426 HV) were determined to be slightly lower in comparison with Stellite-6. It has

been previously reported that the ratio of hardness to elastic modulus, H/$E_Y$ may be used as an indicator of coating durability [54], with higher values of H/$E_Y$ indicating the increased elastic strain to failure capability of the material. From the mechanical tests performed, it is determined that the new HEA composition possesses a H/$E_Y$ value that is slightly higher than the Stellite-6 composition, indicating that it is likely to possess better wear properties.

Initial experimental characterisation of the $Co_{22}Cr_{14}Cu_{18}Ni_{26}Al_{20}$ composition verifies the prediction of a mixed FCC/BCC structure as determined from Figure 48, while Vickers indentation tests return results that are within the preselected and accepted range of hardness values (when compared to the Stellite-6 composition). Further compression tests that have been run on the as-cast samples return results with a much higher yield stress than Stellite-6, suggesting increased performance capabilities in comparison to Stellite-6. The H/$E_Y$ ratio is used as an indication of the applicability of the material for hardfacing purposes, and the obtained value of 2.32 is slightly higher than Stellite-6 (2.08), which may suggest increased enhancement in wear properties. Finally, the $Co_{22}Cr_{14}Cu_{18}Ni_{26}Al_{20}$ was selected to also reduce the Co and Cr content in Stellite-6, to lead to a cost reduction of the raw materials. As the mechanical properties tested thus far suggest that the $Co_{22}Cr_{14}Cu_{18}Ni_{26}Al_{20}$ composition is comparable to Stellite-6, it also offers the benefit of an estimated 28% reduction in the costs of raw materials.

To verify the mechanical properties and wear resistance requires further wear testing such as scratch testing, and tensile tests. Further tests on the corrosion resistance of the new alloy composition must also be completed, as the change in the newly proposed composition's alloying components may modify corrosion behaviour. The up-scalability for the production of this alloy composition also needs to be studied for its feasibility.

The case study performed here has successfully shown the application of the $E_{Dist.}^{X}$-Hardness 2-D plot to design a new composition using hardness as a design criterion.

## 7.5 Conclusions

The following may be summarised from the results presented in this chapter:

- An analysis of the dilatational strain in CCFN-$A_x$ lattices (where A = Al, Ti, V, Mn, and Pd) shows that it is linked to the various mechanical properties in HEAs.

- The enthalpy of mixing is determined to serve as a good indicator of the degree of dilatational strain, and hence mechanical properties.
- This is shown to be applicable to values of $E_{Dist.}^{X}$ as well, and is validated through a 2-D plot of $E_{Dist.}^{X}$-Hardness.
- The 2-D plot of $E_{Dist.}^{X}$-Hardness is used to successfully design an alloy composition that possesses comparable properties to Stellite-6, while optimising the compositional stoichiometry so that the costs of the raw materials may be reduced by 28%.

## 7.6 References


[1] W.-H. Wu, C.-C. Yang, L. Yeh, others, Industrial development of high-entropy alloys, in: Ann. Chim.-Sci. Mater., Paris; New York: Masson, 1978-, 2006: p. 737.

[2] K. Gebauer, Performance, tolerance and cost of TiAl passenger car valves, Intermetallics. 14 (2006) 355–360. doi:10.1016/j.intermet.2005.08.009.

[3] K.J. Patton, A.M. Sullivan, R.B. Rask, M.A. Theobald, Aggregating Technologies for Reduced Fuel Consumption: A Review of the Technical Content in the 2002 National Research Council Report on CAFE, in: 2002. doi:10.4271/2002-01-0628.

[4] P. Kroos, C. Luven, R. Schacherer, Metallic hollow valve, Google Patents, 2014. http://www.google.com/patents/US20140239218.

[5] E.J. Pickering, R. Munoz-Moreno, H.J. Stone, N.G. Jones, Precipitation in the equiatomic high-entropy alloy CrMnFeCoNi, Scr. Mater. 113 (2016).

[6] U. Dahlborg, J. Cornide, M. Calvo-Dahlborg, T.C. Hansen, Z. Leong, L.A. Dominguez, S. Chambreland, A. Cunliffe, R. Goodall, I. Todd, Crystalline structures of some high entropy alloys obtained by neutron and x-ray diffraction, Acta Phys. Pol. A. 128 (2015).

[7] J. Cornide, U. Dahlborg, Z. Leong, L.A. Dominguez, J. Juraszek, S. Jouen, T. Hansen, R. Wunderlich, S. Chambreland, I. Todd, R. Goodall, M. Calvo-Dahlborg, Structure and Properties of Some CoCrFeNi-Based High Entropy Alloys, in: TMS2015 Supplemental Proceedings, 2015.

[8] J. Cornide, M. Calvo-Dahlborg, S. Chambreland, L.A. Dominguez, Z. Leong, U. Dahlborg, A. Cunliffe, R. Goodall, I. Todd, Combined atom probe tomography and TEM investigations of CoCrFeNi, CoCrFeNi-Pdx (x=0.5, 1.0, 1.5) And CoCrFeNi-Sn, Acta Phys. Pol. A. 128 (2015).

[9] J.W. Christian, The theory of transformations in metals and alloys. Pt. 2: [...], 3. ed, Pergamon, Amsterdam, 2002.

[10] A. Gali, E.P. George, Tensile properties of high- and medium-entropy alloys, Intermetallics. 39 (2013) 74–78. doi:10.1016/j.intermet.2013.03.018.

[11] A.J. Zaddach, C. Niu, C.C. Koch, D.L. Irving, Mechanical Properties and Stacking Fault Energies of NiFeCrCoMn High-Entropy Alloy, JOM. 65 (2013) 1780–1789. doi:10.1007/s11837-013-0771-4.

[12] Y. Zhang, T.T. Zuo, Z. Tang, M.C. Gao, K.A. Dahmen, P.K. Liaw, Z.P. Lu, Microstructures and properties of high-entropy alloys, Prog. Mater. Sci. 61 (2014) 1–93.

[13] H. Zhang, Y.-Z. He, Y. Pan, S. Guo, Thermally stable laser cladded CoCrCuFeNi high-entropy alloy coating with low stacking fault energy, J. Alloys Compd. 600 (2014) 210–214. doi:10.1016/j.jallcom.2014.02.121.

[14] F. Otto, Y. Yang, H. Bei, E.P. George, Relative effects of enthalpy and entropy on the phase stability of equiatomic high-entropy alloys, Acta Mater. 61 (2013) 2628–2638. doi:10.1016/j.actamat.2013.01.042.

[15] M.-H. Tsai, J.-W. Yeh, High-Entropy Alloys: A Critical Review, Mater. Res. Lett. 2 (2014) 107–123. doi:10.1080/21663831.2014.912690.

[16] W.R. Wang, W.L. Wang, S.C. Wang, Y.C. Tsai, C.H. Lai, J.W. Yeh, Effects of Al addition on the microstructure and mechanical property of AlxCoCrFeNi high-entropy alloys, Intermetallics. 26 (2012) 44–51.

[17] L.A. Dominguez, R. Goodall, I. Todd, Prediction and validation of quaternary high entropy alloys using statistical approaches, Mater. Sci. Technol. 31 (2015) 1201–1206.

[18] M.T.Z. Butt, C. Bodsworth, Liquid immiscibility in ternary metallic alloys, Mater. Sci. Technol. 7 (1991) 795–802. doi:10.1179/mst.1991.7.9.795.

[19] M.S. Lucas, L. Mauger, J. Munoz, Y. Xiao, A.O. Sheets, S.L. Sematin, Magnetic and vibrational properties of high-entropy alloys, J. Appl. Phys. 109 (2011) 7.

[20] M.-H. Tsai, K.-Y. Tsai, C.-W. Tsai, C. Lee, C.-C. Juan, J.-W. Yeh, Criterion for Sigma Phase Formation in Cr- and V-Containing High-Entropy Alloys, Mater. Res. Lett. 1 (2013) 207–212. doi:10.1080/21663831.2013.831382.

[21] G.A. Salishchev, M.A. Tikhonovsky, D.G. Shaysultanov, N.D. Stepanov, A.V. Kuznetsov, I.V. Kolodiy, A.S. Tortika, O.N. Senkov, Effect of Mn and V on structure and mechanical properties of high-entropy alloys based on CoCrFeNi system, J. Alloys Compd. 591 (2014) 11–21. doi:10.1016/j.jallcom.2013.12.210.

[22] H.P. Chou, Y.S. Chang, S.K. Chen, J.W. Yeh, Microstructure, thermophysical and electrical properties in Al x CoCrFeNi (0 ≤ x ≤2) high-entropy alloys, Mater. Sci. Eng. B. 163 (2009) 184–189.

[23] P. Villars, H. Okamoto, K. Cenzual, eds., ASM Alloy Phase Diagrams Database, ASM International, Materials Park, OH, 2006. http://www1.asminternational.org/AsmEnterprise/APD.

[24] M.-R. Chen, S.-J. Lin, J.-W. Yeh, M.-H. Chuang, S.-K. Chen, Y.-S. Huang, Effect of vanadium addition on the microstructure, hardness, and wear resistance of

Al0.5CoCrCuFeNi high-entropy alloy, Metall. Mater. Trans. A. 37 (2006) 1363–1369. doi:10.1007/s11661-006-0081-3.

[25] A. Haglund, M. Koehler, D. Catoor, E.P. George, V. Keppens, Polycrystalline elastic moduli of a high-entropy alloy at cryogenic temperatures, Intermetallics. 58 (2015) 62–64. doi:10.1016/j.intermet.2014.11.005.

[26] P.S. Branicio, J.Y. Zhang, D.J. Srolovitz, Effect of strain on the stacking fault energy of copper: A first-principles study, Phys. Rev. B. 88 (2013). doi:10.1103/PhysRevB.88.064104.

[27] D. Kashchiev, Nucleation basic theory with applications, Butterworth Heinemann, Oxford; Boston, 2000. http://www.engineeringvillage.com/controller/servlet/OpenURL?genre=book&isbn=9780750646826 (accessed February 20, 2016).

[28] W. Voigt, Theoretische Studien über die Elastizitätsverhältnisse der Kristalle. Göttingen 1887. Abh. königl. Ges. d, Wiss Bd. 34 (1887).

[29] F. Tian, L.K. Varga, J. Shen, L. Vitos, Calculating elastic constants in high-entropy alloys using the coherent potential approximation: Current issues and errors, Comput. Mater. Sci. 111 (2016) 350–358. doi:10.1016/j.commatsci.2015.09.058.

[30] S.L. Shang, A. Saengdeejing, Z.G. Mei, D.E. Kim, H. Zhang, S. Ganeshan, Y. Wang, Z.K. Liu, First-principles calculations of pure elements: Equations of state and elastic stiffness constants, Comput. Mater. Sci. 48 (2010) 813–826. doi:10.1016/j.commatsci.2010.03.041.

[31] J. Vallin, M. Mongy, K. Salama, O. Beckman, Elastic Constants of Aluminum, J. Appl. Phys. 35 (1964) 1825. doi:10.1063/1.1713749.

[32] E.S. Fisher, C.J. Renken, Single-Crystal Elastic Moduli and the hcp → bcc Transformation in Ti, Zr, and Hf, Phys. Rev. 135 (1964) A482–A494. doi:10.1103/PhysRev.135.A482.

[33] D.I. Bolef, R.E. Smith, J.G. Miller, Elastic Properties of Vanadium. I. Temperature Dependence of the Elastic Constants and the Thermal Expansion, Phys. Rev. B. 3 (1971) 4100–4108. doi:10.1103/PhysRevB.3.4100.

[34] H. Bakker, A. Miedema, Enthalpies in alloys: Miedemaś semi-empirical model, Trans Tech Publications, Uetikon-Zuerich, Switzerland ; Enfield, N.H, 1998.

[35] S.R. Nishitani, H. Kawabe, M. Aoki, First-principles calculations on bcc–hcp transition of titanium, Mater. Sci. Eng. A. 312 (2001) 77–83. doi:10.1016/S0921-5093(00)01905-5.

[36] D.G. Pettifor, A Quantum Mechanical Critique of the Miedema Rules for Alloy Formation, Solid State Phys. 40 (1987) 43–92.

[37] M.E. Eberhart, The metallic bond: Elastic properties, Acta Mater. 44 (1996) 2495–2504. doi:10.1016/1359-6454(95)00347-9.

[38] D. Ma, B. Grabowski, F. Körmann, J. Neugebauer, D. Raabe, Ab initio thermodynamics of the CoCrFeMnNi high entropy alloy: Importance of entropy contributions beyond the configurational one, Acta Mater. 100 (2015) 90–97. doi:10.1016/j.actamat.2015.08.050.

[39] A. Kelly, N.H. Macmillan, Strong Solids., Oxf. Univ. Press Walt. Str. Oxf. OX 2 6 DP UK 1986. (1986).

[40] D.W. Lee, H. Kim, A. Strachan, M. Koslowski, Effect of core energy on mobility in a continuum dislocation model, Phys. Rev. B. 83 (2011). doi:10.1103/PhysRevB.83.104101.

[41] M.Ö. Pekgüleryüz, K.U. Kainer, A.A. Kaya, eds., Fundamentals of magnesium alloy metallurgy, Woodhead Publishing, Oxford ; Philadelphia, 2013.

[42] X.X. Wu, X.Y. San, X.G. Liang, Y.L. Gong, X.K. Zhu, Effect of stacking fault energy on mechanical behavior of cold-forging Cu and Cu alloys, Mater. Des. 47 (2013) 372–376. doi:10.1016/j.matdes.2012.12.006.

[43] U. Mizutani, Hume-Rothery rules for structurally complex alloy phases, CRC Press, Boca Raton, 2011.

[44] M. Sakai, The Meyer hardness: A measure for plasticity?, J. Mater. Res. 14 (1999) 3630–3639. doi:10.1557/JMR.1999.0490.

[45] C. Li, J.C. Li, M. Zhao, Q. Jiang, Effect of alloying elements on microstructure and properties of multiprincipal elements high-entropy alloys, J. Alloys Compd. 475 (2009) 752–757. doi:10.1016/j.jallcom.2008.07.124.

[46] C.-C. Tung, J.-W. Yeh, T. Shun, S.-K. Chen, Y.-S. Huang, H.-C. Chen, On the elemental effect of AlCoCrCuFeNi high-entropy alloy system, Mater. Lett. 61 (2007) 1–5. doi:10.1016/j.matlet.2006.03.140.

[47] C.-J. Tong, M.-R. Chen, J.-W. Yeh, S.-J. Lin, S.-K. Chen, T.-T. Shun, S.-Y. Chang, Mechanical performance of the Al x CoCrCuFeNi high-entropy alloy system with multiprincipal elements, Metall. Mater. Trans. A. 36 (2005) 1263–1271. doi:10.1007/s11661-005-0218-9.

[48] V. Kuzucu, M. Ceylan, H. Çelik, I. Aksoy, Microstructure and phase analyses of Stellite 6 plus 6 wt.% Mo alloy, J. Mater. Process. Technol. 69 (1997) 257–263. doi:10.1016/S0924-0136(97)00027-7.

[49] J.W. Yeh, S.K. Chen, S.J. Lin, J.Y. Gan, T.S. Chin, T.T. Shun, C.H. Tsau, S.Y. Chang, Nanostructured high-entropy alloys with multiple principal elements: Novel alloy design concepts and outcomes, Adv. Eng. Mater. 6 (2004) 299–303.

[50] C.-Y. Hsu, T.-S. Sheu, J.-W. Yeh, S.-K. Chen, Effect of iron content on wear behavior of AlCoCrFexMo0.5Ni high-entropy alloys, Wear. 268 (2010) 653–659. doi:10.1016/j.wear.2009.10.013.

[51] R. Mitra, Structural intermetallics and intermetallic matrix composites, CRC Press, Taylor & Francis Group, Boca Raton, 2015.

[52] D. Nguyen-Manh, A. Paxton, D.G. Pettifor, A. Pasturel, On the phase stability of transition metal trialuminide compounds, Intermetallics. 3 (1995) 9–14.

[53] Stellite 6 Alloy Technical Data, (n.d.). http://stellite.com/Portals/0/KMT_Stellite_6Alloy_Data_FINAL.pdf.

[54] A. Leyland, A. Matthews, Design criteria for wear-resistant nanostructured and glassy-metal coatings, Surf. Coat. Technol. 177–178 (2004) 317–324. doi:10.1016/j.surfcoat.2003.09.011.

# 8. Conclusions

The thesis chapters have so far presented two linked themes:

1. The investigations of whether consideration of quantum mechanical principles can increase the accuracy of predictions of HEA phase presence/stability (Chapters 4 and 5).
2. Development a simple predictive scheme that includes quantum mechanical principles which allows for the possibility to design a multiple component system so that an alloy composition which possesses desired combinations of simple and complex structures (Chapters 6 and 7).

In the first results chapter, Chapter 4, the structural stability HEAs was shown to be qualitatively linked to an alloy composition's parameters when displayed as a 2-D plot. These plots are:

1. Enthalpy of mixing against the averaged electronegativity
2. Electron density to the Wigner-seitz radius

Subsequent analysis of the 2-D plots show that the determination of structural stability for both simple and complex phases are highly dependent on the periodicity of the alloy composition (i.e. the primary quantum number). In the first 2-D plot the rate of change of the averaged electronegativity to the electron density at the Wigner-Seitz radius, as defined by the Miedema enthalpy of mixing, is hypothesised to be responsible for the shift in energy levels between FCC/BCC; while the non-conformation of the complex phases to the determined zones of simple structure and/or any fixed zones are attributed to a shift in bond directionality, which is thought to be able to be characterised by the electron density of an alloy unique to that composition. This is subsequently investigated in the second 2-D plot, where the electron density is calculated using the Thomas-Fermi-Dirac equation. The results show a clear differentiation between the simple and complex phases via a drop in electron density for any equivalent Wigner-Seitz radius, which in agreement with the previous results and discussion from the first section.

The second results chapter, Chapter 5, continues by analysing the electronic structure of HEAs using the Rigid Band Approximation (RBA) within Density Functional Theory. By reducing the problem of analysing the electronic structure to a single bandstructure for different CoCrFeNi-$A_x$ (here denoted CCFN-$A_x$) compositions as a function of the *ab-initio* valence electron concentration, it is shown that the accuracy of the FCC-BCC/FCC-Complex phase transitions of HEA alloys can be improved beyond those shown by semi-empirical parameters used (enthalpy of mixing, entropy of mixing, electronegativity difference, or atomic size difference), further strengthening the argument that knowledge of the electronic structure is essential in determining the phases present. Due to the

nature of ab-initio methods, the RBA approximation faces difficulties when new compositions with different components are used in design, instead of following the strategy of A-B alloying, where A is the base composition such as CCFN, and B some alloying addition.

The third results chapter, Chapter 6, focused on utilising the conclusions and corollaries developed in Chapters 4 and 5 to develop a prediction scheme for use in alloy design that is more precise that previous semi-empirical methods. Here, the simple FCC and BCC structures, and the complex structures were linked to a tetragonal cell with different distortions along the c-axis, thus representing them with different $c/a$ ratios. The distorted tetragonal structure is first developed and used to successfully predict the stable structure for Fe and Ni at 0 K, as well as for allotropes of Fe. The scheme is then extended to provide predictions for the HEA compositional families CCFN-$Al_x$, CCFN-$V_x$, CoFN-$V_x$, CCFN-$Ti_x$, and CCFN-$Pd_x$ that were previously used in the RBA analysis. When confronted with experimental XRD validations and the predictions used in the RBA analysis, the results were found to be in relatively good agreement. Furthermore, the scheme was used to predict the structural stability for CCFN-$Mo_x$ and CoFN-$Ti_x$ compositions which were then validated experimentally via XRD characterisation; the results were also found to be in agreement with one another.

In the final results chapter, Chapter 7, the distorted tetragonal scheme was used to design a HEA composition that can be used as a replacement for Stellite-6, which is used for its hardfacing properties, such as in the drive-trains of car engines. By using hardness values as a criteria, a near equimolar $Co_{22}Cr_{14}Cu_{18}Ni_{26}Al_{20}$ composition was shortlisted. Experimental verification of the compositions using Vickers indentation, XRD characterisation, and compression testing shows good results that are very close to those exhibited by Stellite-6 ($Co_{64}Cr_{30}W_5C_1$). The selection of the composition was performed to reduce the Co and Cr content of Stellite-6.

In conclusion, in this thesis the effects of the electronic structure were first determined and confirmed in Chapters 4 and 5. In order to facilitate the selection of new compositions for in-depth investigations and shorten to alloy-design process, a new prediction scheme was developed and discussed in Chapter 6, that offered better prediction capabilities than previous semi-empirical methods. The scheme was verified with the results of the RBA analysis performed in Chapter 5, as well as with predictions from literature, and from experimental results. Finally, in Chapter 7, the developed schemed was put through a test in which a HEA composition that may replace Stellite-6 was designed. Initial characterisation experiments show promising results for the $Co_{22}Cr_{14}Cu_{18}Ni_{26}Al_{20}$ which possesses elastic modulus and hardness values that are very close to

Stellite-6. The composition possesses a yield strength (1,243 MPa) that is 40% higher than Stellite-6 (750 MPa).

# 9. Suggestions of further work

Some suggestions are made here that may be suitable in further exploring the conclusions brought forward in the previous chapters:

1. As the distorted tetragonal scheme is based in part of the energy required to change the spin of an electron, this may be reflected by the change in measured maximum magnetisation. A dataset built up from the analysis of the maximum magnetisation of several bulk metallic glass compositions would therefore allow the prediction of magnetisation properties of materials to be recast in a potentially easier predictive scheme if a trend can be found.
2. Repeat analysis of multiple-component datasets to perform a lattice strain analysis using diffraction characterisation techniques. Either a x-ray or neutron source may be used to consider the lattice strain. As the onset of complex phases appear to be associated with a reduction in the dilatational strain, this may lead to understanding the role of lattice strain in mechanical properties e.g. through formation of stacking faults.
3. Perform a scoping study to examine the possibility of predicting simple solid solution phases of the lightweight elements (Li, Mg, Ca, Na, *etc*.) by extending the analysis of the Mulliken electronegativity.
4. *Ab-initio* calculations of the distorted tetragonal structures to check the relationship between the electron density distribution of the *c/a* ratios associated with complex phases. The distribution should be more covalent-like in nature.

# 10. Appendices

# Appendix A: XRD characterisation

### XRD Data: Rietveld refined peaks

### CCFN and CCFN-$Pd_x$ systems

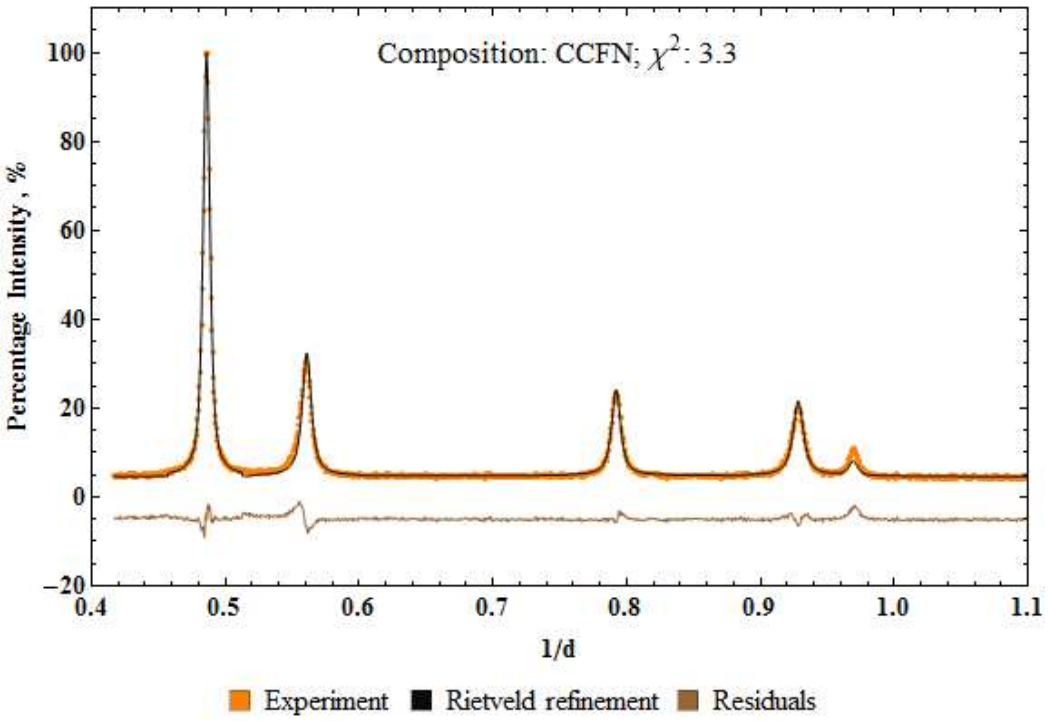


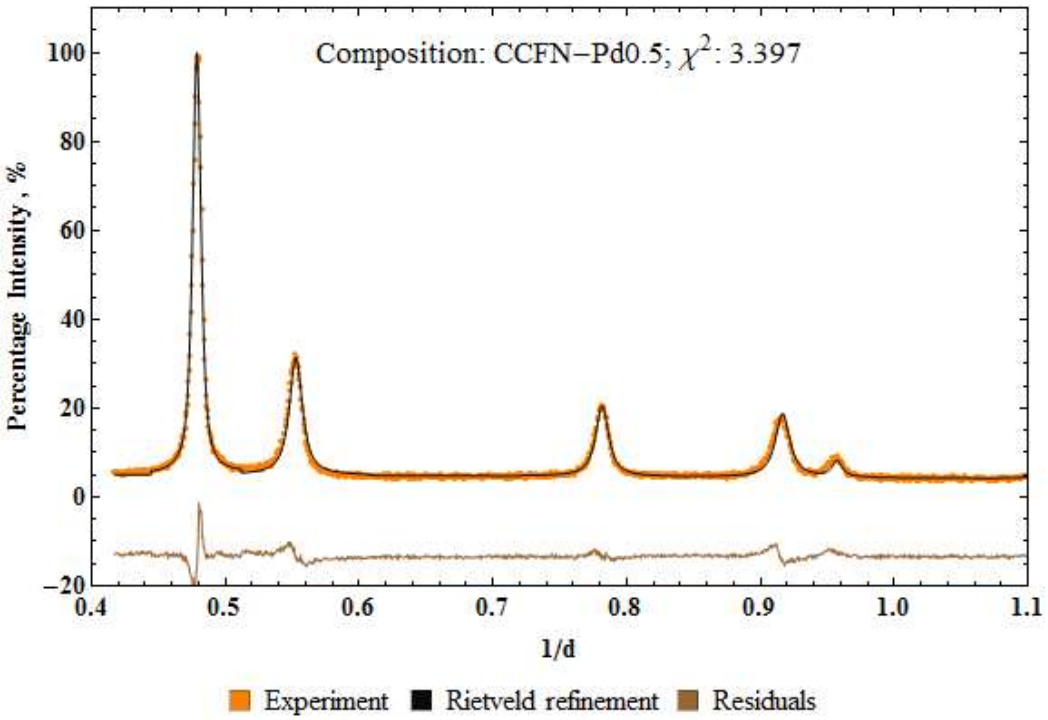

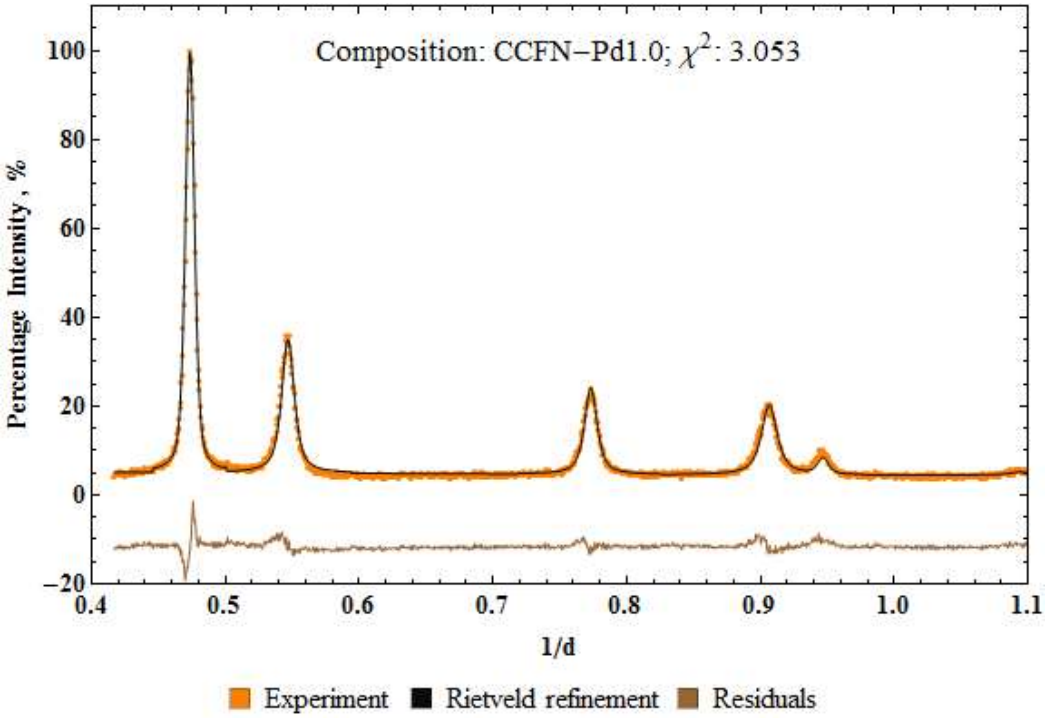
Composition: CCFN−Pd1.0; $\chi^2$: 3.053
Percentage Intensity , %
100
80
60
40
20
0
−20
0.4
0.5
0.6
0.7
0.8
0.9
1.0
1.1
1/d
Experiment
Rietveld refinement
Residuals

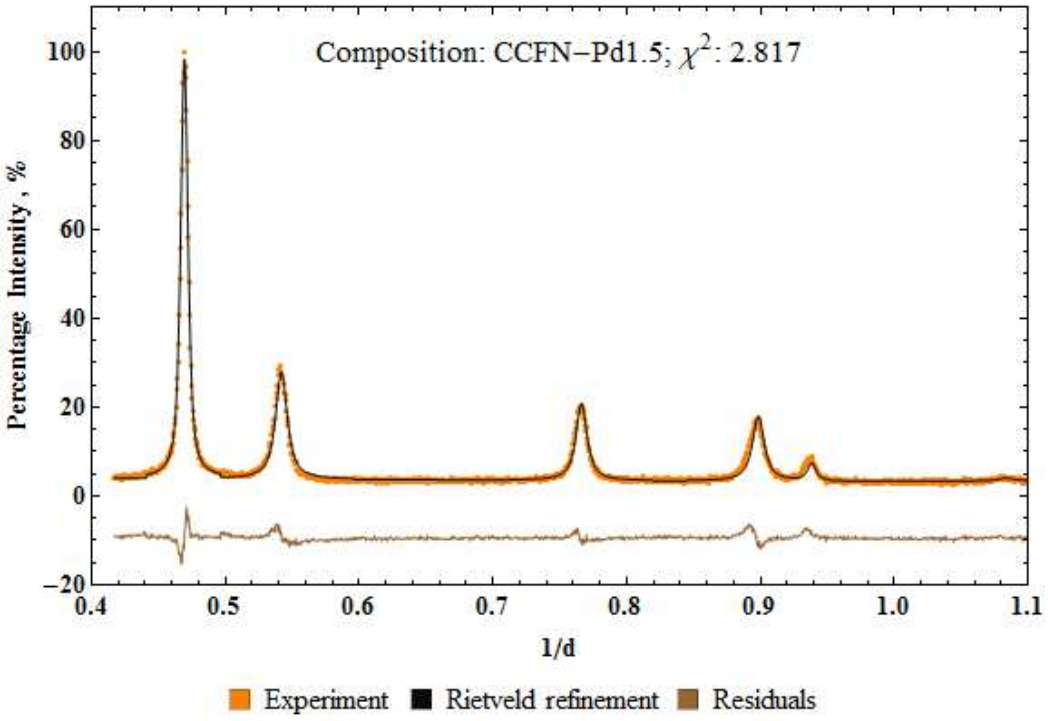
Composition: CCFN−Pd1.5; $\chi^2$: 2.817
Percentage Intensity , %
100
80
60
40
20
0
−20
0.4
0.5
0.6
0.7
0.8
0.9
1.0
1.1
1/d
Experiment
Rietveld refinement
Residuals

**CCFN-Al$_x$ systems**

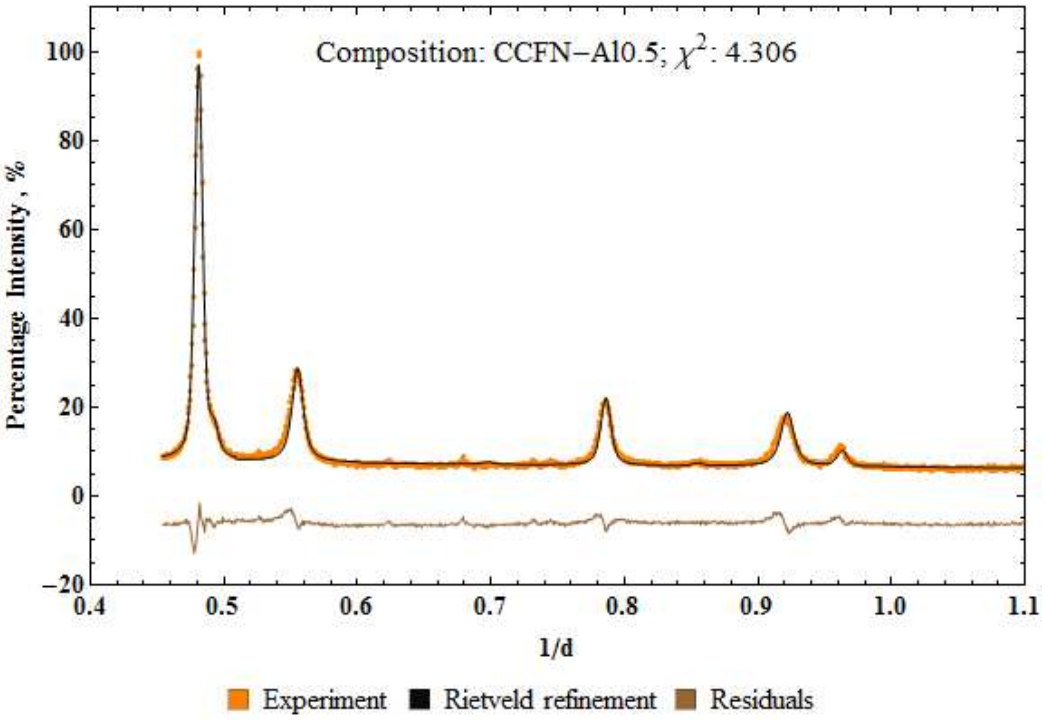


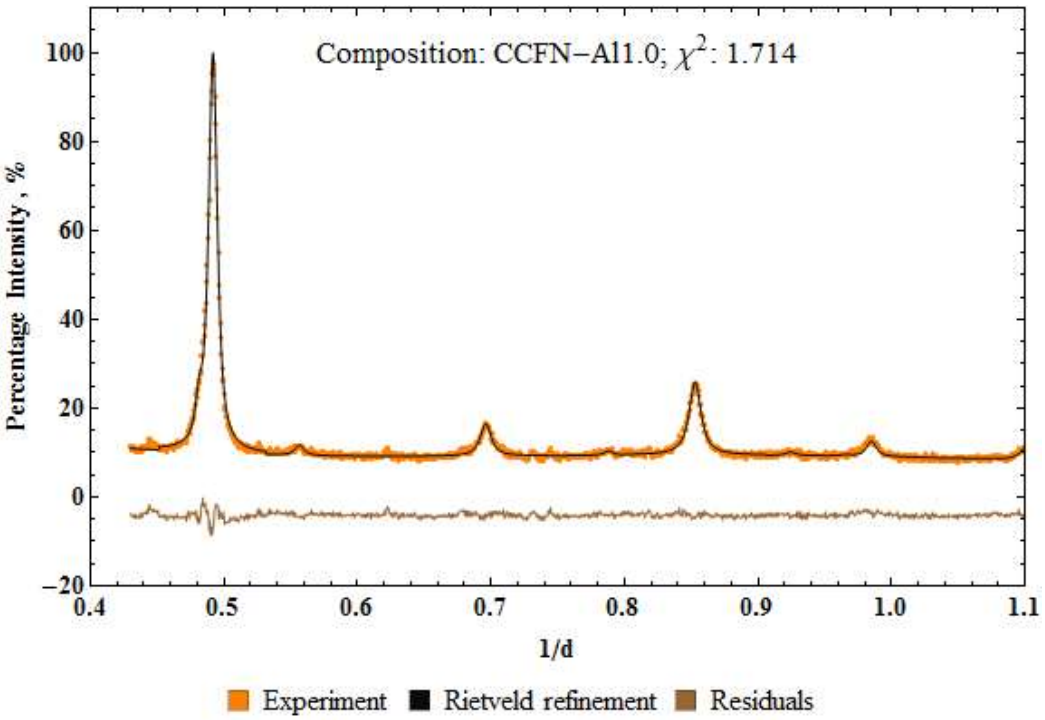

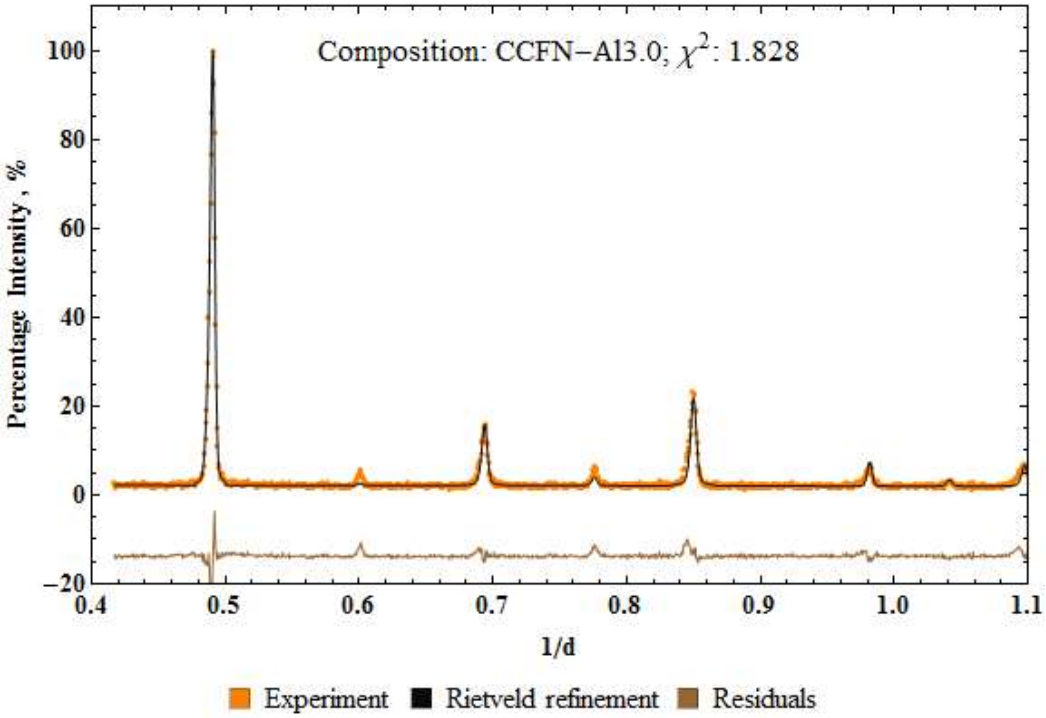
Composition: CCFN−Al3.0; $\chi^2$: 1.828
Percentage Intensity , %
100
80
60
40
20
0
−20
0.4
0.5
0.6
0.7
0.8
0.9
1.0
1.1
1/d
Experiment
Rietveld refinement
Residuals

**CCFN-$V_x$ systems**

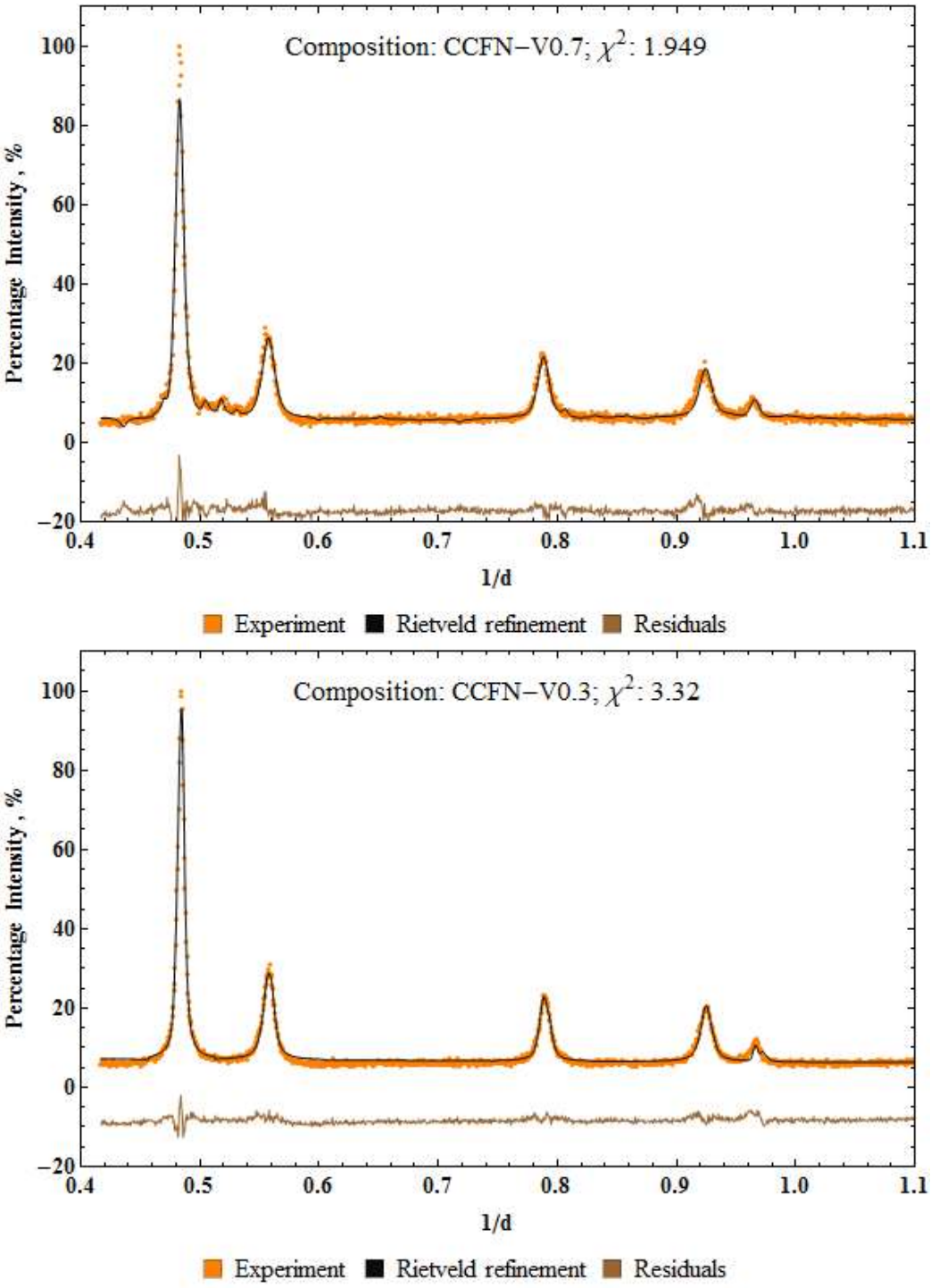

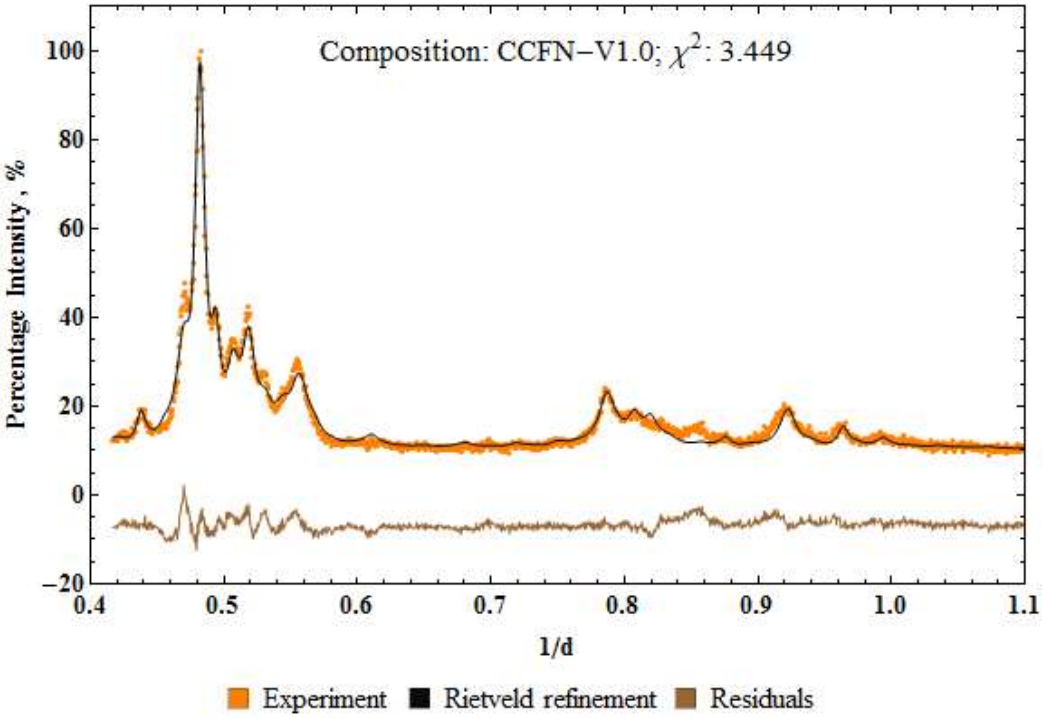
Composition: CCFN−V1.0; $\chi^2$: 3.449
Percentage Intensity , %
100
80
60
40
20
0
−20
0.4
0.5
0.6
0.7
0.8
0.9
1.0
1.1
1/d
Experiment
Rietveld refinement
Residuals

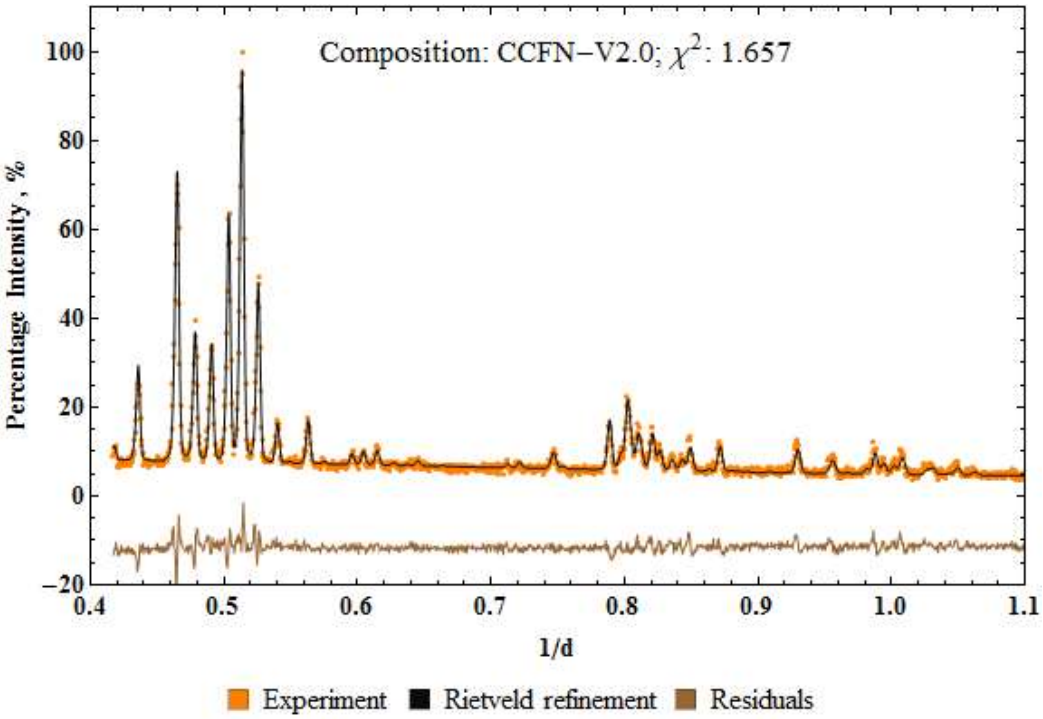
Composition: CCFN−V2.0; $\chi^2$: 1.657
Percentage Intensity , %
100
80
60
40
20
0
−20
0.4
0.5
0.6
0.7
0.8
0.9
1.0
1.1
1/d
Experiment
Rietveld refinement
Residuals

**CoFN-$V_x$ systems**

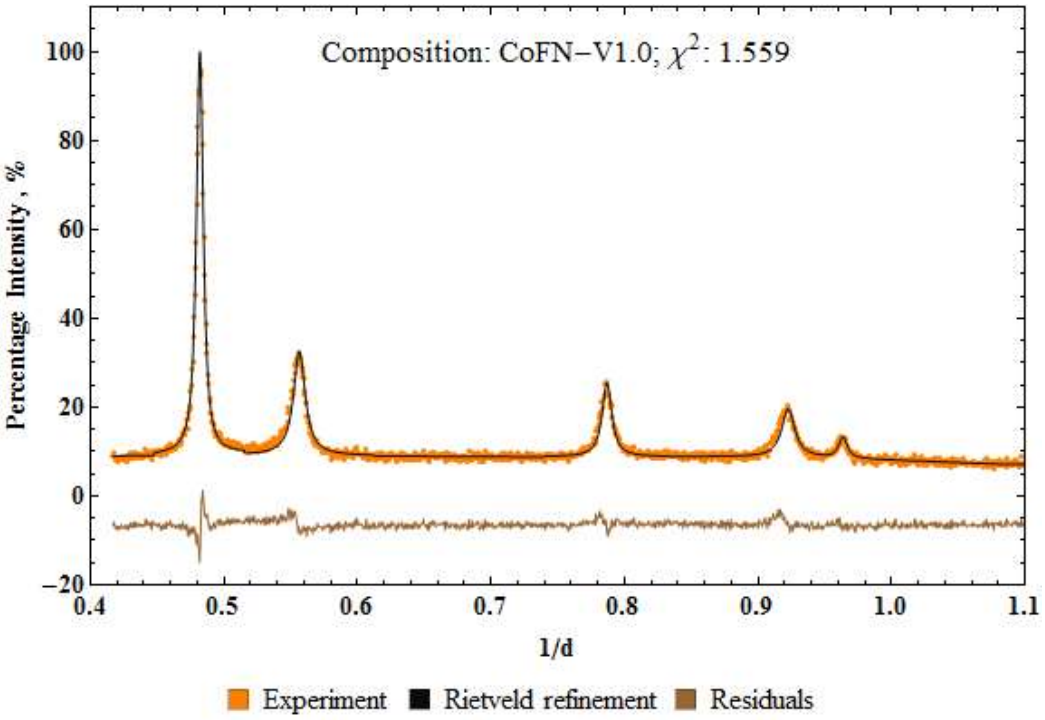


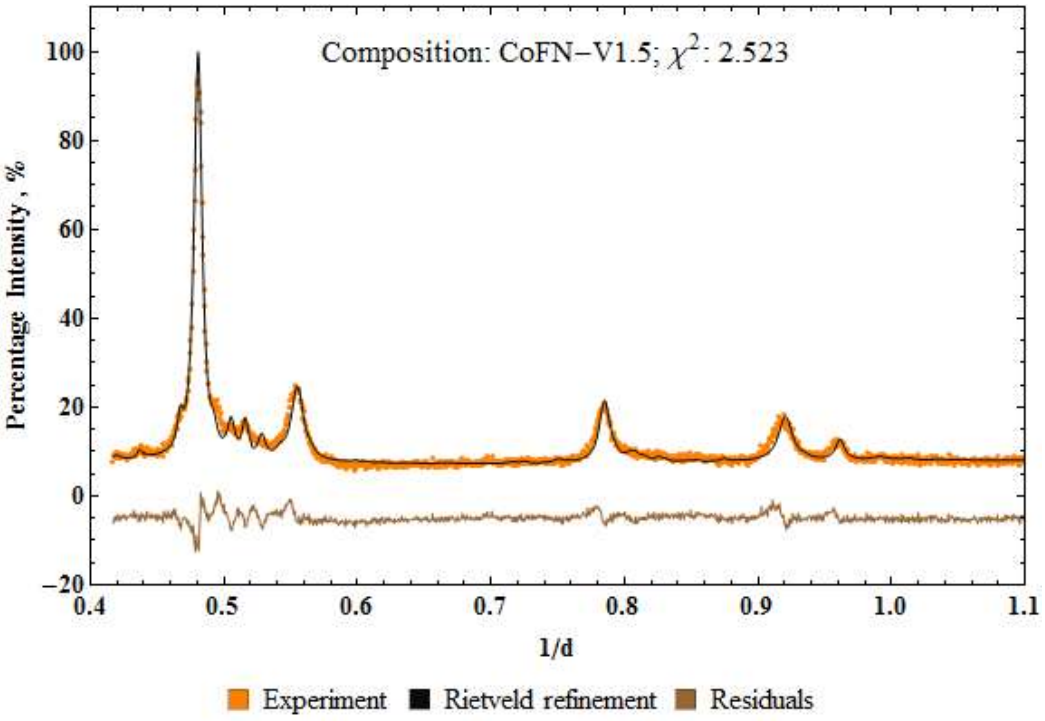

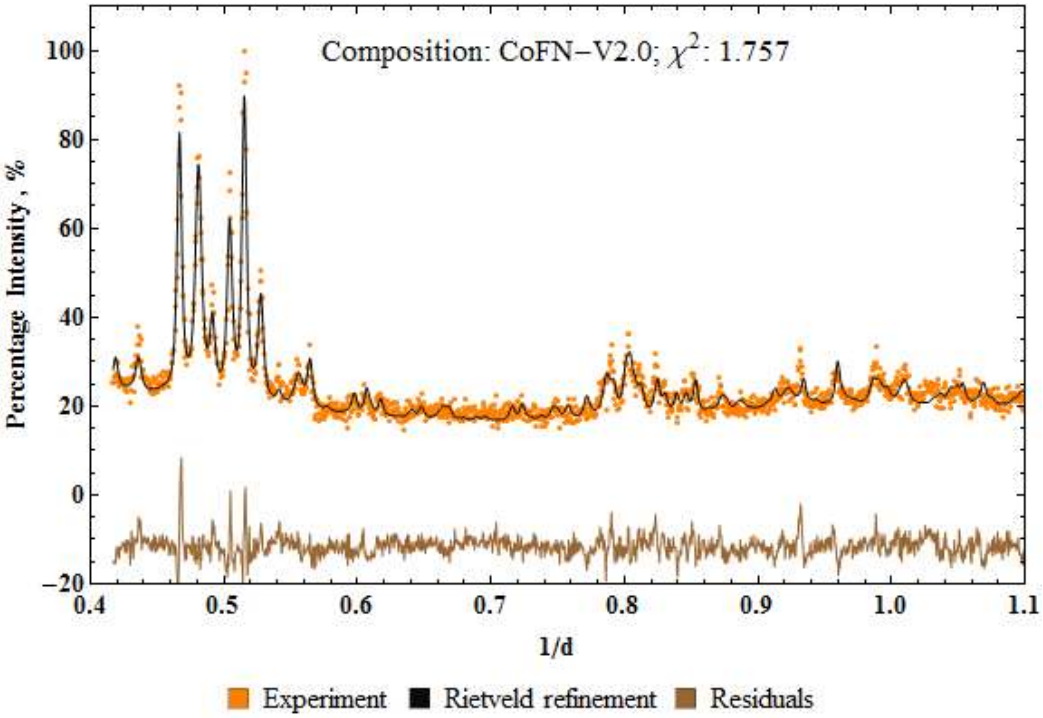
Composition: CoFN−V2.0; $\chi^2$: 1.757
Percentage Intensity , %
100
80
60
40
20
0
−20
0.4
0.5
0.6
0.7
0.8
0.9
1.0
1.1
1/d
Experiment
Rietveld refinement
Residuals

**CCFN-$Ti_x$ systems**

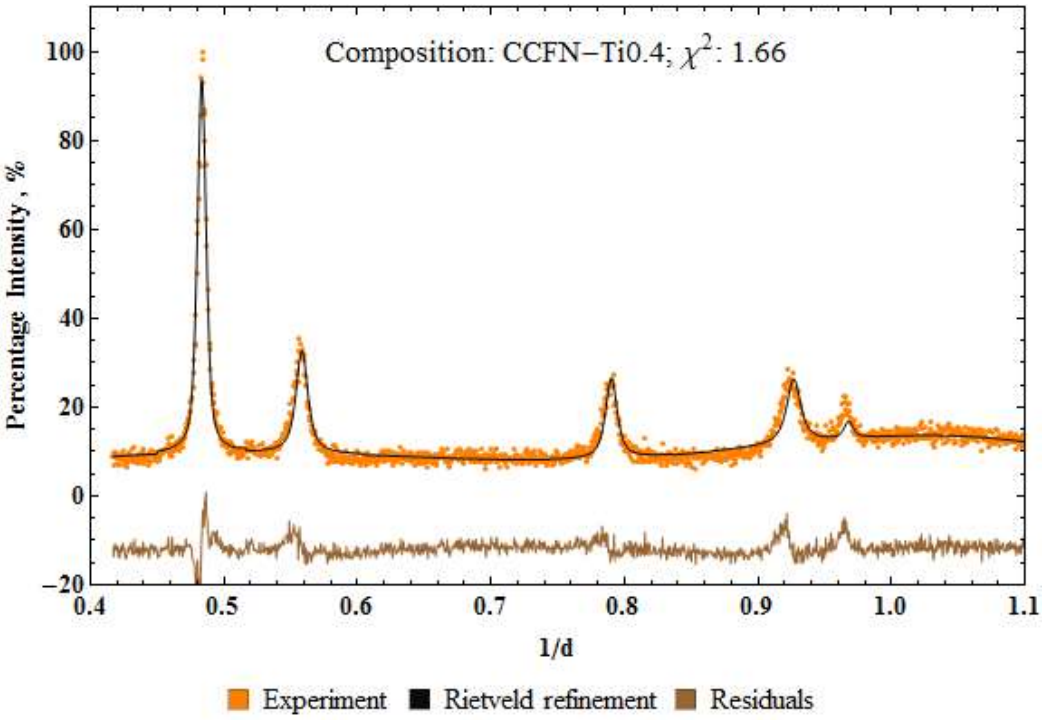


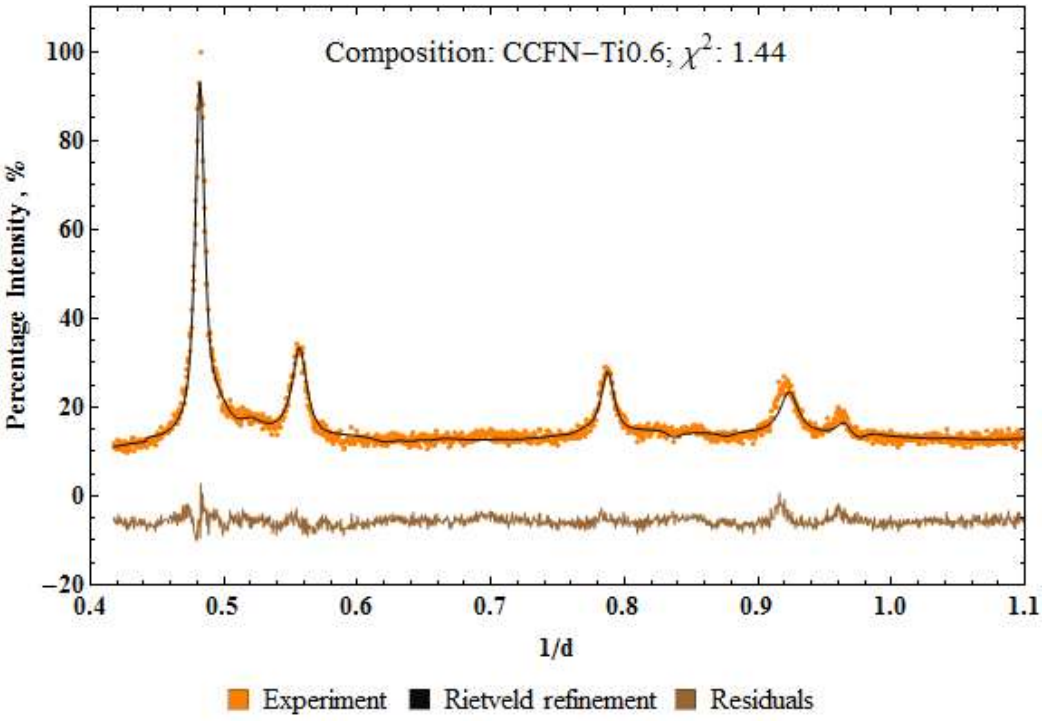

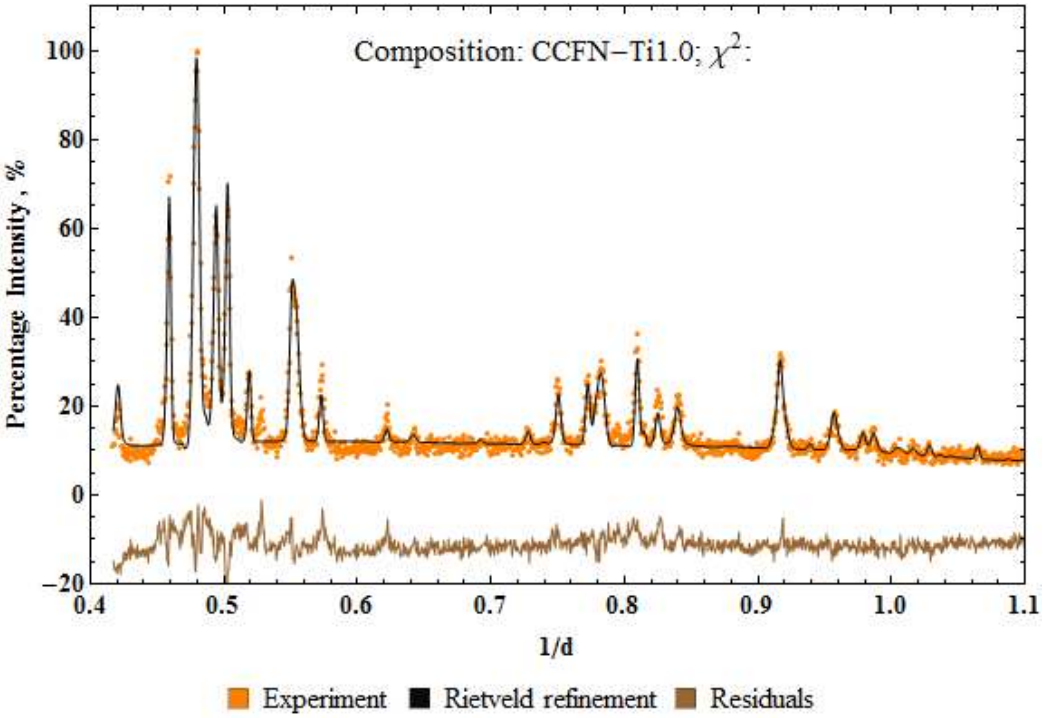
Composition: CCFN−Ti1.0; $\chi^2$:
Percentage Intensity , %
100
80
60
40
20
0
−20
0.4
0.5
0.6
0.7
0.8
0.9
1.0
1.1
1/d
Experiment
Rietveld refinement
Residuals

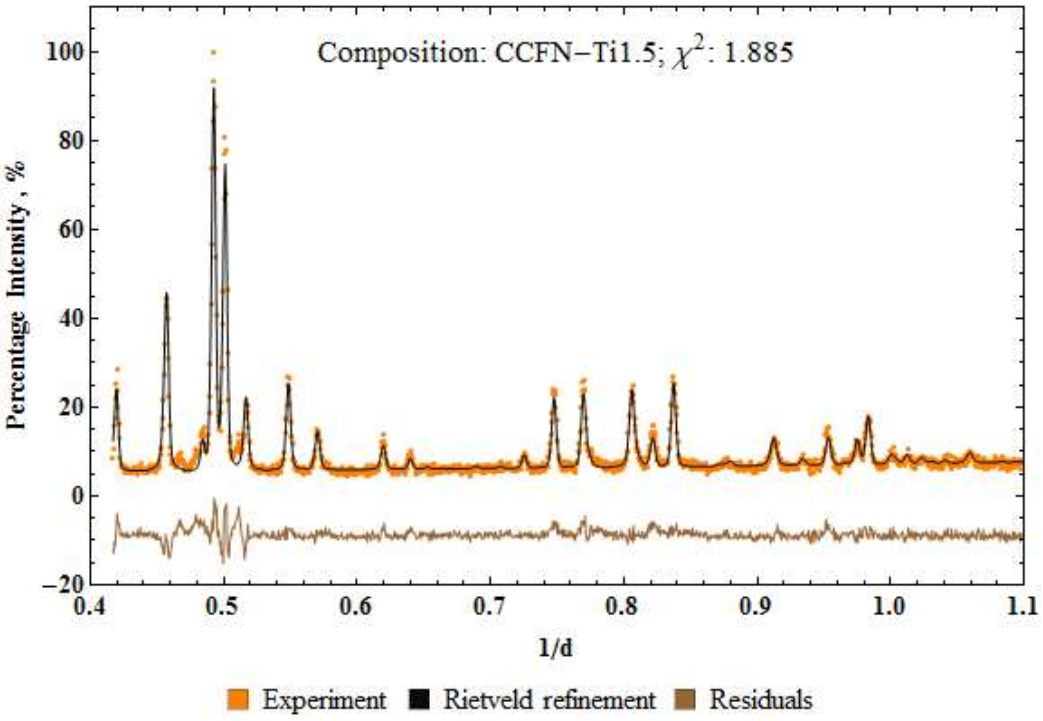
Composition: CCFN−Ti1.5; $\chi^2$: 1.885
Percentage Intensity , %
100
80
60
40
20
0
−20
0.4
0.5
0.6
0.7
0.8
0.9
1.0
1.1
1/d
Experiment
Rietveld refinement
Residuals

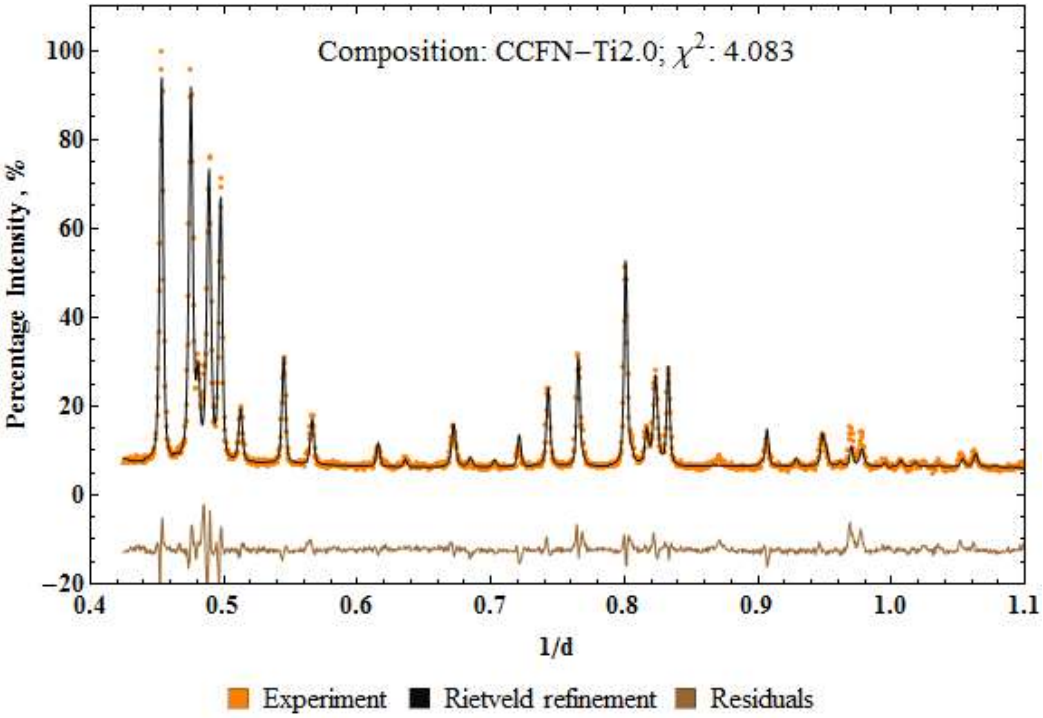
Composition: CCFN−Ti2.0; $\chi^2$: 4.083
Percentage Intensity , %
100
80
60
40
20
0
−20
0.4
0.5
0.6
0.7
0.8
0.9
1.0
1.1
1/d
Experiment
Rietveld refinement
Residuals

## Appendix B: Calculation of errors for compression testing

Performed partly by Yuhe, Huang.

Uncertainty calculations for compression testing was performed following the Manual of Codes of Practice for the Determination of Uncertainties in Mechanical Tests on Metallic Materials [1], with relevant measurement parameters and corresponding symbols shown in Table 1. The sources of uncertainty and their contributions to the measured compression test are considered and shown in Table 2, and are classified as type A and B depending on the way their influences are quantified. Uncertainties evaluated through statistical means are classified as type A while uncertainties evaluated through other means (e.g. via calibration certificate, manufacturer's information) are classified as type B.

Table 18. Selected parameters for measurement of uncertainties.

| Quantity | Symbol | Values |
|---|---|---|
| Applied Load | P | ±0.5% |
| Strain | ε | ±0.5% |
| Specimen original diameter | $d_0$ | ±0.05mm |
| Specimen original gauge length | $l_0$ | ±0.05mm |
| Angle(Specimen/Extensometer) | α | ±1° |
| Load range used for E | ΔP | ±0.5% |
| Elongation range used for E | ΔL | ±0.5% |

In the calculations here the load cell and extensometer uncertainty is 0.05% as obtained from the Zwick Z050 manual. The regression limit was considered to be 2% by considering the average of each calculated Young's modulus slope of the straight line which was fitted to the data utilising the least squares method. The expanded uncertainty, U is obtained by multiplying the combined uncertainty $u_c$ with a coverage factor, k that is selected on the basis of the level of confidence required. For a normal distribution, the coverage factor is considered to be 2, which corresponds to a confidence interval of 95.4%, and is the value used in this publication.

Table 19. Determined uncertainty parameters for CCFN-X (X: Mn, $V_{0.3}$, Pd, $Ti_{0.6}$ and $Al_{0.5}$) compositions.

| Composition | Uncertainty of Proof Strength, $R_{p0.2}$ | Uncertainty of Elastic Modulus, E |
|---|---|---|
| **CCFN** | | |
| **CCFN-Mn** | ±5.16% | ±5.7 |
| **CCFN-$V_{0.3}$** | ±13.22 | ±13.46 |

| | | |
|---|---|---|
| **CCFN-Pd** | ±6.81 | ±7.24 |
| **CCFN-$Ti_{0.6}$** | ±11.16 | ±11.42 |
| **CCFN-$Al_{0.5}$** | ±9.32 | ±9.64 |

Table 2 presents the uncertainties for the compression tests performed in this calculation. The higher uncertainties of CCFN-V and CCFN-Ti may be attributed to the large yield stress which leads to an enhancement of ΔP and $U_{Extenso}$. Detailed information on the calculations may be found below in Table 4-7.

**Glossary of Symbols**

| | |
|---|---|
| $A_0$ | Original cross-sectional area of the parallel length |
| $d_0$ | Original diameter of the parallel length of a cylindrical test-piece |
| E | Young's modulus of elasticity |
| k | Coverage factor used to calculate expanded uncertainty |
| $l_0$ | Original gauge length |
| $L_0$ | Theoretical gauge length |
| P | Load |
| $Rp_{0.2}$ | Proof strength, non-proportional elongation |
| U | Expanded uncertainty |
| U(xi) | Standard uncertainty |
| $u_{Cell}$ | Standard uncertainty on load cell data |
| $u_{Caliper}$ | Standard uncertainty on calliper data |
| $U_E$ | Expanded uncertainty on E |
| $u_{Extenso}$ | Standard uncertainty on extensometer data |
| $U_{Rp0.2}$ | Expanded uncertainty on Rp0.2 |
| ΔL | Elongation increment |
| ΔP | Load increment |
| $U_c(y)$ | Combined uncertainty on the mean result y of a measurand |

Table 20. Template for calculation of compression testing uncertainties.

| Column No. | 1 | 2 | 3 | 4 | 5 | 6 | 7 | 8 | 9 |
|---|---|---|---|---|---|---|---|---|---|
| Source of uncertainty (xi) | | Measurement(Xi) | | Uncertainties | | | | | |
| | | Measurement affected | Nominal or average value | Uncertainty In measurement | Type | Probability Distribution | Divisor dv | Ci | u (Xi) |
| Apparatus | | | | | | | | | |
| Load Cell | | P | (KN) | | B | Rectangular | sqrt(3) | $\frac{l_0}{A_0 \Delta L}$ | u(Cell) |
| Extensometer | | ε | (mm) | | B | Rectangular | sqrt(3) | $\frac{\Delta P l_0}{A_0 \Delta L^2}$ | u(ext) |
| Calliper | | $d_0$ | (mm) | | B | Rectangular | sqrt(3) | $-8\frac{\Delta P l_0}{\pi d_0^3 \Delta L}$ | u(cal) |
| Operator | | | | | | | | | |
| Manual choice of regression limits on graph | | P | (KN) | | A | Normal | 1 | 1 | u(reg) |
| Manual extensometer angular positioning | | ε | (mm) | | A | Normal | 1 | 1 | u(ang) |
| Specimen | | | | | | | | | |
| Original gauge length | | $l_0$ | (mm) | | A | Normal | 1 | 1 | u(gl) |
| | | | | | | | | | |
| Combine standard Uncertainty | | | | | | Normal | | | uc |
| Expanded Uncertainty (with k=2) | | | | | | Normal | | | UE |

| Column No. | 1 | 2 | 3 | 4 | 5 | 6 | 7 | 8 | 9 |
|---|---|---|---|---|---|---|---|---|---|
| Source of uncertainty (xi) | | Measurement(Xi) | | Uncertainties | | | | | |
| | | Measurement affected | Nominal or average value | Uncertainty In measurement | Type | Probability Distribution | Divisor dv | Ci | u (Xi) |
| Apparatus | | | | | | | | | |
| Load Cell | | P | (KN) | | B | Rectangular | sqrt(3) | 1 | u(Cell) |
| Extensometer | | ε | (mm) | | B | Rectangular | sqrt(3) | 1 | u(ext) |
| Young's Modules E | | $R_{P0.2}$ | (Mpa) | | B | Normal | 1 | 1 | u(mod) |
| | | | | | | | | | |
| Combine standard Uncertainty | | | | | | Normal | | | uc |
| Expanded Uncertainty (with k=2) | | | | | | Normal | | | $UR_P0,2$ |

Table 21. Calculation of uncertainties for CCFN-Mn.

| Column No. | 1 | 2 | 3 | 4 | 5 | 6 | 7 | 8 | 9 |
|---|---|---|---|---|---|---|---|---|---|
| Source of uncertainty (xi) | | Measurement(Xi) | | Uncertainties | | | | | |
| | | Measurement affected | Nominal or average value | Uncertainty In measurement | Type | Probability Distribution | Divisor dv | Ci | u (Xi) |
| Apparatus | | | | | | | | | |
| Load Cell | | P | (KN) | 0.5% | B | Rectangular | sqrt(3) | 9.44 | 0.08% |
| Extensometer | | ε | (mm) | 0.5% | B | Rectangular | sqrt(3) | 146.78 | 1.27% |
| Calliper | | $d_0$ | (mm) | 0.05 | B | Rectangular | sqrt(3) | 8.81 | 0.007% |
| Operator | | | | | | | | | |
| Manual choice of regression limits on graph | | P | (KN) | 2% | A | Normal | 1 | 1 | 2% |
| Manual extensometer angular positioning | | ε | (mm) | 1deg | A | Normal | 1 | 1 | 1% |
| Specimen | | | | | | | | | |
| Original gauge length | | $l_0$ | (mm) | 0.05 | A | Normal | 1 | 1 | 0.05% |
| | | | | | | | | | |

| | | | | | | | | |
|---|---|---|---|---|---|---|---|---|
| Combine standard Uncertainty | | | | | Normal | | | 2.58% |
| Expanded Uncertainty (with k=2) | | | | | Normal | | | 5.16% |

| Column No. 1 | 2 | 3 | 4 | 5 | 6 | 7 | 8 | 9 |
|---|---|---|---|---|---|---|---|---|
| Source of uncertainty (xi) | Measurement(Xi) | | Uncertainties | | | | | |
| | Measurement affected | Nominal or average value | Uncertainty In measurement | Type | Probability Distribution | Divisor dv | Ci | u (Xi) |
| Apparatus | | | | | | | | |
| Load Cell | P | (KN) | 0.5% | B | Rectangular | sqrt(3) | 1 | 0.865% |
| Extensometer | ε | (mm) | 0.5% | B | Rectangular | sqrt(3) | 1 | 0.865% |
| Young's Modules E | $R_{P0.2}$ | (Mpa) | 2.58% | B | Normal | 1 | 1 | 2.58% |
| | | | | | | | | |
| Combine standard Uncertainty | | | | | Normal | | | 2.85% |
| Expanded Uncertainty (with k=2) | | | | | Normal | | | 5.7% |

Table 22. Calculation of uncertainties for CCFN-V.

| Column No. 1 | 2 | 3 | 4 | 5 | 6 | 7 | 8 | 9 |
|---|---|---|---|---|---|---|---|---|
| Source of uncertainty (xi) | Measurement(Xi) | | Uncertainties | | | | | |
| | Measurement affected | Nominal or average value | Uncertainty In measurement | Type | Probability Distribution | Divisor dv | Ci | u (Xi) |
| Apparatus | | | | | | | | |
| Load Cell | P | (KN) | 0.5% | B | Rectangular | sqrt(3) | 19.52 | 0.17% |
| Extensometer | ε | (mm) | 0.5% | B | Rectangular | sqrt(3) | 718.1 | 6.22% |
| Calliper | $d_0$ | (mm) | 0.05 | B | Rectangular | sqrt(3) | 20.82 | 0.018% |
| Operator | | | | | | | | |
| Manual choice of regression limits on graph | P | (KN) | 2% | A | Normal | 1 | 1 | 2% |
| Manual extensometer angular positioning | ε | (mm) | 1deg | A | Normal | 1 | 1 | 1% |
| Specimen | | | | | | | | |
| Original gauge length | $l_0$ | (mm) | 0.05 | A | Normal | 1 | 1 | 0.05% |
| | | | | | | | | |
| Combine standard Uncertainty | | | | | Normal | | | 6.61% |
| Expanded Uncertainty (with k=2) | | | | | Normal | | | 13.22% |

| Column No. 1 | 2 | 3 | 4 | 5 | 6 | 7 | 8 | 9 |
|---|---|---|---|---|---|---|---|---|
| Source of uncertainty (xi) | Measurement(Xi) | | Uncertainties | | | | | |
| | Measurement affected | Nominal or average value | Uncertainty In measurement | Type | Probability Distribution | Divisor dv | Ci | u (Xi) |
| Apparatus | | | | | | | | |
| Load Cell | P | (KN) | 0.5% | B | Rectangular | sqrt(3) | 1 | 0.865% |
| Extensometer | ε | (mm) | 0.5% | B | Rectangular | sqrt(3) | 1 | 0.865% |
| Young's Modules E | $R_{P0.2}$ | (Mpa) | 6.61% | B | Normal | 1 | 1 | 6.61% |
| | | | | | | | | |
| Combine standard Uncertainty | | | | | Normal | | | 6.73% |
| Expanded Uncertainty (with k=2) | | | | | Normal | | | 13.46% |

Table 23. Calculation of uncertainties for CCFN-Pd.

| Column No. 1 | 2 | 3 | 4 | 5 | 6 | 7 | 8 | 9 |
|---|---|---|---|---|---|---|---|---|
| Source of uncertainty (xi) | Measurement(Xi) | | Uncertainties | | | | | |
| | Measurement affected | Nominal or average value | Uncertainty In measurement | Type | Probability Distribution | Divisor dv | Ci | u (Xi) |
| Apparatus | | | | | | | | |
| Load Cell | P | (KN) | 0.5% | B | Rectangular | sqrt(3) | 11.79 | 0.102% |
| Extensometer | ε | (mm) | 0.5% | B | Rectangular | sqrt(3) | 294.8 | 2.55% |
| Calliper | $d_0$ | (mm) | 0.05 | B | Rectangular | sqrt(3) | 14.15 | 0.012% |
| Operator | | | | | | | | |
| Manual choice of regression limits on graph | P | (KN) | 2% | A | Normal | 1 | 1 | 2% |
| Manual extensometer angular positioning | ε | (mm) | 1deg | A | Normal | 1 | 1 | 1% |
| Specimen | | | | | | | | |
| Original gauge length | $l_0$ | (mm) | 0.05 | A | Normal | 1 | 1 | 0.05% |
| | | | | | | | | |
| Combine standard | | | | | Normal | | | |

| | | | | | | | | |
|---|---|---|---|---|---|---|---|---|
| Uncertainty | | | | | | | | 3.403% |
| Expanded Uncertainty (with k=2) | | | | | Normal | | | 6.806% |

| Column No. | 1 | 2 | 3 | 4 | 5 | 6 | 7 | 8 | 9 |
|---|---|---|---|---|---|---|---|---|---|
| Source of uncertainty (xi) | | Measurement(Xi) | | Uncertainties | | | | | |
| | | Measurement affected | Nominal or average value | Uncertainty In measurement | Type | Probability Distribution | Divisor dv | Ci | u (Xi) |
| Apparatus | | | | | | | | | |
| Load Cell | | P | (KN) | 0.5% | B | Rectangular | sqrt(3) | 1 | 0.865% |
| Extensometer | | ε | (mm) | 0.5% | B | Rectangular | sqrt(3) | 1 | 0.865% |
| Young's Modules E | | $R_{P0.2}$ | (Mpa) | 3.403% | B | Normal | 1 | 1 | 3.403% |
| | | | | | | | | | |
| Combine standard Uncertainty | | | | | | Normal | | | 3.62% |
| Expanded Uncertainty (with k=2) | | | | | | Normal | | | 7.24% |

Table 24. Calculation of uncertainties for CCFN-Ti.

| Column No. 1 | 2 | 3 | 4 | 5 | 6 | 7 | 8 | 9 |
|---|---|---|---|---|---|---|---|---|
| Source of uncertainty (xi) | Measurement(Xi) | | Uncertainties | | | | | |
| | Measurement affected | Nominal or average value | Uncertainty In measurement | Type | Probability Distribution | Divisor dv | Ci | u (Xi) |
| Apparatus | | | | | | | | |
| Load Cell | P | (KN) | 0.5% | B | Rectangular | sqrt(3) | 14.15 | 0.123% |
| Extensometer | ε | (mm) | 0.5% | B | Rectangular | sqrt(3) | 589.76 | 5.107% |
| Calliper | $d_0$ | (mm) | 0.05 | B | Rectangular | sqrt(3) | 23.59 | 0.0204% |
| Operator | | | | | | | | |
| Manual choice of regression limits on graph | P | (KN) | 2% | A | Normal | 1 | 1 | 2% |
| Manual extensometer angular positioning | ε | (mm) | 1deg | A | Normal | 1 | 1 | 1% |
| Specimen | | | | | | | | |
| Original gauge length | $l_0$ | (mm) | 0.05 | A | Normal | 1 | 1 | 0.05% |
| | | | | | | | | |
| Combine standard Uncertainty | | | | | Normal | | | 5.58% |
| Expanded Uncertainty (with k=2) | | | | | Normal | | | 11.16% |

| Column No. 1 | 2 | 3 | 4 | 5 | 6 | 7 | 8 | 9 |
|---|---|---|---|---|---|---|---|---|
| Source of uncertainty (xi) | Measurement(Xi) | | Uncertainties | | | | | |
| | Measurement affected | Nominal or average value | Uncertainty In measurement | Type | Probability Distribution | Divisor dv | Ci | u (Xi) |
| Apparatus | | | | | | | | |
| Load Cell | P | (KN) | 0.5% | B | Rectangular | sqrt(3) | 1 | 0.865% |
| Extensometer | ε | (mm) | 0.5% | B | Rectangular | sqrt(3) | 1 | 0.865% |
| Young's Modules E | $R_{P0.2}$ | (Mpa) | 5.58% | B | Normal | 1 | 1 | 5.58% |
| | | | | | | | | |
| Combine standard Uncertainty | | | | | Normal | | | 5.71% |
| Expanded Uncertainty (with k=2) | | | | | Normal | | | 11.42% |

Table 25. Calculation of uncertainties for CCFN-Al.

| Column No. 1 | 2 | 3 | 4 | 5 | 6 | 7 | 8 | 9 |
|---|---|---|---|---|---|---|---|---|
| Source of uncertainty (xi) | Measurement(Xi) | | Uncertainties | | | | | |
| | Measurement affected | Nominal or average value | Uncertainty In measurement | Type | Probability Distribution | Divisor dv | Ci | u (Xi) |
| Apparatus | | | | | | | | |
| Load Cell | P | (KN) | 0.5% | B | Rectangular | sqrt(3) | 14.15 | 0.12% |
| Extensometer | ε | (mm) | 0.5% | B | Rectangular | sqrt(3) | 471.81 | 4.09% |
| Calliper | $d_0$ | (mm) | 0.05 | B | Rectangular | sqrt(3) | 18.87 | 0.016% |
| Operator | | | | | | | | |
| Manual choice of regression limits on graph | P | (KN) | 2% | A | Normal | 1 | 1 | 2% |
| Manual extensometer angular positioning | ε | (mm) | 1deg | A | Normal | 1 | 1 | 1% |
| Specimen | | | | | | | | |
| Original gauge length | $l_0$ | (mm) | 0.05 | A | Normal | 1 | 1 | 0.05% |
| | | | | | | | | |
| Combine standard | | | | | Normal | | | |

| | | | | | | | | |
|---|---|---|---|---|---|---|---|---|
| Uncertainty | | | | | | | | 4.66% |
| Expanded Uncertainty (with k=2) | | | | | Normal | | | 9.32% |

| Column No. | 1 | 2 | 3 | 4 | 5 | 6 | 7 | 8 | 9 |
|---|---|---|---|---|---|---|---|---|---|
| Source of uncertainty (xi) | | Measurement(Xi) | | Uncertainties | | | | | |
| | | Measurement affected | Nominal or average value | Uncertainty In measurement | Type | Probability Distribution | Divisor dv | Ci | u (Xi) |
| Apparatus | | | | | | | | | |
| Load Cell | | P | (KN) | 0.5% | B | Rectangular | sqrt(3) | 1 | 0.865% |
| Extensometer | | ε | (mm) | 0.5% | B | Rectangular | sqrt(3) | 1 | 0.865% |
| Young's Modules E | | $R_{P0.2}$ | (Mpa) | 10.103% | B | Normal | 1 | 1 | 4.66% |
| | | | | | | | | | |
| Combine standard Uncertainty | | | | | | Normal | | | 4.82% |
| Expanded Uncertainty (with k=2) | | | | | | Normal | | | 9.64% |

**References**

[1] L Legendre G. Brigodiot and F Tronel, 2000. Determination of Uncertainties in compress testing, Manual Codes of Practice for determination of uncertainties in mechanical tests on metallic materials, Code of No. 8, UNCERT COP08, France.

## Appendix C: Application of the Stoner Model to Rigid Band Approximation

Provided by: Dr. Jan Wrobel, Culham Centre for Fusion Energy

The structural stability of simple FCC and BCC phases, and all other complex phases observed in multi-component alloys can be investigated by using the frozen potential approximation (FPA) to density functional theory (DFT). Within the first order approximation the energy difference between any two non-magnetic structures is given by the difference between their band energies at a fixed equilibrium volume, $V_0$ [67,68,92]:

$$\Delta E_{Non-Mag}^{(1-2)} \approx \Delta E_{Band}^{(1-2)} = \left[2\int_{-\infty}^{\varepsilon_F^{(1)}} \varepsilon D^{(1)}(\varepsilon)d\varepsilon - 2\int_{-\infty}^{\varepsilon_F^{(2)}} \varepsilon D^{(2)}(\varepsilon)d\varepsilon\right]_{\Delta V_0=0} \quad \text{(I)}$$

where $D^{(1)}(\varepsilon)$ and $D^{(2)}(\varepsilon)$ are the densities of states (DOS) per atom with a factor of 2 for a spin to energy $\varepsilon$ and $\varepsilon_F^{(1)}$ and $\varepsilon_F^{(2)}$ are the Fermi energies for structure 1 and 2, respectively. They are determined from the number of valence electrons per atom:

$$n = 2\int_{-\infty}^{\varepsilon_F^{(1)}} D^{(1)}(\varepsilon)d\varepsilon = 2\int_{-\infty}^{\varepsilon_F^{(2)}} D^{(2)}(\varepsilon)d\varepsilon \quad \text{(II)}$$

Frozen potentials for the different atomic species are determined from self-consistent calculations, normally for structures with a small unit cell. They are then transferred into other structures with the same alloy composition and the same equilibrium volume. The difference between the band energies $\Delta E_{Band}^{(1-2)}$ is calculated under the constraint that the potential within the Wigner-Seitz sphere remains unchanged (frozen) when going from one structure type to another. Since the energy difference in the first order frozen potential approximation is computed assuming fixed atomic volumes, this approximation is correct for structures with relatively similar equilibrium atomic volumes like for example FCC and BCC phases, which can be related to each other through the Bain transformation.

Assuming that alloying changes the number of valence electrons per atom but the electronic DOS of different phases remain rigid (the rigid band approximation), the variation of the energy difference as a function of the number of electrons can be evaluated by comparing the band energies, see equation (I)[30,31,93].

Within the present work, the RBA model has been generalised for the case of magnetic materials like CCFN-based alloys using the Stoner model of magnetism[60–62]. In transition metal alloys the latter one introduces magnetism by introducing local exchange fields within the band energy concept. In particular, electrons with spins up and down have different on-site energies depending

on whether their spin is parallel or anti-parallel to the local magnetic moment. The effective on-site energy $\varepsilon_i^{\sigma}$ is given by

$$\varepsilon_i^{\sigma} = \varepsilon_i \pm \frac{1}{2} I_i m_i \tag{III}$$

where $\varepsilon_i$ is the single-particle non-magnetic on-site energy, $m_i = n_i^{\downarrow} - n_i^{\uparrow}$, is the difference between electron occupancies of site $i$ by spin-down and spin-up electrons with a spin index $\sigma$. The Stoner exchange parameter $I_i$ refers to the exchange splitting of on-site energies of electrons with spin up and spin down due to the local magnetic moment $m_i$ [60,61,65].

From equation (III), the energy difference between two magnetic structures, following the Stoner model of magnetism (Stoner Model I), corrected for the double counting contribution, and normalised by the number of atoms, N in both structures can be given by:

$$\Delta E_{Mag}^{(1-2)} = \frac{\Delta E_{Spin-Band}^{(1-2)} + \frac{1}{4}\left[\sum_i I_i m_i^{2(1)} - \sum_i I_i m_i^{2(2)}\right]}{N} \tag{IV}$$

where the first term is the spin-polarised band energy difference between any two magnetic structures at a fixed equilibrium volume $V_0$ (defined below in equation (V)), the second term is the double-counting contribution arising from magnetic interactions[60–62], and $N$ is the number of atoms in both considered structures. $\Delta E_{Spin-Band}^{(1-2)}$ is defined as:

$$\Delta E_{Spin-Band}^{(1-2)} = \left[\int_{-\infty}^{\varepsilon_F^{(1)}} \left(\varepsilon D^{(1)\uparrow}(\varepsilon) + \varepsilon D^{(1)\downarrow}(\varepsilon)\right) d\varepsilon - \int_{-\infty}^{\varepsilon_F^{(2)}} \left(\varepsilon D^{(2)\uparrow}(\varepsilon) + \varepsilon D^{(2)\downarrow}(\varepsilon)\right) d\varepsilon\right]_{\Delta V_0 = 0} \tag{V}$$

where $D^{(1)\uparrow}(\varepsilon)$ and $D^{(2)\uparrow}(\varepsilon)$ are the spin-polarised total DOS per atom for electrons with spin-up and $D^{(1)\downarrow}(\varepsilon)$ and $D^{(2)\downarrow}(\varepsilon)$ are the spin-polarised total DOS per atom for electrons with spin-down. The Stoner parameters in equation (IV) are assumed to be constant for each type of atoms[94]**.** However, application of equation (IV) requires knowledge of the magnetic moments of all atoms as a function of *n* in the system, of which is difficult to be validated experimentally. Therefore, we use an effective Stoner parameter $I_{eff}$ which refers to the exchange splitting of the on-site energies of electrons with spin-up and spin-down due to the average atomic magnetic moment $m_{av}$, defined as:

$$I_{eff}\, m_{av} = \varepsilon_F^{\downarrow} - \varepsilon_F^{\uparrow} \tag{VI}$$

where $\varepsilon_F^{\uparrow}$ and $\varepsilon_F^{\downarrow}$ are the Fermi energies for electrons with spin-up and spin-down, respectively, defined as energies of the non-magnetic total DOS, $D(\varepsilon)$, which are the number of electrons per atom with spin-up and spin-down, obtained from the spin-polarised total DOS. The average magnetic moment of the entire simulation cell from the non-magnetic total DOS is equal to the one obtained from the spin-polarised total DOS and is given by:

$$m_{av} = \int_{-\infty}^{\varepsilon_F} D^{\downarrow}(\varepsilon)d\varepsilon - \int_{-\infty}^{\varepsilon_F} D^{\uparrow}(\varepsilon)d\varepsilon = \int_{\varepsilon_F^{\uparrow}}^{\varepsilon_F^{\downarrow}} D(\varepsilon)d\varepsilon \qquad \text{(VII)}$$

By using the effective Stoner parameter and the average magnetic moment the energy difference between any two magnetic structures in the effective Stoner Model II can now be written as:

$$\Delta E_{Mag}^{(1-2)} = \Delta E_{Spin-Band}^{(1-2)} + \frac{1}{4}\left[I_{eff}^{(1)} {m_{av}^{2}}^{(1)} - I_{eff}^{(2)} {m_{av}^{2}}^{(2)}\right] \qquad \text{(VIII)}$$

Both Stoner Model I and effective Stoner Model II can be justified by the comparison of energy differences with those obtained using the LMTO code. As shown in Table SI the energy differences between the considered magnetic structures and the BCC structures with the same composition calculated using both equation (IV) and (VIII) are in quantitative agreement with each other and in line with the results calculated using the LMTO code. The only exception is that the C14 structure of $Co_9Cr_{12}Fe_9Ni_6$ alloy which is less stable than the BCC phase when equation (VIII) is applied and it is more stable than the BCC phase by using equation (IV) and the LMTO code. However, all the considered methods predict that the FCC phase is the most stable one.

**Table SI**. Average magnetic moments obtained using equation (VII) ( $m_{av}$ ) and energy differences ( $\Delta E_{mag}$ ) between the considered magnetic structures and the BCC structures with the same composition calculated using equations (IV) and (VIII), compared with the results calculated using the LMTO code. $I_{eff}$ is the effective Stoner parameters calculated using equation (VI). Energies, magnetic moments and effective Stoner parameters are given in $eV$, $\mu_\beta$ per atom and $eV/\mu_\beta$, respectively. The valence electron concentration of considered structures is indicated by *n*.

| | Structure | $\Delta E_{Mag}$ (equation (IV)) | $\Delta E_{Mag}$ (equation (VIII)) | $\Delta E_{Mag}$ (LMTO) | $m_{av}$ (equation (VII)) | $m_{av}$ (LMTO) | $I_{eff}$ (equation (VI)) |
|---|---|---|---|---|---|---|---|
| **CCFN $Co_8Cr_8Fe_8Ni_8$ (*n* = 8.25)** | FCC | -0.136 | -0.099 | -0.083 | 0.372 | 0.372 | 1.295 |
| | BCC | | | | 0.421 | 0.421 | 1.302 |
| **CCFN-Al $Co_8Fe_8Ni_8Al_8$ (*n* = 7.5)** | FCC | -0.043 | -0.020 | -0.001 | 0.939 | 0.930 | 3.940 |
| | BCC | | | | 1.011 | 0.990 | 4.392 |
| | B2 | -0.065 | -0.102 | -0.072 | 0.948 | 0.948 | 4.124 |
| **CCFN-Pd $Co_6Cr_7Fe_7Ni_6Pd_6$ (*n* = 8.5)** | FCC | -0.139 | -0.070 | -0.064 | 0.881 | 0.864 | 3.631 |
| | BCC | | | | 0.913 | 0.915 | 3.746 |
| **CCFN-V $Co_9Cr_{12}Fe_9Ni_6$ (*n* = 8.133)** | FCC | -0.147 | -0.123 | -0.073 | 0.350 | 0.344 | 1.228 |
| | BCC | | | | 0.415 | 0.422 | 1.205 |
| | Sigma | -0.151 | -0.120 | -0.069 | 0.312 | 0.317 | 0.993 |
| **CCFN-Ti $Co_9Cr_{12}Fe_9Ni_6$ (*n* = 7.917)** | FCC | -0.063 | -0.027 | -0.021 | 0.687 | 0.171 | 0.987 |
| | BCC | | | | 0.691 | 0.172 | 0.831 |
| | C14 | -0.018 | 0.022 | -0.013 | 0.817 | 0.819 | 0.909 |

## Appendix D: Thomas-Fermi-Dirac Electron Density Code (Mathematica .nb format)

The code is commented, the syntax for comments are (*COMMENT*).

----------test_runge.nb Start----------

**Runge-Kutta for 2nd order ODE**

```
ClearAll["Global`*"]
(*Required equations are defined here*)
\[Epsilon]=(3/(32(\[Pi])^2))^(1/3) Z^(-2/3);
\[Mu]=(5.29*10^-11)((9\[Pi]^2)/(128Z))^(1/3);

(*y''(t)=t(Sqrt[y/t]+(3/(32(22/7)^2))^(1/3)Z^(-2/3))^3 with y(0)=1 and y'(0)=a2*)
(*f[t_]=Pseudo \[Psi] and g[t]=Pseudo \[Psi]' based on Ren et al.'s work*)
f[t_]:=1+a2 t+(4 t^(3/2))/3+(3 t^2 \[Epsilon])/2+t^4 ((2 a2)/15+(77 \[Epsilon]^2)/120)+t^(5/2) ((2
a2)/5+(4 \[Epsilon]^2)/5)+t^(7/2) ((3 a2^2)/70+(5 \[Epsilon])/7+(6 a2 \[Epsilon]^2)/35)+t^3 (1/3+(a2
\[Epsilon])/2+\[Epsilon]^3/6)+t^5 (a2^2/175+(5 \[Epsilon])/28+(137 a2 \[Epsilon]^2)/1400+(17
\[Epsilon]^4)/200)+t^(9/2) (2/27-a2^3/252+(41 a2 \[Epsilon])/210-(a2^2 \[Epsilon]^2)/42+(14
\[Epsilon]^4)/45)+t^6 (4/405+(4 a2^3)/1575+(a2 \[Epsilon])/21+(8 a2^2 \[Epsilon]^2)/525+(509
\[Epsilon]^3)/5040-(2 a2 \[Epsilon]^4)/175)+t^(11/2) ((31 a2)/1485+a2^4/1056+(15397
\[Epsilon]^2)/83160+(83 a2^2 \[Epsilon]^2)/9240+(a2^3 \[Epsilon]^2)/132+(37 a2
\[Epsilon]^3)/3465+\[Epsilon]^5/99)+t^(13/2) ((557 a2^2)/100100-(5 a2^5)/4576+(272
\[Epsilon])/9009+(47 a2^3 \[Epsilon])/48048+(21457 a2 \[Epsilon]^2)/40040-(15 a2^4
\[Epsilon]^2)/4576+(41 a2^2 \[Epsilon]^3)/4004+(149 \[Epsilon]^4)/6600-(a2 \[Epsilon]^5)/286);
g[t_]:=a2+2 Sqrt[t]+3 t \[Epsilon]+4 t^3 ((2 a2)/15+(77 \[Epsilon]^2)/120)+5/2 t^(3/2) ((2 a2)/5+(4
\[Epsilon]^2)/5)+7/2 t^(5/2) ((3 a2^2)/70+(5 \[Epsilon])/7+(6 a2 \[Epsilon]^2)/35)+3 t^2 (1/3+(a2
\[Epsilon])/2+\[Epsilon]^3/6)+5 t^4 (a2^2/175+(5 \[Epsilon])/28+(137 a2 \[Epsilon]^2)/1400+(17
\[Epsilon]^4)/200)+9/2 t^(7/2) (2/27-a2^3/252+(41 a2 \[Epsilon])/210-(a2^2 \[Epsilon]^2)/42+(14
\[Epsilon]^4)/45)+6 t^5 (4/405+(4 a2^3)/1575+(a2 \[Epsilon])/21+(8 a2^2 \[Epsilon]^2)/525+(509
\[Epsilon]^3)/5040-(2 a2 \[Epsilon]^4)/175)+11/2 t^(9/2) ((31 a2)/1485+a2^4/1056+(15397
\[Epsilon]^2)/83160+(83 a2^2 \[Epsilon]^2)/9240+(a2^3 \[Epsilon]^2)/132+(37 a2
\[Epsilon]^3)/3465+\[Epsilon]^5/99)+13/2 t^(11/2) ((557 a2^2)/100100-(5 a2^5)/4576+(272
\[Epsilon])/9009+(47 a2^3 \[Epsilon])/48048+(21457 a2 \[Epsilon]^2)/40040-(15 a2^4
\[Epsilon]^2)/4576+(41 a2^2 \[Epsilon]^3)/4004+(149 \[Epsilon]^4)/6600-(a2 \[Epsilon]^5)/286);
```

```
(*Second diffrential equation \[Psi] following the Poisson relationship=*)
p[t_,y_]:=t (Sqrt[y/t]+(3/(32(\[Pi])^2))^(1/3) Z^(-2/3))^3;

(*Boundary conditions, y[0] and g[0] is equivalent to omiga[0], which represents the null point*)
omiga[0]=0.48;
f[0]=f[omiga[0]^2/2];
g[0]=g[omiga[0]^2/2];
```

**Function to determine a2 and \[Psi]**

```
(*Function to search for each element*)
calculateValues[atomicNumver_,tmaxValue_,a2Max_,a2Min_]:=(
(*Define Variables that are called in function*)
(*Atomic number of the element to be searched*)
Z=atomicNumver;
(*Max number of steps for do function to obtain list of \[Psi] results for each w*)
tmax=tmaxValue;
(*Number of a2 steps to run*)
nmax=10;
(*Min a2*)
a2max=a2Max;
(*Max a2*)
a2min=a2Min;
(*define the step size, da2*)
da2=(a2max-(a2min))/nmax;
Do[{
(*a2 defined as a function of step size*)
a2=a2min+(da2*n);
(*Do start to obtain list of \[Psi] against w*)
Do[{
omiga[n+1]=omiga[n]+0.1;
x[n_]:=omiga[n]^2/2;
h=x[n+1]-x[n];
k1=g[n];
l1=p[x[n],f[n]];
```

```
k2=g[n]+(l1 h)/2;
l2=p[x[n]+h/2,f[n]+(k1 h)/2];

k3=g[n]+(l2 h)/2;
l3=p[x[n]+h/2,f[n]+(k2 h)/2];
k4=g[n]+l3 h;
l4=p[x[n+1],f[n]+k3 h];
f[n+1]=f[n]+(h/6 )(k1+2 k2+2 k3+k4);
g[n+1]=g[n]+(h/6) (l1+2 l2+2l3+l4);
},{n,0,tmax}];

(*Defining table of \[Omega],\[Psi]*)
table1=Table[{omiga[i],f[i],x[i]},{i,0,tmax}];
(*Defining table of \[Omega],\[Psi]^2-\[Psi]/2*)
table3=Table[{omiga[i],Abs[g[i]-f[i]/x[i]]},{i,0,tmax}];
(*Defining variables listed as a function of 0<n<nmax*)
radius[n]=wValue[n]^2/2 \[Mu] 10^10;
wValue[n]=table3[[Ordering[table3[[All,2]],1],1]][[1]];
phi[n]=table1[[Ordering[table3[[All,2]],1],2]][[1]];
xValue[n]=table1[[Ordering[table1[[All,2]],1],3]][[1]];
},{n,0,nmax}];
(*Creating table containing n, a2, \[Omega], Subscript[r, ws], \[Psi]*)
table4=Table[{n,a2min+(da2*n),radius[n],Z/(4\[Pi] \[Mu]^3)
(\[Epsilon]+(phi[n]/xValue[n])^(1/2))^3},{n,0,nmax}];
(*Calling table 4 as an output in tableform*)
table4//TableForm
);
(*Eg: Calculate values for Cu (Z=29) at 50 intervals*)
(*3 decimal places refinement*)
calculateValues[26.17,50,-1.6248,-1.625]
0       -1.625          1.58304         -2.61758*10^28+1.39559*10^28 I
1       -1.62498        1.6545          -2.07559*10^28+1.48789*10^28 I
2       -1.62496        1.80215         -1.71583*10^28+1.53566*10^28 I
3       -1.62494        2.11639         -2.6661*10^27+1.34254*10^28 I
```

| | | | |
|---|---|---|---|
| 4 | -1.62492 | 1.72754 | 9.40891*10^28 |
| 5 | -1.6249 | 1.58304 | 1.55965*10^29 |
| 6 | -1.62488 | 1.51316 | 2.19175*10^29 |
| 7 | -1.62486 | 1.44485 | 2.70941*10^29 |
| 8 | -1.62484 | 1.37812 | 3.03986*10^29 |
| 9 | -1.62482 | 1.37812 | 3.66395*10^29 |
| 10 | -1.6248 | 1.31297 | 4.12254*10^29 |

----------test_runge.nb End----------